UNIVERSITÀ DEGLI STUDI DI MILANO

Scuola di Dottorato in Fisica, Astrofisica e Fisica Applicata
Dipartimento di Fisica

Corso di Dottorato in Fisica, Astrofisica e Fisica Applicata
Ciclo XXIV

Dynamics of

Globular Clusters

Settore Scientifico Disciplinare FIS/05

Supervisore: Professor Giuseppe BERTIN

Coordinatore: Professor Marco BERSANELLI

Tesi di Dottorato di:
Anna Lisa VARRI

Anno Accademico 2010-2011

Commission of the final examination:

External Referee:
Professor Douglas C. Heggie, University of Edinburgh, Department of Mathematics

External Member:
Professor Luca Ciotti, Università degli Studi di Bologna, Dipartimento di Astronomia

Internal Member (Ph.D. supervisor):
Professor Giuseppe Bertin, Università degli Studi di Milano, Dipartimento di Fisica

Final examination:

Saturday, July 14, 2012

Università degli Studi di Milano, Dipartimento di Fisica, Milano, Italy

MIUR subjects:

FIS/05 - Astronomia e Astrofisica

PACS:

98.10.+z	Stellar dynamics and kinematics
98.20.-d	Stellar clusters and associations
98.20.Gm	Globular clusters in the Milky Way

Contents

List of Figures

List of Tables

Introduction

Motivation

Globular star clusters have long been considered the ideal astrophysical systems for the study of stellar dynamics. For such stellar systems, the relevant two-body relaxation times are typically shorter than their age, so that it can be argued that they are close to a thermodynamically relaxed state. A classical problem in stellar dynamics is the search for self-consistent equilibrium solutions of the "collisionless" Boltzmann equation, where the mean potential is generated by the distribution of stars populating the system. In this approach, the starting point is the identification of an appropriate form for the one-particle distribution function in phase space.

Indeed, as a zeroth-order dynamical description, the class of models defined as a truncated Maxwellian distribution function, supplemented by the assumption of spherical symmetry (the King 1966 models), have had remarkable success in the application to observed globular clusters. In recent years, thanks to high resolution space and ground-based observations, great progress has been made in the acquisition of detailed information of the structure of these stellar systems (e.g., see McLaughlin et al. 2006; Anderson & van der Marel 2010). In addition, recent improvements in computational speed of the codes for performing N-body simulations and the availability of accelerator hardware (GRAvity PipEs, Graphic Processing Units) allow us to begin the study of the entire dynamical evolution of selected globular star clusters on a star-by-star basis (see the N-body models of Palomar 14 and M4, by Zonoozi et al. 2011 and D. C. Heggie, respectively).

Such progress calls for a renewed effort on the side of dynamical modelling. In fact, more general analytical models would have a a twofold role. On the observational side, they could serve as a useful guide for the interpretation of the relevant photometric and kinematic observables and they provide a first insight into some observational issues only partly understood, such as the detailed distribution of angular momentum or the physical origin of the deviations from spherical symmetry observed in some globular clusters (e.g., see van den Bergh 2008). On the the theoretical side, realistic analytical models could provide more appropriate initial conditions for numerical simulations (e.g., in which internal rotation and external tidal field are properly taken into account), allowing us to address a number of long-standing issues, such as the interplay between two-body relaxation processes and angular momentum transport or the effects induced by different tidal environments on the dynamical evolution of star clusters.

Thesis overview

Main results

Driven by the motivations described above, the present Thesis is devoted to the study of the internal dynamics of globular clusters, with the aim of providing a more realistic dynamical framework for this class of stellar systems, in which fundamental physical ingredients such as the external tidal field, internal rotation, and weak anisotropy in velocity space are properly taken into account. The main results of the Thesis are summarized below.

Self-consistent triaxial tidal models: As a generalization of the well known family of spherical King models, we constructed a family of triaxial models in which the deviations from sphericity are induced by the presence of an external tidal field, taken into account self-consistently. By considering the simple case of a cluster in circular orbit within a host galaxy, the equilibrium distribution function is obtained from the one describing the spherical models by replacing the energy integral with the relevant Jacobi integral in the presence of the stationary tidal field (see also Heggie & Ramamani 1995). The construction of the model requires the solution of a singular perturbation problem for the relevant Poisson equation. A method of solution to any desired order is devised, with a formulation of the equation for the general term of the perturbation series by means of the *Fáa di Bruno formula* (see Faá di Bruno 1855); the explicit solution up to the second order in the perturbation parameter is provided. In particular, the singularity is cured by the introduction of a boundary layer and, to obtain a uniformly valid solution over the entire domain, an asymptotic matching is performed, by application of the Van Dyke principle (see Van Dyke 1975). A full characterization of the resulting configurations in terms of the relevant intrinsic and projected properties has been given and the range of the predicted flattening is consistent with that observed in most Galactic globular clusters.

Self-consistent axisymmetric rotating models: Following general statistical mechanics considerations, we constructed a family of rigidly rotating models defined as an extension of the King models to the case of axisymmetric equilibria, flattened by solid-body rotation. The relevant distribution function depends only on the Jacobi integral associated with the internal rotation; the structure of the models is determined by solving the relevant Poisson equation with the same perturbation method discussed for the tidal models, since the corresponding singular perturbation problem is formally equivalent. In addition, we also considered a second family of models characterized by differential rotation, designed to be rigid in the central regions and to vanish in the outer parts. In this case the relevant Poisson equation is solved by a spectral iteration method, based on the Legendre expansion of the density and the potential. A full description of the photometric and kinematic observables has been provided and the models in the moderate rotation regime are particularly suited to the description of the observed rotating star clusters. For general interest in stellar dynamics, we also studied the models in the strong rotation regime, which tend to show a central toroidal structure.

Dynamical stability of differentially rotating stellar systems: By means of specifically designed N-body simulations with a direct code (STARLAB, see Portegies Zwart et al. 2001), a full stability analysis of the family of differentially rotating models has been performed. As expected, configurations in the moderate differential rotation regime are found to be dynamically stable. Curiously, there also exists an intermedi-

ate rotation regime in which the systems exhibit a central toroidal structure and are dynamically stable. In turn, a new dynamical instability, characterized by a variety of unstable Fourier modes of the density distribution, is observed in models with high degree of differential rotation, in striking analogy with recent stability analyses of differentially rotating fluids with polytropic equations of state (Centrella et al. 2001; Saijo et al. 2003; Ou & Tohline 2006). The excitation of an unstable mode seems to be triggered by the presence of the relevant corotation point inside the rotating configuration. This result may help to clarify the physical motivation of the "empirical" Ostriker & Peebles stability criterion for rotating stellar systems (Ostriker & Peebles 1973).

Long-term dynamical evolution of rotating stellar systems: The long-term dynamical evolution of the differentially rotating models, studied as isolated systems, has been investigated by means of a comprehensive survey of N-body simulations. This study clarifies how the presence of global angular momentum affects the evolution of stellar systems with respect to the traditional paradigm for the dynamical evolution of nonrotating models (for an elegant summary, see Heggie & Hut 2003) and extends the results obtained in the context of Fokker-Planck evolutionary models with rotation (see Einsel & Spurzem 1999; Kim et al. 2002, among others). In particular, by comparing the evolution of several rotating models with selected nonrotating models, characterized by the same initial structural properties, we found that rotating configurations reach core collapse more rapidly. Following early investigations (Akiyama & Sugimoto 1989), we also interpreted the evolution of a rotating system by distinguishing between a short initial phase, in which the gravo-gyro instability (Hachisu 1979) takes place and subsequently levels off, and a second phase in which the residual rotation no longer affects the dynamical evolution of the system, which experiences the gravothermal catastrophe and reaches core collapse, as it happens for nonrotating configurations.

Observational signatures of internal rotation in Galactic globular clusters: The family of differentially rotating models studied in the present Thesis show a variety of realistic velocity dispersion profiles, characterized by the presence of pressure isotropy and radially-biased anisotropy in the central and intermediate regions, respectively. The kinematical behavior in the outer parts strictly depends on the adopted truncation prescription; in particular, the family which, in the nonrotating limit, reduces to the Wilson spheres is characterized by tangentially-biased anisotropy. This kinematical feature (rarely obtained in equilibrium models) is of great interest as tangentially-biased pressure anisotropy is observed in the presence of internal rotation in globular clusters. For example, the full three-dimensional view of the velocity space of ω Cen, obtained from proper motions and radial velocities measurements, has revealed that this object is characterized by significant rotation and tangential anisotropy in the outer parts (in particular, see van de Ven et al. 2006). We successfully applied such family of models to the interpretation of the structure and kinematics of three Galactic globular cluster, characterized by the presence of internal rotation, namely ω Cen, 47 Tuc, and M15. The selection of the relevant model has been performed by a method which combines a number of physically-based kinematic criteria with a more statistically rigorous best-fit procedure for the determination of the relevant dimensionless parameters and physical scales of the configuration, respectively.

Pressure anisotropy as signature of partial relaxation in Galactic globular clusters: On the observational side, we also performed a photometric and kinematic study

of sample of Galactic globular clusters, by means of spherical King and $f^{(\nu)}$ models. The latter is a family of radially-biased spherical models, explicitly constructed to describe violently relaxed elliptical galaxies (see Bertin & Stiavelli 1993, Bertin & Trenti 2003). The study suggests that less relaxed clusters tend to conform to the picture of formation via incomplete "violent relaxation", i.e. the process associated with the rapid fluctuations of the gravitational potential during the early collapse phase of a self-gravitating system (see Lynden-Bell 1967, van Albada 1982).

Organizational note

The present Thesis consists of three Parts, for a total of eight Chapters. Each part is devoted to the study of the effects on the internal dynamics of globular clusters of a specific physical ingredient. Part I is composed of Chapters 2 and 3 and presents the construction and characterization of self-consistent equilibria in the presence of an external tidal field. Part II spans from Chapter 4 to Chapter 7 and addresses several aspects of the role played by internal rotation in stellar systems, both from the theoretical and observational point of view. Part III, which actually corresponds solely to Chapter 8, is dedicated to the analysis of the effects of anisotropy in the velocity space, with particular reference to the relaxation state of the stellar system. Parts I, III, and a substantial fraction of Part II have appeared as refereed publications in scientific journals; co-authors of the relevant articles are mentioned below. Some variations have been made in the presentation of previously published results, to maintain consistency of style and content structure through the manuscript.

Chapter 1: Globular clusters as quasi-relaxed stellar systems: We set the stage by describing some basic structural and dynamical properties of globular star clusters. Some introductory remarks about the methods traditionally used in stellar dynamics, with emphasis on the description of low-mass stellar systems, are also presented.

Chapter 2. The construction of nonspherical models of quasi-relaxed stellar systems: We consider the general problem of the construction of three-dimensional nonspherical self-consistent solutions of the collisionless Boltzmann equation and we propose an analytical perturbation method and numerical spectral iteration method for solving the relevant Poisson equation. The application to the case in which the stellar system is in the presence of an external (stationary) tidal field is then explicitly discussed. This work has been completed in collaboration with G. Bertin and has been published as an article in *The Astrophysical Journal* (Bertin & Varri 2008), on which the Chapter is based.

Chapter 3. Properties of quasi-relaxed stellar systems in an external tidal field: We describe in systematic detail the intrinsic and the projected structure and kinematics of the models introduced in Chapter 2, covering the entire parameter space, from the case of sub-critical to that of critical tidal strength regime. This work has been completed in collaboration with G. Bertin and has been published as an article in *The Astrophysical Journal* (Varri & Bertin 2009), on which the Chapter is based.

Chapter 4. New self-consistent rotating equilibria: We present two new classes of self-consistent axisymmetric models characterized by the presence of rigid and differential internal rotation, respectively. A full description in terms of the principal photometric and kinematic observables is provided. This work has been com-

pleted in collaboration with G. Bertin and has been published as an article in *Astronomy & Astrophysics* (Varri & Bertin 2012), on which the Chapter is based.

Chapter 5. Dynamical stability of differentially rotating stellar systems: By means of specifically designed N-body simulations a full dynamical stability analysis of the family of differentially rotating models introduced in Chapter 4 has been performed. Dynamical instabilities are shown to occur in several configurations in the strong differential rotation regime. This work has been carried out in collaboration with E. Vesperini, S. L. W McMillan, and G. Bertin and is currently in the final stages of preparation for submission to a scientific journal.

Chapter 6. Long-term dynamical evolution of isolated rotating stellar systems: We report the results of the investigation, performed by means of a dedicated survey of N-body simulations, of the long-term dynamical evolution of selected configurations in the family of differentially rotating models introduced in Chapter 4, studied as isolated systems. This work has been carried out in collaboration with E. Vesperini, S. L. W. McMillan, and G. Bertin and is currently in preparation for submission to scientific journals.

Chapter 7. Observational signatures of rotation in Galactic globular clusters: A first application of the differentially rotating models to the interpretation of the kinematics and morphology of the globular clusters ω Cen, 47 Tuc, and M 15 has been performed in collaboration with P. Bianchini, G. Bertin, and A. Zocchi. This work is in final stages of preparation for submission to a scientific journal.

Chapter 8. Galactic globular clusters in different relaxation conditions: We present the results of an observational investigation of pressure anisotropy as signature of partial relaxation in sample of Galactic globular clusters. This work has been completed in collaboration with A. Zocchi and G. Bertin and has been published as an article in *Astronomy & Astrophysics* (Zocchi et al. 2012), on which the Chapter is based.

Appendix A. Details of the perturbation method: We summarize some definitions and derivations concerning the perturbation method for the solution of the Poisson equation presented in Chapter 2.

Appendix B. Details of the iteration method: We report the derivation of the general solution of the radial part of the Laplacian, as resulting from the spectral iteration method for the solution of the Poisson equation presented in Chapter 2. We summarize the details of the numerical implementation of such method, as applied to the construction of the family of differentially rotating models presented in Chapter 4.

CHAPTER 1

Globular clusters as quasi-relaxed stellar systems

1.1 Basic properties of globular clusters

Globular star clusters can be considered as the "building blocks" of galaxies, because they are among the first recognisable stellar structures that were born on sub-galactic scales and their age is comparable to the age of the Universe. They are compact groups often containing about a million stars, which are held together by their mutual gravitational attraction, and are characterised by a nearly spherical distribution and a high density in the central regions.

For the astronomical community this class of stellar systems has been valuable in many ways, from the first applications of the theory of stellar evolution to recent investigations in the context of what is called "near-field cosmology". The typical range of masses (10^4 to 10^6 $M_\odot$) place globular star clusters at the low-mass end of stellar systems, between open clusters and dwarf galaxies. At this mass range a puzzling dichotomy is observed. On the one hand, the available observations do suggest that globular star clusters do not contain large amounts of dark matter and can generally be well described by Newtonian gravity. On the other hand, there are the more spatially extended dwarf galaxies, whose dynamics appears to be dark matter dominated and which are usually related to cosmological substructures. These classical boundaries have been blurred by the recent discovery of new classes of stellar groups, such as ultra-faint dwarf spheroidals, ultra-massive super star clusters, ultra-compact dwarf galaxies, and dark-matter-poor tidal dwarf galaxies (for recent studies, see Misgeld & Hilker 2011 and Brodie et al. 2011).

The study of the internal dynamics of the low-mass stellar systems in the transition region between classical star clusters and dwarf galaxies is therefore of great importance in the context of structure formation theories because only accurate dynamical models can lead to a reliable interpretation of the photometric and kinematic observables, providing an estimate of the relevant mass-to-light ratio so as to firmly exclude or require the presence of significant amounts of dark matter in these systems. In this context, globular star clusters also play an important role as interesting targets to test major gravitational paradigms, such as Modified Newtonian Dynamics vs. Newtonian Dynamics (see Baumgardt et al. 2005a and Moffat & Toth 2008, among others; for a recent and controversial test performed on the globular cluster NGC 2419, see Ibata et al. 2011 and Sanders 2012).

1.1.1 Galactic globular clusters

Galactic globular clusters can be collectively described as a system of approximately 150 objects, for which there is a clear evidence of the existence of two sub-systems associated to the Galactic disk and with the Galactic halo, respectively (Ashman & Zepf 2008).

Quantity	Mean value
R_0	12.16 kpc
M_V	-7.27 mag
C	1.57
$t_{rel,c}$	1.09×10^8 yr
$t_{rel,h}$	1.12×10^9 yr
R_c	1.14 pc
R_e	2.21 pc
r_{tr}	21.85 pc
$\mu_V(0)$	18.81 mag/arcsec^2
ρ_0	$2.32 \times 10^3\, L_\odot/pc^3$
ϵ	0.06
σ_0	5.5 km/s

Table 1.1: Mean values for selected structural and dynamical properties of Galactic globular clusters. Listed from top to bottom: (1) distance from the Galactic center, (2) absolute magnitude (in the V band), (3) concentration parameter (King 1966), (4) central relaxation time, (5) half-mass relaxation time, (6) projected core radius (HWHM of the surface brightness profile), (7) effective radius (also denoted as projected half-light radius, i.e. the radius within which half of the total luminosity is enclosed, in projection), (8) truncation radius (King 1966), (9) central surface brightness (in V band), (10) central luminosity density, (11) ellipticity, (12) central velocity dispersion. The values presented in the table are calculated from the data reported in the Harris (2010) catalog. To be noted that some parameters are not independent, in particular ρ_0 is derived by making use of $\mu_V(0)$, C, and r_c; $t_{rel,c}$ by making use of M_V, r_c, and C; $t_{rel,h}$ by making use M_V, r_h.

These sub-systems are therefore defined primarily with reference to the distance of star clusters from the Galactic center, but also on the basis of a number of other structural and dynamical properties, such as the metallicity or the morphology of the horizontal branch of the HR diagram. In addition, star clusters of the halo sub-system represent a kinematic tracer of the Galactic gravitational field at large scale, and their spatial distribution provide a stringent constraint for the models of the dark matter distribution in the outer part of the Galaxy. When considered as a system, globular clusters also play a fundamental role in the validation of theories of formation and evolution of the Galaxy itself, as they can offer a record of the chemical and dynamical conditions of its formation phase.

As individual objects, globular clusters are studied with particular reference to two classes of observables, as determined from the photometric and the spectroscopic data, respectively, which provide information about the structural and kinematical properties of the systems. In particular, most dynamical models designed for the description of this class of stellar systems can be constrained by a joint analysis of the surface brightness profile and the velocity dispersion profile. Such observable quantities are usually constructed under the simplifying assumption of spherical symmetry and are traditionally interpreted on the basis of geometrically simple, physically-based dynamical models (presented in some detail in the next Section). Dynamical studies of this kind have led to the determination of structural and kinematical properties for the majority of Galac-

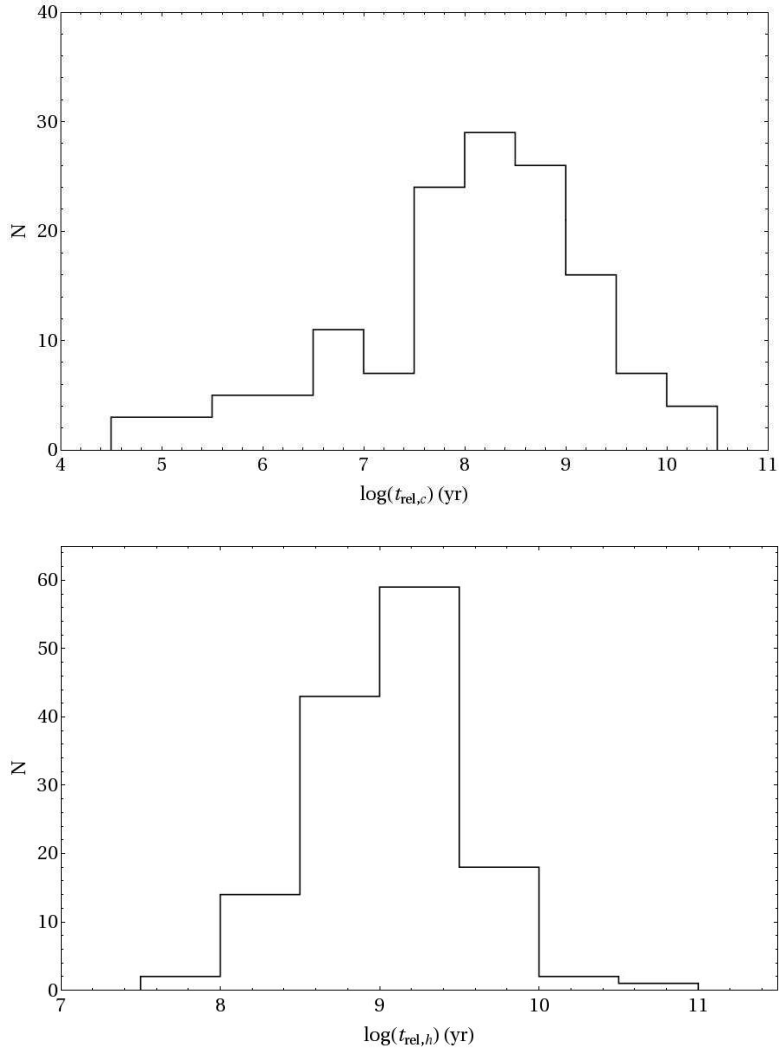

Figure 1.1: Distribution of the central and half-mass relaxation times for Galactic globular clusters, as published in the Harris (2010) catalog.

tic globular clusters. Following the presentation style of Meylan & Heggie (1997) and Heggie & Hut (2003), the mean values of selected parameters are recorded in Table 1.1.

A quantity of particular relevance for the study of the internal dynamics of globular clusters is the relaxation time, which may be regarded as the time scale on which the system approaches thermodynamical equilibrium, as a result of deflections and kinetic energy exchanges associated with the two-body encounters between the stars (a formal definition is provided in the next section). Since globular clusters are characterized by a significant density variation between the central regions and the outer parts, it is critical to distinguish between central ($t_{rel,c}$) and half-mass ($t_{rel,h}$) relaxation time; the distributions of the relevant values, as published in the Harris (2010) catalog, are illustrated in Fig. 1.1.

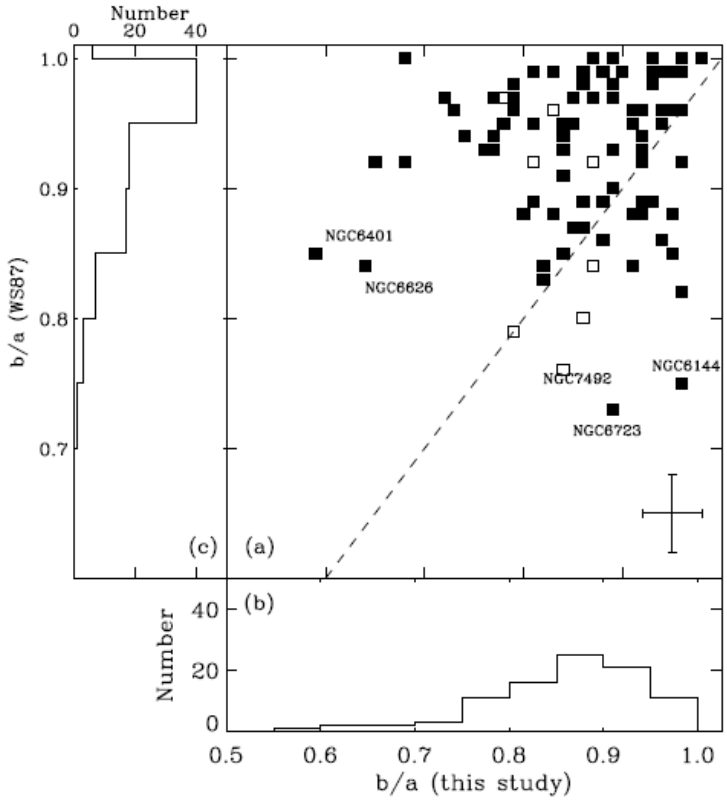

Figure 1.2: (a) Comparison of axial ratios determined by Chen & Chen (2010) and those by White & Shawl (1987) for the 92 Galactic globular clusters common in the two samples. Clusters with reliable measurements (82) are marked as filled squares. The dashed line marks equal values. Median values of measurement errors for both studies are shown in the lower right corner. The offset panels (b) and (c) show the two distributions of axial ratios. From Chen & Chen (2010).

From the morphological point of view, globular cluster present only small deviations from spherical symmetry. Yet, there is observational evidence of flattening, as measured by the ellipticity parameter, defined as $\epsilon = 1 - b/a$, where b/a is the ratio of the minor to major axis of the projected image of a cluster. For a long time, the White & Shawl (1987) database (hereafter denoted as WS87) represented the only comprehensive collection of measurements of the ellipticity of Galactic globular clusters; recently, an alternative homogeneous database of ellipticities has been published by Chen & Chen (2010) (hereafter denoted as CC10). The two distributions of values show significant differences (for a detailed comparison, see Fig. 1.2). In fact, from the WS87 database (93 objects), Galactic clusters appear to be predominantly round, with the peak of the distribution at $\epsilon \approx 0.05$, maximum value of the entire sample given by $\epsilon \approx 0.3$, and axial ratios randomly oriented in space. However, the distribution of the CC10 ellipticities (116 objects, 82 in common with the WS87 database) is peaked at $\epsilon \approx 0.15$, with the majority of the values falling in the range $[0.05, 0.25]$, and maximum value $\epsilon \approx 0.45$. In addition, especially for the clusters in the region of the Galactic Bulge, their major axes preferentially point toward the Galactic Center (see Fig. 1.3).

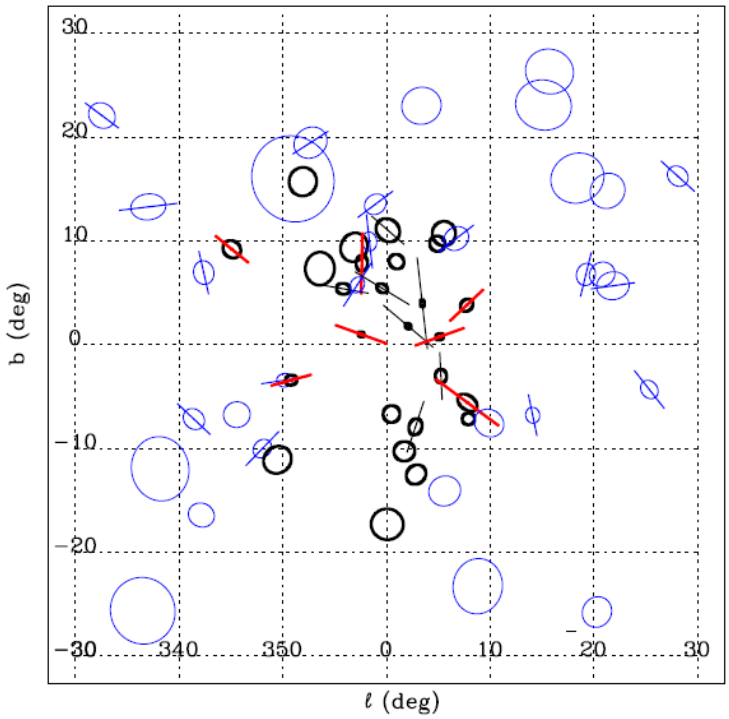

Figure 1.3: Spatial distribution of 57 Galactic globular clusters. Thick black ellipses mark clusters with a distance from the Galactic Center smaller than 2.7 kpc and thin blue ellipses mark those beyond. For clusters flatter than the average value determined by Chen & Chen (2010) ($b/a < 0.87$), a line, the size of which depicts the axial ratio, is drawn through the corresponding ellipse. There are 14 flattened bulge clusters, marked by lines in thick ellipses. For approximately half of these clusters (highlighted in red), the angle between the direction of the major axis and the direction pointing toward the Galactic Center is less than $20\,\mathrm{deg}$. From Chen & Chen (2010)

The apparent discrepancies between the two studies should be interpreted by taking into account that (i) the WS87 values result from an optical study, with the use of a surface photometry technique consisting of consecutive blurring of the digitized images of blue sensitive photographic plates. On the other hand, CC10 ellipticities are determined with a number count technique, based on the analysis of the spatial distribution of 2MASS point sources; (ii) as a result of the different resolution limits of the two approaches, the WS87 measurements mostly refer to the inner regions of the clusters, while CC10 to the outer parts; (iii) unfortunately, in both cases, the cluster flattening values do not refer to a standard isophote, such as the cluster half-light radius (as also noted by van den Bergh 2008 with reference to the WS87 database). In fact, the WS87 axial ratios are derived from the averaged values of the "isophotes" at various distances from the center, while CC10 axial ratios are measured at the location at which a given value of the density contrast with respect to the background is reached. This limitation is crucial because there is observational evidence that the ellipticity of a cluster depends on radius (see Geyer et al. 1983). For instance, in Fig. 1.4 the radial profiles of the axial ratio b/a for three Galactic globular clusters (NGC 104, NGC 7078, and NGC 5139) are illustrated. Therefore, we may conclude that the two database somehow carry complementary in-

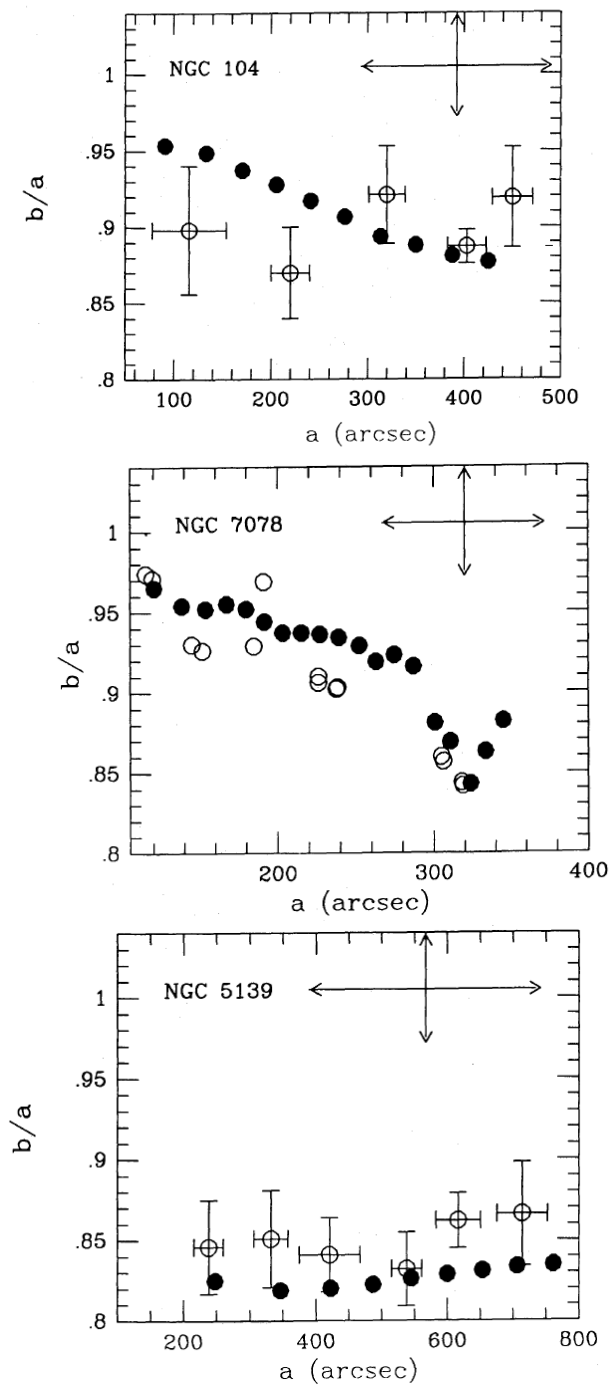

Figure 1.4: Axial ratio as a function of the distance (in ″) from the center of the cluster for (from top to bottom) NGC 104 (47 Tuc), NGC 7078 (M15), and NGC 5139 (ω Cen). Black dots mark the values from White & Shawl (1987); in the upper right of the panels, the typical uncertainties and the correlation lengths of the data are shown as vertical and horizontal arrows, respectively. White dots mark the values from Geyer et al. (1983). From White & Shawl (1987).

Table 1.2: Rotation in Galactic globular clusters

Globular Cluster	σ_0 km s^{-1}	e_σ km s^{-1}	A_{rot} km s^{-1}	e_A km s^{-1}	ϵ	Ref.
NGC 104	9.6	0.6	4.4	0.4	0.09	(3)
NGC 288	2.7	0.8	0.5	0.3	—	(3)
NGC 1851	10.4	0.5	1.6	0.5	0.05	(1),(2)
NGC 1904	5.3	0.4	0.6	0.5	0.01	(1),(2)
NGC 2808	13.4	1.2	3.3	0.5	0.12	(1),(2)
NGC 3201	4.5	0.5	1.2	0.3	0.12	(8)
NGC 4590	2.4	0.9	1.2	0.4	0.05	(3)
NGC 5024	4.4	0.9	0.0	0.5	0.01	(3)
NGC 5139	19.0	1.0	6.0	1.0	0.17	(6), (7)
NGC 5904	7.5	1.0	2.6	0.5	0.14	(1)
NGC 6121	3.9	0.7	1.8	0.2	0.00	(3)
NGC 6171	4.1	0.3	2.9	1.0	0.02	(1),(2)
NGC 6218	4.7	0.9	0.3	0.2	0.04	(3)
NGC 6254	6.6	0.8	0.4	0.5	0.00	(1),(2)
NGC 6388	18.9	0.8	3.9	1.0	0.01	(1),(2)
NGC 6397	4.5	0.6	0.2	0.5	0.07	(1),(9)
NGC 6441	18.0	0.2	12.9	2.0	0.02	(1),(2)
NGC 6656	6.8	0.6	1.5	0.4	0.14	(3)
NGC 6715	16.4	0.4	2.0	0.5	0.06	(4),(5)
NGC 6752	5.7	0.7	0.0	0.0	0.04	(3)
NGC 6809	2.7	0.5	0.5	0.2	0.02	(3)
NGC 6838	2.3	0.2	1.3	0.5	0.00	(1),(2)
NGC 7078	13.5	0.9	3.8	0.5	0.05	(1),(2)
NGC 7099	5.0	0.9	0.0	0.0	0.01	(3)

Notes. Summary of the kinematical properties of selected Galactic globular clusters, as recently presented by Bellazzini et al. 2012. From left to right: cluster identification, central velocity dispersion, error associated with the central velocity dispersion, rotation amplitude, error on the rotation amplitude, ellipticity, references. The references in the last column indicate the source of the velocity dispersions and of the rotation amplitudes. The A_{rot} values from Lane et al. (2010c) have been multiplied by a factor 2 so as to directly compare them with the scale adopted in Bellazzini et al. 2012. Ellipticity values are from White & Shawl (1987).

References. (1) Bellazzini et al. 2012; (2) Harris 2010; (3) Lane et al. 2010c; (4) Ibata et al. 2009; (5) Bellazzini et al. 2008 ; (6) van de Ven et al. 2006; (7) Pancino et al. 2007 ; (8) Cote et al. 1995 ; (9) Meylan & Mayor 1991

formation about the morphology of Galactic globular clusters.

From the kinematical point of view, Galactic globular clusters can be considered as pressure-supported stellar systems, characterized by a high degree of isotropy in the velocity space, as expected for systems close to a thermodynamically relaxed state (see Section 1.3 for further considerations on this point). In addition, internal rotation has been measured in a progressively increasing number of objects. The detection of internal rotation in star clusters is a challenging task, because the typical value of the ratio of mean velocity to velocity dispersion is only of a few tenths, for example $V/\sigma_0 \approx 0.46, 0.32$

for 47 Tucanae and ω Centauri, respectively (see Bellazzini et al. 2012). Ground-based work on nearby Galactic globular clusters has already demonstrated the power of three-dimensional kinematics van Leeuwen et al. (2000). The Hubble Space Telescope (for ω Cen, see Anderson & van der Marel 2010; for 47 Tuc, see Anderson & King 2003) and GAIA, with the planned acquisition of the proper motion of thousands of stars in globular clusters, make this goal within reach, by allowing to measure the component of rotation in the plane of the sky, supplemented by the kinematical information derived from radial velocity measurements. A summary of the kinematical properties of selected Galactic globular clusters is recorded in Table 1.2; the discussion of the effects of internal rotation on the dynamics of this class of stellar system is presented in Subsection 1.4.2.

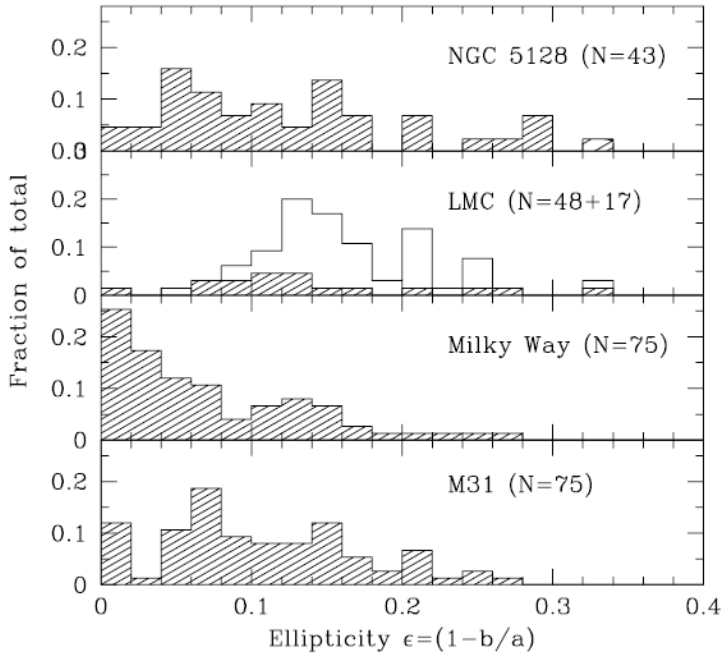

Figure 1.5: Distributions of ellipticities of globular clusters in external galaxies. From Harris et al. (2002)

1.1.2 Extragalactic globular clusters

Globular clusters are present also in external galaxies (Ashman & Zepf 2008). After the first observational studies of relatively small samples of objects in the nearby Magellanic Clouds (e.g., see Elson et al. 1987), the investigation has been extended also to the globular clusters systems in selected galaxies of the Local Group and the Virgo Cluster. In particular, a number of observational programs performed first with WFPC2 and later with ACS on the Hubble Space Telescope have determined high resolution photometric profiles for large samples of globular clusters in Andromeda (M31), the giant elliptical galaxy Centaurus A (NGC 5128), the Small and Large Magellanic Clouds, the dwarf galaxies Fornax and Sagittarium, and the giant elliptical galaxy M87 (see Barmby et al. 2007; Harris et al. 2002, 2006; Mackey & Gilmore 2003b,a,c; Madrid et al. 2009, respec-

tively).

Such photometric studies show that the globular cluster system in M31 is quite similar to the Galactic one, as composed of old, approximately round stellar systems, which can be successfully described in terms of spherical, isotropic, truncated models. However, the majority of the globular clusters in the Magellanic Clouds and Fornax, as well as a significant fraction of clusters in NGC 5128, seem to be systematically younger, more spatially extended and therefore better represented by a power-law density profiles, especially in the outer parts, with respect to the Galactic clusters. In addition, they appear to be flatter, as illustrated in Fig. 1.5.

1.2 Dynamical description of self-gravitating systems

1.2.1 Fundamental time scales

In the study of the internal dynamics of globular clusters it is particularly important to introduce a time scale that measures the dynamical effects associated with the two-body encounters within a self-gravitating stellar system. These encounters can be treated as events of Rutherford scattering, in which a star representing a "test mass" m_t is deflected by another "field star" of the cluster, characterized of mass m. The relaxation time can thus be defined as the time scale beyond which the cumulative effects of subsequent encounters, as measured by the increase of the square of the transverse velocity component with respect to the original direction of motion, becomes comparable to the initial specific energy of a star

$$v_{start}^2 = t_{rel} \int (\Delta v_\perp)^2 2\pi v_{start} n b db \tag{1.1}$$

where b is the impact parameter and n is the number density of the system.

The increment of the transverse velocity may be expressed as

$$\Delta v_\perp = 2 v_{start} \frac{m}{m+m_t} \sin\frac{\theta}{2} \cos\frac{\theta}{2} \tag{1.2}$$

where θ denotes the deflection angle, with $\sin^2(\theta/2) = 1/[1 + (b/b_0)^2]$, where $b_0 = G(m+m_t)/v_{start}^2$. By substituting Eq. (1.2) in Eq. (1.1) and by performing the integration over $[0, b_{max}]$ (with b_{max} maximum value allowed for the impact parameter), it is readily found that

$$t_{rel} \approx \frac{v_{start}^3}{8\pi G^2 n m^2 \ln\Lambda} \tag{1.3}$$

where $\Lambda = b_{max}/b_0$ ($\ln\Lambda$ is often called *Coulomb logarithm*).

By assuming that the stars in the cluster are characterized by the same mass m and that the velocity distribution is approximately a Maxwellian distribution, it can be shown (see Spitzer 1987) that the velocity dispersion σ can be used as a good approximation of the initial velocity v_{start}. An estimate of the relaxation time, such as the values presented in Fig. 1.1, can now be obtained, if we insert the values of the relevant quantities suggested by King (1966) models. To be noted that both the number density and the velocity dispersion are defined as a function of the distance from the center of the system (for simplicity assumed here as spherically symmetric), therefore the relaxation time itself can be expressed as a radial profile. This is the reason why it is appropriate to distinguish between central $t_{rel,c} \propto \sigma(0)^3/n(0)$ and half-mass relaxation time$t_{rel,h} \propto \sigma(r_h)^3/n(r_h)$.

With particular reference to the half-mass relaxation time, from the virial theorem, an alternative expression can be recovered

$$t_{rel,c} \approx \frac{N^{1/2} r_h^{3/2}}{G^{1/2} m^2 \ln \Lambda}, \tag{1.4}$$

where, by assuming the half-mass radius as maximum value for the impact parameter the Coulomb logarithm can be expressed as $\ln \Lambda = \ln(0.4N)$. By defining the dynamical time as $t_{D,h} = 2r_h/\sigma$, the following relation is obtained

$$\frac{t_{rel,h}}{t_{D,h}} \propto \frac{N}{\ln(0.4N)}. \tag{1.5}$$

Within this traditional description of the two-body encounters, other important time scales can be introduced in similar fashion. In particular, from the energy exchange between two stars during a scattering event the time scale associated with the energy equipartition can be defined, while the time scale associated with the dynamical friction is calculated with reference to the decrement of the component of the velocity of the test star parallel to the original direction of motion.

1.2.2 Kinetic description

The relation expressed in Eq. (1.5) is particularly important because, as for globular clusters $N \sim 10^4 - 10^6$, suggests a statistical description for this class of stellar systems in terms of a one-particle distribution function in phase space $f = f(\mathbf{x}, \mathbf{v}, t)$.

In principle, the time evolution of a distribution function is governed by the Boltzmann equation

$$\frac{\partial f}{\partial t} + \mathbf{v}\frac{\partial f}{\partial \mathbf{x}} - \frac{\partial f}{\partial \mathbf{v}}\frac{\partial \Phi_c}{\partial \mathbf{x}} = \left(\frac{\partial f}{\partial t}\right)_{coll} \tag{1.6}$$

where, on the right-hand side the collision integral is often treated in terms of the Fokker-Planck approximation. On the left-hand side Φ_c denotes the mean field potential generated by the entire system, which is associated with the zeroth-order moment of the distribution function (i.e., the density) by means of the Poisson equation.

If we are not interested in providing a description of the long-term evolution of a stellar system, it is appropriate to refer to the equilibrium solutions of the homogeneous equation associated with Eq. (1.6), that is, the "collisionless" Boltzmann equation. With particular reference to globular clusters, the relevant values of the dynamical and relaxation time scale guarantee that, on the one hand, the stellar system rapidly reaches a quasi-stationary state on the dynamical time scale and, on the other hand, that the collisionless description can be applied, at least as a zeroth-order approximation, because the effects of collisions can be ignored.

The collisionless Boltzmann equation can be also expressed in terms of the canonical variables; this form greatly emphasizes the formal and conceptual proximity to the *Liouville theorem*. In other words, an equilibrium solution of the Eq. (1.6) is a function of the integrals of motion of the system. In particular, as stated by the *Jeans theorem*, an equilibrium solution of the collisionless Boltzmann equation depends on phase space coordinates only through the *isolating* integrals of the motion, that is those that effectively reduce the dimensions of the manifold in phase space available to the dynamical system, according to a given distribution function.

The study of self-consistent collisionless equilibrium models has a long tradition not only in stellar dynamics, but also in plasma physics (e.g., see Attico & Pegoraro 1999).

We note that in both research areas a study in the presence of external fields, especially when the external field is bound to break the natural symmetry associated with the one-component problem, is only rarely considered.

1.2.3 Fluid and virial description

For a long time the degree of detail offered by the kinetic description of stellar systems has been somehow redundant with respect to the actual constraints provided by the astrophysical observables. In particular, only recently, by means of high resolution photometry and recent determinations of large datasets of proper motions from the Hubble Space Telescope, supplemented by the radial velocities measured along the line of sight, a 5-dimensional view of an increasing number of Galactic globular clusters has become available. Therefore, the less detailed yet more manageable fluid description (i.e., in terms of the solutions of the generally called Jeans equations) often represented a popular alternative to the phase space description of stellar systems.

Fluid quantities are actually calculated as moments of the relevant distribution function in the velocity space. Correspondingly, their time evolution is governed by a hierarchy of fluid equations, derived from the Boltzmann equation. The derivation leads to an infinite set of fluid equations; however, such hierarchy is actually undetermined, as each new equation introduces a new variable, corresponding to the velocity moment of higher order. This chain of equation may be broken by introducing a "closure equation", which often is described as the equation of state of the system or, in different physical contexts, as an assumption on the form of the pressure tensor in the momentum transport equation; the choice of an appropriate "closure" is highly nontrivial. In the most common astrophysical applications, which usually involve the equations for the first three moments (i.e., continuity, momentum, and energy conservation), the closure simply consists in a truncation of the hierarchy of the fluid equation by means some assumption on the pressure tensor.

For this reason, especially when the stellar system is characterized by the presence of anisotropy in the velocity space, this modeling approach is actually more suited as a simple diagnostic tool for the direct interpretation of the relevant astronomical observable, instead of a powerful method for the construction of a fluid model for which it is possible to recover a kinetic counterpart defined from a distribution function (to be noted that, also in the cases in which such inversion is formally achievable, there is no guarantee that the resulting distribution function is positive definite, and therefore physically meaningful).

By further decreasing the degree of detail of the description of the stellar system, we finally reach the so-called virial description. As in the previous case, the relevant quantities are defined as momenta the in the coordinate space of the previous ones. The fundamental equation is given by the virial theorem in tensor form (from which the traditional scalar form is recovered by considering the trace of the relevant tensors)

$$\frac{1}{2}\frac{d^2 I_{ij}}{dt^2} = 2\left(T_{ij} + \frac{\Pi_{ij}}{2}\right) + W_{ij} \tag{1.7}$$

where I_{ij} is the inertia tensor, W_{ij} is the gravitational energy tensor, and T_{ij} e $\Pi_{ij}/2$ are the ordered and random parts of the kinetic energy tensor. A number of useful global diagnostic tools can be defined starting from these quantities, as discussed in the next Chapters.

1.2.4 N-body simulations

From a theorist's perspective, globular clusters are also an excellent physical realization of the "gravitational N-body problem", which is the problem of understanding the evolution of a system of N point masses interacting by gravitational forces.

The most straightforward and accurate technique to solve the gravitational N-body problem is that of direct summation (e.g, see Aarseth 1999, Spurzem 1999, Portegies Zwart et al. 2001). In this approach, the force exerted on each particle is computed by summing up the contributions from all other particles. The force is used to solve the equations of motion of each body and all the trajectories are computed by means of a numerical solver.

Alternative particle methods adopt the strategy of grouping particles together according to their spatial distribution and compute the force exerted by the whole group instead of considering the contribution of each particle. The most popular example in this class is probably given by the "tree code" (see Barnes & Hut 1986 and Springel et al. 2001), which arranges particles in cells and computes the force contributions from these cells by means of truncated multipole expansions.

A different class of approximated methods includes Monte Carlo methods, Fokker-Planck methods and gaseous methods. Monte Carlo methods (see Hénon 1975; Giersz 1998; Joshi et al. 2000, among others) treat the N-body system as a continuous system in which particles are replaced by spherical shells of matter. Assuming equilibrium in a smooth spherical potential, the global evolution of the system is followed. A similar approach is used in Fokker-Planck methods (e.g., see Cohn 1980 and Murphy et al. 1991), with the difference that distribution functions are used instead of particles. The evolution of the system is followed by direct integration of the Fokker-Planck equation. Gaseous methods (e.g, see Lynden-Bell & Eggleton 1980 and Louis & Spurzem 1991) solve several equations for higher order moments of the Fokker-Planck equation.

Direct N-body simulations are therefore computationally demanding: these methods present an $\mathcal{O}(N^2)$ scaling with the number of particles. Many attempts have been made to reduce their requirements, both from a software and from a hardware point of view. The development of approximated methods was motivated in the first place by the intention to reduce the computational complexity of direct methods, at the expense of a reduced accuracy. From a hardware point of view, special purpose hardware is being built to accelerate the computation of gravitational forces. The GRAPE family of computers (GRavity PipE, see Makino et al. 2003 for a recent summary), has proven very efficient for this purpose. In the very last years, GPUs (Graphic Processing Units) have emerged in the scene of high-performance scientific computing, with great interest from the theoretical astrophysics community (e.g., see Gaburov et al. 2009).

1.3 Simple spherical quasi-relaxed models

1.3.1 Basic assumptions

On the basis of the empirical and theoretical backgrounds provided in the previous sections, the following set of assumptions are now physically well justified for the zeroth-order dynamical description of an individual globular cluster

(i) the dynamical problem is treated in the continuum limit, that is, the granularity of the real stellar system is ignored in the mean field description.

(ii) the system is assumed to be in a quasi-stationary state; therefore the distribution

function, the relevant moments and the self-consistent potential are time independent.

(iii) the system is assumed to be characterized by spherical symmetry; this assumption greatly simplifies the formal construction of the models, as the gravitational potential becomes a function of only the distance from the center of the system and the distribution function depends only on the variables r, v_r, and v_t (the latters being the components of the velocity parallel and trasverse with respect to the radius vector).

(iv) the system is assumed to be close to a thermodynamically relaxed state, as expected from the condition $t_{age} > t_{rel,h}$. Therefore, this assumption allows us to consider a distribution function that depends only on the single-star energy, thus characterized by isotropy in the velocity space. Note that (ii) guarantees that the energy is an integral of the motion, and (iii) suggests that we consider to consider the phase space partition in terms of $E = v^2/2 + \Phi_c(r)$ e J^2 con $J = rv_t$, as natural for spherically symmetric systems. In the general case of $f = f(E, J^2)$, the system may be characterized by the presence of anisotropy in the velocity space ($p_r \neq p_\theta = p_\phi$).

(v) the system is considered as composed by only one component, that is, the stars are considered as a homogeneous population with a constant mass-to-light ratio.

(vi) the system is characterized by the presence of a spatial truncation, representative of the tidal effects of the host galaxy

1.3.2 The role of truncation in phase space

Within the set of assumptions described above, a number of simple equilibrium self-consistent models can be defined. Among the historical results, polytropic spheres played an important role, basically borrowed from the theory of stellar structure. In fact, polytropes are usually presented as fluid models, defined with particular reference to their equation of state $p = K_n \rho^{(n+1)/n}$ where $K_n = B_n^{-1/n}/(n+1)$ with B_n a positive constant. They are equilibrium solution of the Lane-Emden equation, parametrized by the polytropic index n. The relevant distribution function can be defined as

$$f(E) = A(-E)^{n-3/2} \tag{1.8}$$

for $E < 0$ e and vanishing otherwise. The associated density profile is defined as $\rho(r) = B_n[-\Phi_c(r)]^n$, where A is a positive constant and $B_n = 2\pi^{3/2} A\, \Gamma(n - 1/2)/n!$. Configurations with $n \leq 5$ have a finite total mass, the polytrope with $n = 5$ (i.e., the so called Plummer model) is the first of the sequence characterized by a infinite spatial extent.

Interestingly, the limiting case of a sequence of polytropes with $n \to \infty$ can be related (in a nontrivial way, see Hunter 2001) to the isothermal sphere, defined as

$$f(E) = A \exp(-aE) \tag{1.9}$$

where A and a are positive constants; as expected, the relevant equation of state is given by $p = \rho/a$ and the density distribution is defined as $\rho(\psi) = \tilde{A} \exp(\psi)$, with the dimensionless potential $\psi = -a\Phi_c$ and $\tilde{A} = A\sqrt{8\pi^3/a^3}$.

Assumption (vi), the existence of a spatial truncation of the system, suggests that we introduce a truncation in phase space with respect to the distribution function that defines the isothermal sphere. The most popular family in the class of quasi-relaxed models is defined as a Maxwellian distribution function, characterized by the presence of an energy truncation (King 1966)

$$f_K(E) = \begin{cases} A\left[\exp\left(-aE\right) - \exp\left(-aE_0\right)\right] & \text{if } E \leq E_0 \\ 0 & \text{if } E > E_0. \end{cases} \tag{1.10}$$

The cut-off energy E_0 should be interpreted as the threshold value beyond which a star is no longer considered as part of the system. Because of the assumed spherical symmetry, the energy truncation directly translates into the existence of a truncation radius r_{tr}. This family of models is characterized by two physical scales (associated with the positive constants A and a) and one dimensionless parameter Ψ[1], defined as the depth of the central potential well, which provide a measure of the central concentration of the configuration. Alternatively, the concentration can be measured by $C = log(r_t/r_0)$ (there is a one-to-one correspondence between C and Ψ). In addition, it has been demonstrated (Spitzer 1987) that this equilibrium solution of the collisionless Boltzmann equation represents also an approximate solution of the Fokker-Planck equation. Indeed, as a zeroth-order description, these models have had remarkable success in applications to observed globular clusters (e.g., see Djorgovski & Meylan 1994; McLaughlin & van der Marel 2005, and references therein) and provide the standard dynamical paradigm for the calculation of the basic structural and dynamical properties for this class of stellar systems (see Table 1.1).

Yet, the truncation prescription is not unique. In fact, in recent years an alternative family of quasi-relaxed configurations has become increasingly popular for observational applications. The models are defined by the following distribution function

$$f_W(E) = \begin{cases} A\left\{\exp(-aE) - \exp(-aE_0)[1 - a(E - E_0)]\right\} & \text{if } E \leq E_0 \\ 0 & \text{if } E > E_0\ . \end{cases} \tag{1.11}$$

and they represent the spherical isotropic nonrotating limit of a family of rotating models orginally introduced by Wilson (1975). The same definitions for the quantities in Eq. (1.10) and the physical scales and the concentration parameter of the family of models apply here maybe. In this case, the truncation is continuous also with respect to the first derivative in the energy E. In principle, distribution functions characterized by even smoother gradients in correspondence with the energy cut-off may be defined (see Davoust 1977).

As a result, the configurations are spatially more extended with respect to King models, with a similar behavior in the central regions and a less sharp slope of the density distribution in the outer parts. This spatial feature is the reason of the recent success of such family of models in the interpretation of the structures in the surface brightness profiles that, in a relevant fraction of Galactic and extragalactic globular clusters, extend beyond the spatial truncation prescribed by King models. For instance, we show in Fig. 1.6 the direct comparison between the best-fit King and spherical Wilson models for the number density and surface brightness density profiles of the globular cluster M92.

[1]This quantity is often denoted by W_0 in the literature.

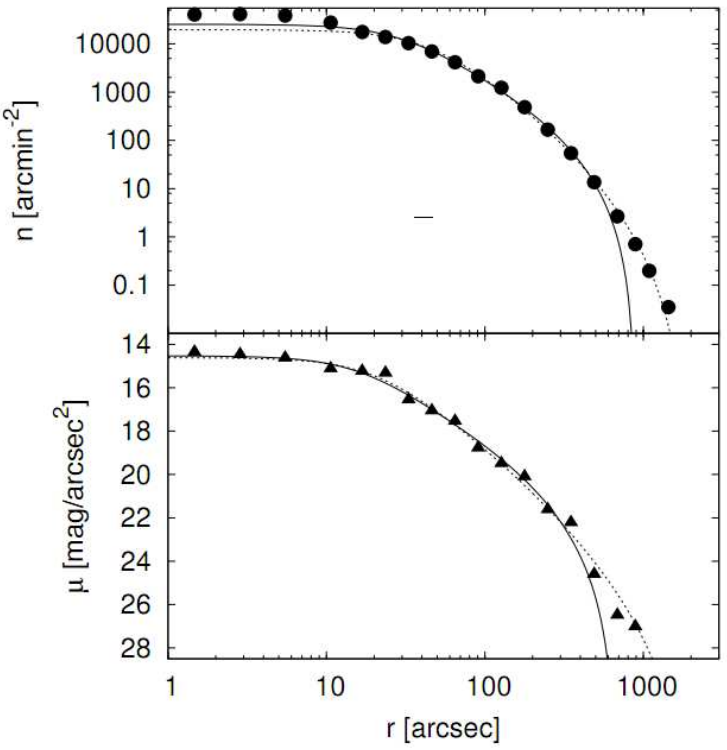

Figure 1.6: The surface brightness and the number density profile of the cluster NGC 6341 (M92) are shown in the top and bottom panel, respectively. The solid lines mark the best-fit King model and the dashed lines the best-fit spherical Wilson model. From Di Cecco et al. (2012).

1.4 Three fundamental physical ingredients

1.4.1 Why do we need a more realistic dynamical framework?

As hinted in Section 1, in recent years great progress has been made in the acquisition of detailed quantitative information about the structure and dynamics of Galactic globular clusters, especially in relation to the measurement of the proper motions of thousands of individual stars (see van Leeuwen et al. 2000; McLaughlin et al. 2006; Anderson & van der Marel 2010). Such progress calls for a renewed effort on the side of modeling. More general analytical models would allow us to address a number of observational issues only partially understood, such as the detailed distribution of angular momentum and the origin of the observed departures from spherical symmetry.

As in the case of the study of elliptical galaxies (e.g., see Bertin & Stiavelli 1993, and references therein), different approaches can be taken to the construction of models. Broadly speaking, two complementary paths can be followed. In the first, "descriptive" approach, under suitable geometrical (on the intrinsic shape) and dynamical (e.g., on the absence or presence of dark matter) hypotheses, the available data for an individual stellar system are imposed as constraints to derive the internal orbital structure (distribution function) most likely to correspond to the observations. This approach is often carried out in terms of codes that generalize a method introduced by Schwarzschild (1979); for

an application to the globular cluster ω Cen, see van de Ven et al. (2006). In the second, "predictive" approach, one proposes a formation/evolution scenario in order to identify a physically justified distribution function for a wide class of objects, and then proceeds to investigate, by comparison with observations of several individual objects, whether the data support the general physical picture that has been proposed. Indeed, King models belong to this latter approach.

The of the main purpose of this Thesis is to extend the analytical description of quasi-relaxed stellar systems, so far basically limited to the simple spherical models outlined in Section 1.3, to the nonspherical case. There are at least three different ways of extending spherical isotropic models of quasi-relaxed stellar systems (such as King models), by modifying the distribution function so as to include: (i) the explicit presence of a nonspherical tidal field; (ii) the presence of internal rotation; (iii) the presence of some pressure anisotropy. These correspond to the physical ingredients that, separately, may be thought to be at the origin of the observed non-spherical shapes.

As shown in Section 1, deviations from spherical symmetry are observed in globular clusters (e.g., see Geyer et al. 1983; White & Shawl 1987; Chen & Chen 2010), and they are often ascribed to internal rotation. In other words, it is frequently believed that tides and pressure anisotropy (and dust obscuration), even though playing some role in individual cases, should not be considered as the primary explanation of the observed flattening of Galactic globular clusters. Such conclusion is suggested by the White & Shawl (1987) database of ellipticities. In fact, it is recognized that the issue of what determines the observed shapes of globular clusters remains unclear (e.g., see King 1961; Frenk & Fall 1982; Fall & Frenk 1985; Davoust & Prugniel 1990; Han & Ryden 1994; Ryden 1996; Goodwin 1997, and references therein).

We might argue that real globular clusters are likely to be not fully relaxed, may possess some rotation and experience time-dependent tides so that analytical refinements beyond the spherical one-component King models would not compete with the currently available numerical simulation tools that allow us to include these and a great variety of other detailed effects that are relevant for the quasi-equilibrium configurations. However, physically simple analytical models, accompanied by the study of more realistic numerical simulations, serve as a useful tool to interpret real data and to provide insights into dynamical mechanisms, even though we know that real objects certainly include features that go well beyond such simple physical models.

In conclusion, mastering the internal structure of spheroidal and triaxial stellar systems through a full spectrum of models, including rotation, is a prerequisite for studies of many empirical and theoretical issues. In addition, it is required for the interpretation of the relevant scaling laws (such as the Fundamental Plane, which appears to extend from the brightest, pressure supported ellipticals down to the low-luminosity end of the distribution of early-type galaxies, and possibly further down to the domain of globular clusters) and for investigations aimed at identifying the presence of invisible matter (in the form of central massive black holes or diffuse dark matter halos) from stellar dynamical measurements.

1.4.2 External tidal field

It is commonly thought that globular clusters can be described as stellar systems of finite size, with a truncation in their density distribution determined by the tidal field of the hosting galaxy. Most of the interesting physical mechanisms that underlie the dynamical evolution of these stellar systems (such as evaporation and core collapse; e.g., see Spitzer 1987; Heggie & Hut 2003) depend on such truncation and are frequently studied

in the context of *spherical* models for which the action of tides is implemented by means of the existence of a suitable truncation radius, supplemented by a recipe for the escape of stars. Therefore, evolutionary models that rely on the assumption of spherical symmetry, such as Monte Carlo models (e.g., for a description of two of the codes currently used, see Giersz 1998; Joshi et al. 2000) and Fokker-Planck models (e.g., for an example of, respectively, the isotropic and anisotropic case, see Chernoff & Weinberg 1990; Takahashi et al. 1997a) are necessarily based on an approximate treatment of the tidal field.

Yet, if tides are indeed responsible for the truncation, they should also induce some deviations from spherical symmetry: in the simplest case of a cluster in circular orbit about the center of the host galaxy, the associated (stationary) tidal field is nonspherical and determines an elongation of the mass distribution in the direction of the center of mass of the host galaxy accompanied by a compression in the direction perpendicular to the orbit plane (e.g., see Spitzer 1987; Heggie & Hut 2003). In Part I of the present Thesis this simple physical model is analyzed in detail, with the aim of constructing a family of tidal triaxial models in which the external tidal field is taken into account self-consistently and the induced geometrical distortions are properly calculated.

Such analytic equilibria are, of course, naturally limited to the treatment of a very idealized configuration of the cluster-galaxy system. In fact, only direct N-body simulations, in which an external tidal field can be taken into account explicitly, provide a tool for the study of the evolution of a tidally perturbed cluster, especially when noncircular orbits are considered, so that tidal effects are time-dependent (e.g., see Baumgardt & Makino 2003). In particular, this approach has recently led to detailed investigations of the rich morphology and kinematics of the tidal tails, i.e. the streams of stars escaped from the cluster (e.g., see Lee et al. 2006a; Küpper et al. 2008, 2010b, 2012).

1.4.3 Internal rotation

In the context of globular clusters, relatively little attention was actually placed on the role of internal rotation. For ellipticals, most of the attention that led to the development of stellar dynamical models, after the first kinematical measurements became available in the mid-70s, was taken by the study of the curious behavior of pressure-supported systems in the presence of anisotropic orbits (see also Schwarzschild 1979, 1982; de Zeeuw 1985). In contrast, very little effort has been made in modeling rotation-dominated ellipticals, even though the entire low-mass end of the distribution of elliptical galaxies might be consistent with a picture of rotation-induced flattening (e.g., see Davies et al. 1983; Emsellem et al. 2011); similar comments apply to bulges.

For globular clusters, given the fact that they only exhibit modest amounts of flattening and given the success of the spherical King models, little work has been carried out in the direction of stationary self-consistent rotating models (with some notable exceptions, that is Woolley & Dickens 1962; Lynden-Bell 1962; Kormendy & Anand 1971; Lupton & Gunn 1987; Lagoute & Longaretti 1996). Therefore, as far as rotation-dominated systems are concerned, much of the currently available modeling tools go back to the pioneering work of Prendergast & Tomer (1970), Wilson (1975), and Toomre (1982), intended to describe ellipticals, and of Jarvis & Freeman (1985) and Rowley (1988), devoted to bulges. In general, we may say that only very few rotating models with explicit distribution function are presently known (for a recent example, see Monari et al. in preparation). In this context, we should also mention the interesting work by Vandervoort (1980) on the collisionless analogues of the Maclaurin and Jacobi ellipsoids.

On the empirical side, a deeper study of quasi-relaxed rotating stellar systems is actu-

ally encouraged by the investigation of the physical orgin of the observed deviation from spherical symmetry. In this respect, a traditional diagnostic tool is offered by the $(V/\sigma, \epsilon)$ diagram, in which the connection between morphology and kinematics is interpreted by means of simple models of rigidly rotating homogeneous fluids (Maclaurin ellipsoids). For this family of models the ratio of ordered to random motions can be expressed as

$$\frac{V}{\sigma} = \frac{\pi}{4}\sqrt{3\frac{2t(e)}{1-2t(e)}} \tag{1.12}$$

where the factor $\pi/4$ is included to take into account the projection effect along the semi-major axis and the function on the right-hand side is defined as

$$t(e) = \frac{K}{|W|} = \frac{3-2e^2}{2e^2} - \frac{3\sqrt{1-e^2}}{2e\ \arcsin e} \tag{1.13}$$

in terms of the polar eccentricity $e = \sqrt{1-(b/a)^2}$. The relation between polar eccentricity e and the projected ellipticity ϵ is given by $e = \sqrt{1-(1-\epsilon)^2}$. This diagram has been widely used for the study of elliptical galaxies (e.g., see Davies et al. 1983; Emsellem et al. 2011), but can be of some interest also for globular clusters. In Fig. 1.7 a selection of rotating globular clusters are represented in such plane; given the small values of ellipticities, the points are primarily located in the lower-left portion of the diagram, in the region characterized by isotropy to mild anisotropy of the pressure tensor.

The connection between flattening and internal rotation has been discussed in detail by means of nonspherical dynamical models in just a handful of cases, in particular for ω Cen (for an oblate rotator nonparametric model, see Merritt et al. 1997; for an orbit-based analysis, see van de Ven et al. 2006; for an application of the Wilson 1975 models, see Sollima et al. 2009), 47 Tuc (Meylan & Mayor 1986), M15 (van den Bosch et al. 2006), and M13 (Lupton et al. 1987). In addition, specifically designed 2D Fokker-Planck models (Fiestas et al. 2006) have been applied to the study of M5, NGC 2808, and NGC 5286. We recall that the detection of internal rotation in globular clusters is a challenging task, because the typical value of the ratio of the amplitude of the projected rotation velocity to the central velocity dispersion is only of a few tenths, for example $V/\sigma_0 \approx 0.46, 0.32$ for 47 Tuc and ω Cen, respectively (from a recent study by Bellazzini et al. 2012; for a summary of the results for several Galactic objects, see Table 1.2 and also Table 7.2 in Meylan & Heggie 1997). However, great progress made in the acquisition of photometric and kinematical information, and in particular of the proper motion of thousands of stars (for ω Cen, see van Leeuwen et al. 2000, Anderson & van der Marel 2010; for 47 Tucanae, see Anderson & King 2003 and McLaughlin et al. 2006), makes this goal within reach (see Lane et al. 2009, Lane et al. 2010b for new kinematical measurements, in which rotation, when present, is clearly identified).

On the one hand, two general questions provide further motivation to study quasi-relaxed rotating stellar systems. On the one hand, many papers have studied the role of rotation in the general context of the dynamical evolution of globular clusters, but a solid interpretation is still missing. Early investigations (Agekian 1958; Shapiro & Marchant 1976) suggested that initially rotating systems should experience a loss of angular momentum induced by evaporation, that is, angular momentum would be removed by stars escaping from the cluster. Because of the small number of particles, N-body simulations were initially (Aarseth 1969; Wielen 1974; Akiyama & Sugimoto 1989) unable to clearly describe the complex interplay between relaxation and rotation. Later investigations, primarily based on a Fokker-Planck approach (Goodman 1983; Einsel & Spurzem

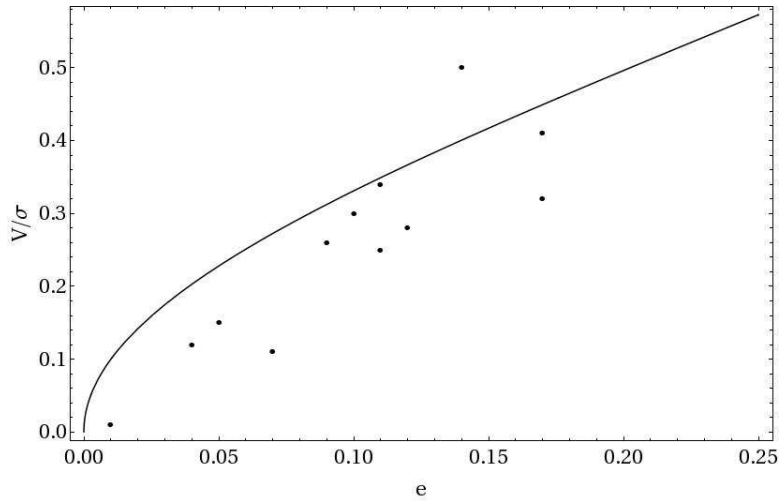

Figure 1.7: $(V/\sigma, \epsilon)$ diagram for selected Galactic globular clusters. Data are taken from Table 7.2 of Meylan & Heggie 1997.

1999; Kim et al. 2002; Fiestas et al. 2006) have clarified this point, not only by testing the proposed mechanism of angular momentum removal by escaping stars, but also by showing that rotation accelerates the entire dynamical evolution of the system. More recent N-body simulations (Boily 2000; Ernst et al. 2007; Kim et al. 2008) confirm these conclusions and show that, when a three-dimensional tidal field is included, such acceleration is enhanced even further. The mechanism of angular momentum removal is generally considered to be the reason why Galactic globular clusters are much rounder than the (younger) clusters in the Magellanic Clouds, for which an age-ellipticity relation has been noted (Frenk & Fall 1982), but other mechanisms might operate to produce the observed correlations (Meylan & Heggie 1997; van den Bergh 2008).

On the other hand, the role of angular momentum during the initial stages of cluster formation should be better clarified. In the context of dissipationless collapse, relatively few investigations have considered the role of angular momentum in numerical experiments of violent relaxation (e.g., the pioneering studies by Gott 1973; see also Aguilar & Merritt 1990). Interestingly, the final equilibrium configurations resulting from such collisionless collapse show a central region with solid body rotation, while the external parts are characterized by differential rotation.

It would thus be desirable to construct rotating models to be tested on low luminosity ellipticals, bulges, and globular clusters, especially now that important progress has been made in the collection and analysis of kinematical data. Presumably, many of these stellar systems are quasi-relaxed, at least in their central regions. In which directions should we explore deviations from the strictly relaxed case? We try to answer to this question in Part II of the present Thesis, with the construction of two new families of rotating equilibria, explicitly designed to describe, at least in the moderate rotation regime, the properties of globular clusters.

1.4.4 Anisotropy in velocity space

The zeroth-order dynamical interpretation of globular clusters in terms of quasi-relaxed stellar systems present some limitations also with respect to the assumed properties of the velocity space. In fact, these stellar systems are inhomogeneous, with a clear trend to become less collisional in their outer parts (note that by applying the formula for the relaxation time (Chandrasekhar 1942) to the outer boundary of a King model, we find that σ^3/ρ diverges quickly as we approach the truncation radius). In this respect, it might even be, in principle, that their outer structure is not too far from that of bright elliptical galaxies for which violent relaxation is thought to have acted primarily to make the inner system quasi-relaxed, while the outer parts are more and more dominated by radially-biased anisotropic pressure. This line of argument motivates the use of the generalization of King models to the anisotropic case (i.e., the so-called Michie-King models, in which the truncated Maxwellian is associated with the anisotropic factor of the Eddington models, see Gunn & Griffin 1979).

Some studies of Galactic globular clusters in terms of anisotropic models, constrained simultaneously by density and velocity dispersion profiles, are actually available, mainly based on multi-mass Michie-King models (e.g., see Gunn & Griffin 1979, Meylan et al. 1995, and Meylan & Mayor 1991 for M3, ω Centauri, and NGC 6397, respectively), but a systematic and homogeneous investigation is still missing. Note that, on the galactic side, investigations of these issues, starting with the mid 1970s, have led to the remarkable discovery that bright ellipticals are generally supported by anisotropic pressure and contain significant amounts of dark matter inside the effective radius $R_{\rm e}$ (e.g., see Chap. 24 in Bertin 2000). From the study of elliptical galaxies it has also been learned that structurally different models (as diagnosed by their kinematics or characterized by their virial coefficients) may have remarkably similar photometric profiles (e.g., see Appendix D of Bertin et al. 2002).

In Part III of the present Thesis we wish to investigate this issue in detail, by performing a systematic combined photometric and kinematic analysis of a sample of globular clusters under different relaxation conditions, as measured by their core relaxation time. Systems characterized by shorter relaxation time scales are expected to be better described by isotropic King models, while less relaxed systems might be interpreted by means of non-truncated, radially-biased anisotropic $f^{(\nu)}$ models, originally designed to represent stellar systems produced by a violent relaxation formation process and applied here for the first time to the study of globular clusters.

Several families of dynamical models have been developed to represent the final state of numerical simulations of the violent relaxation process thought to be associated with the formation of bright elliptical galaxies via collisionless collapse (for a review, see Bertin & Stiavelli 1993). These models show a characteristic anisotropy profile, with an inner isotropic core and an outer envelope that becomes dominated by radially-biased anisotropic pressure. They provide a good representation of the photometric and kinematic properties of elliptical galaxies. Here we will refer to the family of spherical, anisotropic, non-truncated $f^{(\nu)}$ models (which have been revisited recently in detail by Bertin & Trenti 2003).

The distribution function that defines these models depends on specific energy E and angular momentum J:

$$f^{(\nu)} = \begin{cases} A \exp\left[-aE - d\left(\frac{J^2}{|E|^{3/2}}\right)^{\nu/2}\right] & E \leq 0 \\ 0 & E > 0 \ , \end{cases} \tag{1.14}$$

where A, a, d, and ν are positive constants, defining two scales and two dimensionless parameters. For applications, as described by Bertin & Trenti (2003), the dimensionless parameter ν can be fixed at $\nu = 1$. Therefore, similarly to the King models, after integration of the relevant Poisson equation the $f^{(\nu)}$ models are a one-parameter family of models, parametrized by their central concentration, which can be expressed by the central dimensionless potential $\Psi = -a\Phi(0)$.

The physical scales can be expressed as $r_{\rm scale} = d^{-1/\nu}a^{-1/4}$ and $M_{\rm scale} = d^{-3/\nu}a^{-9/4}$. By definition, these models are non-truncated and, because of this, are likely to be less suited to describe the outer parts of globular clusters. A study of globular clusters based on truncated $f^{(\nu)}$ models is postponed to a separate investigation. We recall that the surface brightness profiles for concentrated models ($\Psi \gtrsim 7$) are very close to de Vaucouleurs profile, while for low values of Ψ the models exhibit a sizeable core.

Part I
External Tidal Field

CHAPTER 2

The construction of nonspherical models of quasi-relaxed stellar systems

2.1 Introduction

In order to better address the role of tides in determining the observed structure of globular clusters, in the present Chapter we construct a family of self-consistent nonspherical equilibrium models of quasi-relaxed stellar systems, obtained from the spherical case by including in their distribution function the effects associated with the presence of an external tidal field explicitly. Our models consider the stellar system in circular orbit within the host galaxy, for simplicity assumed to be spherically-symmetric. Therefore, in the corotating frame of reference, the tidal field experienced by the system is stationary and the Jacobi integral H is available. In this physical picture the typical dynamical time associated with the orbits inside the cluster is assumed to be much smaller than the external orbital time. The procedure starts by replacing the single-star energy E with the Jacobi integral in the relevant distribution function $f_K(H) = A[\exp(-aH) - \exp(-aH_0)]$ if $H \leq H_0$, with H_0 the cut-off constant, and $f_K(H) = 0$ otherwise. Thus the collisionless Boltzmann equation is satisfied. The construction of the self-consistent models then requires the solution of the associated Poisson-Laplace equation, that is of a second-order elliptic partial differential equation in a free boundary problem, because the boundary of the configuration, which represents the separation between the Poisson and Laplace domains, can be determined only *a posteriori*. The idea of using the Jacobi integral for the construction of tidal triaxial models had been proposed also by Weinberg (1993). A first-order analysis of the triaxial tidal problem addressed in this Chapter was carried out by Heggie & Ramamani (1995).

The Chapter is organized as follows. Section 2.2 introduces the reference physical model, in which a globular cluster is imagined to move on a circular orbit inside a host galaxy treated as a frozen background field. The distribution function for such a cluster is then identified and the relevant parameter space defined. Section 2.3 sets the mathematical problem associated with the construction of the related self-consistent models. For models generated by the spherical $f_K(E)$, Section 2.4 gives the complete solution in terms of matched asymptotic expansions. Alternative methods of solutions are briefly discussed in Section 2.5. In addition, in Section 2.6 it is shown how the method can be applied to the study of the three-dimensional effects of tides on other isotropic truncated models, different from King models. The concluding Section 2.7 gives a summary of the Chapter, with a short discussion of the results obtained.

Technically, the mathematical problem of a singular perturbation with a free boundary that is faced here is very similar to the problem noted in the theory of rotating stars, starting with Milne (see Tassoul 1978; Milne 1923; Chandrasekhar 1933; Krogdahl 1942;

Chandrasekhar & Lebovitz 1962; Monaghan & Roxburgh 1965). The problem was initially dealt with inadequate tools; a satisfactory solution of the singular perturbation problem was obtained only later, by Smith (1975, 1976).

2.2 The physical model

2.2.1 The tidal potential

As a reference case, we consider an idealized model in which the center of mass of a globular cluster is imagined to move on a circular orbit of radius R_0, characterized by orbital frequency Ω, inside a host galaxy. For simplicity, we focus on the motion of the stars inside the globular cluster and model the galaxy, taken to have very large mass, by means of a *frozen* gravitational field (which we will call the galactic field, described by the potential Φ_G), with a given overall symmetry. This choice makes us ignore interesting effects that are generally present in the full interaction between a "satellite" and a galaxy; in a sense, we are taking a complementary view of an extremely complex dynamical situation, with respect to other investigations, such as those that lead to a discussion of the mechanism of dynamical friction (in which the globular cluster or satellite is modeled as a rigid body and the stars of the galaxy are taken as the "live" component; see Bontekoe & van Albada 1987; Bertin et al. 2003; Arena & Bertin 2007; and references therein). Therefore, we will be initially following the picture of a *restricted three-body problem*, with one important difference, that the "secondary" is not treated as a point mass but as a "live" stellar system, described by the cluster mean-field potential Φ_C. In this extremely simple orbital choice for the cluster center of mass, in the corotating frame the associated tidal field is time-independent and so we can proceed to the construction of a stationary dynamical model.

We consider the galactic potential Φ_G to be spherically symmetric, that is, $\Phi_G = \Phi_G(R)$, with $R = \sqrt{X^2+Y^2+Z^2}$, in terms of a standard set of Cartesian coordinates (X, Y, Z), so that $\Omega^2 = (d\Phi_G(R)/dR)_{R_0}/R_0$. Let (X, Y) be the orbit plane of the center of mass of the cluster. We then introduce a local rotating frame of reference, so that the position vector is given by $\mathbf{r} = (x, y, z)$, with origin in the center of mass of the cluster and for which the x-axis points away from the center of the galactic field, the y-axis follows the direction of the cluster rotation in its orbit around the galaxy, and the z-axis is perpendicular to the orbit plane (according to the right-hand rule). In such rotating local frame, the relevant Lagrangian, describing the motion of a star belonging to the cluster, is (cf. Chandrasekhar 1942, Eq. [5.510]):

$$\mathcal{L} = \frac{1}{2}\{\dot{x}^2+\dot{y}^2+\dot{z}^2+\Omega^2[(R_0+x)^2+y^2]+2\Omega(R_0+x)\dot{y}-2\Omega\dot{x}y\}-\Phi_G(R)-\Phi_C(x,y,z)\,, \quad (2.1)$$

where $R = \sqrt{(R_0+x)^2+y^2+z^2}$ and the terms responsible for centrifugal and Coriolis forces are explicitly displayed.

If we suppose that the size of the cluster is small compared to R_0, we can adequately represent the galactic field by its linear approximation with respect to the local coordinates (the so-called "tidal approximation"). The corresponding equations of the motion

for a single star in the rotating local frame are:

$$\ddot{x} - 2\Omega\dot{y} - (4\Omega^2 - \kappa^2)x = -\frac{\partial\Phi_C}{\partial x} \,, \tag{2.2}$$

$$\ddot{y} + 2\Omega\dot{x} = -\frac{\partial\Phi_C}{\partial y} \,, \tag{2.3}$$

$$\ddot{z} + \Omega^2 z = -\frac{\partial\Phi_C}{\partial z} \,, \tag{2.4}$$

where κ is the epicyclic frequency at R_0, given by $\kappa^2 = 3\Omega^2 + (d^2\Phi_G/dR^2)_{R_0}$. Note that the assumed symmetry for Φ_G introduces a cancellation between the kinematic term $y\Omega^2$ and the gradient of the galactic potential $\partial\Phi_G/\partial y$ and makes the vertical acceleration $-\partial\Phi_G/\partial z$ approximately equal to $-z\Omega^2$.

These equations admit an energy (isolating) integral of the motion, known as the Jacobi integral:

$$H = \frac{1}{2}(\dot{x}^2 + \dot{y}^2 + \dot{z}^2) + \Phi_T + \Phi_C \,, \tag{2.5}$$

where

$$\Phi_T = \frac{1}{2}\Omega^2 \left(z^2 - \nu x^2\right) \tag{2.6}$$

is the tidal potential. Here $\nu \equiv 4 - \kappa^2/\Omega^2$ is a generally positive dimensionless coefficient.

Thus, at the level of single star orbits, we note that, in general, the tidal potential leads to a compression in the z-direction, a stretching in the x-direction, and leaves the y-direction untouched. The tidal potential is static, breaks the spherical symmetry, but is characterized by reflection symmetry with respect to the three natural coordinate planes; strictly speaking, the symmetry with respect to (y, z) is applicable only in the limit of an infinitely massive host galaxy (see Spitzer 1987). In turn, we will see that the geometry of the tidal potential induces a non-spherical distortion of the cluster shape collectively, in particular an elongation along the x-axis and a compression along the z-axis. In practice, the numerical coefficient ν that defines quantitatively the induced distortion depends on the galactic potential. We recall that we have $\nu = 3$ for a Keplerian potential, $\nu = 2$ for a logarithmic potential, while for a Plummer model the dimensionless coefficient depends on the location of the circular orbit with respect to the model scale radius b, with $\nu(R_0) = 3R_0^2/(b^2 + R_0^2)$ (for a definition of the Plummer model see, e.g., Bertin 2000).

Different assumptions on the geometry of the galactic field can be treated with tools similar to those developed here, leading to a similar structure of the equations of the motion, with a slight modification of the tidal field. In particular, for an axisymmetric galactic field, the tidal potential differs from the one obtained here only by the z-term (Chandrasekhar 1942; Heggie & Hut 2003). This case is often considered, for example by referring to a globular cluster in circular orbit on the (axisymmetric) disk of our Galaxy (see Heggie & Ramamani 1995; Ernst et al. 2008), for which Φ_T is then formulated in terms of the Oort constants.

In the physical model outlined in this Section, the typical dynamical time associated with the star orbits inside the cluster is much smaller than the (external) orbital time associated with Ω. Therefore, in an asymptotic sense, the equilibrium configurations that we will construct in the rest of the Chapter can actually be generalized, with due qualifications, to more general orbits of the cluster inside a galaxy, provided we interpret the results that we are going to obtain as applicable only to a small piece of the cluster orbit.

2.2.2 The distribution function

As outlined in the Section 2.1, we wish to extend the description of quasi-relaxed stellar systems (so far basically limited to spherical models associated with distribution functions $f = f(E)$, dependent only on the single-star specific energy $E = v^2/2 + \Phi_C$) to the non spherical case, by including the presence of a non-spherical tidal field explicitly. Given the success of the spherical King models in the study of globular clusters, we will focus on the extension of models based on $f_K(E)$, which is defined as a "lowered" Maxwellian, continuous in phase space, with an energy cut-off that implies the existence of a boundary at the truncation radius r_{tr}.

Therefore, we will consider (partially) self-consistent models characterized by the distribution function:

$$f_K(H) = A[\exp(-aH) - \exp(-aH_0)] \tag{2.7}$$

if $H \leq H_0$ and $f_K(H) = 0$ otherwise, in terms of the Jacobi integral defined by Eq. (2.5). Here H_0 is the cut-off value for the Jacobi integral, while A and a are positive constants.

In velocity space, the inequality $H \leq H_0$ identifies a spherical region given by $0 \leq v^2 \leq 2\psi(\mathbf{r})/a$, where:

$$\psi(\mathbf{r}) = a\{H_0 - [\Phi_C(\mathbf{r}) + \Phi_T(x, z)]\} \tag{2.8}$$

is the dimensionless escape energy. Therefore, the boundary of the cluster is defined as the relevant zero-velocity surface by the condition $\psi(\mathbf{r}) = 0$ and is given only implicitly by an equipotential (*Hill*) surface for the total potential $\Phi_C + \Phi_T$; in fact, its geometry depends on the properties of the tidal potential (of known characteristics; see Eq. [2.6]) and of the cluster potential (unknown *a priori*, to be determined as the solution of the associated Poisson equation).

The value of the cut-off potential H_0 should be chosen in such a way that the surface that defines the boundary is closed. The last (i.e., outermost) closed Hill surface is a *critical* surface, because it contains two saddle points that represent the Lagrangian points of the restricted three-body problem outlined in the previous subsection. From Eqs. (2.2)-(2.4), we see that such Lagrangian points are located symmetrically with respect to the origin of the local frame of reference and lie on the x-axis. Their distance from the origin is called the *tidal radius*, which we denote by r_T, and can be determined from the condition:

$$\frac{\partial \psi}{\partial x}(r_T, 0, 0) = 0 \, . \tag{2.9}$$

If, as a zero-th order approximation, we use a simple Keplerian potential for the cluster potential Φ_C, we recover the classical expression (e.g., see Spitzer 1987):

$$r_T^{(0)} = \left(\frac{GM}{\Omega^2 \nu}\right)^{1/3} , \tag{2.10}$$

where M is the total mass of the cluster.

As for the spherical King model, the density profile associated with the distribution function (4.3) is given by:

$$\rho(\psi) = \hat{A} e^{\psi} \gamma\left(\frac{5}{2}, \psi\right) \equiv \hat{A} \hat{\rho}(\psi) \, , \tag{2.11}$$

where $\hat{A} = 8\pi A \sqrt{2} e^{-aH_0}/(3a^{3/2})$. We recall that the incomplete gamma function has non-negative real value only in correspondence to a non-negative argument. In the following, we will denote the central density of the cluster by $\rho_0 = \hat{A}\hat{\rho}(\Psi)$, where $\Psi \equiv \psi(\mathbf{0})$ is the depth of the central potential well.

2.2.3 The parameter space

The models defined by $f_K(H)$ are characterized by two physical scales (e.g., the two free constants A and a, or, correspondingly, the total mass M and the central density ρ_0 of the cluster) and two dimensionless parameters. The first dimensionless parameter can be defined, as in the spherical King models, to measure the *concentration* of the cluster. We can thus consider the quantity Ψ, introduced at the end of the previous subsection, or we may refer to the commonly used concentration parameter:

$$C = \log(r_{tr}/r_0) \ , \tag{2.12}$$

where $r_0 = \sqrt{9/(4\pi G\rho_0 a)}$ is a scale length related to the size of the core and r_{tr} is the truncation radius of the spherical King model associated with the same value of the central potential well Ψ (the relation between C and Ψ is one-to-one; e.g., see Bertin 2000).

The second dimensionless parameter characterizes the strength of the (external) tidal field:

$$\epsilon \equiv \frac{\Omega^2}{4\pi G\rho_0} \ . \tag{2.13}$$

The definition arises naturally from the dimensionless formulation of the Poisson equation that describes the (partially) self-consistent problem (to be addressed in the next Section).

In principle, for a given choice of the dimensional scales (A and a) the truncation radius or the concentration parameter of a spherical King model can be set arbitrarily. In practice, the physical motivation of the models suggests that the truncation radius r_{tr} should be taken to be of the order of (and not exceed) the tidal radius r_T, introduced in the previous subsection (see Eq. [2.9]). We may thus define an *extension parameter*, as the ratio between the truncation radius of the corresponding spherical model and the tidal radius r_T:

$$\delta \equiv \frac{r_{tr}}{r_T} \ . \tag{2.14}$$

For a given value of the central potential well Ψ, there exists a (maximum) critical value for the tidal strength parameter, which we will denote by ϵ_{cr}, corresponding to the maximum value for the extension parameter δ_{cr}, which can be found by solving the system:

$$\begin{cases} \dfrac{\partial \psi}{\partial x}(r_T, 0, 0; \epsilon_{cr}) = 0 \\ \psi(r_T, 0, 0; \epsilon_{cr}) = 0 \ . \end{cases} \tag{2.15}$$

From this system, if we use the zero-th order Keplerian approximation for Φ_C, we find that $\delta_{cr}^{(0)} = 2/3$ (see Spitzer 1987).

For our two-parameter family of models we thus expect two tidal regimes to exist. For models characterized by the pairs (Ψ, ϵ) near the critical condition $\delta \approx \delta_{cr}$ the tidal distortion should be maximal, while for models with pairs well below criticality only small departures from spherical symmetry should occur. A thorough exploration of the parameter space will be carried out in the next Chapter. In closing, we note that the models proposed and studied by Heggie & Ramamani (1995) correspond to the pairs in parameter space that we have called critical.

2.3 The mathematical problem

The (partially) self-consistent models associated with the distribution function defined by Eq. (4.3) are constructed by solving the relevant Poisson equation. In terms of the dimensionless escape energy ψ, given by Eq. (3.1), the Poisson equation (for $\psi \geq 0$) can be written as:

$$\nabla^2(\psi + a\Phi_T) = -\frac{9}{r_0^2}\frac{\rho}{\rho_0} = -\frac{9}{r_0^2}\frac{\hat{\rho}(\psi)}{\hat{\rho}(\Psi)} \,, \tag{2.16}$$

where r_0 is the scale length introduced in Sect. 2.2.3 (see Eq. [2.12]). We then rescale the coordinates and introduce the dimensionless position vector $\hat{\mathbf{r}} = \mathbf{r}/r_0$, so that $\hat{\nabla}^2 = r_0^2\nabla^2$ and $a\Phi_T \equiv \epsilon T = 9\epsilon(\hat{z}^2 - \nu\hat{x}^2)/2$, where we have made use of the tidal parameter introduced in Eq. (2.13). Therefore, the Poisson equation, for $\psi \geq 0$, can be written in dimensionless form as:

$$\hat{\nabla}^2\psi = -9\left[\frac{\hat{\rho}(\psi)}{\hat{\rho}(\Psi)} + \epsilon(1-\nu)\right] \,, \tag{2.17}$$

while for negative values of ψ we should refer to:

$$\hat{\nabla}^2\psi = -9\epsilon(1-\nu) \,, \tag{2.18}$$

that is, the Laplace equation $\hat{\nabla}^2(a\Phi_C) = 0$.

The mathematical problem is completed by specifying the appropriate boundary conditions. As for the spherical King models, we require regularity of the solution at the origin

$$\psi(\mathbf{0}) = \Psi \,, \tag{2.19}$$

$$\hat{\nabla}\psi(\mathbf{0}) = \mathbf{0} \,, \tag{2.20}$$

and, at large radii:

$$\psi + \epsilon T \to aH_0 \,, \tag{2.21}$$

which corresponds to $a\Phi_C \to 0$.

Poisson and Laplace domains are thus separated by the surface defined by $\psi = 0$ which is unknown *a priori*; in other words, we have to solve an **elliptic partial differential equation in a free boundary problem**.

In the ordinary differential problem that characterizes the construction of spherical models with finite mass, the condition of vanishing cluster potential at large radii (together with the regularity conditions at the origin) overdetermines the problem, which can then be seen as an eigenvalue problem (e.g., see Sect. 2.5 in Bertin & Stiavelli 1993). Indeed, for the King models the integration of the Poisson equation from the origin outwards, with "initial conditions" (2.19)-(2.20), sets the relation between the ratio r_{tr}/r_0 and Ψ in order to meet the requirement (2.21), with r_{tr}/r_0 thus playing the role of an "eigenvalue".

In the more complex, three-dimensional situation that we are facing here, the existence of two different domains, internal (Poisson) and external (Laplace), suggests the use of the method of matched asymptotic expansions in order to obtain a uniform solution across the separation free surface. The solution in the internal and external domains are expressed as an asymptotic series with respect to the tidal parameter ϵ, which is assumed to be small (following the physical model described in the previous Section):

$$\psi^{(int)}(\hat{\mathbf{r}};\epsilon) = \sum_{k=0}^{\infty}\frac{1}{k!}\psi_k^{(int)}(\hat{\mathbf{r}})\epsilon^k \,, \tag{2.22}$$

$$\psi^{(ext)}(\hat{\mathbf{r}};\epsilon) = \sum_{k=0}^{\infty} \frac{1}{k!} \psi_k^{(ext)}(\hat{\mathbf{r}}) \epsilon^k \ , \tag{2.23}$$

with spherical symmetry assumed for the zero-th order terms. The internal solution should obey the boundary conditions (2.19)-(2.20), while the external solution should satisfy Eq. (2.21). The two representations should be properly connected at the surface of the cluster.

On the other hand, for any small but finite value of ϵ the boundary, defined by $\psi = 0$, will be different from the unperturbed boundary, defined by $\psi_0 = 0$, so that, for each of the two representations given above, there will be a small region in the vicinity of the surface of the cluster where the leading term is vanishingly small and actually smaller than the remaining terms of the formal series. Therefore, we expect the validity of the expansion to break down where the second term becomes comparable to the first, i.e where $\psi_0 = \mathcal{O}(\epsilon)$. This region can be considered as a *boundary layer*, which should be examined in "microscopic" detail by a suitable rescaling of the spatial coordinates and for which an adequate solution $\psi^{(lay)}$, expressed as a different asymptotic series, should be constructed. To obtain a uniformly valid solution over the entire space, an asymptotic matching is performed between the pairs ($\psi^{(int)}$, $\psi^{(lay)}$) and ($\psi^{(lay)}$, $\psi^{(ext)}$), thus leading to a solution ψ, obeying all the desired boundary conditions, in terms of three different, but matched, representations. This method of solution is basically the same method proposed by Smith (1975) for the analogous mathematical problem that arises in the determination of the structure of rigidly rotating fluid polytropes.

2.4 Solution in terms of matched asymptotic expansions

The complete solution to two significant orders in the tidal parameter is now presented. The formal solution to three orders is also displayed because of the requirements of the Van Dyke principle of asymptotic matching (cf. Van Dyke 1975, Eq. [5.24]) that we have adopted.

Here one important comment is in order. Strictly speaking, the complete solution for $a\Phi_C$ derived by the method of matched asymptotic expansions illustrated in this Section is a well-justified global uniform solution only for sub-critical (underfilled) models. Close to the condition of criticality, i.e., when $\hat{r}_{tr} \sim \hat{r}_T$, in the vicinity of the boundary surface the tidal term ϵT (which is considered a small correction in the construction of the asymptotic solution) becomes comparable to the cluster term $a\Phi_C$, so that the asymptotic solution is expected to break down. For such models, the iteration method described that will be described in Section 2.5.2 of Chapter 2, which does not rely on the assumption that the tidal term is small, is preferred and expected to lead quickly to more accurate solutions. In practice, in line with previous work on the similar problem for rotating polytropes mentioned in the Introduction, we argue that the use of the second-order asymptotic solution constructed in Chapter 2 will give sufficiently accurate solutions in the determination of the critical value of the tidal parameter ϵ_{cr} from the system in Eq. (2.15) and in the consequent assessment of the general properties of models even when close to the critical case. The main reason at the basis of this argument is that, even for close-to-critical models, only very few stars populate the region where the asymptotic analysis breaks down, so that the overall solution should be only little affected. A direct comparison between selected critical models calculated with both the perturbation and the iteration method Will be presented in the next Chapter (see Section 3.6)

2.4.1 Internal region

If we insert the series (2.22) in the Poisson equation (2.17), under the conditions (2.19)-(2.20), we obtain an (infinite) set of Cauchy problems for ψ_k. The problem for the zero-th order term (i.e., the unperturbed problem with $\epsilon = 0$) is the one defining the construction of the spherical and fully self-consistent King models:

$$\psi_0^{(int)\,''} + \frac{2}{\hat{r}}\psi_0^{(int)\,\prime} = -9\frac{\hat{\rho}\left(\psi_0^{(int)}\right)}{\hat{\rho}(\Psi)} \,, \tag{2.24}$$

with $\psi_0^{(int)}(0) = \Psi$ and $\psi_0^{(int)\,\prime}(0) = 0$, where the symbol $'$ denotes derivative with respect to the argument $\hat{r}$. We recall that the truncation radius $\hat{r}_{tr}$, which defines the boundary of the spherical models, is given implicitly by $\psi_0^{(int)}(\hat{r}_{tr}) = 0$.

Let us introduce the quantities:

$$R_j(\hat{r};\Psi) \equiv \frac{9}{\hat{\rho}(\Psi)}\frac{d^j\hat{\rho}}{d\psi^j}\bigg|_{\psi_0^{(int)}} \,. \tag{2.25}$$

These quantities depend on $\hat{r}$ implicitly, through the function $\psi_0^{(int)}$; in turn, the dependence on Ψ is both explicit (through the term $\hat{\rho}(\Psi)$) and implicit (because the function $\psi_0^{(int)}(\hat{r})$ depends on the value of Ψ). For convenience, we give the expression of the first terms of the sequence (cfr. Eq. [2.11]): $R_1 = [9/\hat{\rho}(\Psi)][\hat{\rho}(\psi_0^{(int)}) + (\psi_0^{(int)})^{3/2}]$, $R_2 = R_1 + 27(\psi_0^{(int)})^{1/2}/[2\hat{\rho}(\Psi)]$, $R_3 = R_2 + 27(\psi_0^{(int)})^{-1/2}/[4\hat{\rho}(\Psi)]$. Note that for $\psi_0^{(int)} \to 0$, that is, for $\hat{r} \to \hat{r}_{tr}$, $R_1 \to 0$, $R_2 \to 0$, whereas for $j \geq 3$ the quantities R_j actually *diverge*. This is one more indication of the singular character of our perturbation analysis, which brings in some fractional power dependence on the perturbation parameter ϵ (see also expansion [2.46]).

Therefore, the equations governing the next two orders (for $\psi_k^{(int)}$ with $k = 1, 2$) can be written as:

$$\left[\hat{\nabla}^2 + R_1(\hat{r};\Psi)\right]\psi_1^{(int)} = -9(1-\nu) \tag{2.26}$$

$$\left[\hat{\nabla}^2 + R_1(\hat{r};\Psi)\right]\psi_2^{(int)} = -R_2(\hat{r};\Psi)(\psi_1^{(int)})^2 \tag{2.27}$$

with $\psi_1^{(int)}(\mathbf{0}) = \psi_2^{(int)}(\mathbf{0}) = 0$ and $\hat{\nabla}\psi_1^{(int)}(\mathbf{0}) = \hat{\nabla}\psi_2^{(int)}(\mathbf{0}) = \mathbf{0}$. The equation for $k = 3$ is recorded in Appendix A.1, where we also describe the structure of the general equation for $\psi_k^{(int)}$.

For any given order of the expansion, the operator acting on the function $\psi_k^{(int)}$ (see the left-hand side of Eqs. [2.26] and [2.27]) is the same, that is, a Laplacian "shifted" by the function $R_1(\hat{r};\Psi)$. If we thus expand every term $\psi_k(\hat{\mathbf{r}})$ in spherical harmonics[1]:

$$\psi_k^{(int)}(\hat{\mathbf{r}}) = \sum_{l=0}^{\infty}\sum_{m=-l}^{l}\psi_{k,lm}^{(int)}(\hat{r})Y_{lm}(\theta,\phi) \,, \tag{2.28}$$

the three-dimensional differential problem is reduced to a one-dimensional (radial) problem, characterized by the following second order, linear ordinary differential operator:

[1] We use orthonormalized real spherical harmonics with Condon-Shortley phase; with respect to the toroidal angle ϕ, they are even for $m \geq 0$ and odd otherwise.

$$\mathcal{D}_l = \frac{d^2}{d\hat{r}^2} + \frac{2}{\hat{r}}\frac{d}{d\hat{r}} - \frac{l(l+1)}{\hat{r}^2} + R_1(\hat{r};\Psi)\ . \tag{2.29}$$

In general, for a fixed value of l, two independent solutions to the homogeneous problem $\mathcal{D}_l f = 0$ are expected [2] to behave like $\hat{r}^l$ and $1/\hat{r}^{l+1}$ for $\hat{r} \to 0$. Because of the presence of $R_1(\hat{r};\Psi)$, solutions to equations where $\mathcal{D}_l$ appears have to be obtained numerically.

For $k = 1$ (see Eq. [2.26]) we thus have to address the following problem. For $l = 0$, the relevant equation is:

$$\mathcal{D}_0 f_{00} = -9(1-\nu), \tag{2.30}$$

where $f_{00} \equiv \psi^{(int)}_{1,00}/\sqrt{4\pi}$, with $f_{00}(0) = f'_{00}(0) = 0$. Here we do not have to worry about including solutions to the associated homogeneous problem, because one of the two independent solutions would be singular at the origin and the other would be forced to vanish by the required condition at $\hat{r} = 0$. For $l \geq 1$ we have:

$$\mathcal{D}_l \psi^{(int)}_{1,lm} = 0 \tag{2.31}$$

with $\psi^{(int)}_{1,lm}(0) = \psi^{(int)'}_{1,lm}(0) = 0$. Both Eq. (2.31) and the associated boundary conditions are homogeneous. Therefore, the solution is undetermined by an m-dependent multiplicative constant: $\psi^{(int)}_{1,lm}(\hat{r}) = A_{lm}\gamma_l(\hat{r})$, with $\gamma_l(\hat{r}) \sim \hat{r}^l$ for $\hat{r} \to 0$ (the singular solution is excluded by the boundary conditions at the origin). Then the complete formal solution is:

$$\psi^{(int)}_1(\hat{\mathbf{r}}) = f_{00}(\hat{r}) + \sum_{l=1}^{\infty}\sum_{m=-l}^{l} A_{lm}\gamma_l(\hat{r})Y_{lm}(\theta,\phi)\ , \tag{2.32}$$

where the constants are ready to be determined by means of the asymptotic matching with $\psi^{(lay)}_1(\hat{\mathbf{r}})$ at the boundary layer.

For $k = 2$ (see Eq. [2.27]) the relevant equations are:

$$\mathcal{D}_l \psi^{(int)}_{2,lm} = -R_2(\hat{r};\Psi)\left[{\psi^{(int)}_1}^2\right]_{lm}\ , \tag{2.33}$$

where on the right-hand side the function $\psi^{(int)}_1$ is that derived from the solution of the first order problem (which shows the progressive character of this method for the construction of solutions). In Appendix A.2 the equations for the six relevant harmonics are displayed explicitly. The boundary conditions to be imposed at the origin are again homogeneous: $\psi^{(int)}_{2,lm}(0) = \psi^{(int)'}_{2,lm}(0) = 0$. For a fixed harmonic (l,m) with $l > 0$, the general solution of Eq. (2.33) is the sum of a particular solution (which we will denote by $g_{lm}(\hat{r})$) and of a regular solution to the associated homogeneous problem given by Eq. (2.31) (which we will call $B_{lm}\gamma_l(\hat{r})$, with $\gamma_l(\hat{r})$ the same functions introduced for the first order problem). Obviously, the particular solution exists only when Eq. (2.33) is non-homogeneous, that is, only for those values of (l,m) that correspond to a non-vanishing coefficient in the expansion of $(\psi^{(int)}_1)^2$ in spherical harmonics. As noted in

[2] We note that $R_1(0,\Psi) = 9[1+\Psi^{3/2}/\hat{\rho}(\Psi)]$, that is, a numerical positive constant. Therefore, for $\hat{r} \to 0$ the operator $\mathcal{D}_l$ tends to the operator associated with the spherical Bessel functions of the first and of the second kind (e.g., see Abramowitz & Stegun 1965, Eq. [10.1.1] for the equation and Eqs. [10.1.4] and [10.1.5] for the limiting values of the functions for small argument).

the first order problem ($k = 1$), the associated homogeneous problem for $l = 0$ has no non-trivial solution. Then we can express the complete solution as:

$$\psi_2^{(int)}(\hat{\mathbf{r}}) = g_{00}(\hat{r}) + \sum_{l=1}^{\infty} \sum_{m=-l}^{l} [g_{lm}(\hat{r}) + B_{lm}\gamma_l(\hat{r})]Y_{lm}(\theta, \phi) \,, \tag{2.34}$$

where B_{lm} are constants to be determined from the matching with the boundary layer.

Similarly, for $k = 3$ the solution can be written as:

$$\psi_3^{(int)}(\hat{\mathbf{r}}) = h_{00}(\hat{r}) + \sum_{l=1}^{\infty} \sum_{m=-l}^{l} [h_{lm}(\hat{r}) + C_{lm}\gamma_l(\hat{r})]Y_{lm}(\theta, \phi) \,, \tag{2.35}$$

where h_{lm} are particular solutions and C_{lm} are constants, again to be determined from the matching with the boundary layer.

Because the differential operator $\mathcal{D}_l$ and the boundary conditions at the origin are the same for the reduced radial problem of every order, we have thus obtained the general structure of the solution for the internal region (see Appendix A.1).

2.4.2 External region

Here we first present the general solution and then proceed to set up the asymptotic series (2.23).

The solution to Eq. (2.18) describing the external region, that is, in the Laplace domain, can be expressed as the sum of a particular solution ($-\epsilon T(\hat{\mathbf{r}})$) and of the solutions to the radial part of the Laplacian operator consistent with the boundary condition (2.21):

$$\psi^{(ext)}(\hat{\mathbf{r}}) = \alpha - \frac{\lambda}{\hat{r}} - \sum_{l=1}^{\infty} \sum_{m=-l}^{l} \frac{\beta_{lm}}{\hat{r}^{l+1}} Y_{lm}(\theta, \phi) - \epsilon T(\hat{\mathbf{r}}) \,. \tag{2.36}$$

Here we note that the tidal potential contributes only with spherical harmonics of order $l = 0, 2$ with even values of m:

$$T_{00}(\hat{r}) = -3\sqrt{\pi}(\nu - 1)\hat{r}^2 \,, \tag{2.37}$$

$$T_{20}(\hat{r}) = 3\sqrt{\frac{\pi}{5}}(2 + \nu)\hat{r}^2 \,, \tag{2.38}$$

$$T_{22}(\hat{r}) = -3\sqrt{\frac{3\pi}{5}}\nu\hat{r}^2 \,. \tag{2.39}$$

At this point we can proceed to set up the asymptotic series, by expanding the constant coefficients α, λ, and β_{lm} with respect to ϵ:

$$\alpha = aH_0 = \alpha_0 + \alpha_1\epsilon + \frac{1}{2!}\alpha_2\epsilon^2 + .. \,, \tag{2.40}$$

$$\lambda = \lambda_0 + \lambda_1\epsilon + \frac{1}{2!}\lambda_2\epsilon^2 + .. \,, \tag{2.41}$$

$$\beta_{lm} = a_{lm}\epsilon + \frac{1}{2!}b_{lm}\epsilon^2 + \frac{1}{3!}c_{lm}\epsilon^3 + .. \,. \tag{2.42}$$

The last expansion starts with a first order term because the density distribution of the unperturbed problem is spherically symmetric.

For convenience, we give the explicit expression of the external solution up to third order:

$$\psi^{(ext)}(\hat{\mathbf{r}}) = \alpha_0 - \frac{\lambda_0}{\hat{r}} + \left\{ \alpha_1 - \frac{\lambda_1}{\hat{r}} - \frac{T_{00}(\hat{r})}{2\sqrt{\pi}} - \sum_{l=1}^{\infty} \sum_{m=-l}^{l} \left[\frac{a_{lm}}{\hat{r}^{l+1}} + T_{lm}(\hat{r}) \right] Y_{lm}(\theta,\phi) \right\} \epsilon$$
$$+ \frac{1}{2!} \left[\alpha_2 - \frac{\lambda_2}{\hat{r}} - \sum_{l=1}^{\infty} \sum_{m=-l}^{l} \frac{b_{lm}}{\hat{r}^{l+1}} Y_{lm}(\theta,\phi) \right] \epsilon^2 + \frac{1}{3!} \left[\alpha_3 - \frac{\lambda_3}{\hat{r}} - \sum_{l=1}^{\infty} \sum_{m=-l}^{l} \frac{c_{lm}}{\hat{r}^{l+1}} Y_{lm}(\theta,\phi) \right] \epsilon^3 \quad (2.43)$$

2.4.3 Boundary layer

The boundary layer is the region where the function ψ becomes vanishingly small. Since the unperturbed gravitational field at the truncation radius is finite, $\psi_0'(\hat{r}_{tr}) \neq 0$, for any value of Ψ, based on a Taylor expansion of ψ_0 about $\hat{r} = \hat{r}_{tr}$ we may argue that the region in which the series (2.22) breaks down can be defined by $\hat{r}_{tr} - \hat{r} = \mathcal{O}(\epsilon)$. In this boundary layer we thus introduce a suitable change of variables:

$$\eta = \frac{\hat{r}_{tr} - \hat{r}}{\epsilon} \,, \quad (2.44)$$

take the ordering $\psi^{(lay)} = \mathcal{O}(\epsilon)$, and thus rescale the solution by introducing the function $\tau \equiv \psi^{(lay)}/\epsilon$. For positive values of τ the Poisson equation (2.17) thus becomes:

$$\frac{\partial^2 \tau}{\partial \eta^2} - \frac{2\epsilon}{\hat{r}_{tr} - \epsilon\eta} \frac{\partial \tau}{\partial \eta} + \frac{\epsilon^2}{(\hat{r}_{tr} - \epsilon\eta)^2} \Lambda^2 \tau = -\frac{9}{\hat{\rho}(\Psi)} \epsilon \hat{\rho}(\epsilon\tau) - 9\epsilon^2(1-\nu) \,, \quad (2.45)$$

where Λ^2 is the angular part of the Laplacian in spherical coordinates. For negative values of τ we can write a similar equation, corresponding to Eq. (2.18), which is obtained from Eq. (2.45) by dropping the term proportional to $\hat{\rho}(\epsilon\tau)$.

With the help of the asymptotic expansion for small argument of the incomplete gamma function (e.g., see Bender 1999, Eq. [6.2.5]), we find:

$$\hat{\rho}(\epsilon\tau) \sim \frac{2}{5} \tau^{5/2} \epsilon^{5/2} + \frac{4}{35} \tau^{7/2} \epsilon^{7/2} + \dots \,, \quad (2.46)$$

so that, within the boundary layer, the contribution of $\hat{\rho}(\epsilon\tau)$ (which is the one that distinguishes the Poisson from the Laplace regime) becomes significant only beyond the tidal term, as a correction $\mathcal{O}(\epsilon^{7/2})$.

Therefore, up to $\mathcal{O}(\epsilon^2)$ we can write:

$$\tau = \tau_0 + \tau_1 \epsilon + \frac{1}{2!} \tau_2 \epsilon^2 . \quad (2.47)$$

To this order, which is required for a full solution up to $k = 2$ of the global problem (see Eqs. [2.22] and [2.23]), by equating in Eq. (2.45) the first powers of ϵ separately, we obtain the relevant equations for the first three terms:

$$\frac{\partial^2 \tau_0}{\partial \eta^2} = 0 \,, \quad (2.48)$$

$$\frac{\partial^2 \tau_1}{\partial \eta^2} = \frac{2}{\hat{r}_{tr}} \frac{\partial \tau_0}{\partial \eta} \,, \tag{2.49}$$

$$\frac{\partial^2 \tau_2}{\partial \eta^2} = \frac{4}{\hat{r}_{tr}} \left[\frac{\partial \tau_1}{\partial \eta} + \frac{\eta}{\hat{r}_{tr}} \frac{\partial \tau_0}{\partial \eta} \right] - \frac{2}{\hat{r}_{tr}^2} \Lambda^2 \tau_0 - 18(1-\nu) \,. \tag{2.50}$$

The equations are easily integrated in the variable η, to obtain the solutions:

$$\tau_0 = F_0(\theta, \phi)\eta + G_0(\theta, \phi) \,, \tag{2.51}$$

$$\tau_1 = \frac{F_0(\theta, \phi)}{\hat{r}_{tr}} \eta^2 + F_1(\theta, \phi)\eta + G_1(\theta, \phi) \,, \tag{2.52}$$

$$\begin{aligned} \tau_2 = {} & \frac{2F_0(\theta, \phi)}{\hat{r}_{tr}^2} \eta^3 - \frac{1}{3\hat{r}_{tr}^2} \Lambda^2 F_0(\theta, \phi)\eta^3 + \frac{2F_1(\theta, \phi)}{\hat{r}_{tr}} \eta^2 \\ & -9(1-\nu)\eta^2 - \frac{1}{\hat{r}_{tr}^2} \Lambda^2 G_0(\theta, \phi)\eta^2 + F_2(\theta, \phi)\eta + G_2(\theta, \phi) \,. \end{aligned} \tag{2.53}$$

The six free angular functions that appear in the formal solutions will be determined by the matching procedure.

2.4.4 Asymptotic matching to two orders

In order to obtain the solution, we must perform separately the relevant matching for the pairs $(\psi^{(int)}, \psi^{(lay)})$ and $(\psi^{(lay)}, \psi^{(ext)})$. We follow the Van Dyke matching principle, which requires that we compare the second order expansion of the internal and external solutions with the third order expansion of the boundary layer solution. The full procedure is described in Appendix A.3.

To first order (i.e., up to $k = 1$ in series [2.22] and [2.23]), from the matching of the pair $(\psi^{(int)}, \psi^{(lay)})$ we find the free angular functions of (2.51) and (2.52):

$$F_0(\theta, \phi) = -\psi_0^{(int)\prime}(\hat{r}_{tr}) \,, \tag{2.54}$$

$$G_0(\theta, \phi) = \psi_1^{(int)}(\hat{r}_{tr}, \theta, \phi) \,, \tag{2.55}$$

$$F_1(\theta, \phi) = -\frac{\partial \psi_1^{(int)}}{\partial \hat{r}}(\hat{r}_{tr}, \theta, \phi) \,, \tag{2.56}$$

$$G_1(\theta, \phi) = \frac{1}{2} \psi_2^{(int)}(\hat{r}_{tr}, \theta, \phi) \,. \tag{2.57}$$

From the matching of the pair $(\psi^{(ext)}, \psi^{(lay)})$ we connect $\psi^{(ext)}$ to the same angular functions, thus proving that the matching to first order is equivalent to imposing continuity of the solution up to second order and of the first radial derivative up to first order. This allows us to determine the free constants that are present in the first two terms of (2.43) and in (2.32):

$$\alpha_0 = \frac{\lambda_0}{\hat{r}_{tr}} \,, \tag{2.58}$$

$$\lambda_0 = \hat{r}_{tr}^2 \psi_0^{(int)'}(\hat{r}_{tr}) \,, \tag{2.59}$$

$$\alpha_1 = f_{00}(\hat{r}_{tr}) + \hat{r}_{tr} f'_{00}(\hat{r}_{tr}) + \frac{3T_{00}(\hat{r}_{tr})}{2\sqrt{\pi}} \,, \tag{2.60}$$

$$\lambda_1 = \hat{r}_{tr}^2 f'_{00}(\hat{r}_{tr}) + \frac{\hat{r}_{tr} T_{00}(\hat{r}_{tr})}{\sqrt{\pi}} \,, \tag{2.61}$$

$$A_{2m} = -\frac{5T_{2m}(\hat{r}_{tr})}{\hat{r}_{tr}\gamma'_2(\hat{r}_{tr}) + 3\gamma_2(\hat{r}_{tr})} \,, \tag{2.62}$$

$$a_{2m} = -\hat{r}_{tr}^3 [A_{2m}\gamma_2(\hat{r}_{tr}) + T_{2m}(\hat{r}_{tr})] \,. \tag{2.63}$$

Note that $A_{lm} = a_{lm} = 0$ if $l \neq 2$, for every value of m, and that the constants for $l = 2$ are non-vanishing only for $m = 0, 2$. The constants that identify the solution are thus expressed in terms of the values of the unperturbed field $\psi_0^{(int)'}$, of the "driving" tidal potential T_{lm}, and of the solutions f_{00} and γ_2 (see Eqs. [2.30] and [2.31]) taken at $\hat{r} = \hat{r}_{tr}$.

The boundary surface of the first order model is defined implicitly by $\psi_0^{(ext)}(\hat{r}) + \psi_1^{(ext)}(\hat{r}, \theta, \phi)\epsilon = 0$, that is, the spherical shape of the King model is modified by monopole and quadrupole contributions, which are even with respect to toroidal and poloidal angles and characterized by reflection symmetry with respect to the three natural coordinates planes. As might have been expected from the physical model, the spherical shape is thus modified only by spherical harmonics (l, m) for which the tidal potential has non-vanishing coefficients. Mathematically, this is non-trivial, because the first order equation in the internal region Eq. (2.26) is non-homogeneous only for $l = 0$; the quadrupole contribution to the internal solution is formally "hidden" by the use of the function ψ (which includes the tidal potential) and is unveiled by the matching which demonstrates that A_{2m} with $m = 0, 2$ are non-vanishing.

The first order solution can be inserted into the right-hand side of Eq. (2.33) to generate non-homogeneous equations (and thus particular solutions) only for $l = 0, 2, 4$ and corresponding positive and even values of m (see Appendix A.2). We can thus proceed to construct the second order solution in the same way described above for the first order solution. From the matching of the pair $(\psi^{(int)}, \psi^{(lay)})$ we determine the missing angular functions:

$$F_2(\theta, \phi) = -\frac{\partial \psi_2^{(int)}}{\partial \hat{r}}(\hat{r}_{tr}, \theta, \phi) \,, \tag{2.64}$$

$$G_2(\theta, \phi) = \frac{1}{3}\psi_3^{(int)}(\hat{r}_{tr}, \theta, \phi) \,, \tag{2.65}$$

which are then connected to the properties of $\psi^{(ext)}$ by the matching of the pair $(\psi^{(ext)}, \psi^{(lay)})$. This is equivalent to imposing continuity of the solution up to third order and of the first radial derivative up to second order and leads to the determination of the free constants that appear in the third term of (2.43) and in (2.34):

$$\alpha_2 = g_{00}(\hat{r}_{tr}) + \hat{r}_{tr} g'_{00}(\hat{r}_{tr}) \,, \tag{2.66}$$

$$\lambda_2 = \hat{r}_{tr}^2 g'_{00}(\hat{r}_{tr}) \,, \tag{2.67}$$

$$B_{2m} = -\frac{\hat{r}_{tr} g'_{2m}(\hat{r}_{tr}) + 3 g_{2m}(\hat{r}_{tr})}{\hat{r}_{tr}\gamma'_2(\hat{r}_{tr}) + 3\gamma_2(\hat{r}_{tr})} \,, \tag{2.68}$$

$$b_{2m} = -\hat{r}_{tr}^3 [g_{2m}(\hat{r}_{tr}) + B_{2m}\gamma_2(\hat{r}_{tr})] \,, \tag{2.69}$$

$$B_{4m} = -\frac{\hat{r}_{tr} g'_{4m}(\hat{r}_{tr}) + 5 g_{4m}(\hat{r}_{tr})}{\hat{r}_{tr}\gamma'_4(\hat{r}_{tr}) + 5\gamma_4(\hat{r}_{tr})} \,, \tag{2.70}$$

$$b_{4m} = -\hat{r}_{tr}^5 [g_{4m}(\hat{r}_{tr}) + B_{4m}\gamma_4(\hat{r}_{tr})] \,. \tag{2.71}$$

Here $B_{lm} = b_{lm} = 0$ if $l \neq 2, 4$ for every value of m; the only non-vanishing constants with $l = 2, 4$ are those with even m.

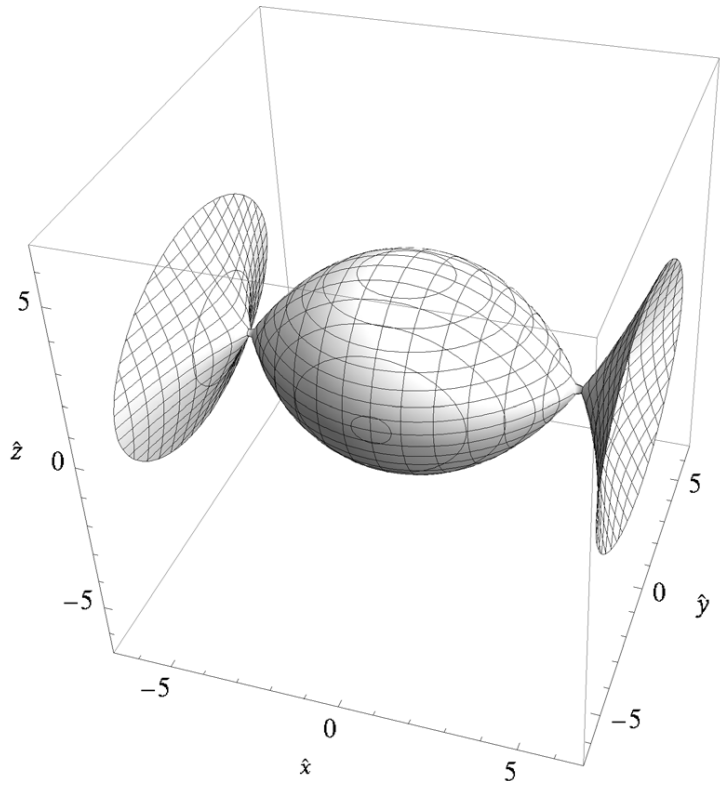

Figure 2.1: The critical Hill surface (in dimensionless variables) for a second-order model with $\Psi = 2$ and $\epsilon = 7.043 \times 10^{-4}$ (corresponding to $\delta_{cr}^{(2)} = 0.671$); the galactic potential is Keplerian ($\nu = 3$).

Therefore, the second order solution has non-vanishing contributions only for $l = 0, 2, 4$, that is, for those harmonics for which the particular solution to Eq. (2.27) is non-trivial. *By induction*, it can be proved (see Appendix A.4) that the k-th order solution is characterized by $l = 0, 2, .., 2k$ harmonics with corresponding positive and even values of m. In reality, the discussion of the matching to higher orders ($k > 3$) would require a re-definition of the boundary layer, because the density contribution on the right-hand

side of Eq. (2.45) (for positive values of τ) comes into play. The asymptotic matching procedure carries through also in this more complex case but, for simplicity, is omitted here. We should also keep in mind that in an asymptotic analysis the inclusion of higher order terms does not necessarily lead to better accuracy in the solution; the optimal truncation in the asymptotic series depends on the value of the expansion parameter (in this case, on the value of ϵ) and has to be judged empirically.

In conclusion, starting from a given value of the King concentration parameter Ψ and from a given strength of the tidal field ϵ, the uniform triaxial solution is constructed by numerically integrating Eqs. (2.24), (2.30), (2.31), and (2.33) and by applying the constants derived in this subsection to the asymptotic series expansion (2.22)-(2.23). The numerical integrations can be performed efficiently by means of standard Runge-Kutta routines. The boundary surface of the model is thus defined by $\psi_0^{(ext)}(\hat{r}) + \psi_1^{(ext)}(\hat{r},\theta,\phi)\epsilon + \psi_2^{(ext)}(\hat{r},\theta,\phi)\epsilon^2/2 = 0$, while the internal density distribution is given by $\rho = \rho(\psi_0^{(int)}(\hat{r}) + \psi_1^{(int)}(\hat{r},\theta,\phi)\epsilon + \psi_2^{(int)}(\hat{r},\theta,\phi)\epsilon^2/2)$, with the function ρ defined by Eq. (2.11). Any other "observable" quantity can be reconstructed by suitable integration in phase space of the distribution function $f_K(H)$ defined by Eq. (4.3), with H defined by Eq. (2.5), and $\Phi_T + \Phi_C = H_0 - [\psi_0^{(int)}(\hat{r}) + \psi_1^{(int)}(\hat{r},\theta,\phi)\epsilon + \psi_2^{(int)}(\hat{r},\theta,\phi)\epsilon^2/2]/a$.

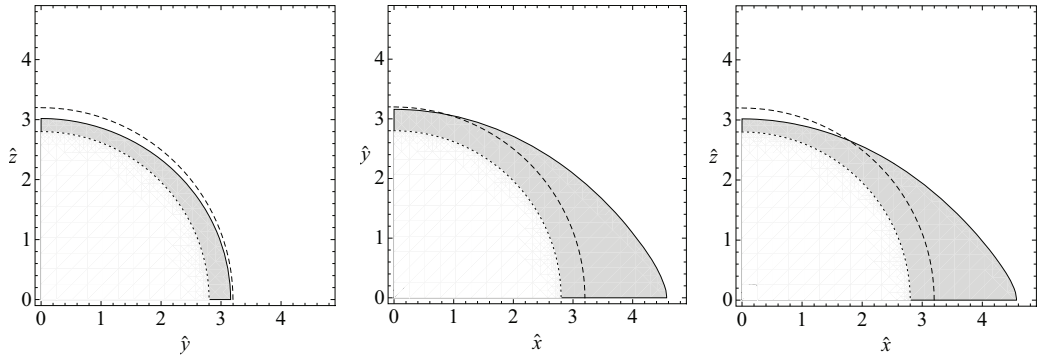

Figure 2.2: Sections in the three coordinate planes for a second-order model with $\Psi = 2$ and $\epsilon = 7.000 \times 10^{-4}$, characterized by high tidal distortion ($\delta = 0.669 \approx \delta_{cr}^{(2)}$, see Fig. 2.1) illustrating the boundary surface of the triaxial model (solid), of the internal region (dotted), and of the corresponding spherical King model (dashed); the filled area represents the inner region of the boundary layer. Note the compression and the elongation with respect to the unperturbed configuration in the $\hat{z}$- and $\hat{x}$-direction, respectively. The galactic potential is Keplerian ($\nu = 3$).

In Figs. 2.1 and 2.2 we illustrate the main characteristics of one triaxial model constructed with the method described in this Section.

2.5 Alternative methods of solution

2.5.1 The method of strained coordinates

The mathematical problem described in Sect. 2.3 can also be solved by the method of *strained coordinates*, an alternative method usually applied to non-linear hyperbolic differential equations (e.g., see Van Dyke 1975, Chapter 6) and considered by Smith (1976) in the solution of the singular free-boundary perturbation problem that arises in the study of rotating polytropes.

Starting from a series representation of the form (2.22) and (2.23) for the solution defined in the Poisson and Laplace domains, respectively, a transformation is considered from spherical coordinates $(\hat{r}, \theta, \phi)$ to "strained coordinates" (s, p, q):

$$\begin{aligned} \hat{r} &= s + \epsilon \hat{r}_1(s,p,q) + \frac{1}{2}\epsilon^2 \hat{r}_2(s,p,q) + ... \\ \theta &= p \\ \phi &= q \, , \end{aligned} \tag{2.72}$$

where $\hat{r}_k(s,p,q)$ are initially unspecified straining functions. We note that the zero-th order problem is defined by the same Eq. (2.24) with the same boundary conditions but with the variable $\hat{r}$ replaced by s. The unperturbed spherical boundary in the strained space is defined by $s = s_0$, where $\psi_0^{(int)}(s_0) = 0$. To each order, the effective boundary of the perturbed configuration remains described by the surface $s = s_0$, while in physical coordinates the truncation radius actually changes as a result of the straining functions $\hat{r}_k$ that are determined progressively.

The Laplacian expressed in the new coordinates, $\widetilde{\nabla}^2$, can be written as an asymptotic series: $\widetilde{\nabla}^2 = L_0 + \epsilon L_1 + 1/2\epsilon^2 L_2 + ...$, where L_k are linear second order operators [3] in which $\hat{r}_j(s,p,q)$ (with $j = 1,..,k$) and their derivatives appear. For convenience, we record the zero-th and first order operators:

$$L_0 \equiv \frac{d^2}{ds^2} + \frac{2}{s}\frac{d}{ds} \, , \tag{2.73}$$

$$L_1 \equiv -\left(2\frac{\partial \hat{r}_1}{\partial s}\right)\frac{d^2}{ds^2} - \left(\frac{\partial^2 \hat{r}_1}{\partial s^2} + \frac{2}{s}\frac{\partial \hat{r}_1}{\partial s} + \frac{1}{s^2}\Lambda^2 \hat{r}_1 + \frac{2}{s^2}\hat{r}_1\right)\frac{d}{ds} \, , \tag{2.74}$$

where Λ^2 is the standard angular part of the Laplacian, written with angular coordinates (p,q). The general k-th order operator can be decomposed as $L_k = L_1 + F_k$, where F_k is, in turn, a second order operator in which $\hat{r}_j(s,p,q)$ (with $j = 1,..,k-1$) appear and L_1 is defined as in Eq. (2.74) but with $\hat{r}_k(s,p,q)$ instead of $\hat{r}_1(s,p,q)$; these operators appear in the relevant equation for $\psi_k^{(int)}$:

$$[L_0 + R_1(\psi;\epsilon)]\psi_k^{(int)} = L_k \psi_0^{(int)} \tag{2.75}$$

which corresponds to the general k-th order equation of the previous method.

Following a set of constraints that guarantee the regularity of the series (2.22) in the strained space, the equations that uniquely identify the straining functions to any desired order can be found and solved numerically; structurally, they somewhat correspond to Eqs. (2.31) and (2.33). Therefore, the internal and external solutions can be worked out and patched by requiring continuity of the solution and of the first derivative with respect to the variable s at the boundary surface defined by $s = s_0$, in general qualitative analogy with the method described in the previous section.

This method is formally more elegant than the method of matched asymptotic expansions but requires a more significant numerical effort because, even though the number of equations to be solved at each order is the same, the operator that plays here a central role in the equations for the straining functions, $L_1\psi_0^{(int)}$ (interpreted as an operator acting on $\hat{r}_k[s,p,q]$), is more complex than $\mathcal{D}_l$ (defined in Eq. (2.29)).

[3] Surfaces with constant s in the strained space are assumed to correspond to surfaces with constant $\psi^{(int)}$ in the physical space, that is, $\psi^{(int)} = \psi^{(int)}(s)$; therefore, L_k (with $k \geq 0$) is an ordinary differential operator for $\psi^{(int)}$.

2.5.2 Iteration

This technique follows the approach taken by Prendergast & Tomer (1970) and by Wilson (1975), for the construction of self-consistent dynamical models of differentially rotating elliptical galaxies, and later by Longaretti & Lagoute (1996), for their extension of King models to the rotating case.

In terms of the function:

$$u(\hat{\mathbf{r}}) \equiv a[H_0 - \Phi_C(\hat{\mathbf{r}})] = \psi(\hat{\mathbf{r}}) + \epsilon T(\hat{\mathbf{r}}) \; , \tag{2.76}$$

inside the cluster the Poisson equation can be written as:

$$\hat{\nabla}^2 u = -\frac{9}{\hat{\rho}(\Psi)}\hat{\rho}(u - \epsilon T) \; , \tag{2.77}$$

while outside the cluster the Laplace equation is simply:

$$\hat{\nabla}^2 u = 0 \; . \tag{2.78}$$

The boundary conditions at the origin are $u(\mathbf{0}) = \Psi$ and $\hat{\nabla} u(\mathbf{0}) = \mathbf{0}$, because the tidal potential $T(\hat{\mathbf{r}})$ is a homogeneous function; the condition at large radii is $u \to aH_0$.

The basic idea is to get an improved solution $u^{(n)}$ of the Poisson equation by evaluating the "source term" on the right-hand side with the solution obtained in the immediately previous step:

$$\hat{\nabla}^2 u^{(n)} = -\frac{9}{\hat{\rho}(\Psi)}\hat{\rho}(u^{(n-1)} - \epsilon T) \; . \tag{2.79}$$

The iteration is seeded by inserting as $u^{(0)}$, on the right-hand side of Eq. (2.79), the spherical solution of the King models. The iteration continues until convergence is reached.

In order to solve Eq. (2.79), we expand in spherical harmonics the solution and, correspondingly, the dimensionless density distribution:

$$u^{(n)}(\hat{\mathbf{r}}) = \sum_{l=0}^{\infty} \sum_{m=-l}^{l} u_{lm}^{(n)}(\hat{r}) Y_{lm}(\theta, \phi) \; , \tag{2.80}$$

$$\hat{\rho}^{(n)}(\hat{\mathbf{r}}) = \sum_{l=0}^{\infty} \sum_{m=-l}^{l} \hat{\rho}_{lm}^{(n)}(\hat{r}) Y_{lm}(\theta, \phi) \; , \tag{2.81}$$

so that the reduced radial problems for the functions $u_{lm}^{(n)}(\hat{r})$ are:

$$\left[\frac{d^2}{d\hat{r}^2} + \frac{2}{\hat{r}}\frac{d}{d\hat{r}} - \frac{l(l+1)}{\hat{r}^2}\right] u_{lm}^{(n)} = -\frac{9}{\hat{\rho}(\Psi)}\hat{\rho}_{lm}^{(n-1)} \; , \tag{2.82}$$

with boundary conditions $u_{00}^{(n)}(0) = \Psi$, $u_{lm}^{(n)}(0) = 0$ and $u_{00}^{(n)\prime}(0) = u_{lm}^{(n)\prime}(0) = 0$. Here, in contrast with the structure of the governing equations for $\psi_k^{(int)}$ of Subsections 2.4.1 and 2.4.2, the radial part of the Laplacian appears with no "shift", for which the homogeneous solutions are known analytically. Thus the full solution to Eq. (2.82) can be obtained in integral form by the standard method of *variation of the arbitrary constants*:

$$u_{00}^{(n)}(\hat{r}) = \Psi - \frac{9}{\hat{\rho}(\Psi)}\left[\int_0^{\hat{r}} \hat{r}' \hat{\rho}_{00}^{(n-1)}(\hat{r}') d\hat{r}' - \frac{1}{\hat{r}}\int_0^{\hat{r}} \hat{r}'^2 \hat{\rho}_{00}^{(n-1)}(\hat{r}') d\hat{r}'\right] \; , \tag{2.83}$$

$$u_{lm}^{(n)}(\hat{r}) = \frac{9}{(2l+1)\hat{\rho}(\Psi)} \left[\hat{r}^l \int_{\hat{r}}^{\infty} \hat{r}'^{1-l} \hat{\rho}_{lm}^{(n-1)}(\hat{r}') d\hat{r}' + \frac{1}{\hat{r}^{l+1}} \int_0^{\hat{r}} \hat{r}'^{l+2} \hat{\rho}_{lm}^{(n-1)}(\hat{r}') d\hat{r}' \right] . \quad (2.84)$$

The complete calculation can be found in the Appendix 2. Here we only remark that this integral form is valid in both Poisson and Laplace domains because it contains simultaneously the regular and the singular homogeneous solutions of the Laplacian. In the derivation, all the boundary conditions have been used; in particular, the two conditions at the origin are sufficient to obtain expression (2.83), while for expression (2.84) the one concerning the radial derivative at the origin is used together with the one that describes the behavior at large radii (i.e. $u_{lm}^{(n)} \to 0$ for $l \geq 1$). Furthermore, from the condition at large radii evaluated for the harmonic $l = 0$, that is, $u_{00}^{(n)}/\sqrt{4\pi} \to aH_0^{(n)}$ (here the notation reminds us that the value of H_0 is known only approximately and it changes slightly at every iteration), we find:

$$aH_0^{(n)} \equiv \frac{\Psi}{\sqrt{4\pi}} - \frac{9}{\sqrt{4\pi}\hat{\rho}(\Psi)} \int_0^{\infty} \hat{r}' \hat{\rho}_{00}^{(n-1)}(\hat{r}') d\hat{r}' , \quad (2.85)$$

where we should recall that beyond a certain radius $\hat{\rho}_{00}^{(n-1)}$ vanishes.

In terms of the function u, the boundary of the cluster is given implicitly by: $u(\hat{\mathbf{r}}) = \epsilon T(\hat{\mathbf{r}})$. Therefore, the radial location at which the $\hat{\rho}_{lm}^{(n-1)}$ vanishes is determined numerically from:

$$\hat{\rho}_{lm}^{(n-1)}(\hat{r}) = \int_0^{2\pi} \int_{-1}^{1} \hat{\rho}[u^{(n-1)}(\hat{r}, \theta, \phi) - \epsilon T(\hat{r}, \theta, \phi)] Y_{lm}(\theta, \phi) d(cos\theta) d\phi . \quad (2.86)$$

In practice, to perform the iteration, the definition of a grid in spherical coordinates and of a suitable algorithm, in order to perform the expansion and the resummation in spherical harmonics of u and $\hat{\rho}$, is required; the number of angular points of the grid and the maximum harmonic indices (l, m) admitted in the series (2.80) and (2.81) are obviously related.

2.6 Extension of other isotropic truncated models

The procedure developed in Sects. 3 and 4 can be applied also to extend other isotropic truncated models, different from the King models, to the case of tidal distortions. Here we briefly describe the case of low-n polytropes ($1 < n < 5$), which are particularly well suited to the purpose, because they are characterized by a very simple analytical expression for the density as a function of the potential; this class of models was also considered by Weinberg (1993). In the distribution function that defines the polytropes (e.g., see Bertin 2000), we may thus replace the single star energy with the Jacobi integral (see definition [2.5]) and consider:

$$f_P(H) = A(H_0 - H)^{n-3/2} , \quad (2.87)$$

for $H \leq H_0$, and a vanishing distribution otherwise. Unlike the King family discussed in the main text, these models have no dimensionless parameter to measure the concentration of the stellar system, which depends only on the polytropic index n; in fact, the spherical fully self-consistent polytropes are characterized only by two physical scales,

which are associated with the cut-off constant H_0 and the normalization factor A. Below we consider values of $n < 5$, so that the models have finite radius. Therefore, the relevant parameter space for the tidally distorted models is represented just by the tidal strength parameter ϵ (see definition [2.13]), which, for a given value of the index n, has a (maximal) critical value. The definition in Eq. (2.14) for the extension parameter δ is still valid if by r_{tr} we denote the radius of the unperturbed spherical configuration. The associated density functional is given by:

$$\rho(\psi) = \rho_0 \psi^n \,, \tag{2.88}$$

where the dimensionless escape energy is given by:

$$\psi(\mathbf{r}) = \{H_0 - [\Phi_C(\mathbf{r}) + \Phi_T(\mathbf{r})]\} \left(\frac{c_n}{\rho_0}\right)^{1/n} \,, \tag{2.89}$$

with $c_n \equiv (2\pi)^{3/2}\Gamma(n-1/2)A/n!$. The boundary of the perturbed configuration is defined by $\psi(\mathbf{r}) = 0$, following the same arguments described in the main text. Here ρ_0 can be interpreted as the central density if we set $\psi(\mathbf{0}) = 1$.

For $\psi \geq 0$, the relevant equation for the construction of the self-consistent tidally distorted models is the Poisson equation, which, in dimensionless form, is given by:

$$\hat{\nabla}^2 \psi = -[\psi^n - \epsilon(1-\nu)] \,, \tag{2.90}$$

while for negative values of ψ we must refer to Eq. (2.18). Here the rescaling of variables has been performed by means of the scale length $\zeta \equiv \sqrt{\rho_0^{1/n-1}/(4\pi G c_n^{1/n})}$. The relevant boundary conditions are given by $\psi(\mathbf{0}) = 1$ instead of (2.19), while (2.20) and (2.21) hold unchanged.

If the polytropic index is in the range $1 < n < 5$, the solution up to second order presented in Sect. 2.4 is fully applicable, provided that we note that the problem for the zero-th order term of the series (2.22) is now given by the Lane-Emden equation (see, e.g. Chandrasekhar 1939):

$$\psi_0^{(int)\,''} + \frac{2}{\hat{r}} \psi_0^{(int)\,\prime} = -\left(\psi_0^{(int)}\right)^n \,, \tag{2.91}$$

with $\psi_0^{(int)}(0) = 1$ and $\psi_0^{(int)\,\prime}(0) = 0$, where the symbol $'$ denotes derivative with respect to the argument $\hat{r}$; explicitly, the truncation radius $\hat{r}_{tr}$ is now defined by $\psi_0^{(int)}(\hat{r}_{tr}) = 0$, that is, it represents the radius of the so-called *Emden sphere*. Correspondingly, the quantities called R_j in the main text must be re-defined as:

$$R_j(\hat{r}; n) \equiv \left.\frac{d^j \psi^n}{d\psi^j}\right|_{\psi_0^{(int)}} \,; \tag{2.92}$$

the value of j at which the quantity R_j may start to diverge depends on the index n. Obviously, in Eq. (2.45), that is, in the Poisson equation defined in the boundary layer, $\hat{\rho}(\epsilon\tau)$ must be replaced by $(\epsilon\tau)^n$. This makes it clear that the value of the polytropic index n directly affects the order, with respect to the perturbation parameter, at which the density contribution on the right-hand side of Eq. (2.45) comes into play and therefore changes the matching procedure. If $n > 1$, the density contribution emerges only after the second order and thus the full procedure described in Sect. 4 is valid. In contrast, if

$n \leq 1$ the procedure described in the main text is applicable only up to first order while the calculation of second order terms would require a re-definition of the boundary layer (as it happens for the case discussed in the main text when terms of order $k > 3$ are desired). In closing, we note that the procedure presented in this Chapter can be applied also to isotropic truncated models with more complicated expressions for the density functional (e.g. the family of models f_{1n} proposed by Davoust (1977), without boundary conditions on tangential velocity, for which the density functionals are expressed in terms of the error function and of the Dawson integral), bearing in mind the last *caveat* about the possibility that the density contribution may affect at some order the boundary layer, thus requiring a reformulation of the results presented in Sect. 2.4.

2.7 Discussion and conclusions

Spherical King models are physically justified models of quasi-relaxed stellar systems with a truncation radius argued to "summarize" the action of an external tidal field. Such simple models have had great success in representing the structure and dynamics of globular clusters, even though the presence of the tidal field is actually ignored. Motivated by these considerations and by the recent major progress in the observations of globular clusters, in this Chapter we have developed a systematic procedure to construct self-consistent non-spherical models of quasi-relaxed stellar systems, with special attention to models for which the non-spherical shape is due to the presence of external tides.

The procedure developed in this Chapter starts from a distribution function identified by replacing, in a reference spherical model, the single star energy with the relevant Jacobi integral, thus guaranteeing that the collisionless Boltzmann equation is satisfied. Then the models are constructed by solving the Poisson equation, an elliptic partial differential equation with free boundary. The procedure is very general and can lead to the construction of several families of non-spherical equilibrium models. In particular, we have obtained the following results:

- We have constructed models of quasi-relaxed triaxial stellar systems in which the shape is due to the presence of external tides; these models reduce to the standard spherical King models when the tidal field is absent.
- For these models we have outlined the general properties of the relevant parameter space; in next Chapter we will provide a thorough description of this two-parameter family of models, also in terms of projected quantities, as appropriate for comparisons with the observations.
- We have given a full, explicit solution to two orders in the tidal strength parameter, based on the method of matched asymptotic expansions; by comparison with studies of analogous problems in the theory of rotating polytropic stars, this method appears to be most satisfactory.
- We have also discussed two alternative methods of solution, one of which is based on iteration seeded by the spherical solution; together with the use of dedicated N-body simulations, the ability to solve such a complex mathematical problem in different ways will allow us to test the quality of the solutions in great detail.
- By suitable change of notation and physical re-interpretation, the procedure developed in this Chapter can be applied to the construction of non-spherical quasi-relaxed stellar systems flattened by solid-body rotation (see Chapter 4.2).

- The same procedure can also be applied to extend to the triaxial case other isotropic truncated models (such as low-n polytropes), that is, models that do not reduce to King models in the absence of external tides.

We hope that this contribution, in addition to extending the class of self-consistent models of interest in stellar dynamics, will be the basis for the development of simple quantitative tools to investigate whether the observed shape of globular clusters is primarily determined by internal rotation, by external tides, or by pressure anisotropy.

CHAPTER 3

Properties of quasi-relaxed stellar systems in an external tidal field

3.1 Introduction

In the previous Chapter, we have constructed a family of self-consistent triaxial models of quasi-relaxed stellar systems, shaped by the tidal field of the host galaxy, as an extension of the well-known spherical King models. For a given tidal field, the models are characterized by two physical scales (such as total mass and central velocity dispersion) and two dimensionless parameters (the concentration parameter and the tidal strength). The most significant departures from spherical symmetry occur when the truncation radius of the corresponding spherical King model is of the order of the tidal radius, which, for a given tidal strength, is set by the maximum concentration value admitted. For such maximally extended (or "critical") models, the outer boundary has a generally triaxial shape, given by the zero-velocity surface of the relevant Jacobi integral, which is basically independent of the concentration parameter. In turn, the external tidal field can give rise to significant global departures from spherical symmetry (as measured, for example, by the quadrupole of the mass distribution of the stellar system) only for low-concentration models, for which the allowed maximal value of the tidal strength can be relatively high. In this Chapter, we describe in systematic detail the intrinsic and the projected structure and kinematics of the models, covering the entire parameter space, from the case of sub-critical (characterized by "underfilling" of the relevant Roche volume) to that of critical models. The intrinsic properties can be a useful starting point for numerical simulations and other investigations that require initialization of a stellar system in dynamical equilibrium. The projected properties are a key step in the direction of a comparison with observed globular clusters and other candidate stellar systems.

The Chapter is organized as follows. In Section 3.2 we present a thorough description of the relevant parameter space. The intrinsic and projected density distributions are discussed in Section 3.3, with special emphasis on the global and local quantities that can be used as diagnostics of deviations from spherical symmetry. Intrinsic and projected kinematics are addressed in Section 3.4. The details of the calculation of the global quantities from the multipole expansion of the cluster potential are given in Section 3.5. The comparison between the perturbation and the iteration approach for the solution of the relevant Poisson equation is briefly presented in Section 3.6. The concluding Section 3.7 gives the summary with a discussion of the results obtained and a comment on the complex physical phenomena that a large body of evolutionary models based on numerical investigations has shown to characterize the periphery of globular clusters.

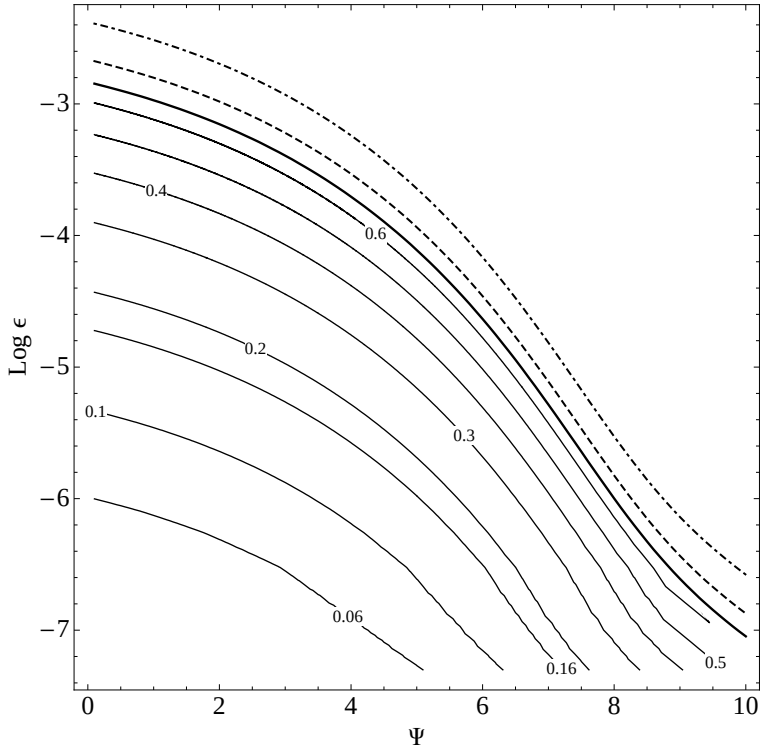

Figure 3.1: Parameter space for second-order models. The uppermost solid line represents the critical values of the tidal strength parameter for models in which the potential of the hosting galaxy is Keplerian ($\nu = 3$); thin solid lines represent contour levels of the extension parameter δ. The dashed line is the critical curve for models within a logarithmic potential ($\nu = 2$). The dot-dashed line gives the critical condition for a potential with $\nu = 1$ (e.g., that of a Plummer sphere evaluated at $R_0 = b/\sqrt{2}$, with b the model scale radius).

3.2 The parameter space

The triaxial tidal models are characterized by two physical scales (corresponding to the two free constants A and a in the distribution function $f_K(H)$) and two dimensionless parameters. The latter parameters are best introduced by referring to the formulation of the Poisson equation in terms of the dimensionless escape energy

$$\psi(\hat{r}) = a\, H_0 - [a\, \Phi_C(\hat{r}) + \epsilon\, T(\hat{x}, \hat{z})] \,, \tag{3.1}$$

where $a\Phi_C$ is the dimensionless cluster mean-field potential (to be determined self-consistently) and $T(\hat{x}, \hat{z}) = 9(\hat{z}^2 - \nu\hat{x}^2)/2$ represents the tidal potential (with the numerical coefficient $\nu = 4 - \kappa^2/\Omega^2$, where κ and Ω are respectively the epicyclic and orbital frequency, depending on the potential of the hosting galaxy); the hat on the spatial coordinates denotes that they are measured in units of the scale length $r_0 = [9/(4\pi G\rho_0 a)]^{1/2}$.

Then the first parameter, already available in the spherical case, is the concentration of the system and can be expressed as a dimensionless measure of the central depth of the potential well: $\Psi \equiv \psi(0)$. The second parameter, the tidal strength ϵ in Eq. (3.1), is

defined as

$$\epsilon \equiv \frac{\Omega^2}{4\pi G\rho_0} \,, \tag{3.2}$$

i.e. as the ratio of the square of the orbital frequency (of the revolution of the stellar system around the center of the hosting galaxy) to the square of the dynamical frequency associated with the central density ρ_0 of the stellar system. Alternatively, the effect of the tidal field can be measured by the extension parameter

$$\delta \equiv \hat{r}_{tr}/\hat{r}_T \,, \tag{3.3}$$

where $\hat{r}_{tr} = \hat{r}_{tr}(\Psi)$ is the *truncation* radius of the spherical King model characterized by the same value of Ψ and $\hat{r}_T$ is the *tidal* (or *Jacobi*) radius, i.e. the distance from the origin (the center of the stellar system) of the two nearby Lagrangian points of the restricted three-body problem considered in our simple physical picture. A given model will be labelled by the pair of values (Ψ, ϵ) or, equivalently, by the pair (Ψ, δ). The dimensionless cut-off constant aH_0 can be expressed in a natural way as an asymptotic series with respect to the tidal parameter $aH_0 = \alpha_0 + \alpha_1\epsilon + \alpha_2\epsilon^2/2 + ...$ where the terms α_i, as discussed in Chapter 2, depend only on Ψ.

Much like the Hill surfaces for the standard restricted three-body problem, we now consider the family of zero-velocity surfaces defined by the condition $\psi(\hat{r}) = 0$, which represents the boundary of our models. These surfaces can be open or closed, depending on the value of the cut-off constant aH_0, which is determined by the selected values of the two dimensionless parameters that characterize the model. To be consistent with the hypothesis of stationarity, we only consider closed configurations. We call "critical models" those that are bounded by the critical zero-velocity surface (which is the outermost available closed surface). For each value of Ψ, the critical value of the tidal parameter can be found by (numerically) solving the system

$$\begin{cases} \partial_{\hat{x}}\psi(\hat{x} = \hat{r}_T, \hat{y} = 0, \hat{z} = 0; \epsilon_{cr}) = 0 \\ \psi(\hat{x} = \hat{r}_T, \hat{y} = 0, \hat{z} = 0; \epsilon_{cr}) = 0 \,, \end{cases} \tag{3.4}$$

where the unknowns are $\hat{r}_T$ and ϵ_{cr}. The method of matched asymptotic expansions proposed in Chapter 2 for the solution of the relevant Poisson-Laplace equation requires an expansion in spherical harmonics, therefore it can be easily recognized that the first condition of Eq. (3.4) is equivalent to the requirement of vanishing gradient, which identifies the saddle points of the critical surface. In the general case, the condition $\partial_{\hat{x}}\psi(\hat{r}_T, 0, 0; \epsilon) = 0$ determines the value of $\hat{r}_T$ for a given tidal strength ϵ , therefore $\hat{r}_T = \hat{r}_T(\Psi, \epsilon)$.

By using in the escape energy defined in Eq. (3.1) the zeroth-order expression for the cluster potential $(a\Phi_C^{(\text{ext})})^{(0)}(\hat{r}) = \lambda_0/\hat{r}$ and for the cut-off constant[1], the system in Eq. (3.4) becomes

$$\begin{cases} \dfrac{\lambda_0}{\hat{r}_T^2} + 9\,\epsilon_{cr}\,\nu\hat{r}_T = 0 \\ \alpha_0 - \dfrac{\lambda_0}{\hat{r}_T} + \dfrac{9}{2}\,\epsilon_{cr}\,\nu\hat{r}_T^2 = 0 \,, \end{cases} \tag{3.5}$$

thus leading to an expression for $\hat{r}_T^{(0)}$ in terms of the dimensionless truncation radius of the corresponding spherical King model and a first estimate of the critical value of ϵ

$$\hat{r}_T^{(0)} = \frac{3}{2}\frac{\lambda_0}{\alpha_0} = \frac{3}{2}\hat{r}_{tr} \,, \tag{3.6}$$

[1] We recall from Chapter 2 that $\lambda_0 = \hat{r}_{tr}^2\psi_0^{(\text{int})\prime}(\hat{r}_{tr})$ and $\alpha_0 = \lambda_0/\hat{r}_{tr}$, with $\psi_0^{(\text{int})}$ the zeroth-order term of the asymptotic series of the internal solution. $aH_0 = \alpha_0$

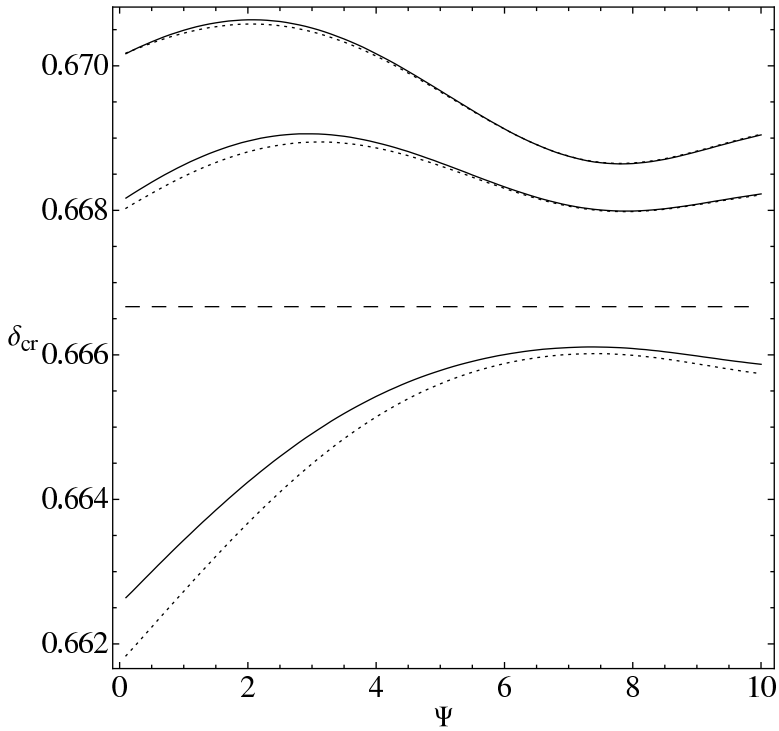

Figure 3.2: Critical values of the extension parameter for first-order models (dotted) and second-order models (solid) with different potentials of the hosting galaxy ($\nu = 3, 2, 1$ from top to bottom). The dashed horizontal line shows the value 2/3 that is found when a zeroth-order approximation for $a\Phi_C$ is used (see Eq. (3.6)).

$$\epsilon_{cr}^{(0)} = -\frac{8\alpha_0^3}{243\,\nu\,\lambda_0^2} = -\frac{8}{243\,\nu}\frac{1}{\hat{r}_{tr}^3}\lambda_0\,. \tag{3.7}$$

The first expression can also be written as $\delta_{cr}^{(0)} = 2/3$ (see Spitzer 1987). We recall that $\lambda_0 = \lambda_0(\hat{r}_{tr})$ and that $\hat{r}_{tr} = \hat{r}_{tr}(\Psi)$. Therefore, the right-hand side of Eqs. (3.6) and (3.7) depends only on the value of Ψ.

If we make use of the full second-order asymptotic solution for the escape energy $(\psi^{(\rm ext)})^{(2)}$, in which the second-order expressions for the cluster potential (recorded in Eq. (3.37)) and the cut-off constant are used, the system in Eq. (3.4) can be re-arranged and written in standard form

$$\begin{cases} A(\hat{r}_T)\epsilon_{cr}^2 + 2\,B(\hat{r}_T)\epsilon_{cr} + C(\hat{r}_T) = 0 \\ D(\hat{r}_T)\epsilon_{cr}^2 + 2\,E(\hat{r}_T)\epsilon_{cr} + F(\hat{r}_T) = 0\,, \end{cases} \tag{3.8}$$

with

$$\begin{aligned} A(\hat{r}_T) = \lambda_2\hat{r}_T^4 - (b_{20} - b_{22}\sqrt{3})\frac{3}{4}\sqrt{\frac{5}{\pi}}\hat{r}_T^2 + b_{40}\frac{45}{16\sqrt{\pi}} \\ -b_{42}\frac{15}{8}\sqrt{\frac{5}{\pi}} + b_{44}\frac{15}{16}\sqrt{\frac{35}{\pi}}\,, \end{aligned} \tag{3.9}$$

$$B(\hat{r}_T) = \lambda_1 \hat{r}_T^4 - (a_{20} - a_{22}\sqrt{3})\frac{3}{4}\sqrt{\frac{5}{\pi}}\hat{r}_T^2 + 9\nu\hat{r}_T^7 \,, \tag{3.10}$$

$$C(\hat{r}_T) = 2\lambda_0 \hat{r}_T^4 \,, \tag{3.11}$$

$$D(\hat{r}_T) = \alpha_2 \hat{r}_T^5 - \lambda_2 \hat{r}_T^4 + (b_{20} - b_{22}\sqrt{3})\frac{1}{4}\sqrt{\frac{5}{\pi}}\hat{r}_T^2 - b_{40}\frac{9}{16\sqrt{\pi}} + b_{42}\frac{3}{8}\sqrt{\frac{5}{\pi}} - b_{44}\frac{3}{16}\sqrt{\frac{35}{\pi}} \,, \tag{3.12}$$

$$E(\hat{r}_T) = \alpha_1 \hat{r}_T^5 - \lambda_1 \hat{r}_T^4 + (a_{20} - a_{22}\sqrt{3})\frac{1}{4}\sqrt{\frac{5}{\pi}}\hat{r}_T^2 + \frac{9}{2}\nu\hat{r}_T^7 \,, \tag{3.13}$$

$$F(\hat{r}_T) = 2(\alpha_0 \hat{r}_T^5 - \lambda_0 \hat{r}_T^4) \,, \tag{3.14}$$

where the relevant constants (λ_i with $i = 0, 1, 2$, a_{lm} with $l = 0, 2$ and b_{lm} with $l = 0, 2, 4$ $m = 0, 2, ..., l$), which are determined by the matching process, are defined in Section 2.4.4 of Chapter 2. [The corresponding system based on the first-order solution for $\psi^{(\text{ext})}$ can be recovered by setting $A(\hat{r}_T) = D(\hat{r}_T) = 0$.] This system has been solved numerically, by means of the Newton-Raphson method, since the equations are nonlinear in $\hat{r}_T$ (in particular, they are polynomials of fifth and seventh-order, for the first and second-order solution respectively). As noted in the discussion of the simpler Eq. (3.5), the solution for ϵ_{cr} can then be represented as a function of the concentration parameter Ψ. The parameter space of the first and second-order models has been explored by means of an equally spaced grid from $\epsilon = 5 \times 10^{-8}$ to $\epsilon = 1 \times 10^{-2}$ at steps of 5×10^{-7} and from $\Psi = 0.1$ to $\Psi = 10$ at steps of 0.1.

The parameter space for the second-order models is presented in Fig. 3.1. The plot provides the contour levels of the extension parameter δ, with the uppermost solid line corresponding to $\delta = \delta_{cr} \approx 2/3$ (thus identifying the critical models), based on the choice $\nu = 3$ (Keplerian host galaxy). The critical curves for $\nu = 2$ (host galaxy characterized by flat rotation curve) and for $\nu = 1$ (Plummer potential evaluated at $R_0 = b/\sqrt{2}$, with b the model scale radius) are shown as a dashed and dot-dashed line, respectively.

Sub-critical, underfilled models (bottom-left corner of the figure), with $\delta \ll \delta_{cr}$, are only little affected by the tidal perturbation. The maximally deformed models are those with $\delta \approx \delta_{cr}$ (close to the uppermost solid line, i.e. close-to-critical configurations). Figure 3.1 shows that the critical value for the tidal strength parameter depends strongly on concentration, with a variation of almost four orders of magnitude in the explored range of Ψ. The figure also indicates that for lower values of ν the critical curve moves upwards, i.e. the available parameter space increases.

The difference between the critical value of the tidal strength parameter for first and second-order models (for a chosen value of ν) is very small, around 10^{-5} for low-concentration models, down to 10^{-9} or less for models with $\Psi \approx 10$. The critical value of the extension parameter δ depends only weakly on concentration and on ν, as illustrated in Fig. 3.2.

In closing this section, we should reiterate that, in spite of the abundant use of symbols required by the analysis, the family of models that we have studied is characterized by two dimensionless parameters (Ψ, ϵ). [As an alternative pair, we may refer to the standard concentration parameter $C = log(r_{tr}/r_0)$, equivalent to Ψ and frequently used in

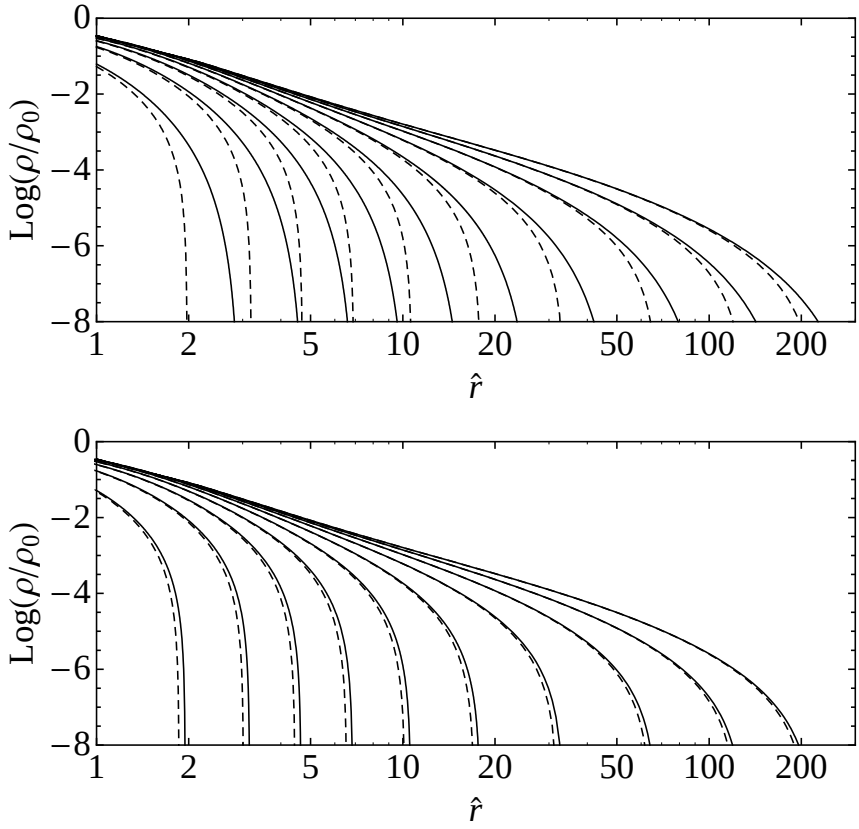

Figure 3.3: Intrinsic density profiles (normalized to the central value) for critical second-order models with $\nu = 3$ and $\Psi = 1, 2, ..., 10$ (from left to right). Top panel (a): profile of the triaxial models along the $\hat{x}$-axis (solid) and of the corresponding spherical King models (dashed). Bottom panel (b): profile of the triaxial models along the $\hat{y}$-axis (solid) and the $\hat{z}$-axis (dashed).

the context of spherical King models, and to the extension parameter $\delta = \hat{r}_{tr}/\hat{r}_T$, equivalent to ϵ.] The free constants A and a that appear in the distribution function $f_K(H)$ set the two physical scales. In turn, the models constructed by Heggie & Ramamani (1995) are a one-parameter family of models, because these authors focused on the critical case and did not discuss the sub-critical regime.

3.3 Intrinsic and projected density distribution

3.3.1 Intrinsic density profile

The models are characterized by reflection symmetry with respect to the three natural coordinate planes. With respect to the unperturbed configuration (i.e. the spherical King model with the same value of Ψ), they exhibit an elongation along the $\hat{x}$-axis (defined by the direction of the center of the host galaxy), a compression along the $\hat{z}$-axis (the direction perpendicular to the orbit plane of the globular cluster), and only a very modest compression along the $\hat{y}$-axis.

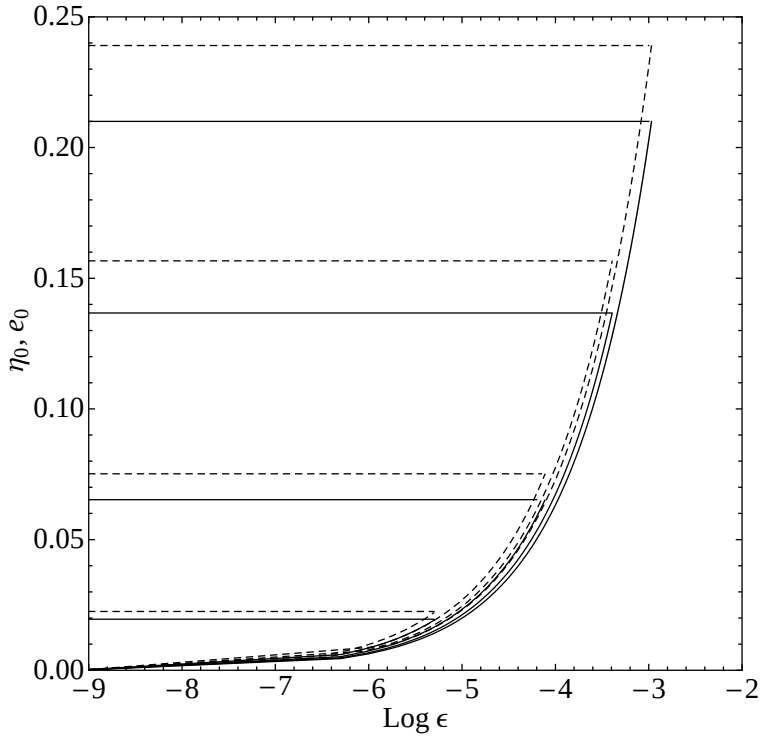

Figure 3.4: Central values of the polar (e_0; dashed) and equatorial (η_0; solid) eccentricities of the isodensity surfaces of second-order models with $\nu = 3$, $\Psi = 1, 3, 5, 7$ (from top to bottom) and $\epsilon \in [0, \epsilon_{cr}(\Psi)]$. Horizontal lines mark the maximum value of e_0 and η_0 reached by the critical models (i.e., for $\epsilon = \epsilon_{cr}(\Psi)$).

Models with $\delta \leq 0.2$, regardless of the value of Ψ, are practically indistinguishable from the corresponding spherical King models; significant departures from spherical symmetry occur for models with $\delta \approx 0.4$ or higher. In Fig. 3.3.a we show the density profile along the $\hat{x}$-axis for a selection of critical second-order models with $\nu = 3$ in comparison with that of the corresponding spherical King models; note that for a model with $\Psi = 2$ the elongation is already significant at $Log(\rho/\rho_0) \approx -4$, while for a model with $\Psi = 8$ a similar elongation is reached only at much lower density levels ($Log(\rho/\rho_0) \approx -7$). The corresponding profiles along the $\hat{y}$-axis and the $\hat{z}$-axis are given in Fig. 3.3.b.

For completeness, we checked the dependence of our density profiles on the potential of the host galaxy. Consistent with the general trends suggested by Fig. 3.2, the elongation along the $\hat{x}$-axis and the compression along the $\hat{z}$-axis for the models with $\nu = 3$ turn out to be slightly weaker than for the models with smaller values of ν.

Since the dimensionless density distribution of a model, identified by (Ψ, ϵ), is given by $\hat{\rho} = \hat{\rho}[\psi(\hat{r})]$, where ψ is the dimensionless escape energy and $\hat{\rho}$ is a monotonically increasing function that vanishes for vanishing argument, there is a one-to-one correspondence between isodensity and isovelocity surfaces, the latter being defined by the condition $\psi^{(int)}(\hat{r}) = S$, where S is a constant (with $0 \leq S \leq \Psi$). We recall that non-spherical models often exhibit equipotential surfaces rounder than the isodensity sur-

faces (e.g., see Evans 1993; Ciotti & Bertin 2005). The reason for the presence of this property in our models is that the supporting distribution function depends only on the Jacobi integral, i.e. the (isolating) energy integral in the rotating frame. Therefore, for each value of S, we can define the semi-axes $\hat{a}$, $\hat{b}$, and $\hat{c}$ of the corresponding triaxial isodensity surface, by means of the intersections of the surface with the $\hat{x}$, $\hat{y}$, and $\hat{z}$ axes, which turn out to follow the ordering $\hat{a} \geq \hat{b} \geq \hat{c}$. The shape of the triaxial configuration can thus be described in terms of the polar and equatorial eccentricities, defined as $e = [1 - (\hat{c}/\hat{a})^2]^{1/2}$ and $\eta = [1 - (\hat{b}/\hat{a})^2]^{1/2}$, respectively.

A surprising result can be derived analytically. In the innermost region $\hat{r} \ll \hat{r}_{tr}$ (i.e., for $S \sim \Psi$), the dimensionless escape energy can be expanded to second order in the dimensionless radius

$$\psi^{(int)}(\hat{\mathbf{r}}) \sim \Psi - \frac{3}{2}\hat{r}^2 + \epsilon\hat{r}^2 \left[-\frac{3}{2}(1-\nu) + A_{20}Y_{20}(\theta,\phi) + \right. \tag{3.15}$$

$$\left. A_{22}Y_{22}(\theta,\phi)] + \frac{\epsilon^2}{2}\hat{r}^2 \left[(1+B_{20})Y_{20}(\theta,\phi) + (1+B_{22})Y_{22}(\theta,\phi)\right] \right. .$$

Here some terms of the second-order solution do not contribute (e.g., it can be readily checked that $\psi^{(int)}_{2,4m}(\hat{r}) \sim \hat{r}^4$ and $\psi^{(int)}_{2,00}(\hat{r}) \sim \hat{r}^6$). Then by setting $\psi^{(int)}(\hat{a},0,0) = \psi^{(int)}(0,\hat{b},0) = \psi^{(int)}(0,0,\hat{c})$, we find that in the innermost region the eccentricities tend to the following non-vanishing central values

$$e_0 = \frac{\{\epsilon(A_{22} - \sqrt{3}A_{20} + (\epsilon/2)[1 + B_{22} - \sqrt{3}(1+B_{20})])\sqrt{15/\pi}\}^{1/2}}{\{6 + 2\epsilon[3(1-\nu) - A_{20}\sqrt{5/\pi}] - \epsilon^2(1+B_{20})\sqrt{5/\pi}\}^{1/2}} , \tag{3.16}$$

$$\eta_0 = \frac{\{\epsilon[2A_{22} + (1+B_{22})\epsilon]\sqrt{15/\pi}\}^{1/2}}{\{6 + \epsilon d_1 + (\epsilon^2/2)d_2\}^{1/2}} , \tag{3.17}$$

where

$$d_1 = 6(1-\nu) + (A_{20} + \sqrt{3}A_{22})\sqrt{5/\pi} \tag{3.18}$$

$$d_2 = [1 + B_{20} + \sqrt{3}(1+B_{22})]\sqrt{5/\pi} \tag{3.19}$$

which depend explicitly on the tidal strength and implicitly on the concentration. This result is nontrivial. In fact, since the tidal potential is a homogeneous function of the spatial coordinates, naively we might expect that in their central region the models reduce to a perfectly spherical shape (i.e., $e_0 = \eta_0 = 0$), even for finite values of the tidal strength. Instead, e_0 and η_0 are $\mathcal{O}(\epsilon^{1/2})$ and strictly vanish only in the limit of vanishing tidal strength.

Figure 3.4 shows the central values of the eccentricities for second-order models with $\nu = 3$ and selected values of concentration, as a function of tidal strength within the range $[0, \epsilon_{cr}(\Psi)]$. Consistent with the general trends identified in the discussion of the parameter space, low-concentration models show the most significant departures from spherical symmetry. The full eccentricity profiles (as a function of the major axis) are shown in Fig. 3.5 for a selection of critical second-order models; here the calculation of e and η has been performed by numerically determining the values of the semi-axes of a number of reference isovelocity surfaces, defined by $\psi^{(int)}(\hat{r}) = S_i = (25-i)\Psi/25 - 0.01$ with $i = 0, .., 25$. Outside the central region, the profiles increase monotonically and, independently of concentration, at the boundary they reach approximately a fixed

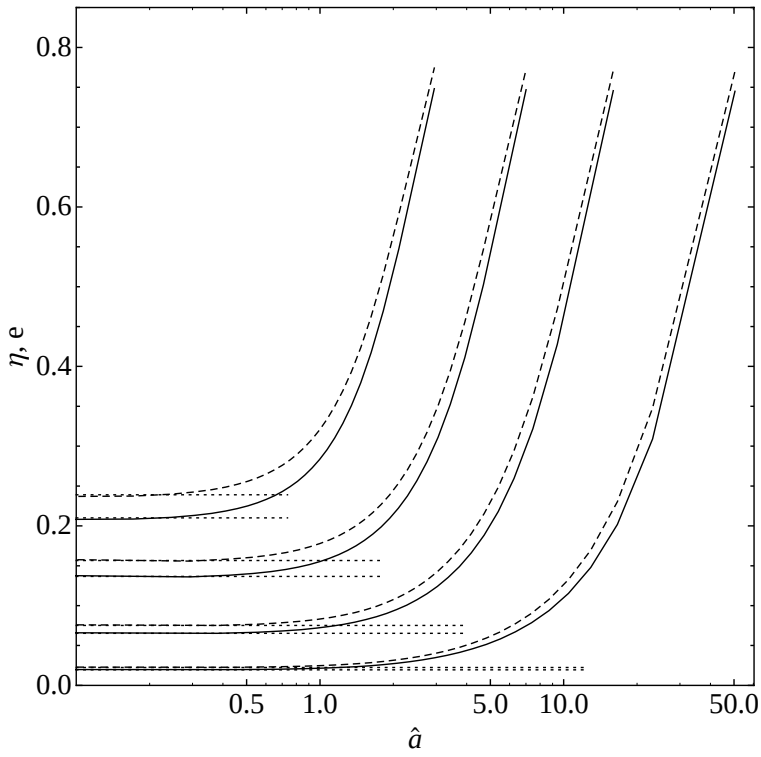

Figure 3.5: Profiles of the polar (e; dashed) and equatorial (η; solid) eccentricities of the isodensity surfaces for selected critical second-order models with $\nu = 3$ and $\Psi = 1, 3, 5, 7$ (from left to right). Dotted horizontal lines show the central eccentricity values (see Eqs. (4.16) and (3.17)).

maximum value ($e \approx 0.78$ and $\eta \approx 0.74$), which corresponds to the fact that the shape of the boundary surface of a critical model ($\delta_{cr}^{(0)} = 2/3$; see also Fig. 3.2) depends only modestly on concentration.

3.3.2 Comparison with the models constructed by Heggie & Ramamani (1995)

The method used in Chapter 2 for the construction of the models illustrated here can be summarized as follows. The solution in the internal (Poisson) and external (Laplace) domains are expressed as an asymptotic series with respect to the dimensionless parameter ϵ, representing the tidal strength (defined in Eq. (3.2)), which is considered to be small. The kth-order term of the asymptotic series of the internal and external solution are denoted by $\psi_k^{(\mathrm{int})}(\hat{r})$ and $\psi_k^{(\mathrm{ext})}(\hat{r})$ respectively, so that the zeroth-order terms define the standard spherical King models. The quantity $(\psi^{(\mathrm{ext})})^{(k)}$ indicates the kth-order external solution, i.e. the corresponding asymptotic series truncated at the term $\psi_k^{(\mathrm{ext})}$; a similar notation holds for the internal solution. The validity of the expansion breaks down where the second term is comparable to the first, i.e. where $\psi_0 = \mathcal{O}(\epsilon)$. This singularity is cured by introducing a *boundary layer* in which both the spatial coordinates and the

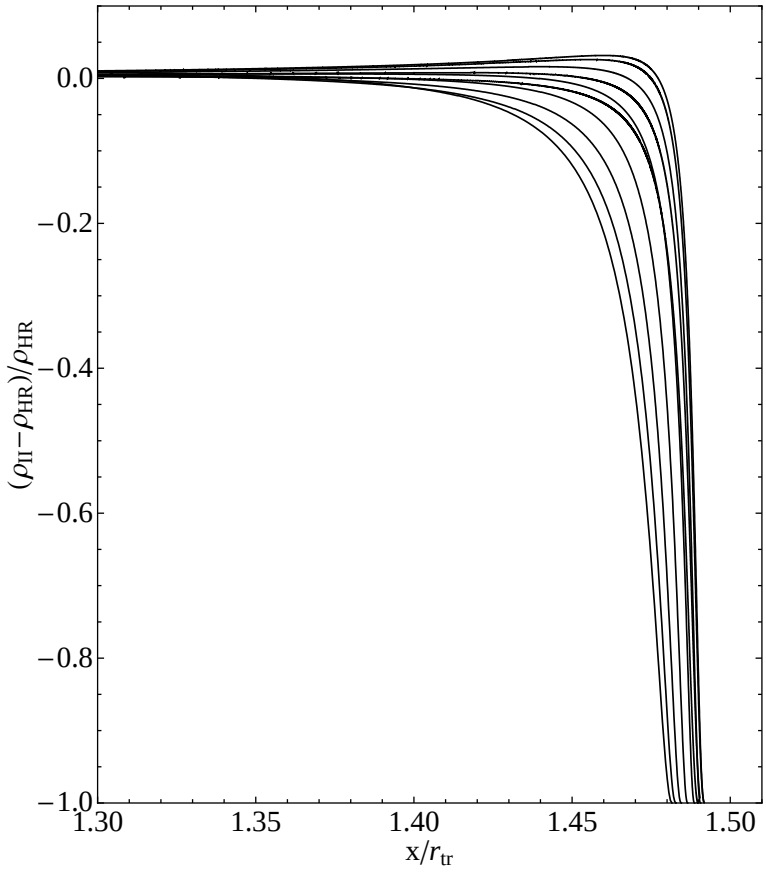

Figure 3.6: Relative difference between the intrinsic density profiles of critical second-order models (ρ_{II}) constructed in this Chapter and those of the corresponding (first-order) models (ρ_{HR}) described by Heggie & Ramamani (1995). The comparison has been performed along the three axes in the whole internal+boundary region (see main text). Here we illustrate the difference along the x-axis in the boundary layer ($\Psi = 1, 2, ..., 10$ from left to right). At variance with Fig. 3.3, the spatial coordinate is scaled with respect to the truncation radius instead of the scale radius r_0.

solution $\psi^{(\mathrm{lay})}$ are suitably rescaled with respect to the tidal parameter. To obtain a uniformly valid solution over the entire space, an asymptotic matching (see Van Dyke 1975, Eq. (5.24)) is performed between the pairs $(\psi^{(\mathrm{int})}, \psi^{(\mathrm{lay})})$ and $(\psi^{(\mathrm{lay})}, \psi^{(\mathrm{ext})})$. Each term $\psi_k(\hat{r})$ is then expanded in spherical harmonics with radial coefficients $\psi_{k,\,lm}(\hat{r})$. The internal region requires a numerical solution of the Cauchy problems for the radial coefficients (we used a fourth-order Runge-Kutta code) while in the external region a formal solution with multipolar structure is available and in the boundary layer the integration in the radial variable can be performed analytically.

The models described by Heggie & Ramamani (1995) are also based on a perturbation approach, but the method used is different from ours, provides a solution of the Poisson equation that is first-order with respect to the tidal parameter, and is restricted to the "critical" case; actually, as noted in Section 3.2 after Eq. (3.7), the perturbation approach is bound to break down in the critical case. Technically speaking, their method is in the

form of a "patching" procedure, in contrast with our asymptotic matching. Therefore, the models constructed in Chapter 2, while consistent, to first order, with those of Heggie & Ramamani (1995), are more general. We also recall that our method is also applicable to systems described by different distribution functions (see Section 2.6).

We have thus performed a quantitative comparison between the intrinsic density profiles of our critical second-order models and those of the models[2] by Heggie & Ramamani (1995), both referred to the case in which the host galaxy is Keplerian ($\nu = 3$). As desired, there is substantial consistency except for the outermost part of the boundary layer in which our models are slightly more compact, due to a global "boxiness" effect induced by the second-order term present in our models in which harmonics of order $l = 4$ also play a role. In Fig. 3.6 we represent the relative difference between the two density profiles evaluated along the x-axis (with the coordinates scaled with respect to the truncation radius instead of the usual scale radius r_0) for selected values of Ψ. A similar behaviour is found also along the y-axis, for y/r_{tr} in the range $[0.80, 1]$, and along the z-axis, for z/r_{tr} in the range $[0.80, 0.95]$. In the central part of the internal region, along the principal axes, the relative difference is smaller than 5 percent for every value of Ψ we tested, while near the transition to the boundary layer (i.e $x/r_{tr} \lesssim 1$ and $y/r_{tr},\ z/r_{tr} \lesssim 0.8$) a difference of 20 percent can be reached in the case of highly concentrated models ($\Psi = 8, 9, 10$). We interpret these differences as due to the combined effects of the patching vs. matching adopted process and of the different grid on which the Cauchy problems for the radial coefficients are solved (we used a regular radial grid while Heggie & Ramamani (1995) used a more complex tabulation resulting from their choice of taking the zeroth-order cluster potential as the independent variable and of the function $ln(1 + \hat{r}^2)$ instead of $\hat{r}$).

3.3.3 Global quantities

The previous discussion has focused on the shape of the isodensity surfaces of the models. In particular, some interesting conclusions have been derived based on a local analysis of the central region and of the outer boundary of the configuration. The maximal departures from spherical symmetry are reached at the periphery, but these hinge on the distribution of the very small number of stars that populate the outer region of the cluster. We may thus wish to study some global quantities that better characterize whether significant amounts of mass (and, correspondingly, of light) are actually involved in the deviation of the model from spherical symmetry. One standard such global measure is provided by the quadrupole moment tensor

$$Q_{ij} = \int_V (3x_i x_j - r^2\delta_{ij})\rho(\mathbf{r})d^3r = \hat{A}r_0^5 \int_V (3\hat{x}_i\hat{x}_j - \hat{r}^2\delta_{ij})\hat{\rho}(\hat{\mathbf{r}})d^3\hat{r} = \hat{A}r_0^5\hat{Q}_{ij} \ , \tag{3.20}$$

with the integration to be performed in the volume V of the entire configuration. Here the notation for the function $\hat{\rho}$ and for the constant $\hat{A}$ is the same as in Eq. (2.11). In contrast with the frequently used inertia tensor $I_{ij} = \int_V \rho x_i x_j d^3r$ (e.g., see Chandrasekhar 1969, chap. 2), the quadrupole moment is defined in such a way that in the spherical limit it vanishes identically. In our coordinate system it is diagonal. Note that the tidal distortions require that the non-vanishing terms of the inertia tensor follow the

[2] For this purpose, we used the code that implements the models described by Heggie & Ramamani (1995), written by D. C. Heggie and available within the STARLAB software environment (Portegies Zwart et al. 2001)

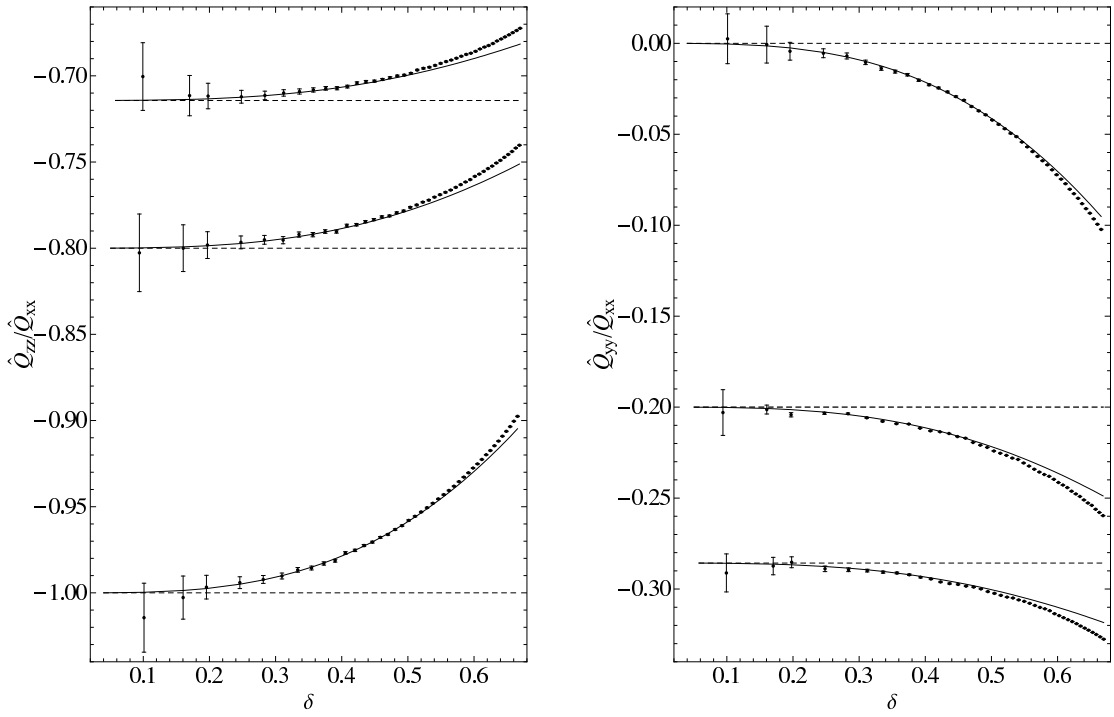

Figure 3.7: Ratio of two pairs of quadrupole moments for the second-order models with $\Psi = 5$, $0.1 \leq \delta \leq \delta_{cr}(\Psi)$, and $\nu = 1, 2, 3$ (in the left panel, the sequence of models with different ν values runs from bottom to top; in the right panel, it runs from top to bottom). The values obtained from numerical integration over the entire triaxial volume (dots) are compared to the analytical approximations (solid line) given by Eqs. (3.26) and (3.25); the analytical estimates of the ratios for first order models are also shown (dashed horizontal lines). The propagation of the errors of the numerical integration leads to the plotted error bars.

ordering $I_{xx} \geq I_{yy} \geq I_{zz}$; to visualize the geometry of the system, we may thus also refer to the average polar and equatorial eccentricities $\bar{e}$ and $\bar{\eta}$ defined by the relations $I_{yy} = (1 - \bar{\eta}^2) I_{xx}$, $I_{zz} = (1 - \bar{e}^2) I_{xx}$. In general, we have $Q_{yy}/Q_{xx} = (\bar{e}^2 - 2\bar{\eta}^2)/(\bar{e}^2 + \bar{\eta}^2)$ and $Q_{zz}/Q_{xx} = (\bar{\eta}^2 - 2\bar{e}^2)/(\bar{e}^2 + \bar{\eta}^2)$, with the prolate configuration identified by $\bar{e} = \bar{\eta}$, i.e. $Q_{yy}/Q_{xx} = Q_{zz}/Q_{xx} = -1/2$.

Since most of the mass is contained in the inner regions, global quantities can be evaluated approximately by neglecting the contribution from the region corresponding to the boundary layer. We can thus use the second-order solutions for ρ obtained in Chapter 2 by the method of matched asymptotic expansions and conveniently reduce the calculation of global quantities to an easier integration in spherical coordinates inside the sphere of radius $\hat{r}_{tr}$. Therefore, for the quadrupole moment tensor we find

$$\hat{Q}_{ij}^{(2)} = \hat{Q}_{ij,1}\epsilon + \hat{Q}_{ij,2}\frac{\epsilon^2}{2} \,. \tag{3.21}$$

We emphasize that this estimate is expected to be a good approximation only for those

models for which the contribution of the boundary layer is negligible with respect to the one of the internal sphere of radius $\hat{r}_{tr}$.

The relevant components on the diagonal can be expressed in terms of the matching constants of the external solution (for the relevant definitions, see Eqs. (2.63) and (2.69) in Chapter 2)

$$\hat{Q}^{(2)}_{xx} = \frac{2}{9}\sqrt{5\pi}\hat{\rho}(\Psi)\left[\left(a_{20}\epsilon + b_{20}\frac{\epsilon^2}{2}\right) -\sqrt{3}\left(a_{22}\epsilon + b_{22}\frac{\epsilon^2}{2}\right)\right], \tag{3.22}$$

$$\hat{Q}^{(2)}_{yy} = \frac{2}{9}\sqrt{5\pi}\hat{\rho}(\Psi)\left[\left(a_{20}\epsilon + b_{20}\frac{\epsilon^2}{2}\right) +\sqrt{3}\left(a_{22}\epsilon + b_{22}\frac{\epsilon^2}{2}\right)\right], \tag{3.23}$$

$$\hat{Q}^{(2)}_{zz} = -\frac{4}{9}\sqrt{5\pi}\hat{\rho}(\Psi)\left(a_{20}\epsilon + b_{20}\frac{\epsilon^2}{2}\right). \tag{3.24}$$

We recall that the constants a_{20} and b_{20} are positive, while a_{22} and b_{22} are negative (and larger in magnitude). Therefore, $\hat{Q}^{(2)}_{xx}$ is positive and $\hat{Q}^{(2)}_{yy}$ and $\hat{Q}^{(2)}_{zz}$ are negative, consistent with the detailed elongation and compressions observed in the density profile. A summary of the derivation of these formulae is provided in Appendix B.

As a measure of the degree of triaxiality of a given configuration, we have calculated the following ratios

$$\frac{\hat{Q}^{(2)}_{yy}}{\hat{Q}^{(2)}_{xx}} = \frac{(a_{20} + b_{20}\epsilon/2) + \sqrt{3}\,(a_{22} + b_{22}\epsilon/2)}{(a_{20} + b_{20}\epsilon/2) - \sqrt{3}\,(a_{22} + b_{22}\epsilon/2)}, \tag{3.25}$$

$$\frac{\hat{Q}^{(2)}_{zz}}{\hat{Q}^{(2)}_{xx}} = \frac{-2\,(a_{20} + b_{20}\epsilon/2)}{(a_{20} + b_{20}\epsilon/2) - \sqrt{3}\,(a_{22} + b_{22}\epsilon/2)}, \tag{3.26}$$

which depend explicitly on the tidal strength parameter and implicitly on the concentration parameter. In the limit of vanishing tidal strength, we find

$$\frac{\hat{Q}_{yy}}{\hat{Q}_{xx}} \sim \frac{\hat{Q}^{(1)}_{yy}}{\hat{Q}^{(1)}_{xx}} = \frac{T_{20}(\hat{r}_{tr}) + \sqrt{3}T_{22}(\hat{r}_{tr})}{T_{20}(\hat{r}_{tr}) - \sqrt{3}T_{22}(\hat{r}_{tr})} = -\frac{\nu - 1}{2\nu + 1}, \tag{3.27}$$

$$\frac{\hat{Q}_{zz}}{\hat{Q}_{xx}} \sim \frac{\hat{Q}^{(1)}_{zz}}{\hat{Q}^{(1)}_{xx}} = \frac{-2T_{20}(\hat{r}_{tr})}{T_{20}(\hat{r}_{tr}) - \sqrt{3}T_{22}(\hat{r}_{tr})} = -\frac{2 + \nu}{2\nu + 1}, \tag{3.28}$$

where $T_{2m}(\hat{r})$ are the quadrupole coefficients of the tidal potential (see Eqs. (2.38) and (2.39) in Chapter 2). This result is nontrivial, because, in this limit, numerator and denominator are both expected to vanish. Note that only for $\nu = 1$ the ratio $\hat{Q}_{yy}/\hat{Q}_{xx} = \mathcal{O}(\epsilon)$.

Earlier in this Chapter we mentioned that two physical scales, such as total mass and central velocity dispersion, correspond to the two dimensional constants A and a that

appear in the distribution function $f_K(H)$. In fact, the total mass of the system is given by

$$M = \int_V \rho(r) d^3r = \hat{A} r_0^3 \int_V \hat{\rho}(\hat{r}) d^3\hat{r} = \hat{A} r_0^3 \hat{M} \ . \tag{3.29}$$

If we insert the second-order solution for ρ obtained in Chapter 2, we find

$$\begin{aligned} \hat{M}^{(2)} &= \int_0^{2\pi} d\phi \int_0^{\pi} d\theta \sin\theta \int_0^{\hat{r}_{tr}} d\hat{r}\, \hat{r}^2\, \hat{\rho}^{(2)}(\hat{r}, \theta, \phi) \\ &= \hat{M}_0 + \epsilon \hat{M}_1 + \frac{\epsilon^2}{2} \hat{M}_2 \ , \end{aligned} \tag{3.30}$$

with

$$\hat{M}_i = \hat{M}_i(\Psi) = -\frac{4\pi \hat{\rho}(\Psi)}{9} \lambda_i \ . \tag{3.31}$$

Here each term of the expansion is related to the corresponding constant with $l = 0$ (i.e., the monopole term) of the expression of the external solution of the Poisson-Laplace equation calculated by means of the method of matched asymptotic expansion (for the relevant definitions, see Eqs. (2.59),(2.61),(2.67) in Chapter 2).

The quality of the analytical estimates for the total mass and the quadrupole moment tensor has been checked by comparing the values obtained from asymptotic analysis with those resulting from direct numerical integration of Eq. (3.29) and Eq. (3.20) respectively, in which the density profile $\hat{\rho} = \hat{\rho}[\psi(\hat{r})]$ is used without any additional expansion. The integration of the distribution function over the entire space, required by those global quantities, has been performed by means of an Adaptive Monte Carlo method (the algorithm VEGAS, see Press et al. 1992, Section 7.8), well suited for our geometry. For the quadrupole, the results are illustrated in Fig. 3.7. For the mass, the dimensionless function $\hat{M}^{(2)}(\Psi)$ is basically unchanged (within 0.5 percent) with respect to the function characterizing the spherical King models; the Monte Carlo integration is very accurate, with relative errors around 10^{-5}, and the analytical approximation given by Eq. (3.30) shows an excellent agreement for every value of Ψ in the whole range of the extension parameter $[0, \delta_{cr}(\Psi)]$.

The average eccentricities for critical second-order models as a function of concentration, with $0.1 \leq \Psi \leq 10$, for two different choices of the host galaxy potential ($\nu = 3, 1$), are shown in Fig. 3.8. The values are calculated directly from the definitions given earlier in this subsection in terms of $\hat{\rho} = \hat{\rho}[\psi(\hat{r})]$ with no additional expansions. A non-monotonic dependence on concentration is revealed, with generally higher average eccentricities attained by low-concentration models. The trends of the polar and equatorial eccentricities are basically the same, as shown by the fact that the related curves in the plot can be matched approximately by a rigid translation. As expected (see Section 3.3.1), models with $\nu = 1$ show a larger separation between polar and equatorial eccentricities than models with $\nu = 3$. The presence of a minimum for the curves at $\Psi \approx 6.5$ occurs approximately at the location where the function $Log[\epsilon_{cr}(\Psi)]$ shows an inflection point (regardless of the value of ν; see Fig. 3.1).

3.3.4 Projected density profile

Under the assumption of a constant mass-to-light ratio, projected models can be compared with the observations. We have then computed surface (projected) density profiles and projected isophotes. The projection has been performed along selected directions,

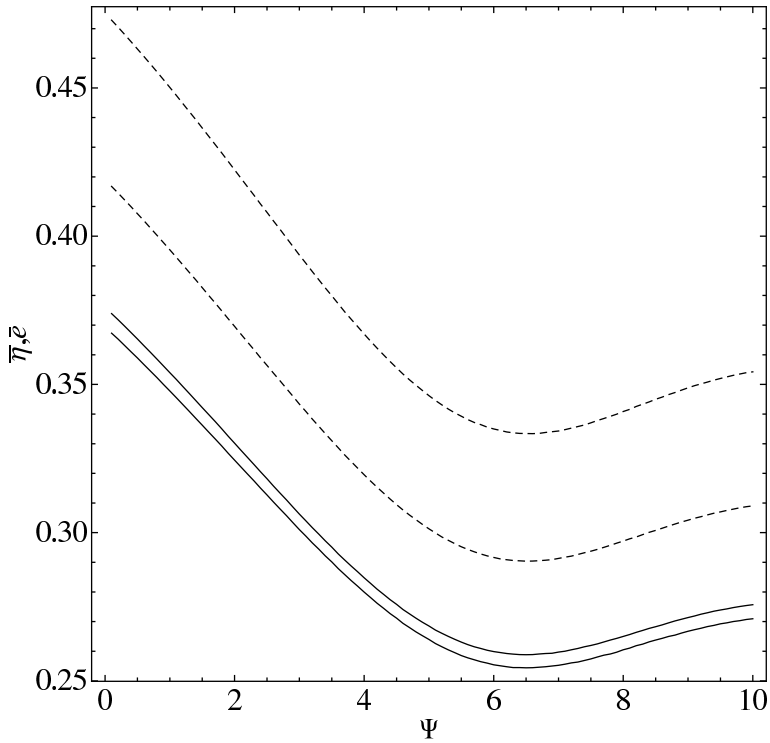

Figure 3.8: Average polar ($\bar{e}$; dashed) and equatorial ($\bar{\eta}$; solid) eccentricities for critical second-order models as a function of concentration, with $0.1 \leq \Psi \leq 10$, for two different host potentials. Models with $\nu = 3$ correspond to the inner pair of curves, while models with $\nu = 1$ to the outer pair. The eccentricities have been determined numerically from their definitions (see main text) in terms of $\hat{\rho} = \hat{\rho}[\psi(\hat{\mathbf{r}})]$, without any additional expansion; the relative errors are around 10^{-5}.

identified by the viewing angle (θ, ϕ), corresponding to the $\hat{z}_P$ axis of a new coordinate system related to the intrinsic system by the transformation $\hat{x}_P = R\hat{x}$; the rotation matrix $R = R_1(\theta)R_3(\phi)$ is expressed in terms of the viewing angles, by taking the $\hat{x}_P$ axis as the line of nodes (see Ryden 1991, for an equivalent projection rule). Given the symmetry of our models (see Section 3.3.1), viewing angles can be chosen from the first octant only. In particular, we used a 4×4 polar grid defined by $\theta_i = i\,\pi/6$ and $\phi_j = j\,\pi/6$ with $i, j = 0, .., 3$, and calculated (by numerical integration, using the Simpson rule) the dimensionless projected density

$$\hat{\Sigma}(\hat{x}_P, \hat{y}_P) = \int_{-\hat{z}_{sp}}^{\hat{z}_{sp}} \hat{\rho}(\hat{r}_P) d\hat{z}_P \ , \tag{3.32}$$

where $\hat{z}_{sp} = (\hat{x}_e^2 - \hat{x}_P^2 - \hat{y}_P^2)^{1/2}$ with $\hat{x}_e$ the edge of the cluster along the $\hat{x}$ axis of the intrinsic coordinate system (i.e., we "embedded" the triaxial configuration in a sphere of radius given by its maximal extension). The projection plane $(\hat{x}_P, \hat{y}_P)$ has been sampled on an equally-spaced 108×108 square grid centered at the origin (note that for $\hat{x}_P^2 + \hat{y}_P^2 \geq \hat{x}_e^2$ the projected density is correctly set to zero).

The morphology of the isophotes of a given projected image can be described in terms of the *ellipticity* profile, defined as $\varepsilon = 1 - \hat{b}_P/\hat{a}_P$ where $\hat{a}_P$ and $\hat{b}_P$ are the semi-axes, as a function of the major axis $\hat{a}_P$. As already noted for the (intrinsic) eccentricity

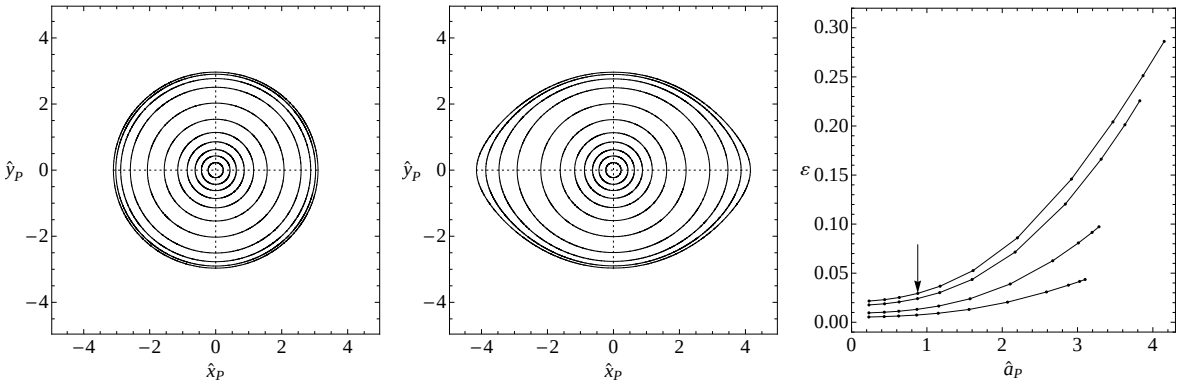

Figure 3.9: Projections of a second-order critical model ($\Psi = 2$ and $\nu = 3$) along the $\hat{x}$ axis (left panel [a]) and along the $\hat{y}$ axis (central panel [b]). The ellipticity profiles (right panel [c], from bottom to top) refer to the projections along directions identified by $(\theta = \pi/2, \phi = i\,\pi/6)$ with $i = 0, ..., 3$; dots represent the locations of the isophotes drawn in panels [a],[b], which correspond to selected values of Σ/Σ_0 in the range $[0.9, 10^{-6}]$. The arrow indicates the position of the half-light isophote (practically the same for every projection considered in the figure).

profiles, the deviation from circularity increases with the distance from the origin. In the inner region, the ellipticity is consistent with the central eccentricities e_0 and η_0 calculated in Section 3.3.1.

By taking lines of sight different from the axes of the symmetry planes, we have also checked whether the projected models would exhibit isophotal twisting. For all the cases considered, the position angle of the major axis remains unchanged over the entire projected image. Tests made by changing the resolution of the grid confirm that, even in the most triaxial case ($\nu = 1$), no significant twisting is present.

The first two panels of Fig. 3.9 show the projected images of a critical second-order model with $\Psi = 2$ and $\nu = 3$ along the $(\pi/2, 0)$ and $(\pi/2, \pi/2)$ directions, (i.e., the $\hat{x}$ and $\hat{y}$ axis of the intrinsic system), corresponding, respectively, to the least and to the most favorable line of sight for the detection of the intrinsic flattening of the model. For the same model, the third panel illustrates the ellipticity profiles for various lines of sight.

Figure 3.10 shows the surface density profiles along the $\hat{x}_P$ and $\hat{y}_P$ axes of the projection plane for ten critical second-order models with $\nu = 3$, viewed along the $(\pi/2, \pi/2)$ direction. As a further characterization, for the same models in the lower panel we also present the surface density profiles obtained by averaging the projected density distribution on circular annuli; this conforms to the procedure often adopted by observers in dealing with density distributions with very small departures from circular symmetry (e.g., see Lanzoni et al. 2007). As expected, circular-averaged profiles lie between the corresponding regular profiles taken along the principal axes of the projected image.

3.4 Intrinsic and projected kinematics

By construction, the models are characterized by isotropic velocity dispersion. The intrinsic velocity dispersion can be determined directly as the second moment in velocity

space (normalized to the intrinsic density) of the distribution function

$$\sigma^2(\psi) = \frac{2}{5a}\frac{\gamma\,(7/2,\psi)}{\gamma\,(5/2,\psi)} = \frac{1}{a}\hat{\sigma}^2(\psi)\;, \tag{3.33}$$

where γ represents the incomplete gamma function (near the boundary of the configuration, the velocity dispersion profile scales as $\hat{\sigma}^2(\psi) \sim (2/7)\psi$). This shows that the isodensity surfaces of the models are in a one-to-one correspondence with the isovelocity and isobaric surfaces (defined by $\sigma^2[\psi(\hat{r})] = \text{const}$). As noted for the intrinsic density profiles in Section 3.3.1, a compression along the $\hat{z}$ axis and an elongation along $\hat{x}$ axis occur also for the intrinsic velocity dispersion profiles. In Fig. 3.11.a we present the intrinsic velocity dispersion profiles along the $\hat{x}$ axis for the same critical models illustrated in Fig. 3.3 compared to the profiles of the corresponding spherical King models. The behavior of the projected velocity dispersion profiles near the boundary is significantly different from that of the spherical models.

The projected velocity moments can be calculated by integrating along the line of sight (weighted by the intrinsic density) the corresponding intrinsic quantities. Therefore, the projected velocity dispersion is given by

$$\sigma_P^2(\hat{x}_P,\hat{y}_P) = \frac{\int_{-\hat{z}_{sp}}^{\hat{z}_{sp}} \sigma^2(\hat{\mathbf{r}}_P)\rho(\hat{\mathbf{r}}_P)d\hat{z}_P}{\Sigma(\hat{x}_P,\hat{y}_P)} =$$

$$\frac{2}{5a}\frac{\int_{-\hat{z}_{sp}}^{\hat{z}_{sp}} \gamma[7/2,\psi(\hat{\mathbf{r}}_P)]\exp[\psi(\hat{\mathbf{r}}_P)]d\hat{z}_P}{\hat{\Sigma}(\hat{x}_P,\hat{y}_P)} = \frac{1}{a}\hat{\sigma}_P^2(\hat{x}_P,\hat{y}_P)\;. \tag{3.34}$$

Figure 3.11.b shows the projected velocity dispersion profiles along the $\hat{x}_P$ and $\hat{y}_P$ axis of the projection plane for the same models displayed in Fig. 3.10 (the line of sight is defined by $(\pi/2,\pi/2)$).

3.5 Global quantities from the multipole expansion of the cluster potential

Based on the expansion in spherical harmonics of $1/|\hat{r}-\hat{r}'|$ given in Eq. (3.70) of Jackson (1999), the external potential generated by our model can be expressed by means of the following multipole expansion

$$a\Phi_C^{(\text{ext})}(\hat{r}) = -\frac{9}{4\pi\hat{\rho}(\Psi)}\int_V d^3\hat{r}'\frac{\hat{\rho}(\hat{r}')}{|\hat{r}-\hat{r}'|} = -\frac{9}{\hat{\rho}(\Psi)}\sum_{l=0}^{+\infty}\frac{1}{2l+1}\sum_{m=-l}^{+l}\hat{q}_{lm}\frac{Y_{lm}(\theta,\phi)}{\hat{r}^{l+1}}\;, \tag{3.35}$$

where the multipole coefficients are defined as

$$\hat{q}_{lm} = \int_V d^3\hat{r}' Y_{lm}(\theta',\phi')\hat{r}'^{\,l}\hat{\rho}(\hat{r}')\;, \tag{3.36}$$

with the integration to be performed in the volume V with boundary surface defined by $\psi = 0$. This general expression can be compared with the second-order solution of the Laplace equation obtained in Chapter 2

$$\begin{aligned}\left(a\Phi_C^{(\text{ext})}\right)^{(2)}(\hat{r}) \;=\; & \left[\lambda_0+\lambda_1\epsilon+\lambda_2\frac{\epsilon^2}{2}\right]\frac{1}{\hat{r}} + \left[a_{20}\epsilon+b_{20}\frac{\epsilon^2}{2}\right]\frac{Y_{20}(\theta,\phi)}{\hat{r}^3} + \left[a_{22}\epsilon+b_{22}\frac{\epsilon^2}{2}\right]\frac{Y_{22}(\theta,\phi)}{\hat{r}^3} \\ & + b_{40}\frac{\epsilon^2}{2}\frac{Y_{40}(\theta,\phi)}{\hat{r}^5} + b_{42}\frac{\epsilon^2}{2}\frac{Y_{42}(\theta,\phi)}{\hat{r}^5} + b_{44}\frac{\epsilon^2}{2}\frac{Y_{44}(\theta,\phi)}{\hat{r}^5}\;,\end{aligned} \tag{3.37}$$

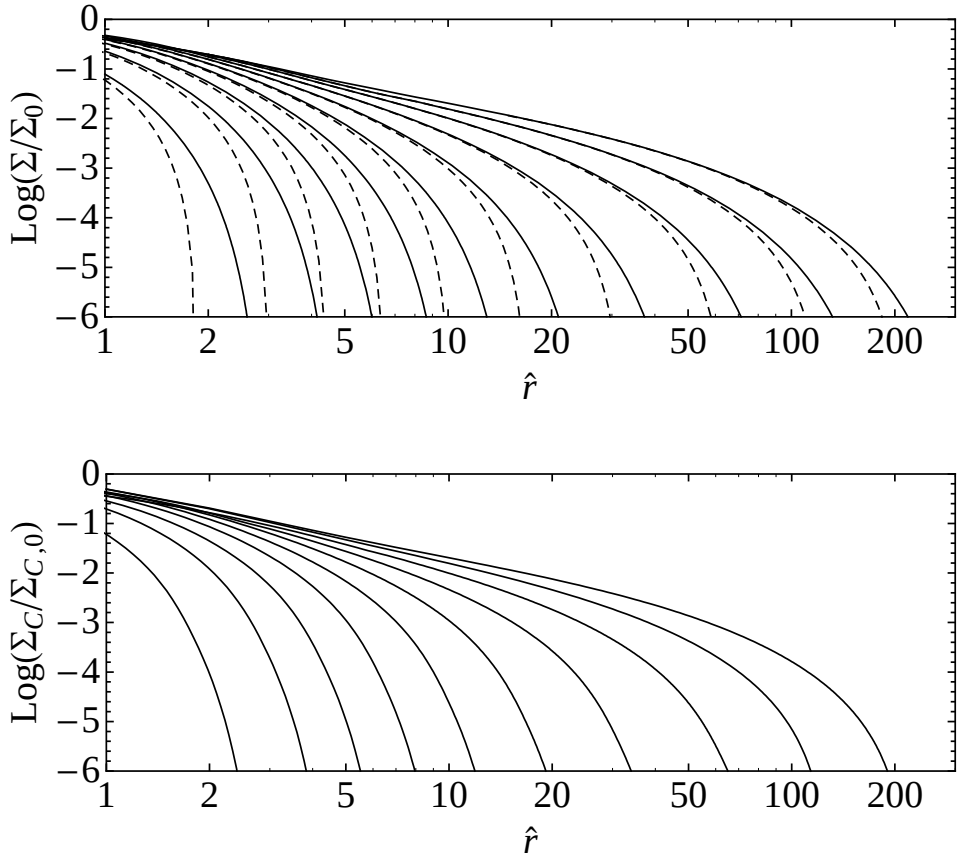

Figure 3.10: Projected density profiles (normalized to the central value) for the same ten second-order critical models displayed in Fig. 3.3. Top panel (a): the models are viewed from the $\hat{y}$ axis and the profiles taken along the two principal axes in the projection plane (along $\hat{x}_P$ (solid) and $\hat{y}_P$ (dashed), i.e. along the $\hat{x}$ and $\hat{z}$ axes of the intrinsic frame of reference). Bottom panel (b): the projection is performed on the same line of sight of the previous panel, but the profiles are taken by averaging the projected surface density on circular annuli, as if the image were intrinsically circular.

in order to determine the relation between the second-order multipole coefficients $\hat{q}_{lm}^{(2)}$ (i.e. calculated by means of the second-order expression for the density) and the matching constants that appear in Eq. (3.37). Therefore, we find that

$$\lambda_0 + \lambda_1\epsilon + \lambda_2\frac{\epsilon^2}{2} = -\frac{9}{\sqrt{4\pi}\hat{\rho}(\Psi)}\,\hat{q}_{00}^{(2)}\,, \tag{3.38}$$

so that Eq. (3.31) follows. For the higher-order harmonics we find the following relations for the non-vanishing coefficients

$$a_{2m}\epsilon + b_{2m}\frac{\epsilon^2}{2} = -\frac{9}{5\hat{\rho}(\Psi)}\,\hat{q}_{2m}^{(2)}\,, \tag{3.39}$$

for $m = 0, 2$ and

$$b_{4m}\frac{\epsilon^2}{2} = -\frac{1}{\hat{\rho}(\Psi)}\,\hat{q}^{(2)}_{4m}\,, \tag{3.40}$$

for $m = 0, 2, 4$.

Recalling that we are using *real* spherical harmonics with the Condon-Shortley phase, we get

$$\hat{q}_{20} = \frac{1}{4}\sqrt{\frac{5}{\pi}}\hat{Q}_{zz}\,, \tag{3.41}$$

$$\hat{q}_{22} = \frac{1}{12}\sqrt{\frac{15}{\pi}}(\hat{Q}_{xx} - \hat{Q}_{yy})\,. \tag{3.42}$$

To determine all the nontrivial components of the quadrupole moment tensor, we use the condition $\mathrm{Tr}(\hat{Q}_{ij}) = 0$. Therefore, for the second-order solution of Chapter 2, the system

$$\begin{cases} \hat{Q}^{(2)}_{xx} - \hat{Q}^{(2)}_{yy} = -\dfrac{20}{3}\sqrt{\dfrac{\pi}{15}}\hat{\rho}(\Psi)\left(a_{22}\epsilon + b_{22}\dfrac{\epsilon^2}{2}\right) \\ \hat{Q}^{(2)}_{zz} = -\dfrac{20}{9}\sqrt{\dfrac{\pi}{5}}\hat{\rho}(\Psi)\left(a_{20}\epsilon + b_{20}\dfrac{\epsilon^2}{2}\right) \\ \hat{Q}^{(2)}_{xx} + \hat{Q}^{(2)}_{yy} + \hat{Q}^{(2)}_{zz} = 0\,, \end{cases} \tag{3.43}$$

leads to the expressions recorded in Eqs. (3.22)-(3.24).

3.6 Perturbation vs. iteration

For completeness, we calculated selected models also by means of the iteration method described in Section 2.5.2, in order to verify the quality of the solution obtained with the method of matched asymptotic expansions, in particular in the critical regime. This technique follows the approach proposed by Prendergast & Tomer (1970). The basic idea is to get an improved solution of the Poisson equation (see Eq. (2.77) in Chapter 2) by evaluating the right-hand side with the solution obtained from the immediately previous step, starting from the spherical King models taken as initial "seed solutions". In our code, the required spherical harmonic analysis and synthesis of density and potential have been performed by means of the S2kit 1.0 package (Kostelec & Rockmore 2004), which makes use of FFTW 3.2.1 (Frigo & Johnson 2005). We decided to truncate the harmonic series at $l = 4$ in order to be consistent with the maximum harmonic index admitted by the second-order asymptotic solution. The iteration stops when convergence to four significant digits in the whole domain of the solution is reached.

For selected values of the concentration parameter in the range $0.1 \leq \Psi \leq 10$ (for simplicity, we considered only the case of an external potential with $\nu = 3$), the corresponding critical value of the tidal strength parameter obtained with the iteration method is consistent to 10^{-3} with the value determined by the numerical solution of Eq. (3.8), in which the constants obtained from the asymptotic matching are used. For a critical model up to 20 iteration steps are required for convergence, while a subcritical solution typically takes in 4 to 8 steps.

3.7 Discussion and conclusions

3.7.1 A comment on the complex structure of the outer regions

In Chapter 2 we have noted the singular character of the mathematical problem associated with the free boundary set by the three-dimensional surface of these tidally truncated models. In Section 3.2 of the present Chapter, we have further emphasized the additional singularity that characterizes close-to-critical models (see comment after Eq. (3.7)). As is true in general in the study of boundary layers and similar problems, it is no wonder that in the vicinity of such critical boundaries, a number of complex physical effects may take place and play an important role in determining the detailed structure of the solution. On the other hand, the properties of the derived solution away from the boundary are quite robust (see Sections 3.3 and 3.5). As to some of the subtle properties of the expected distribution function close to the edge of a cluster, it is interesting to summarize here below the main results that emerge from a vast body of evolutionary models (N-body, Fokker-Planck, Monte Carlo, gas), on the issue of the interplay between pressure anisotropy and tidal effects.

Since the first solutions of the Fokker-Planck equation by means of a Monte Carlo approach, as described by Hénon (1971) or Spitzer & Hart (1971), it has been shown that one-component *isolated spherical* clusters, starting from a variety of initial conditions (see Spitzer 1987, chap.4 and references therein), develop a core-halo structure in which the central parts are almost isotropic while the outer regions are characterized by *radial* anisotropy. A commonly reported interpretation is that the halo is mainly populated by stars scattered out from the core on radial orbits. If the evolution of a cluster is influenced not only by internal processes but also by the presence of an external tidal field, the growth of pressure anisotropy is significantly damped. Direct N-body simulations (e.g., see Giersz & Heggie 1997; Aarseth & Heggie 1998; Baumgardt & Makino 2003; Lee et al. 2006b), anisotropic Fokker-Planck (e.g., see Takahashi et al. 1997b), and Monte Carlo models (e.g., see Giersz 2001) of both single and multi-mass systems suggest that clusters in circular orbits (and even in eccentric orbits, see Baumgardt & Makino 2003), starting from isotropic initial conditions, tend to preserve pressure isotropy, except for the outermost parts which become *tangentially* anisotropic due to the preferential loss of stars on radial orbits, induced by the tidal field. The overall agreement on this result is nontrivial, because of the aforementioned differences in the treatment of the external tidal field. Even extreme cases of time-dependent tides, such as disk shocking, influence the degree of pressure anisotropy since it has been shown that they may represent a dominant mechanism ("shock relaxation") of the energy redistribution, leading to a substantial isotropy, of the weakly bound stars (see Oh & Lin 1992; Kundic & Ostriker 1995, both papers are based on a Fokker-Planck approach).

These results confirm that, of course, the properties of the models constructed in Chapter 2 and described here should be taken only as a zeroth-order reference frame, to single out the precise role of external tides, and should not be taken literally as a realistic representation of real objects since a number of simplifying assumptions are made. On the other hand, by comparing data with such an idealized reference model it will be possible to better assess the role of tides with respect to other physical ingredients studied separately.

3.7.2 Summary and concluding remarks

The main results that we have obtained from the detailed analysis of the family of tidal triaxial models can be summarized as follows:

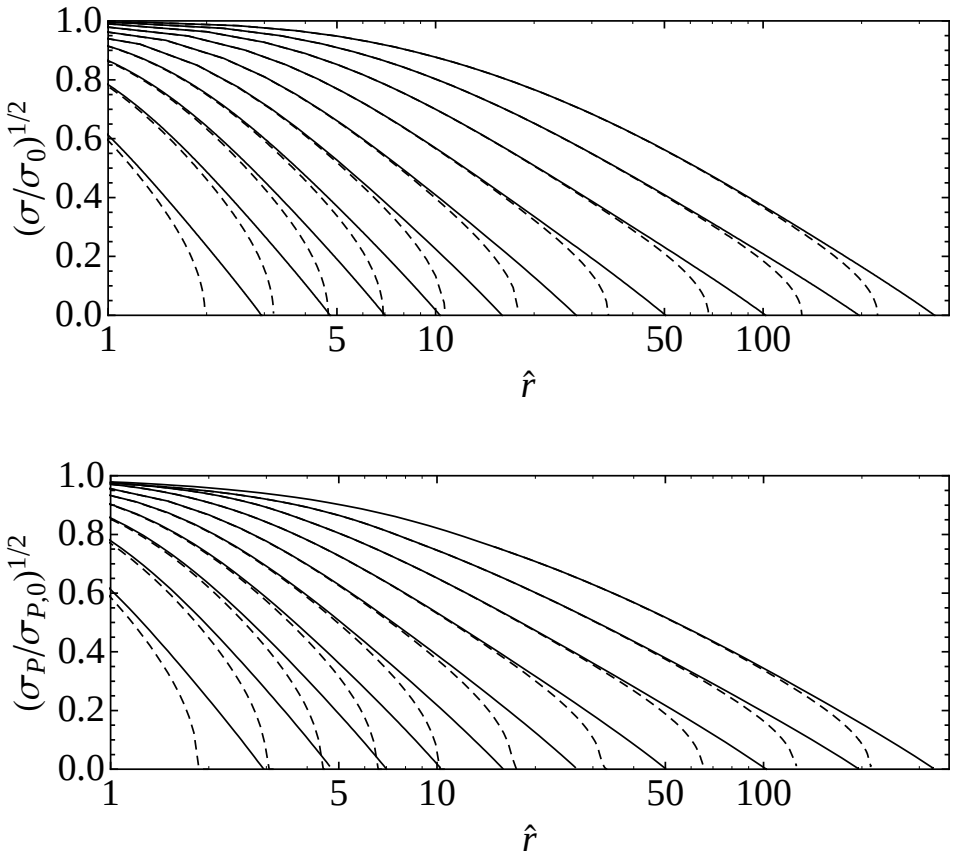

Figure 3.11: Top panel (a): intrinsic velocity dispersion profiles (solid, normalized to the central value) along the $\hat{x}$ axis for the same ten second-order critical models illustrated in Fig. 3.3.a compared to the corresponding spherical King models (dashed). Bottom panel (b): projected velocity dispersion profiles (normalized to the central value) for the same ten second-order critical models illustrated in Fig. 3.10.a, viewed along the same direction. Solid and dashed lines show the profiles along the $\hat{x}_P$ axis and $\hat{y}_P$ of the projection plane, respectively.

- Two tidal regimes exist, namely of low and high-deformation, which are determined by the combined effect of the tidal strength of the field and of the concentration of the cluster. The degree of deformation increases with the degree of filling of the relevant Roche volume. Far from the condition of Roche volume filling, the models are almost indistinguishable from the corresponding spherical King models. A number of studies have investigated the evolution of tidally perturbed stellar systems initially underfilling their Roche lobe (e.g., see Gieles & Baumgardt 2008; Vesperini et al. 2009), concluding that some of the relevant dynamical processes, in particular evaporation, depend on the degree of filling of the Roche volume. The intrinsic properties of the models discussed in this Chapter can be useful for setting self-consistent nonspherical initial conditions of numerical simulations aiming at studying in further details the evolution of configurations starting from

sub-critical tidal equilibria.

- For a given tidal strength, there exists a maximum value of concentration for which a closed configuration is allowed (see Fig. 3.1). In such "critical" case, the truncation radius of the corresponding spherical King models is of the same order of the tidal radius of the triaxial model. The shape of the boundary of the maximally deformed models is given by the "critical" zero-velocity surface of the relevant Jacobi integral and is basically independent of concentration, while the deformation of the internal region strongly depends on the value of the critical tidal strength and is more significant for low-concentration models. This statement agrees with a general trend noted by White & Shawl (1987) for the globular cluster system of our Galaxy.

- The structure of the models can be described in terms of the polar and equatorial eccentricity profiles of the intrinsic isodensity surfaces. The maximal departures from spherical symmetry are reached in the outskirts.

- For finite tidal strength, the central values of the polar and equatorial eccentricities are finite, $\mathcal{O}(\epsilon^{1/2})$; this result is nontrivial since the tidal potential which induces the perturbation is a quadratic homogeneous function of the spatial coordinates.

- Global measures of the degree of triaxiality in terms of the quadrupole moment tensor have been introduced and calculated for different values of the tidal strength and different potentials of the host galaxy. The potential of the host galaxy sets the geometry of the tidal perturbation, as nicely shown by the analytic expressions for the ratios of the components of the quadrupole moment tensor, which, in the case of first-order models, reduce to simple functions of the coefficient ν. Average eccentricities have been calculated from the inertia tensor components, evaluated numerically.

- As a key step in the direction of a comparison with observations, projected density profiles and ellipticity profiles have been calculated for a number of models for several lines of sight.

- The study of the relevant (projected) isophotes indicates that no isophotal twisting occurs. This result is nontrivial since the models are nonstratified and centrally-concentrated, conditions under which, in principle, isophotal twist may occur (see Stark (1977); models based on Stäckel potentials are also known to be twist-free, as shown by Franx (1988)).

- Finally, close to the boundary, the intrinsic and projected kinematics shows significant differences with respect to that of spherical models.

Since our models are all characterized by monotonically increasing ellipticity profiles, they cannot explain the variety of behavior of observed ellipticity profiles (see Geyer et al. 1983), but the range of the predicted flattening ($\varepsilon < 0.3$) is consistent with that observed in most globular clusters (see White & Shawl (1987) for the clusters in the Milky Way and Frenk & Fall (1982) for those in the LMC). Therefore, with the exception of special clusters such as Omega Centauri, we think that the modest but frequently observed deviations from spherical symmetry might have their origin traced to tides.

Finally, since our models are intrinsically more elongated (in the direction of the center of the host galaxy) than spherical King models, they might be useful for interpreting

clusters with a surface brightness profile extending beyond that predicted by the spherical King models. Recent investigations (see McLaughlin & van der Marel 2005) suggest that such "extra-tidal" structures are a fairly generic feature, especially for extragalactic clusters, and not just a transient property, present only at young ages.

Part II
Internal Rotation

CHAPTER 4

New self-consistent rotating equilibria

4.1 Introduction

In the present Chapter, we consider two families of axisymmetric rotating models: the first one is characterized by the presence of solid-body rotation and isotropy in velocity space. Indeed, full relaxation in the presence of nonvanishing total angular momentum suggests the establishment of solid-body rotation through the dependence of the relevant distribution function $f = f(H)$ on the Jacobi integral $H = E - \omega J_z$ (see Landau & Lifshitz 1969). But, for applications to real stellar systems, one may take advantage of the fact that the collisional relaxation time may be large in the outer regions, so that in the outer parts the constraint of solid-body rotation might be released. In particular, for globular clusters we may argue that the outer parts fall into a tide-dominated regime, for which evaporation tends to erase systematic rotation even if initially present, as confirmed by previous studies based on the Fokker-Planck method (Goodman 1983; Einsel & Spurzem 1999; Kim et al. 2002; Fiestas et al. 2006). For the truncation, we may then consider a heuristic prescription to simulate the effects of tides, much like for the spherical King models.

In view of possible applications to globular clusters, we thus consider a second class of axisymmetric rotating models based on a distribution function dependent only on the energy and on the z-component of the angular momentum $f = f(I)$ where $I = I(E, J_z)$, with the property that $I \sim E$ for stars with relatively high z-component of the angular momentum, while $I \sim H = E - \omega J_z$ for relatively low values of J_z. Such models are indeed defined in order to have differential rotation, designed to be rigid in the center and to vanish in the outer parts, where the energy truncation becomes effective. As far as the velocity dispersion is concerned, this family may show a variety of profiles (depending on the values of the relevant free parameters), all of them characterized by the presence of isotropy in the central region. We thus add two classes of self-consistent models to the relatively short list of rotating stellar dynamical models currently available.

One aspect that plays an important role in defining a physically motivated distribution function, which often goes unnoticed (but see Hunter 1977, Davoust 1977, and Rowley 1988), is the choice of the truncation prescription in phase space. The advantages and the limitations of alternative options available for the second family of models will be discussed in detail. In this context, we will also address the issue of whether these differentially rotating models fall within the class of systems for which rotation is constant on cylinders.

The Chapter is structured as follows. The properties of the family of rigidly rotating models, constructed on the basis of general statistical mechanics considerations, are illustrated in Sect. 4.2. The family of differentially rotating models, designed for the

application to rotating globular clusters, is introduced in Sect. 4.3, where we briefly describe the method used for the solution of the self-consistent problem and discuss the relevant parameter space. Section 4.4 is devoted to a study of the intrinsic properties and Sect. 4.5 to the projected observables derived from differentially rotating models.

After illustrating in Sect. 4.6 the effect of different truncation prescriptions in phase space, a discussion of the spherical nonrotating limit of our families of models in presented in Sect. 4.7, and the details of the alternative truncation option for the second family are recorded in Sect. 4.8. We summarize the results and present our conclusions in Sect. 4.9.

4.2 Rigidly rotating models

4.2.1 The distribution function

The construction of rigidly rotating configurations characterized by nonuniform density is a classical problem in the theory of rotating stars, starting with Milne (Milne 1923; Chandrasekhar 1933), but it basically remained limited to the study of a fluid with polytropic equation of state, for which the solution of the relevant Poisson equation can be obtained by means of a semi-analytical approach (for a comprehensive description, see Chaps. 5 and 10 in Tassoul (1978); for an enlightening presentation of the general problem of rotating compressible masses, see Chap. 9 in Jeans 1928). The reader is referred to Chapter 2 for a discussion of the application of some of the mathematical methods developed in that context to the construction of nonspherical truncated self-consistent stellar dynamical models. The deviations from spherical symmetry studied in Chapter 2 are induced by the presence of a stationary perturbation characterized by a quadrupolar structure, that is, either an external tidal field or internal solid-body rotation.

It is well known that in the presence of finite total angular momentum of the system, relaxation leads to solid-body rotation (e.g., see Landau & Lifshitz 1969). If we denote by ω the angular velocity of such rigid rotation and assume that it takes place around the z axis, in the statistical mechanical argument that leads to the derivation of the Maxwell-Boltzmann distribution one finds that in the final distribution function the single particle energy E is replaced by the quantity $E - \omega J_z$. Following this picture, we may consider the extension of King models to the case of internal rigid rotation. This extension is conceptually simpler than that addressed in Chapter 2, because the perturbation associated with internal rotation, while breaking spherical symmetry, preserves axial symmetry. We note that the models described below differ from those studied by Kormendy & Anand (1971), which were characterized by a different, discontinuous truncation, and those by Prendergast & Tomer (1970) and by Wilson (1975), which were characterized by a different truncation prescription and by differential rotation.

The relevant physical model is that of a rigidly rotating isolated globular cluster characterized by angular velocity $\boldsymbol{\omega} = \omega \hat{e}_z$, with respect to a frame of reference with the origin in the center of mass of the cluster. We then introduce a second frame of reference, co-rotating with the cluster, in which the position vector is given by $\mathbf{r} = (x, y, z)$. In such rotating frame, the Lagrangian describing the motion of a star belonging to the cluster is given by:

$$\mathcal{L} = \frac{1}{2}(\dot{x}^2 + \dot{y}^2 + \dot{z}^2 + 2\omega \dot{y} x - 2\omega \dot{x} y) - \Phi_{cen}(x, y) - \Phi_C(x, y, z) \, , \tag{4.1}$$

where $\Phi_{cen}(x, y) = -(x^2 + y^2)\omega^2/2$ is the centrifugal potential; the energy integral of the

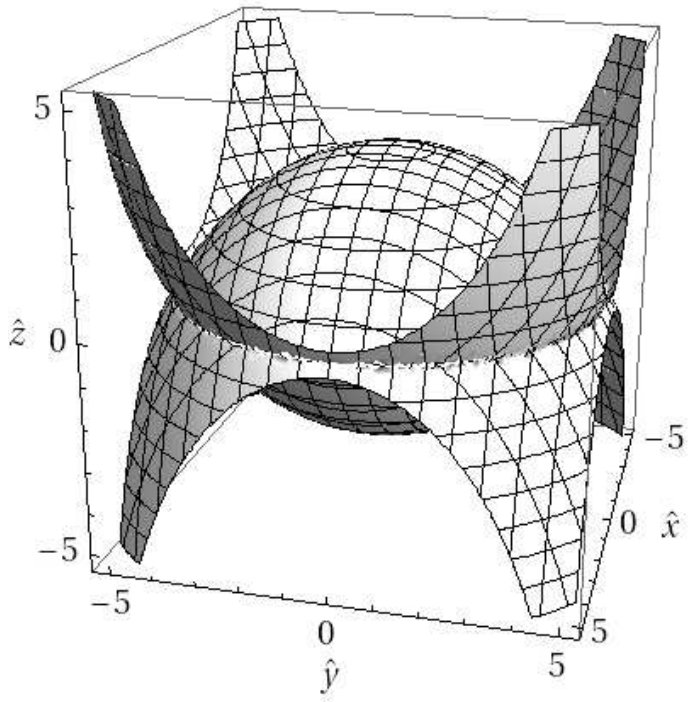

Figure 4.1: The boundary surface, defined implicitly by $\psi(\hat{\mathbf{r}}) = 0$, of a critical second-order rigidly rotating model with $\Psi = 2$. The configuration is axisymmetric; the points on the equatorial plane are saddle points (see Sect. 4.2.2 for details). Rotation takes place around the $\hat{z}$-axis. The spatial coordinates are expressed in appropriate dimensionless units (see Eq. (4.6)).

motion (called the Jacobi integral) is:

$$H = \frac{1}{2}(\dot{x}^2 + \dot{y}^2 + \dot{z}^2) + \Phi_{cen} + \Phi_C \ . \tag{4.2}$$

As in the tidal case, the extension of the family of King models is performed by considering the distribution function:

$$f_K^r(H) = A\mathrm{e}^{-aH_0}\left[\mathrm{e}^{-a(H-H_0)} - 1\right] \tag{4.3}$$

for $H \leq H_0$ and $f_K^r(H) = 0$ otherwise, where

$$H = E - \omega J_z \tag{4.4}$$

denotes the Jacobi integral, with ω the angular velocity of the rigid rotation (hence the superscript r), assumed to take place around the $z-$axis. The quantities E and J_z are the specific one-star energy and z-component of the angular momentum, H_0 represents a cut-off constant of the Jacobi integral, while A and a are positive constants. The dimensionless energy is defined by:

$$\psi(\mathbf{r}) = a\{H_0 - [\Phi_C(\mathbf{r}) + \Phi_{cen}(x, y)]\} \ , \tag{4.5}$$

and the boundary of the cluster, implicitly defined as $\psi(\mathbf{r}) = 0$, is an equipotential surface for the total potential $\Phi_C + \Phi_{cen}$. Its geometry, reflecting the properties of the centrifugal potential, is characterized by symmetry with respect to the z-axis and reflection symmetry with respect to the equatorial plane (x, y). The constant ψ family of surfaces, much like the Hill surfaces of the tidal case, is characterized by a *critical* surface which distinguishes the closed from the opened ones and in which the points on the equatorial plane are all saddle points. Note that, by construction, in the limit of vanishing internal rotation, this family of models reduces to the family of spherical King (1966) models (see Section 4.7 for a summary of the main properties of the family in the nonrotating limit).

The construction of the models requires the integration of the associated nonlinear Poisson equation, which, after scaling the spatial coordinates with respect to the scale length

$$r_0 = \left(\frac{9}{4\pi G \rho_0 a} \right)^{1/2} , \tag{4.6}$$

can be written as

$$\hat{\nabla}^2 \psi^{(int)} = -9 \left[\frac{\hat{\rho}_K(\psi^{(int)})}{\hat{\rho}_K(\Psi)} - 2\chi \right] , \tag{4.7}$$

where

$$\chi \equiv \frac{\omega^2}{4\pi G \rho_0} \tag{4.8}$$

is the dimensionless parameter that characterizes the rotation strength and

$$\Psi \equiv \psi^{(int)}(\mathbf{0}) \tag{4.9}$$

is the depth of the potential well at the center. The dimensionless density profile is given by

$$\hat{\rho}_K(\psi) = \frac{\rho_K(\psi)}{\hat{A}} = \mathrm{e}^{\psi} \gamma \left(\frac{5}{2}, \psi \right) , \tag{4.10}$$

where

$$\hat{A} = \frac{8\pi 2^{1/2} A}{3a^{3/2}} \mathrm{e}^{-aH_0} \tag{4.11}$$

and γ denotes the incomplete gamma function. Therefore, the central density is given by $\rho_0 = \hat{A}\hat{\rho}_K(\Psi)$. Outside the cluster, for negative values of ψ, we should refer to the Laplace equation

$$\hat{\nabla}^2 \psi^{(ext)} = 18\chi \, . \tag{4.12}$$

The relevant boundary conditions are given by the requirement of regularity of the solution at the origin and by the condition that $\psi^{(ext)} + a\Phi_{cen} \to aH_0$ at large radii. The Poisson (internal) and Laplace (external) domains are thus separated by the boundary surface, which is unknown *a priori*. Therefore, we have to solve an elliptic partial differential equation in a free boundary problem. In particular, here we illustrate the properties of the solutions of the Poisson-Laplace equation obtained by using a perturbation method, which also requires an expansion of the solution in Legendre series. To obtain a uniformly valid solution over the entire space, an asymptotic matching is performed between the internal and the external solution, using the Van Dyke principle (see Van Dyke Van Dyke (1975)). This method of solution is basically the same as proposed by Smith (1975) for the construction of rotating configurations with polytropic index $n = 3/2$. We

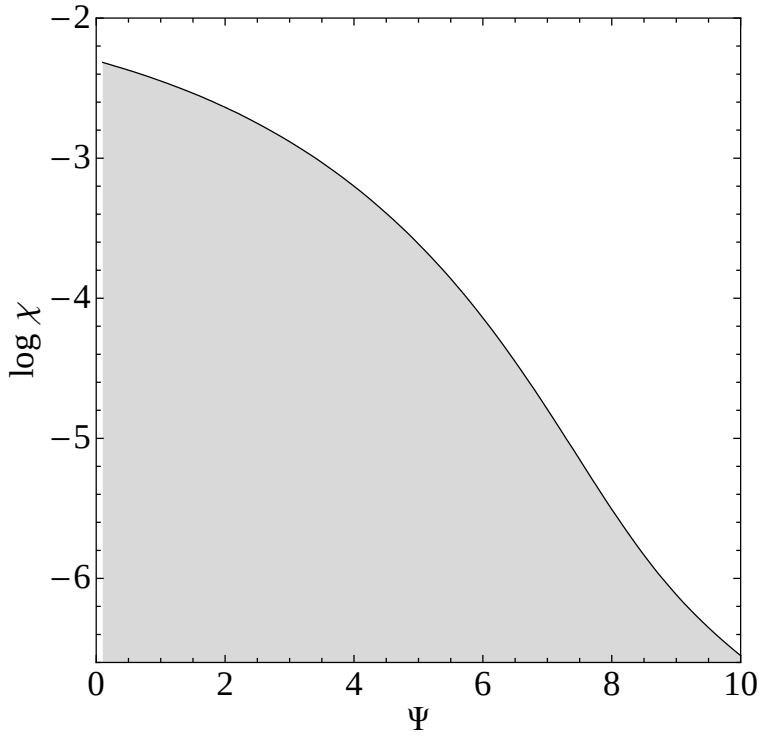

Figure 4.2: Parameter space for second-order rigidly rotating models. The solid line represents the critical values of the rotation strength parameter χ_{cr} and the grey region identifies the values (Ψ, χ) for which the resulting models are bounded by a closed constant-ψ surface (subcritical models).

have calculated the complete solution up to second-order in the rotation strength parameter χ. The final solution is expressed in spherical coordinates $\hat{\mathbf{r}} = (\hat{r}, \theta, \phi)$ and the resulting configurations are characterized by axisymmetry (i.e., the density distribution and the potential do not depend on the azimuthal angle ϕ). For the details of the method for the construction of the solution the reader is referred to Appendix A.5, in which the complete calculation is provided.

4.2.2 The parameter space

The resulting models are characterized by two dimensional scales (e.g., the total mass and the core radius) and two dimensionless parameters. As in the spherical King models, the first parameter measures the *concentration* of the configuration; we thus consider the quantity[1] Ψ (see Eq. (4.9)) or equivalently $c \equiv \log(r_{tr}/r_0)$, where r_{tr} is the truncation radius of the spherical King model associated with a given value of Ψ. The second dimensionless parameter χ (see Eq. (4.8)) characterizes the *rotation strength* measured in terms of the frequency associated with the central density of the cluster.

For every value of the dimensionless central concentration Ψ there exists a maximum value of the rotation strength parameter, corresponding to a critical model, for which the

[1] In the literature, the parameter Ψ is often denoted by W_0.

boundary is given by the critical constant-ψ surface. The boundary surface of a representative critical model (with $\Psi = 2$) is depicted in Fig. 4.1; the surface is such that all the points on the equatorial plane are saddle points, where the centrifugal force balances the self-gravity. We refer to their distance from the origin as $\hat{r}_B$, the *break-off radius*. In the constant-ψ family of surfaces associated with a given value of Ψ, the critical surface thus separates the open from the closed surfaces. Consistent with the assumption of stationarity, only configurations bounded by closed surfaces are considered here. This unique geometrical characterization suggests that the effect of the rotation may be expressed also in terms of an *extension* parameter

$$\delta = \frac{\hat{r}_{tr}}{\hat{r}_B} \, , \tag{4.13}$$

which provides an indirect measure of the deviations from sphericity of a configuration, by considering the ratio between the truncation radius of the corresponding spherical King model and the break-off radius of the associated critical surface. Therefore, a given model may be labelled by the pair (Ψ, χ) or equivalently by the pair (Ψ, δ). For a given Ψ, there is thus a maximum value of the allowed rotation, which we may express as χ_{cr} or δ_{cr}. A model with $\delta < \delta_{cr}$ may be called subcritical.

For each value of Ψ, the critical value of the rotation parameter can be found by numerically solving the system[2]

$$\begin{cases} \partial_{\hat{r}} \, \psi(\hat{r} = \hat{r}_B, \theta = \pi/2; \chi_{cr}) = 0 \\ \psi(\hat{r} = \hat{r}_B, \theta = \pi/2; \chi_{cr}) = 0 \, , \end{cases} \tag{4.14}$$

where the unknowns are $\hat{r}_B$ and χ_{cr}. In terms of the extension parameter, for a given Ψ, the critical condition occurs when $\delta = \delta_{cr} = \hat{r}_{tr}/\hat{r}_B \approx 2/3$. This value is obtained by inserting in Eq. (4.14) the zeroth-order expression for the cluster potential, as discussed in detail in Sect. 3.2 of Chapter 3 for the tidal problem (see p. 251-255 in Jeans 1928 for an equivalent discussion referred to the purely rotating Roche model, that is a rotating configuration in which a small region with infinite density is surrounded by an "atmosphere" of negligible mass).

The parameter space for the second-order models is presented in Fig. 4.2 (which corresponds to Fig. 3.1 of Chapter 3 describing the tidal models). Two rotation regimes exist, namely the regime of low-deformation ($\delta \ll \delta_{cr}$, bottom left corner), where internal rotation does not affect significantly the morphology of the configuration, which remains very close to spherical symmetry, and that of high-deformation ($\delta \approx \delta_{cr}$, close to the solid line), where the model is highly affected by the nearly critical rotation velocity, especially in the outer parts. Note that the actual regime depends on the combined effect of rotation strength and of concentration. In other words, the models described here belong to the class of rotating configurations characterized by equatorial break-off ("region of equatorial break-off", see Fig. 44, p. 267 in Jeans 1928), for which the limiting case is given by the purely rotating Roche model.

[2]For brevity, here we omit the explicit structure of the system. The reader is referred to Eqs. (3.8)-(3.14) in Chapter 3, with respect to which several differences occur, because in the axisymmetric rotation problem the coefficients of the asymptotic series are best expanded in (normalized) Legendre polynomials (rather than spherical harmonics). In particular, with respect to Chapter 3: (i) the coefficients with $m \neq 0$ must be dropped; (ii) the coefficients with $l \neq 0$ must be multiplied by the factor $(\pi/4)^{1/2}$, because of the different normalization used in the two systems of orthonormal functions; (iii) the expressions are evaluated at $\hat{r}_B$ instead of $\hat{r}_T$. As in Chapter 2, for the definition of the Legendre polynomials we refer to Eqs. (22.3.8) and (22.2.10) of (Abramowitz & Stegun 1965).

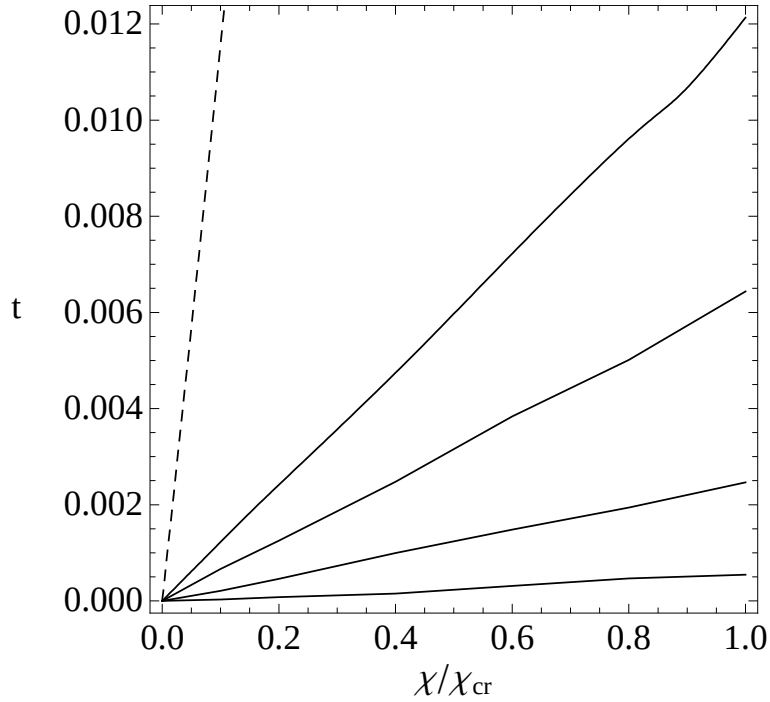

Figure 4.3: Values of the ratio between ordered kinetic energy and gravitational energy $t = K_{ord}/|W|$ for selected rigidly rotating models characterized by $\Psi = 1, 3, 5, 7$ (solid lines, from top to bottom) and χ in the range $[0, \chi_{cr}]$. For comparison, the dashed line indicates the values of t for the sequence of Maclaurin oblate spheroids in the limit of small eccentricity.

A global kinematical characterization, complementary to the information provided by the rotation strength parameter χ, is offered by the parameter $t = K_{ord}/|W|$, defined as the ratio between ordered kinetic energy and gravitational energy. Figure 4.3 illustrates the relation between the two parameters for models with selected values of Ψ and increasing values of χ, up to the critical configuration characterized by χ_{cr}. The parameter t increases linearly for increasing values of χ (with a slope dependent on the concentration parameter Ψ). A similar linear relation is observed for small values of eccentricity ($e << 1$) in the sequence of Maclaurin oblate spheroids $t(e) \sim \chi(e) \sim 2e^2/15$ (for the definitions of the two parameters in the context of Maclaurin spheroids, see Eqs. (10.20) and (10.24) in Bertin (2000)); in Fig. 4.3 the relevant linear relation is normalized with respect to the maximum value of the rotation strength parameter attained in the sequence of Maclaurin spheroids $\chi_{max} = 0.11233$ (see Eq. (10), p. 80 in Chandrasekhar 1969).

4.2.3 Intrinsic properties

The geometry of the models, reflecting the properties of the centrifugal potential, is characterized by symmetry around the $\hat{z}$-axis and reflection symmetry with respect to the equatorial plane $(\hat{x}, \hat{y})$. As expected, compared to the corresponding spherical King models, the rotating models stretch out on the equatorial plane and are slightly flattened along the direction of the rotation axis (see Fig. 4.4 for the density profiles of selected critical second order models evaluated on the equatorial plane and along the $\hat{z}$-axis). In

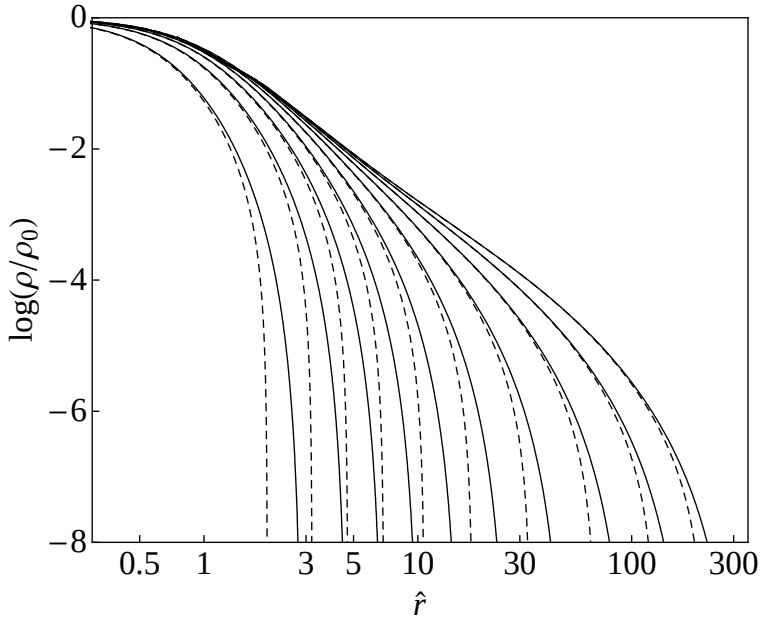

Figure 4.4: Intrinsic density profiles (normalized to the central value) evaluated on the equatorial plane (solid lines) and along the $\hat{z}$-axis (dashed lines) for critical second-order rigidly rotating models with $\Psi = 1, 2, ..., 10$ (from left to right).

general, configurations in the low-deformation regime ($\delta \ll \delta_{cr}$), regardless of the value of concentration Ψ, are almost indistinguishable from the corresponding spherical King models.

Models in the intermediate and high-deformation regime ($\delta \approx \delta_{cr}$) show modest deviations from spherical symmetry in the central regions, while they are significantly flattened in the outer parts. The intrinsic eccentricity profile, defined as $e = [1 - (\hat{b}/\hat{a})^2]^{1/2}$, where $\hat{a}$ and $\hat{b}$ are semi-major and semi-minor axes of the isodensity surfaces, is a monotonically increasing function of the semi-major axis (see Fig. 4.5 for the eccentricity profiles of selected critical second-order models). We recall that the geometry of the boundary surface of a critical model depends only slightly on the value of the concentration parameter. In particular, in the critical case, the break-off radius $\hat{r}_B$ represents the distance from the center of the outermost points of the boundary surface on the equatorial plane and the truncation radius $\hat{r}_{tr}$ is approximately the distance of the last point on the polar axis (i.e., the $\hat{z}$-axis). Therefore, since $\delta_{cr} = \hat{r}_{tr}/\hat{r}_B \approx 2/3$, the value of the termination points of the eccentricity profiles of critical models is approximately the same ($e \approx 0.75$; see the termination points of the solid lines in Fig. 4.5).

In addition, by using the multipolar structure of the solution of the Poisson-Laplace equation obtained with the perturbation method, the asymptotic behavior of the eccentricity profiles in the central regions can also be evaluated analytically. Since the distribution function depends only on the Jacobi integral (i.e., the isolating energy integral in the corotating frame of reference), the density and the velocity dispersion profiles are functions of only the escape energy (see Eqs. (4.10) and (4.19), respectively). Therefore, there is a one-to-one correspondence between equipotential, isodensity, and isobaric surfaces and the eccentricity profiles can be calculated with reference to just one of these families

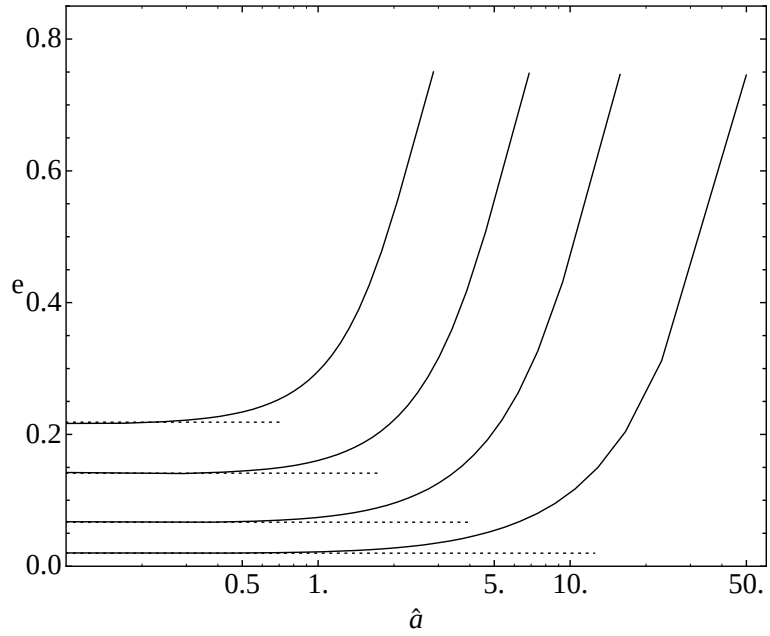

Figure 4.5: Eccentricity profiles of the isodensity surfaces for selected critical second-order rigidly rotating models, with $\Psi = 1, 3, 5, 7$ (from top to bottom); dotted horizontal lines show the central eccentricities values estimated analytically (see Eq. (4.16)).

of surfaces. In fact, if expanded to second order in the dimensionless radius, the escape energy in the internal region reduces to:

$$\begin{aligned} \psi^{(int)}(\hat{r},\theta) &= \Psi + \frac{1}{2}\left[-3 + 6\chi + 2A_2 U_2(\theta)\,\chi + \right. \\ &\quad \left. (B_2+1)U_2(\theta)\chi^2\right]\hat{r}^2 + \mathcal{O}(\hat{r}^4)\,, \end{aligned} \tag{4.15}$$

where $U_2(\theta)$ denotes the normalized Legendre polynomial with $l = 2$ and A_2, B_2 are appropriate (negative) coefficients, depending on Ψ, which are determined by asymptotically matching the internal and external solution, in order to have continuity on the entire domain (see Eqs. (2.62) and (2.68) in Chapter 2, to be interpreted as indicated in Appendix A.5). By setting $\psi^{(int)}(\hat{a}, \pi/2) = \psi^{(int)}(\hat{b}, 0)$, we thus find that, in the innermost region, the eccentricity tends to the following nonvanishing central value

$$e_0 = \frac{[6A_2\,\chi + 3(B_2+1)\,\chi^2]^{1/2}}{[6\sqrt{2/5}(2\chi-1) + 4A_2\,\chi + 2(B_2+1)\,\chi^2]^{1/2}}\,. \tag{4.16}$$

Therefore, the central value of the eccentricity is finite, of order $\mathcal{O}(\chi^{1/2})$, and strictly vanishes only in the limit of vanishing rotation strength. This result is nontrivial because the centrifugal potential (which induces the deviations from sphericity) is a homogeneous function of the spatial coordinates. Therefore, we might naively expect that, in their central regions, the models reduce to a perfectly spherical shape (i.e., $e_0 = 0$), even for finite values of the rotation strength. This property has been noted also in the family of triaxial

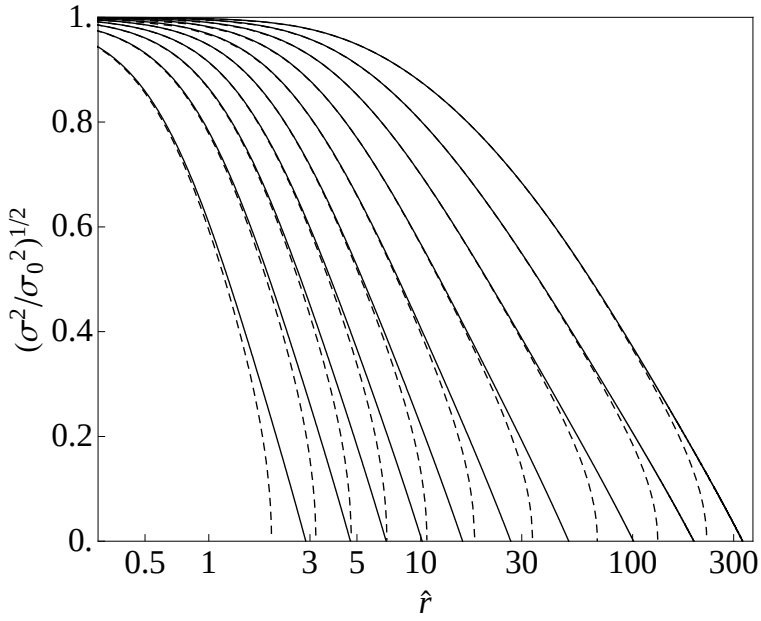

Figure 4.6: Intrinsic velocity dispersion profiles (normalized to the central value) evaluated on the equatorial plane (solid lines) and along the $\hat{z}$-axis (dashed lines) for selected critical second-order rigidly rotating models with $\Psi = 1, 2, ..., 10$ (from left to right).

tidal models, in which the tidal potential plays the role of the centrifugal potential (see Sect. 3.3.1 of Chapter 3).

Deviations from spherical symmetry can also be described, in a global way, by the quadrupole moment tensor, defined as

$$\begin{aligned} Q_{ij} &= \int_V (3x_i x_j - r^2\delta_{ij})\rho(\mathbf{r})d^3r = \\ &\hat{A}r_0^5 \int_V (3\hat{x}_i\hat{x}_j - \hat{r}^2\delta_{ij})\hat{\rho}(\hat{\mathbf{r}})d^3\hat{r} = \hat{A}r_0^5\hat{Q}_{ij} \ , \end{aligned} \tag{4.17}$$

where the integration is performed in the volume V of the entire configuration. It can be easily shown that in our coordinate system the tensor is diagonal and that $Q_{xx} = Q_{yy}$. The components of the tensor can be calculated explicitly

$$\hat{Q}^{(2)}_{xx} = \hat{Q}^{(2)}_{yy} = -\frac{\hat{Q}^{(2)}_{zz}}{2} = 2\pi\frac{\sqrt{10}}{9}\hat{\rho}_K(\Psi)\left(a_2\chi + b_2\frac{\chi^2}{2}\right) \ , \tag{4.18}$$

The quantities a_2 and b_2 are appropriate (positive) coefficients, depending on Ψ, resulting from the asymptotic matching of the internal and external solution of the Poisson-Laplace equation. The sign of the components are consistent with the above mentioned compression and stretching of the density distribution. The expression in Eq. (4.18) is calculated from the second-order external solution; the first-order expression is recovered by dropping the quadratic term in the parameter χ. At variance with the tidal case, the ratio $\hat{Q}_{zz}/\hat{Q}_{xx}$ is independent of the rotation parameter χ. This analytical result has

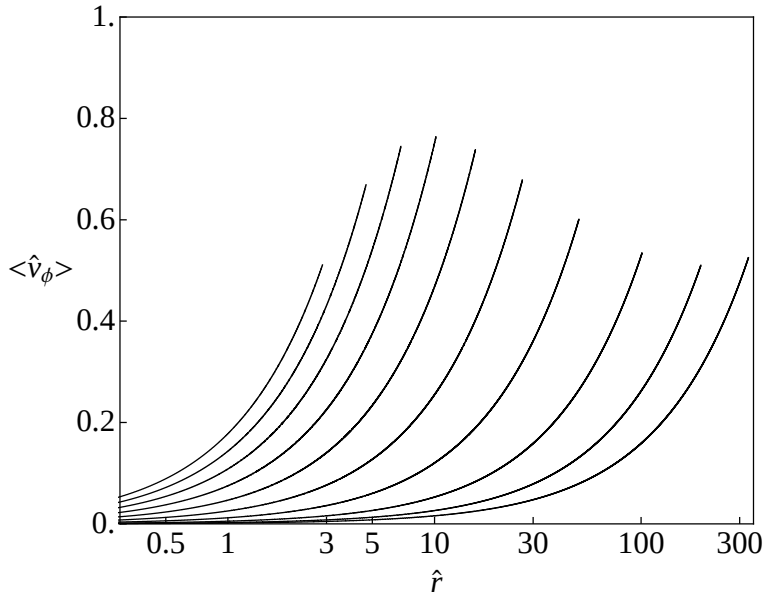

Figure 4.7: Mean rotation velocity profiles on the equatorial plane for the selected critical second-order rigidly rotating models with $\Psi = 1, 2, ..., 10$ (from left to right). The mean velocity increases linearly with radius because the rotation is rigid (see Eq. (4.20); note the logarithmic scale of the horizontal axis). The values of the termination points of the curves depend on the value of χ_{cr} (which decreases as Ψ increases, see Fig. 4.2) and on the extension of the models on the equatorial plane (which increases as Ψ increases, see Fig. 4.4).

been compared to the ratio of the components of the quadrupole tensor determined by direct numerical integration (performed by means of the algorithm VEGAS, see Press et al. 1992) and good agreement has been found. [3] For the tidal case, the detailed calculation can be found in Sects. 3.3 and 3.5 of Chapter 3; such calculation is easily adapted to the rotating case.

By construction, the models are isotropic in velocity space, with the dimensionless scalar velocity dispersion given by

$$\hat{\sigma}_K^2(\psi) = \frac{2}{5}\frac{\gamma(7/2,\psi)}{\gamma(5/2,\psi)} \,. \tag{4.19}$$

As noted for the intrinsic density profiles, a compression along the vertical axis and a stretching along the equatorial plane occur also for the velocity dispersion profiles (the profiles of selected critical second-order models are shown in Fig. 4.6).

The mean rotation velocity (which is subtracted away when the corotating frame of reference is considered) characterizing the models is defined as $\langle \mathbf{v} \rangle = \omega\, \hat{\mathbf{e}}_z \times r\, \hat{\mathbf{e}}_r = \langle v_\phi \rangle \hat{\mathbf{e}}_\phi$; in the adopted dimensionless units, the azimuthal component can be written as

$$\langle \hat{v}_\phi \rangle = \langle v_\phi \rangle a^{1/2} = 3\chi^{1/2} \hat{r} \sin\theta \,. \tag{4.20}$$

[3] Strictly speaking, the analytical expressions for the components of the quadrupole moment tensor refer only to the inner region, because the contribution from the boundary layer, where ψ is of order $\mathcal{O}(\chi)$, is neglected.

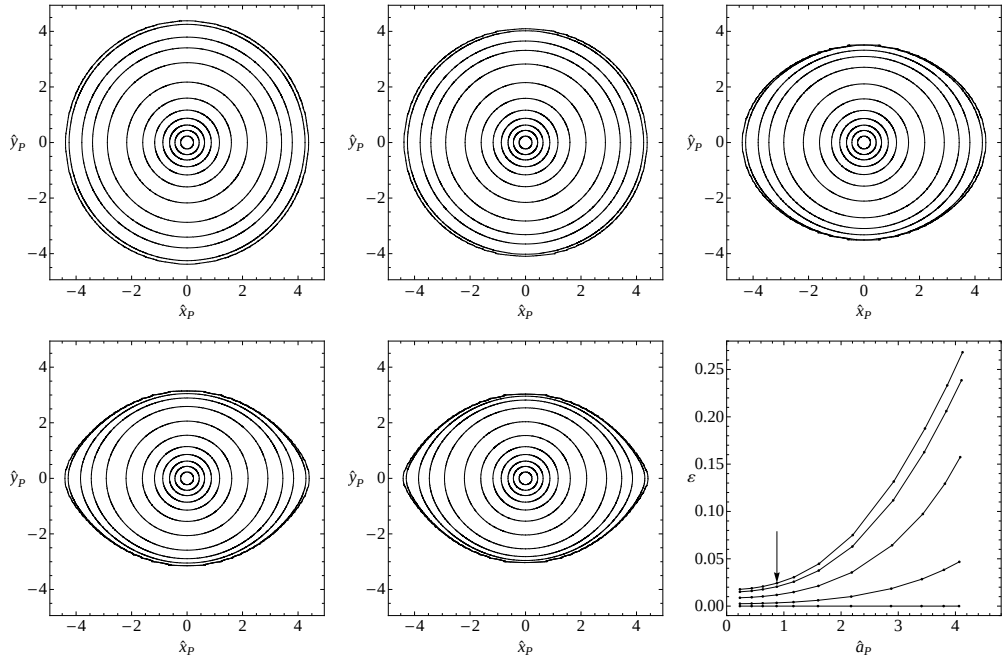

Figure 4.8: Projections along directions identified by $\phi = 0$ and $\theta = i(\pi/8)$ with $i = 0, .., 4$ (from left to right, top to bottom) of a critical second-order rigidly rotating model with $\Psi = 2$; the first and the fifth panel represent the projections along the $\hat{z}$-axis ("face on") and the $\hat{x}$-axis ("edge-on") of the intrinsic coordinate system, respectively. Solid lines mark the isophotes, corresponding to selected values of Σ/Σ_0 in the range $[0.9, 10^{-7}]$. The last panel shows the ellipticity profiles, as functions of the semi-major axis of the projected image $\hat{a}_P$, referred to the lines of sight considered in the previous panels (from bottom to top). Dots represent the locations of the isophotes and the arrow marks the position of the half-light isophote (practically the same for every projection considered in the figure).

As expected, the mean velocity is constant on cylinders (in our coordinate system, the cylindrical radius is defined by $\hat{R} = \hat{r}\sin\theta$). The relevant dimensionless angular velocity is linked to the rotation strength parameter by the following relation $\hat{\omega} = 3\chi^{1/2}$ (the numerical factor 3 is due to the adopted scale length, see Eq. (4.6)). The rotation profiles of selected second-order critical models are represented in Fig. 4.7. For all the models, as we approach the boundary of the configuration, the ratio $\langle\hat{v}_\phi\rangle/\hat{\sigma}_K$ quickly diverges since at the boundary the rotation velocity tends to a finite value while the velocity dispersion vanishes; this behavior is observed in every direction (except for the $\hat{z}$-axis, on which the rotation velocity vanishes by definition).

4.2.4 Projected properties

For a comparison of the models with the observations (under the assumption of a constant mass-to-light ratio), we have then computed surface (projected) density profiles and isophotes. The projection has been performed along selected directions, identified by the viewing angle (θ, ϕ) corresponding to the $\hat{z}_P$ axis of a new coordinate system related to the intrinsic system by the transformation $\hat{\mathbf{x}}_P = R\hat{\mathbf{x}}$; the rotation matrix $R = R_1(\theta)R_3(\phi)$ is expressed in terms of the viewing angles, by taking the $\hat{x}_P$ axis as the

line of nodes (i.e., the same projection rule we adopted for the triaxial tidal models, see Sect. 3.4 in Chapter 3). Since the rigidly rotating models are characterized by axisymmetry with respect to the $\hat{z}$-axis and reflection symmetry with respect to the equatorial plane, it is sufficient to choose the viewing angles from the $(\hat{x}, \hat{z})$-plane of the intrinsic coordinate system. In particular, we used the line of sights defined by $\theta_i = i(\pi/8)$ and $\phi = 0$ with $i = 0, .., 4$, and we calculated (by numerical integration, using the Romberg's rule) the dimensionless projected density

$$\hat{\Sigma}(\hat{x}_P, \hat{y}_P) = \int_{-\hat{z}_{sp}}^{\hat{z}_{sp}} \hat{\rho}(\hat{\mathbf{r}}_P) d\hat{z}_P \ , \tag{4.21}$$

where $\hat{z}_{sp} = (\hat{x}_e^2 - \hat{x}_P^2 - \hat{y}_P^2)^{1/2}$ with $\hat{x}_e$ the edge of the model along the $\hat{x}$ axis of the intrinsic coordinate system. The projection plane $(\hat{x}_P, \hat{y}_P)$ has been sampled on an equally-spaced square cartesian grid centered at the origin.

The first five panels of Fig. 4.8 show the projected images of a critical second-order model with $\Psi = 2$; the first and the fifth panel correspond, respectively, to the least and to the most favorable line of sight for the detection of the intrinsic flattening of the model (the $\hat{z}$ and $\hat{x}$-axis of the intrinsic coordinate system, that is "face-on" and "edge-on" view).

The morphology of the isophotes of a given projected image can be described in terms of the *ellipticity* profile, defined as $\varepsilon = 1 - \hat{b}_P/\hat{a}_P$ where $\hat{a}_P$ and $\hat{b}_P$ are the principal semi-axes, as a function of the semi-major axis $\hat{a}_P$. As already noted for the (intrinsic) eccentricity profile, the deviation from circularity increases with the distance from the origin. In the inner region, the central value of the ellipticity is consistent with the central eccentricity e_0 calculated in the previous subsection. The last panel of Fig. 4.8 illustrates the ellipticity profiles corresponding to the projections displayed in the previous panels. In addition, the isophotes of models in the high deformation regime ($\delta \approx \delta_{cr}$), if projected along appropriate line of sights, show clear departures from a pure ellipse, that can be characterized as a "disky" overall trend (e.g., see Jedrzejewski 1987), particularly evident in the outer parts (see fourth and fifth panels in Fig. 4.8).

Because the family of rigidly rotating models is characterized by simple kinematical properties (pressure isotropy and solid-body rotation), that have been already presented in detail with reference to three-dimensional configurations, for brevity, the derivation of the projected kinematical properties is omitted here.

4.3 Differentially rotating models

4.3.1 Choice of the distribution function

As indicated in the Introduction, theoretical and observational motivations have brought us to look for more realistic configurations, characterized by differential rotation. Thus we focus our attention on axisymmetric systems, within the class of distribution functions that depend only on the energy E and the z-component of the angular momentum J_z, and we consider the integral

$$I(E, J_z) = E - \frac{\omega J_z}{1 + b J_z^{2\,c}} \ , \tag{4.22}$$

where ω, b, and $c > 1/2$ are positive constants. The quantity $I(E, J_z)$ reduces to the Jacobi integral for small values of the z-component of the angular momentum and tends to the

Table 4.1: Summary of the properties of the families of models studied in the present Chapter.

Family of models	Distribution function	Dimensionless parameters	Internal rotation	Anisotropy profile	Isophote shape
$f_K^r(H)$	$A\mathrm{e}^{-aH_0}[\mathrm{e}^{-a(H-H_0)}-1]$	Ψ, χ	solid-body	$(0,0,0)$	disky
$f_{WT}^d(I)$	$A\mathrm{e}^{-aE_0}[\mathrm{e}^{-a(I-E_0)}-1+a(I-E_0)]$	$\Psi, \chi, \bar{b}, c$	differential	$(0,>0,-2)$	boxy
$f_{PT}^d(I)$	$A\mathrm{e}^{-aE_0}\mathrm{e}^{-a(I-E_0)}$	$\Psi, \chi, \bar{b}, c$	differential	$(0,>0,0)$	boxy

Notes. The relevant integrals are defined as $H = E - \omega J_z$ and $I = E - \omega J_z/(1 + bJ_z^{2\,c})$, with the corresponding cut-off constants given by H_0 and E_0. The dimensionless parameters are defined as follows: $\Psi = \psi(\mathbf{0})$ represents a measure of the concentration, $\chi = \omega^2/(4\pi G\rho_0)$ a measure of the (central) rotation strength, and, for the family of differentially rotating models, $\bar{b} = br_0^{2c}a^{-c}$ and $c > 1/2$ determine the shape of the rotation profile. The pressure anisotropy profiles are characterized in terms of the values of the anisotropy parameter $\alpha = 1 - \sigma_{\phi\phi}^2/\sigma_{rr}^2$ in the central, intermediate, and outer regions of a model; values of α greater than, lower than, and equal to zero indicate radially-biased, tangentially-biased anisotropy, and isotropy in velocity space, respectively. For each family of models, the first and third values of α are calculated analytically as the limiting values for small and large radii. For physical reasons discussed earlier in this Chapter, the focus is on the first two families.

single-star energy in the limit of high values of J_z. Therefore, if we refer to a distribution function of the form $f = f(I)$, we may argue that ω is related to the angular velocity in the central region of the system, characterized by approximately solid-body rotation, whereas the positive constants b, c will determine the shape of the radial profile of the rotation profile. In view of the arguments that have led to the truncation prescription that characterizes King model, we decided to introduce a truncation in phase-space based exclusively on the single-star energy with respect to a cut-off constant E_0.

For simplicity, we consider two families of distribution functions. The first family is defined as

$$f_{WT}^d(I) = A\mathrm{e}^{-aE_0}\left[\mathrm{e}^{-a(I-E_0)} - 1 + a(I-E_0)\right] \tag{4.23}$$

if $E \leq E_0$ and $f_{WT}^d(I) = 0$ otherwise, so that both $f_{WT}^d(I)$ and its derivative with respect to E are continuous. We refer to this truncation prescription as Wilson truncation (hence the subscript WT) because, in the limit of vanishing internal rotation ($\omega \to 0$), this family reduces to the spherical limit of the distribution function proposed by Wilson (1975). The superscript d in Eq. (4.23) indicates the presence of differential rotation.

The second family is defined by the distribution function

$$f_{PT}^d(I) = A\mathrm{e}^{-aE_0}\mathrm{e}^{-a(I-E_0)} \tag{4.24}$$

if $E \leq E_0$ and $f_{PT}^d(I) = 0$ otherwise; therefore the function, characterized by plain truncation (hence the subscript PT), is discontinuous with respect to E. In the limit of vanishing internal rotation, it reduces to the spherical limit of the function proposed by Prendergast & Tomer (1970), which leads to the truncated isothermal sphere (see also Woolley & Dickens 1962). A summary of the main properties and definitions of the relevant nonrotating limit of the two families of models is presented in Section 4.7.

In both cases the distribution functions are positive definite $f_{WT}^d(I),\ f_{PT}^d(I) \geq 0$, by construction. Curiously, a naive extension of King models $f = f_K^d(I)$ with a similar truncation in energy alone would define a distribution function that is not positive definite in the whole domain of definition.

Sharp gradients or discontinuities in phase space (such as the ones associated with the truncation prescription of $f^d_{PT}(I)$) are expected to be associated with evolutionary processes dictated either by collective modes or by any small amount of collisionality. Therefore, the first truncation prescription, corresponding to a smoother distribution in phase space, is to be preferred from a physical point of view as the basis for a realistic equilibrium configuration (in principle, we might have referred to even smoother functions; see Davoust 1977). In addition, a full analysis of the configurations defined by $f^d_{WT}(I)$ shows that this family of models exhibits a number of interesting intrinsic and projected properties, more appropriate for application to globular clusters, with respect to the models defined by $f^d_{PT}(I)$.

Therefore, the following Sects. 4.4 and 4.5 are devoted to the full characterization of the family of models defined by $f^d_{WT}(I)$ (for a summary of the properties of the families of models studied in the present Chapter, see Table 4.1). The intrinsic properties of the family of models defined by $f^d_{PT}(I)$ are summarized in Section 4.8. In this investigation, we decided to briefly mention and to keep also the second family not only because it extends a well-known family of models, but also because it allows us to check directly an important aspect of model construction that had been noted by Hunter (1977). This is that the truncation prescription affects the density distribution in the outer parts of the models significantly.

4.3.2 The construction of the models

The construction of the models requires the integration of the relevant Poisson equation, supplemented by a set of boundary conditions equivalent to the one described in Sect. 2 for rigidly rotating models. In this case, we obtain the solution by means of an iterative approach, based on the method proposed by Prendergast & Tomer (1970), in which an improved solution $\psi^{(n)}$ of the dimensionless Poisson equation is obtained by evaluating the source term on the right-hand side with the solution from the immediately previous step (for an application of the same method to the construction of configurations shaped by an external tidal field, see Sect. 2.5.2 in Chapter 2)

$$\hat{\nabla}^2\psi^{(n)} = -\frac{9}{\hat{\rho}_0}\hat{\rho}\left(\hat{r},\theta,\psi^{(n-1)}\right) \ ; \tag{4.25}$$

here the dimensionless escape energy is given by

$$\psi(\mathbf{r}) = a[E_0 - \Phi_C(\mathbf{r})] \ , \tag{4.26}$$

the dimensionless radius is defined as $\hat{r} = r/r_0$, with the same scale length introduced in Eq. (4.6), and $\hat{\rho}_0$ indicates the dimensionless central density. The relevant density profile $\rho = \hat{A}\hat{\rho}$, with $\hat{A}$ defined as in Eq. (4.11), results from the integration in velocity space of the distributions function defined by $f^d_{WT}(I)$. It is clear that the general strategy for the construction of the self-consistent solution is applicable also to the density derived from $f^d_{PT}(I)$.

The iteration is seeded by the corresponding spherical models, that is, the Wilson and the Prendergast-Tomer spheres respectively, and is stopped when numerical convergence is reached (see Appendix B.2 for details). At each iteration step, the scheme requires the expansion in Legendre series of the density and the potential

$$\psi^{(n)}(\hat{\mathbf{r}}) = \sum_{l=0}^{\infty}\psi^{(n)}_l(\hat{r})U_l(\cos\theta) \ , \tag{4.27}$$

$$\hat{\rho}^{(n)}(\hat{\mathbf{r}}) = \sum_{l=0}^{\infty} \hat{\rho}_l^{(n)}(\hat{r}) U_l(\cos\theta) \, . \tag{4.28}$$

The associated Cauchy problems for the radial functions $\psi_l^{(n)}(\hat{r})$ are therefore

$$\left[\frac{d^2}{d\hat{r}^2} + \frac{2}{\hat{r}} \frac{d}{d\hat{r}} - \frac{l(l+1)}{\hat{r}^2} \right] \psi_l^{(n)} = -\frac{9}{\hat{\rho}_0} \hat{\rho}_l^{(n-1)} \, , \tag{4.29}$$

supplemented by the following boundary conditions

$$\psi_0^{(n)}(0) = \Psi\sqrt{2} \, , \tag{4.30}$$

$$\psi_l^{(n)}(0) = 0 \, , \text{for } l \neq 0 \tag{4.31}$$

$$\psi_0^{(n)\prime}(0) = \psi_l^{(n)\prime}(0) = 0 \, , \tag{4.32}$$

where Ψ is the depth of the dimensionless potential well at the center. By using the method of variation of arbitrary constants, the radial functions can be expressed in integral form as follows

$$\begin{aligned} \psi_0^{(n)}(\hat{r}) &= \Psi\sqrt{2} - \frac{9}{\hat{\rho}_0} \left[\int_0^{\hat{r}} \hat{r}' \hat{\rho}_0^{(n-1)}(\hat{r}') d\hat{r}' \right. \\ &\quad \left. - \frac{1}{\hat{r}} \int_0^{\hat{r}} \hat{r}'^2 \hat{\rho}_0^{(n-1)}(\hat{r}') d\hat{r}' \right] \, , \end{aligned} \tag{4.33}$$

$$\begin{aligned} \psi_l^{(n)}(\hat{r}) &= \frac{9}{(2l+1)\hat{\rho}_0} \left[\hat{r}^l \int_{\hat{r}}^{\infty} \hat{r}'^{1-l} \hat{\rho}_l^{(n-1)}(\hat{r}') d\hat{r}' \right. \\ &\quad \left. + \frac{1}{\hat{r}^{l+1}} \int_0^{\hat{r}} \hat{r}'^{l+2} \hat{\rho}_l^{(n-1)}(\hat{r}') d\hat{r}' \right] \, . \end{aligned} \tag{4.34}$$

The factor $\sqrt{2}$ appearing in Eqs. (4.30) and (4.33) is due to the normalization assumed for the Legendre polynomials.

4.3.3 The parameter space

Much like in the case of rigidly rotating models, in both families $f_{WT}^d(I)$ and $f_{PT}^d(I)$, the resulting models are characterized by two scales, associated with the positive constants A and a, and two dimensionless parameters (Ψ, χ), measuring concentration and central rotation strength, respectively. In addition, two new dimensionless parameters, namely c and

$$\bar{b} = b \, r_0^{2c} \, a^{-c} \, , \tag{4.35}$$

determine the shape of the rotation profile. Variations in the parameter $\bar{b}$ and c are found to be less important. Minor changes in the model properties are found up to $\bar{b}, \, c \approx 4$, above which the precise value of c has only little impact on the properties of the configurations.

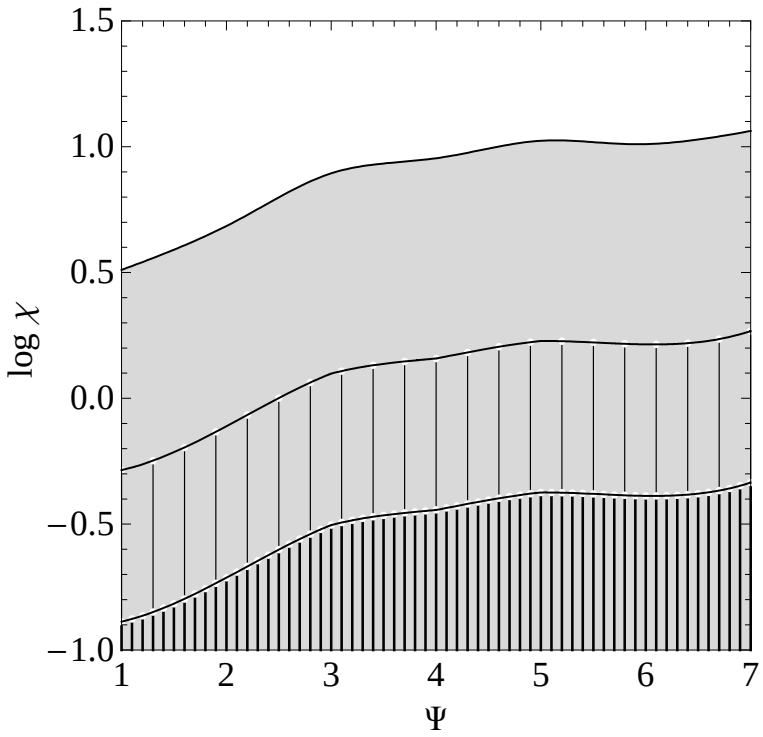

Figure 4.9: Two-dimensional parameter space, given by central rotation strength χ vs. concentration Ψ, of differentially rotating models defined by $f^d_{WT}(I)$; the remaining parameters are fixed at $\bar{b} = c = 1$. The upper solid line marks the maximum admitted values of χ, for given values of concentration Ψ, that is the underlying area indicates pairs (Ψ, χ) for which models can be constructed. The intermediate and the lower solid lines mark the values of $\hat{\omega}/\hat{\omega}_{max} = 0.4, 0.2$, respectively. The gray, wide-striped, and thin-striped areas represent the extreme, rapid, and moderate rotation regimes, respectively.

For each family of differentially rotating models, for given values $(\Psi, \bar{b}, c)$ there exists a maximum value of the central rotation strength parameter χ_{max}, corresponding to the last configuration for which the iteration described in Sect. 4.3.2 converges. Such maximally rotating configurations exhibit highly deformed morphologies, characterized by the presence of a sizable central toroidal structure, which will be described in detail in the following sections.

As for the parameter space of rigidly rotating models, it is useful to introduce different rotation regimes, defined on the basis of the deviations from spherical symmetry introduced by the presence of differential rotation. With particular reference to the parameter space of the models defined by $f^d_{WT}(I)$, we introduce some threshold values in central dimensionless angular velocity, which, in this family of models, is related to the central rotation strength parameter χ by the relation $\hat{\omega} = 3\chi^{1/2}$, as for the rigidly rotating models. In particular, configurations in the moderate rotation regime have $\hat{\omega}/\hat{\omega}_{max} < 0.2$ (the thin-striped area in Fig. 4.9), are quasi-spherical in the outer parts, while they are progressively more flattened when approaching the central region, as the value of χ increases. For the models falling in this rotation regime, the central toroidal structure is

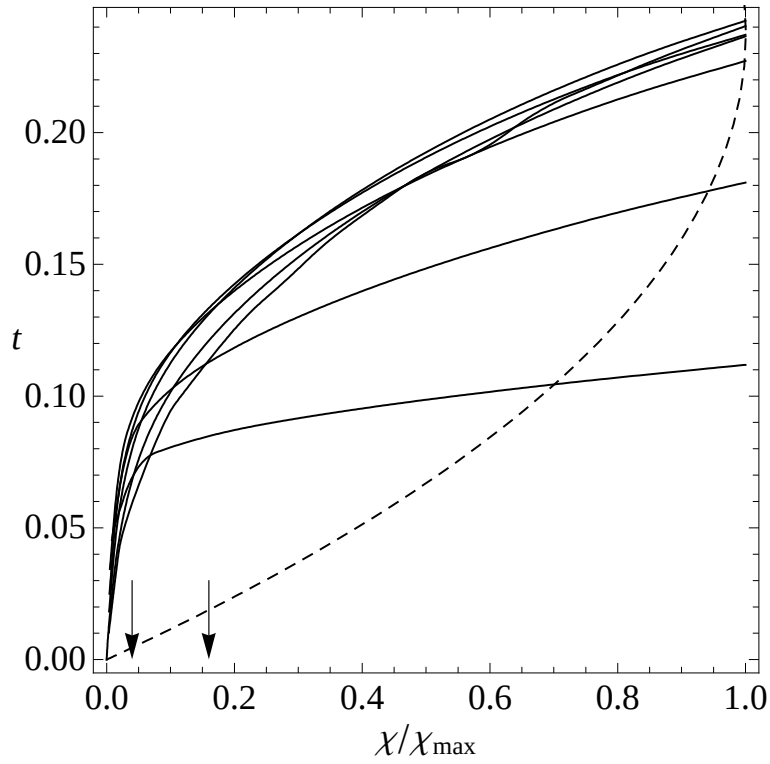

Figure 4.10: Values of the ratio between ordered kinetic energy and gravitational energy $t = K_{ord}/|W|$ for selected sequences of differentially rotating models characterized by $\Psi = 1, 2, .., 7$ (from bottom to top) and χ in the range $[0, \chi_{max}]$; the remaning parameters are fixed at $\bar{b} = c = 1$. The arrows mark the threshold values of χ for the moderate and rapid rotation regimes, illustrated in Fig. 4.9. For comparison, the dashed line represents the values of t for the sequence of Maclaurin oblate spheroids (with $e < 0.92995$; this eccentricity value corresponds to spheroids with maximum value of the rotation parameter $\chi_{max} = 0.11233$).

absent or, when low values of the concentration parameter Ψ are considered, not significant. Configurations with $0.2 < \hat{\omega}/\hat{\omega}_{max} < 0.4$ (the wide-striped area in Fig. 4.9) are defined as rapidly rotating models. The extreme rotation regime is defined by the condition $\hat{\omega}/\hat{\omega}_{max} > 0.4$ (the gray area in Fig. 4.9); in this case, the models always show a central toroidal structure, which becomes more extended as the central rotation strength increases. In particular, in the last regime, the entire volume of a configuration is dominated by the central toroidal structure.

As for the rigidly rotating models described in Sect. 2, a global kinematical characterization is offered by the parameter $t = K_{ord}/|W|$, defined as the ratio between ordered kinetic energy and gravitational energy. Figure 4.10 illustrates the relation between the two parameters, for models with selected values of Ψ, $\bar{b}$, and c. Note that the transition from rapid to extreme rotation corresponds to values of the parameter t in the range $[0.075, 0.135]$ (the precise value depends on the value of Ψ). A naive application of the Ostriker & Peebles (1973) criterion, which states that axisymmetric stellar systems with $t > 0.14$ are dynamically unstable with respect to bar modes, would suggest that the majority of the models in the extreme rotation regime are dynamically unstable. A detailed

stability analysis of the configurations in the three rotation regimes has been performed by means of specifically designed N-body simulations and will be presented in next Chapters.

To provide a systematic description of the intrinsic and projected properties, we will study the equilibrium configurations as sequences of models characterized by a given value of concentration Ψ, in the range $[1, 7]$, and increasing values of χ, up to the maximum value allowed; such sequences are constructed by fixing $\bar{b} = c = 1$ (unless otherwise stated).

4.4 Intrinsic properties of the differentially rotating models

4.4.1 The intrinsic density profile

The relevant density profile is obtained by integration in velocity space of the distribution function $f^d_{WT}(I)$ (see Eq. (4.23)). It is convenient to introduce in the velocity space a spherical coordinate system (v, μ, λ), in which v is magnitude of the velocity vector, while μ and λ are the polar and azimuthal angle, respectively. After some manipulation, the density profile can be expressed in dimensionless form as

$$\begin{aligned} \hat{\rho}_{WT}(\hat{r}, \theta, \psi) &= \frac{3}{4}\mathrm{e}^{\psi} \int_0^{\psi} ds\, \mathrm{e}^{-s} s^{1/2} \int_{-1}^{+1} dt\; g(s, t, \hat{r}, \theta) \\ &\quad -\psi^{3/2} - \frac{2}{5}\psi^{5/2}\,, \end{aligned} \tag{4.36}$$

where the function in the integrand is defined as

$$g(s, t, \hat{r}, \theta) = \exp\left(\frac{3\chi^{1/2} t\, \hat{r} \sin\theta\, (2s)^{1/2}}{1 + \bar{b}\left[t\, \hat{r} \sin\theta\, (2s)^{1/2}\right]^{2c}} \right)\,; \tag{4.37}$$

for completeness, we note that the two dimensionless variables in the double integral can be expressed in terms of the previous variables as $t = \cos\mu$ and $s = av^2/2$. Because the distribution function depends only on the energy E and the z-component of the angular momentum J_z, the resulting models are axisymmetric and therefore the density profile depends only on the radius $\hat{r}$ and the polar angle θ. The density depends on the spatial coordinates explicitly and implicitly, through the dimensionless escape energy $\psi(\hat{r}, \theta)$; such explicit dependence is the reason why, in this case, the isodensity, equipotential, and isobaric surfaces are not in one-to-one correspondence, at variance with the family of rigidly rotating models. The presence in Eq. (4.36) of the terms with fractional powers of ψ is due to the adopted truncation in phase space; in particular, it is directly related to the presence of the terms $\mathrm{e}^{-aE_0}[-1 + a(I - E_0)]$ in Eq. (4.23).

The central value of the density profile depends only on the concentration parameter Ψ and is given by $\hat{\rho}_{WT,0} = (2/5)\mathrm{e}^{\Psi}\gamma\,(7/2, \Psi)$, consistent with the central value of the density profile obtained in the nonrotating limit $\hat{\rho}_{WT,S}(\Psi)$ (see Eq. (4.65) in Section 4.7). This result corresponds to the fact that the integral $I(E, J_z)$ (see Eq. (4.22)) reduces to the Jacobi integral for small values of J_z, which implies that the rotation is approximately rigid in the central regions of a configuration (see the next subsection for details); therefore, the mean rotation velocity vanishes at the origin and the density distribution reduces to its nonrotating limit.

The double integral in Eq. (4.36) requires a numerical integration (see Appendix B.2 for details). Some insight into the behavior of the density profile can be gained by calculating the relevant asymptotic expansions in the central region and in the outer parts.

Around the origin, up to second order in radius, the density profile reduces to

$$\hat{\rho}_{WT}(\hat{r},\theta,\Psi) = \hat{\rho}_{WT,0} + \frac{1}{2}\mathrm{e}^{\Psi}\gamma\left(\frac{5}{2},\Psi\right)\left[9\chi\sin^2\theta + \left.\frac{\partial^2\psi}{\partial\hat{r}^2}\right|_0\right]\hat{r}^2 + \mathcal{O}(\hat{r}^4)\,, \tag{4.38}$$

which depends explicitly on the concentration Ψ and the central rotation strength χ, and implicitly on the parameters $\bar{b}$ and c, through the second order derivative of the escape energy evaluated at $\hat{r}=0$. Such derivative can be calculated from the radial functions given in Eqs. (4.33)-(4.34)

$$\left.\frac{\partial^2\psi}{\partial\hat{r}^2}\right|_0 = \psi_0''(0)U_0(\theta) + \psi_2''(0)U_2(\theta) = \\ = -3 + \frac{C_2}{2}\left(\frac{5}{2}\right)^{1/2}\left(-1+3\cos^2\theta\right)\,, \tag{4.39}$$

where the quantity

$$C_2 \equiv \frac{18}{5\hat{\rho}_0}\int_0^{+\infty} d\hat{r}'\,\frac{1}{\hat{r}'}\hat{\rho}_2(\hat{r}') \tag{4.40}$$

depends implicitly on the parameter Ψ through the function $\hat{\rho}_2(\hat{r})$ and $\hat{\rho}_0$. The quantity C_2 is negative-definite since the quadrupole radial function of the density $\hat{\rho}_2(\hat{r})$ is negative on the entire domain of definition of the solution of the Poisson equation; the sign of the quadrupolar function is negative because the configurations in our family of models are always oblate. In passing, we also note that the the expansion around $\hat{r}=0$ of the escape energy up to second order in radius is given by

$$\psi(\hat{r},\theta) = \Psi + \frac{1}{2}\left.\frac{\partial^2\psi}{\partial\hat{r}^2}\right|_0\hat{r}^2 + \mathcal{O}(\hat{r}^4)\,. \tag{4.41}$$

Since the boundary of a configuration is defined by the condition $\psi(\hat{r},\theta)=0$, the density profile in the outer parts can be evaluated by performing an expansion with respect to $\psi \ll 1$

$$\hat{\rho}_{WT}(\hat{r},\theta,\psi) = \frac{9}{5}\chi\hat{r}^2\sin^2\theta\,\psi^{5/2} + \mathcal{O}(\psi^{7/2})\,; \tag{4.42}$$

the terms with fractional powers of ψ that appear in Eq. (4.36) cancel out with the first terms of the expansion of the double integral (which reduces to the incomplete gamma function).

The density profiles evaluated on the principal axes for a sequence of models with $\Psi=2$, $\bar{b}=c=1$, and increasing values of the rotation strength parameter χ are illustrated in Fig. 4.11; the corresponding dimensionless escape energy profiles are displayed in Fig. 4.12. Configurations characterized by moderate rotation show monotonically decreasing profiles, whereas models with rapid rotation have the maximum value of the density profile in a position displaced with respect to the origin; in the extreme rotation regime, also the maximum value of the escape energy is off-centered. The sections of the isodensity and equipotential surfaces (presented in the first two rows of Fig. 4.13) clearly show that the offset of the density peak corresponds to the existence of a curious toroidal structure; the condition for the existence of such structure is discussed in Sect. 4.4.3.

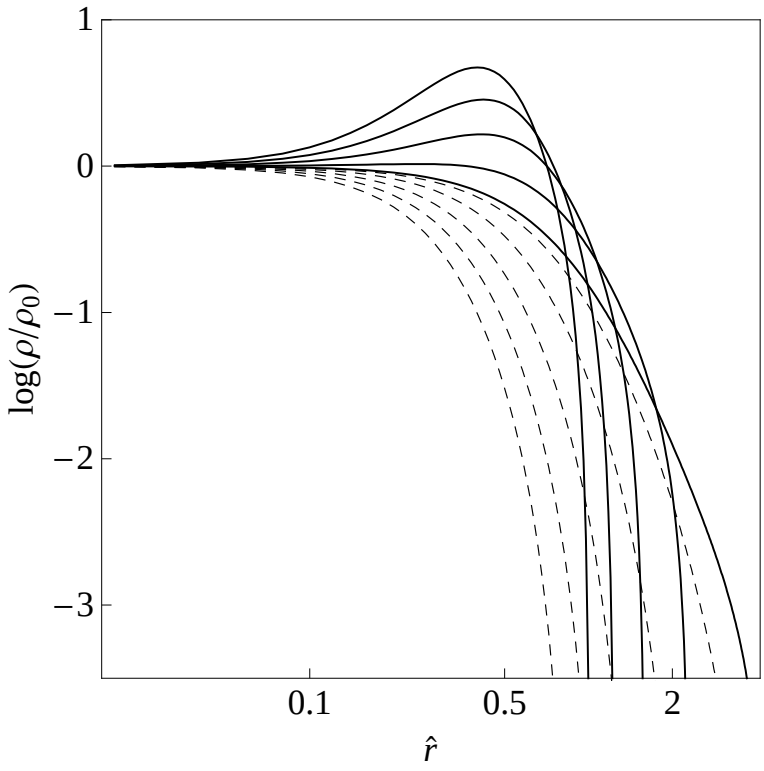

Figure 4.11: Intrinsic density profiles (normalized to the central value) evaluated on the equatorial plane (solid lines) and along the $\hat{z}$-axis (dashed lines) for a sequence of differentially rotating models defined by $f^d_{WT}(I)$, with $\Psi = 2$ and $\chi = 0.04, 0.36, 1.00, 1.96, 3.24$ (from right to left; slower rotating models are more extended); the remaining parameters are fixed at $\bar{b} = c = 1$.

4.4.2 The intrinsic kinematics

The calculation of the first order moment in velocity space of the distribution function $f^d_{WT}(I)$ confirms that only the azimuthal component of the mean velocity is nonvanishing. The mean velocity in dimensionless form

$$\begin{aligned}\langle \hat{v}_\phi \rangle_{WT}(\hat{r},\theta,\psi) &= \frac{3}{2^{3/2}\hat{\rho}_{WT}} \int_0^\psi ds\, s \int_{-1}^{+1} dt\; t\; [g(s,t,\hat{r},\theta)\mathrm{e}^{-s}\mathrm{e}^{\psi} \\ &\quad - \ln g(s,t,\hat{r},\theta)] \end{aligned} \tag{4.43}$$

can be calculated by numerically. As for the density profile, it is useful to evaluate the asymptotic expansion of Eq. (4.43) in the central regions and in the outer part of a given configuration. By performing a first order expansion in the radius with respect to the origin, we found that the mean rotation velocity reduces to the following expression

$$\langle \hat{v}_\phi \rangle_{WT}(\hat{r},\theta) = 3\chi^{1/2}\hat{r}\sin\theta + \mathcal{O}(\hat{r}^3)\,, \tag{4.44}$$

which corresponds to rigid rotation, with dimensionless angular velocity $\hat{\omega} = 3\chi^{1/2}$; the expression does not depend on the concentration parameter, consistent with the asymptotic properties of the integral $I(E, J_z)$.

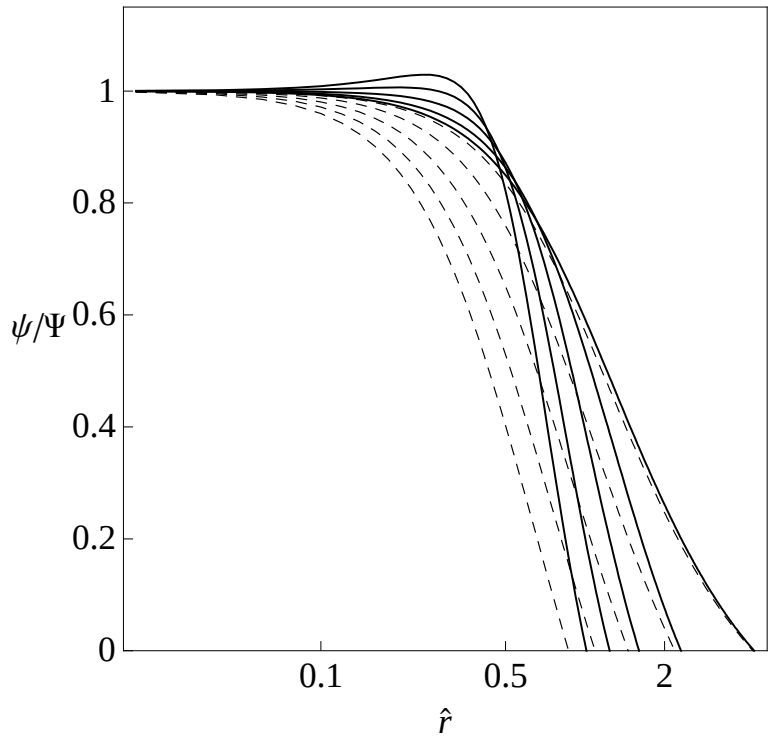

Figure 4.12: Dimensionless escape energy (normalized to the central value) evaluated on the equatorial plane (solid lines) and along the $\hat{z}$-axis (dashed lines) for the sequence of differentially rotating models displayed in Fig. 4.11.

In the outer parts of the models the mean rotation velocity is of order $\mathcal{O}(\psi)$ and thus vanishes at the boundary. The relevant numerical coefficients depend on the value of the parameter c; for example, for $c = 1$ we have

$$\langle \hat{v}_\phi \rangle_{WT}(\hat{r}, \theta, \psi) = \frac{2(2 + 6\bar{b}\hat{r}^2 \sin^2\theta + 9\chi\hat{r}^2 \sin^2\theta)}{21(\chi^{1/2}\hat{r}\sin\theta)}\,\psi\,. \tag{4.45}$$

The mean rotation velocity profiles on the equatorial plane for a selected sequence of models are displayed in Fig. 4.14: as the value of the central rotation strength parameter increases, the mean velocity profile becomes steeper in the inner parts and the maximum value increases; the central part of the profiles is well approximated by rigid rotation, as in Eq. (4.44).

By evaluating the second-order moments in velocity space of the distribution function $f^d_{WT}(I)$, it can be easily shown that, in our coordinate system, the pressure tensor $p_{ij} = (\hat{A}/a)\hat{p}_{ij}$ is diagonal and that the radial component is equal to the polar one $\hat{p}_{rr} = \hat{p}_{\theta\theta}$. Therefore, in the following, only the nontrivial components are discussed.

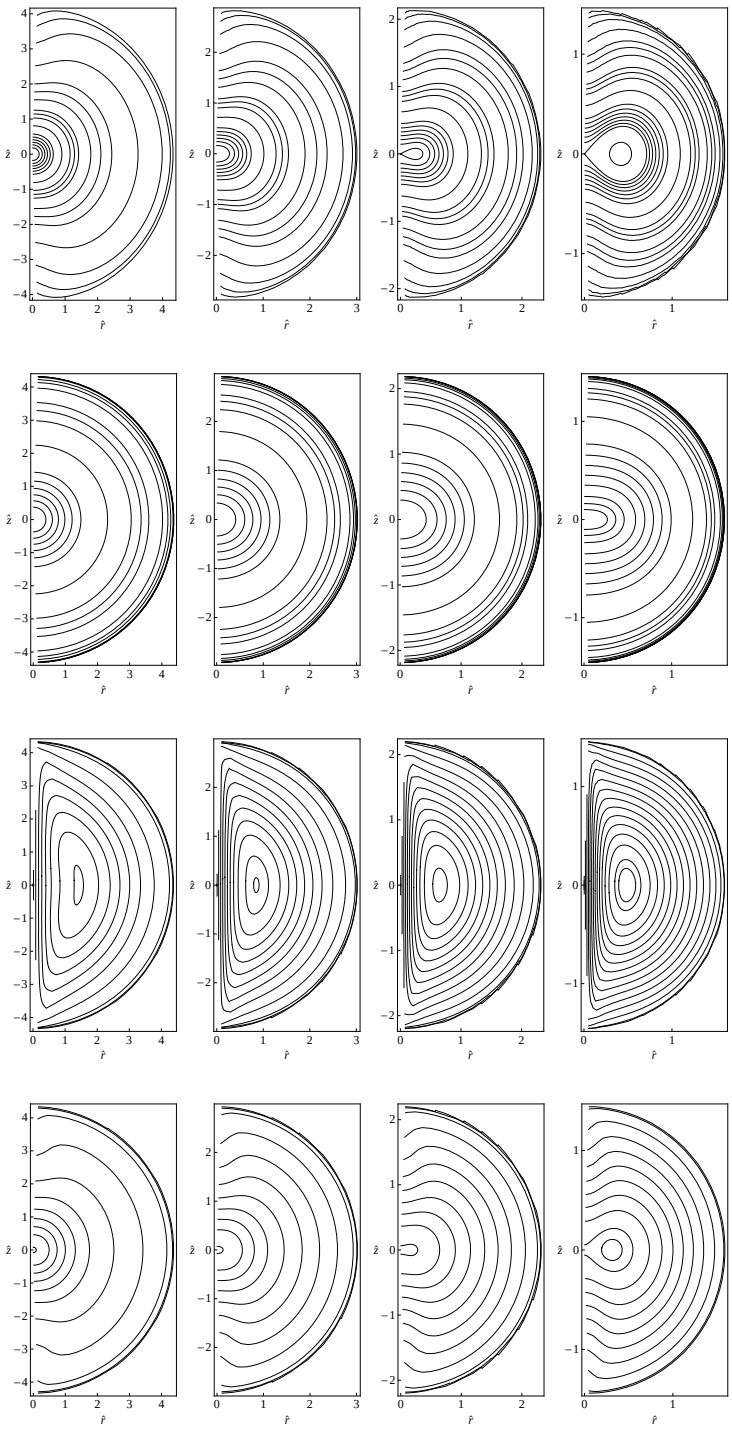

Figure 4.13: Meridional sections of the isodensity, equipotential, isovelocity, and isobaric surfaces (from top row to bottom row) for a sequence of four differentially rotating models characterized by $\Psi = 2$, $\bar{b} = c = 1$, and $\chi = 0.04, 0.16, 0.36, 1.0$ (from left column to right column; note the change in the scale of the axes). The first and second models are in the moderate rotation regime, the third has rapid rotation, and the last represents the beginning of the extreme rotation regime.

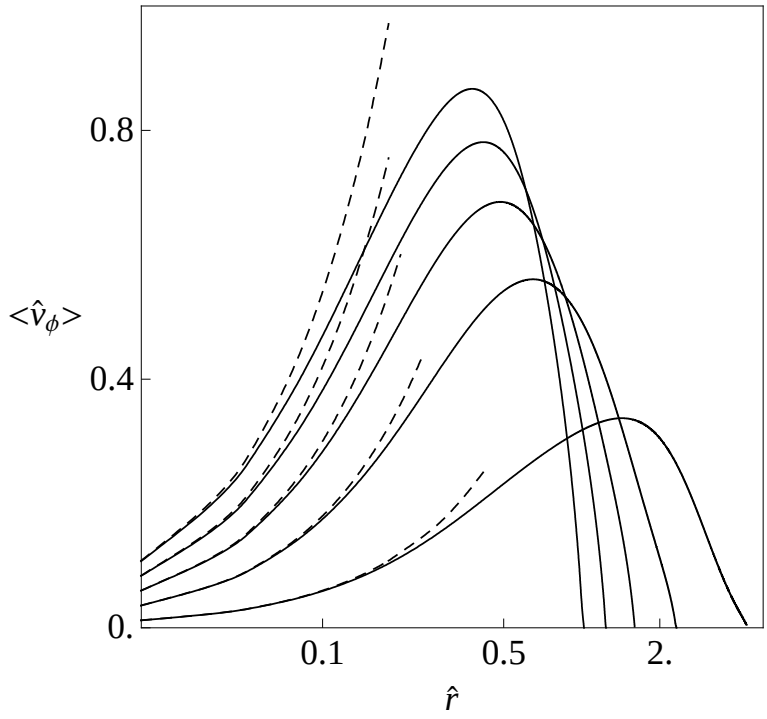

Figure 4.14: Mean rotation velocity profiles on the equatorial plane (solid lines) for the sequence of differentially rotating models defined by $f^d_{WT}(I)$, with $\Psi = 2$ and $\chi = 0.04, 0.36, 1.00, 1.96, 3.24$ (the same sequence displayed in Figs. 4.11 and 4.12, from bottom to top). Dashed lines indicated the asymptotic behavior in the central regions, which corresponds to rigid rotation (see Eq. (4.44) and Sect. 4.4.2).

The radial and azimuthal components in dimensionless form are given by

$$\begin{aligned}\hat{p}_{W,rr}(\hat{r},\theta,\psi) &= \frac{3}{4}\mathrm{e}^{\psi}\int_0^{\psi} ds\,\mathrm{e}^{-s}s^{3/2}\int_{-1}^{+1} dt\;(1-t^2)\;g(s,t,\hat{r},\theta) \\ &\quad -\frac{2}{5}\psi^{5/2}-\frac{4}{35}\psi^{7/2}\,, \end{aligned} \tag{4.46}$$

$$\begin{aligned}\hat{p}_{W,\phi\phi}(\hat{r},\theta,\psi) &= \frac{3}{2}\mathrm{e}^{\psi}\int_0^{\psi} ds\,\mathrm{e}^{-s}s^{3/2}\int_{-1}^{+1} dt\;t^2\;g(s,t,\hat{r},\theta) - \\ &\quad -\frac{2}{5}\psi^{5/2}-\frac{4}{35}\psi^{7/2}-\hat{\rho}_{WT}\langle\hat{v}_\phi\rangle^2_{WT}\,, \end{aligned} \tag{4.47}$$

where the presence of the terms with fractional powers of ψ should be interpreted as in Eq. (4.36). The expansion up to second order in radius gives

$$\begin{aligned}\hat{p}_{W,rr}(\hat{r},\theta,\Psi) &= \hat{\rho}_{WT,0}+\frac{1}{5}\mathrm{e}^{\Psi}\gamma\left(\frac{7}{2},\Psi\right)\left[9\chi\sin^2\theta\right. \\ &\quad \left.+\left.\frac{\partial^2\psi}{\partial\hat{r}^2}\right|_0\right]\hat{r}^2+\mathcal{O}(\hat{r}^4)\,. \end{aligned} \tag{4.48}$$

We also found that, to second order in radius, the pressure is isotropic $\hat{p}_{W,\phi\phi}(\hat{r},\theta,\Psi) = \hat{p}_{W,rr}(\hat{r},\theta,\Psi)$. The components of the pressure tensor evaluated at the origin reduces to $\hat{p}_{WT,0} = (4/35)\mathrm{e}^{\Psi}\gamma\,(9/2,\Psi)$, consistent with the value obtained in the nonrotating limit $\hat{p}_{WT,S}(\Psi)$ (see Eq. (4.66) in Section 4.7).

The asymptotic behavior of the pressure tensor components in the outer part can be written as

$$\hat{p}_{W,rr}(\hat{r},\theta,\psi) = \frac{18}{35}\chi\hat{r}^2\sin^2\theta\,\psi^{7/2} + \mathcal{O}(\psi^{9/2})\,, \tag{4.49}$$

$$\hat{p}_{W,\phi\phi}(\hat{r},\theta,\psi) = \frac{54}{35}\chi\hat{r}^2\sin^2\theta\,\psi^{7/2} + \mathcal{O}(\psi^{9/2})\,, \tag{4.50}$$

respectively.

The relation between the dimensionless pressure and velocity dispersion tensor is given by $\hat{\sigma}^2_{ij} = \hat{p}_{ij}/\hat{\rho}$. The profiles of the radial and azimuthal component of the velocity dispersion tensor of a selected sequence of models, evaluated on the equatorial plane, are displayed in Fig. 4.15. For configurations in the moderate rotation regime the profiles are monotonically decreasing with the radius, with some variations in the slope in the intermediate and external parts, while for configurations in the rapid and extreme rotation regimes, their peak is off-centered. The sections in the meridional plane of the isobaric surfaces, defined with respect to the trace of the pressure tensor, show the presence of a central toroidal structure for the fast rotating models of the sequence (see the last row in Fig. 4.13).

The intrinsic kinematics can be further characterized by means of the anisotropy parameter[4] , defined as

$$\alpha = 1 - \frac{p_{\phi\phi}}{p_{rr}} = 1 - \frac{\sigma^2_{\phi\phi}}{\sigma^2_{rr}}\,. \tag{4.51}$$

From the asymptotic behavior of the pressure tensor components in the central region (see Eq. (4.48)), we find that $\alpha \to 0$ for $\hat{r} \to 0$, while from the expansion in outer parts (see Eqs. (4.49)-(4.50)), we find that $\alpha \to -2$ as we approach the boundary. These limiting values do not depend on the dimensionless parameters that characterize the family $f^d_{WT}(I)$. In other words, the central region of the configurations is always characterized by isotropy in velocity space, while the regions next to the boundary show a strong tangentially-biased pressure anisotropy. The radial profiles of the anisotropy parameter for a selected sequence of models are displayed in Fig. 4.16. The values of α in the intermediate region of a given configuration depend on the values of the relevant dimensionless parameters $(\Psi, \bar{b}, c)$. In fact, from an exploration of the entire four-dimensional parameter space, we found that, by increasing the value of c, the portion of a model dominated by radial anisotropy becomes slightly less extended, while, if the value of $\bar{b}$ is increased, it increases (see Fig. 4.17, top panels). In turn, by increasing the value of the concentration, as measured by Ψ, the models are characterized by a significant radially-biased pressure anisotropy, which appears also in the intermediate region. By decreasing the value of the concentration, the intermediate region turns out to be dominated by tangential anisotropy, like in the outer parts (Fig. 4.17, bottom panels).

[4]In the literature, the anisotropy parameter is often defined as $\beta = 1 - (\sigma^2_{\phi\phi} + \sigma^2_{\theta\theta})/2\sigma^2_{rr}$; for axisymmeric systems, for which $\sigma^2_{\theta\theta} = \sigma^2_{rr}$, the relation with the parameter adopted in the present Chapter is given by $\alpha = 2\beta$. Here we prefer to keep the same notation used in van Albada (1982) and in other articles.

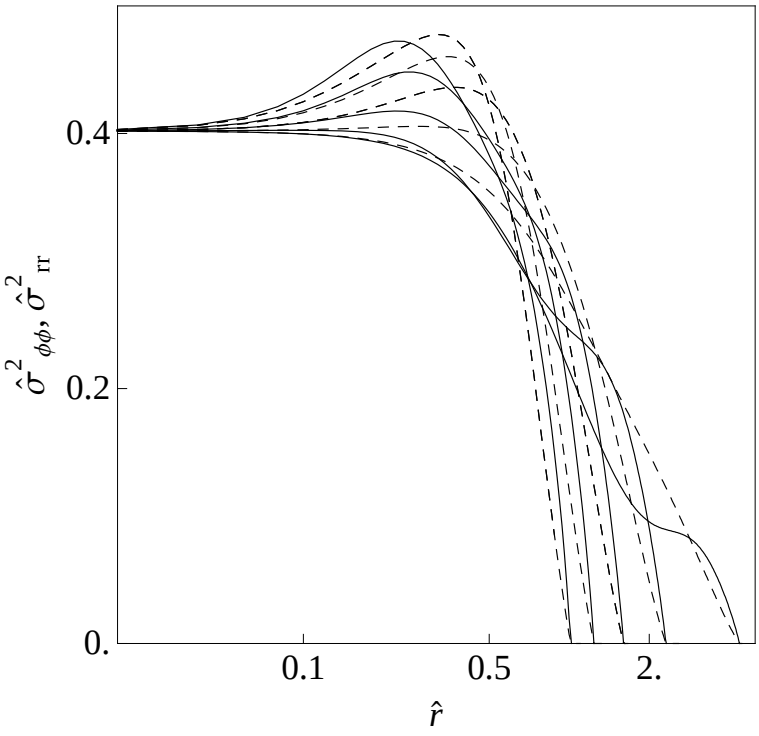

Figure 4.15: Squared velocity dispersion profiles for the azimuthal (solid lines) and radial component (dashed lines) of the sequence of differentially rotating models displayed in Fig. 4.14 (from right to left). The profiles are evaluated on the equatorial plane.

4.4.3 The condition for the existence of the central toroidal structure

In general, configurations with rapid rotation may exhibit highly deformed morphologies. In the context of rotating fluids, the regime of strong differential rotation has been successfully explored, at least for polytropes. Stoeckly (1965) and Geroyannis (1990) found that rapidly rotating polytropic fluids show a central toroidal structure; in addition, a self-consistent method for the construction of rapidly differentially rotating fluid systems with a great variety of shapes has been proposed by Hachisu (1986). In stellar dynamics, this regime has been rarely explored: Lynden-Bell (1962) and Prendergast & Tomer (1970) noted that some models with strong differential rotation show the density peak in a ring on their plane of symmetry.

The existence of a central toroidal structure in a given model of our family can be studied by using the asymptotic expansion of the density in the central regions, expressed in Eq. (4.38). In fact, if the second order derivative of the density with respect to the radius is positive, then the maximum value of the radial density profile is displaced from the geometric center of the configuration, so that a central toroidal structure is formed. Therefore, the relevant condition on the sign of the derivative can be expressed as

$$9\chi \sin^2\theta - 3 + \frac{C_2}{2}\left(\frac{5}{2}\right)^{1/2}\left(-1+3\cos^2\theta\right) > 0\,, \tag{4.52}$$

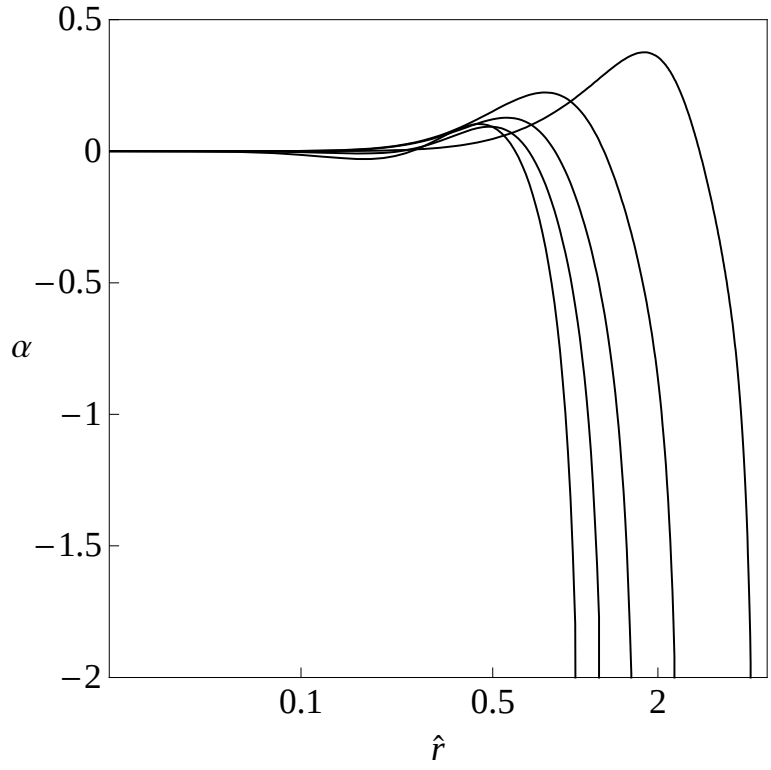

Figure 4.16: Radial profiles of the anisotropy parameter for the sequence of differentially rotating models displayed in Fig. 4.15, evaluated on the equatorial plane (from right to left). All models are characterized by $\alpha = 0$ (isotropy) at the center and $\alpha = -2$ (tangentially-biased anisotropy) at the boundary.

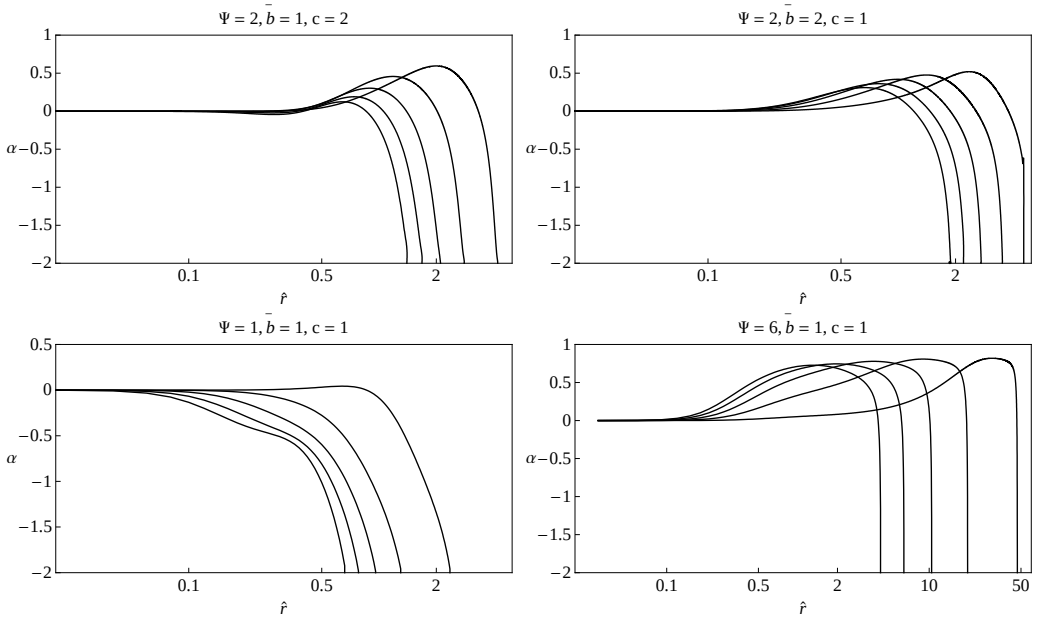

Figure 4.17: Radial profiles of the anisotropy parameter for selected sequences of differentially rotating models, evaluated on the equatorial plane. Top panels: the sequences are characterized by $\Psi = 2$, $\chi = 0.04, 0.16, 0.36, 0.64, 1.00$ (in each panel, from right to left); the left and right panels show the effect of increasing of parameters c and $\bar{b}$, respectively. Bottom panels: the sequences are characterized by $\bar{b} = c = 1$, $\chi = 0.04, 0.16, 0.36, 0.64, 1.00$ (in each panel, from right to left); the left and right panels show the effect of decreasing and increasing the concentration parameter Ψ, respectively.

which, on the equatorial plane (i.e., at $\theta = \pi/2$), reduces to a simple condition for the central rotation strength parameter

$$\chi > \frac{1}{3} + \frac{C_2}{18}\left(\frac{5}{2}\right)^{1/2} . \tag{4.53}$$

The expression on the right-hand side depends implicitly on the dimensionless parameters Ψ, $\bar{b}$, and c through the quantity C_2, defined by Eq. (A.2). Since C_2 is negative-definite, the condition $\chi > 1/3$ provides the upper limit to Eq. (4.53). Actually, the models characterized by values of χ immediately above the threshold given by Eq. (4.53), show a very small central toroidal structure, with a shallow increase of the density with respect to the geometric center of the configuration (e.g., for the model with $\Psi = 2$ and $\chi = 0.36$, illustrated in Fig. 4.11, the density peak, at the center of the toroidal structure, is merely $\log(\rho/\rho_0) = 0.014$ and the central structure itself is barely visible in the meridional sections of the isodensity surfaces, depicted in the third panel of the first row of Fig. 4.13). To construct a model with a sizable central toroidal structure, the value of the parameter χ should be at least twice the threshold given by the above-mentioned condition (e.g., see the last panel of the first row of Fig. 4.13). In conclusion, by comparing Figs. 4.9 and 4.18, we note that, for configurations in the moderate rotation regime (i.e., with $\hat{\omega}/\hat{\omega}_{max} \leq 0.2$), the central toroidal structure is absent or very small, while starting from the rapid rotation regime, the structure is always present and becomes more

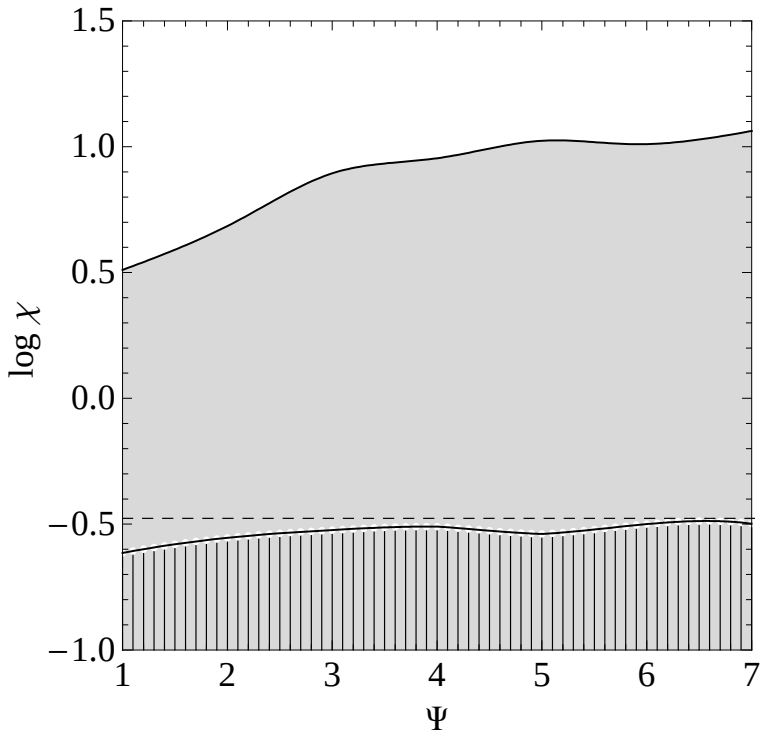

Figure 4.18: Two-dimensional parameter space of differentially rotating models (Ψ, χ); the remaining parameters are fixed at values $\bar{b} = c = 1$. The upper solid line marks the maximum admitted values of χ, as in Fig. 4.9. The lower solid line marks the values of χ at which the models start to exhibit a central toroidal structure; the dashed line marks the upper limit of the condition for the existence of the central toroidal structure (see Eq. (4.53)).

extended as the value of the central rotation strength increases.

The presence of the central toroidal structure can be also be interpreted in terms of to the intrinsic kinematical properties the models. From the radial component of the Jeans equation, expressed in dimensionless spherical coordinates,

$$\frac{1}{\hat{\rho}}\frac{\partial \hat{\rho}}{\partial \hat{r}}\frac{\hat{\sigma}_{rr}^2}{\hat{r}} = \frac{1}{\hat{r}}\frac{\partial \psi}{\partial \hat{r}} + \frac{\langle \hat{v}_\phi \rangle^2}{\hat{r}^2} - \left[\frac{1}{\hat{r}}\frac{\partial \hat{\sigma}_{rr}^2}{\partial \hat{r}} + \frac{\hat{\sigma}_{rr}^2 - \hat{\sigma}_{\phi\phi}^2}{\hat{r}^2}\right] , \tag{4.54}$$

the sign of the first order derivative of the density with respect to the radius (on the left-hand side of Eq. (4.54)) depends on (i) the difference between the angular velocity associated with the circular orbit of a single star $\hat{\omega}_c = [-(1/\hat{r})\partial_{\hat{r}}\psi]^{1/2}$ and the angular velocity of the model $\hat{\omega}$, associated to the mean rotation velocity $\langle \hat{v}_\phi \rangle = \hat{\omega}\hat{r}\sin\theta$, (ii) a more complex pressure term (in square brackets on the right-hand side of Eq. (4.54)). To check for the presence of the central toroidal structure, it is sufficient to study the Jeans equation in the central region of the model. Therefore, by inserting the relevant asymptotic expansions for the mean velocity and the escape energy (see Eqs. (4.44) and (4.41)), the term (i) reduces to the expression indicated on the left-hand side of Eq. (4.52), and, by inserting the relevant asymptotic expansions for the pressure tensor components, the

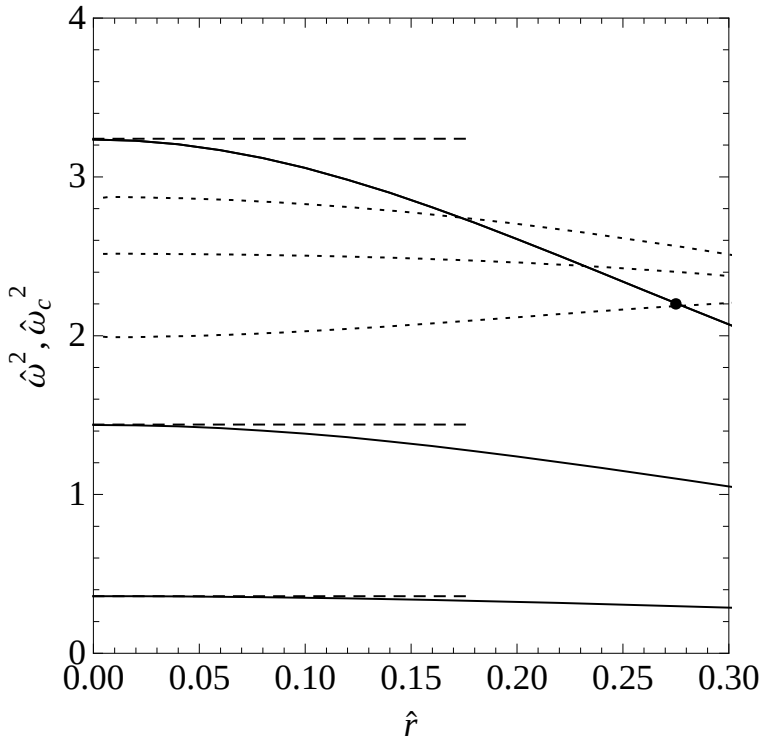

Figure 4.19: Squared angular velocity (solid lines) evaluated in the central parts of the equatorial plane for the first three differentially rotating models displayed in Fig. 4.13, that is with $\Psi = 2$, $\bar{b} = c = 1$, and $\chi = 0.04, 0.16, 0.36$ (from bottom to top). Dashed lines indicate the asymptotic behavior at small radii, characterized by solid-body rotation, that is constant angular velocity. Dotted lines represent the angular velocity associated with the circular orbit of a single star, evaluated on the equatorial plane for the same models (from top to bottom). For the first two models $\hat{\omega}_c > \hat{\omega}$, while for the third $\hat{\omega} > \hat{\omega}_c$ in the inner part, where the toroidal structure is present (the black filled circle marks the position where $\hat{\omega} = \hat{\omega}_c$) .

term (ii) can be written as

$$\left[9\chi \sin^2\theta - 3 + \frac{C_2}{2}\left(\frac{5}{2}\right)^{1/2}\left(-1 + 3\cos^2\theta\right)\right] \times \left[1 - \frac{5}{7}\frac{\gamma(9/2,\Psi)\gamma(5/2,\Psi)}{\gamma(7/2,\Psi)^2}\right]. \tag{4.55}$$

By combining the asymptotic expressions of terms (i) and (ii), it follows[5] that the requirement of a positive density gradient on the left-hand side of the Jeans equation is equivalent to the condition expressed by Eq. (4.52).

In conclusion, we have independently tested the validity of the condition for the existence of the central toroidal structure derived at the beginning of this section. We have also shown that the requirement of positivity of term (i) in the radial Jeans equation is a *necessary and sufficient* condition for the presence of the central toroidal structure. In

[5]The coefficient given by $1 - (5/7)[\gamma(9/2,\Psi)\gamma(5/2,\Psi)]/\gamma(7/2,\Psi)^2$ is nonnegative for every value of Ψ.

other words, the central toroidal structure exists if and only if, in the central region, the angular velocity associated with the internal rotation is higher than the angular velocity associated with the circular orbit of a single star. Figure 4.19 shows the relevant angular velocities for the first three models of the sequence considered in Fig. 4.13; it is apparent that, for the configuration in which the central toroidal structure is present, $\hat{\omega} > \hat{\omega}_c$. This result strictly depends on the adopted truncation in phase space for the distribution function $f^d_{WT}(I)$; in fact, in Section 4.8 we show that for the alternative distribution function $f^d_{PT}(I)$, the condition on the angular velocities is a necessary but *not* sufficient condition for the existence of the central toroidal structure.

4.4.4 The condition for maximally rotating models

If we consider a sequence of models with fixed values of $\Psi, \bar{b}, c$ and increasing values of χ, the central toroidal structure becomes progressively more extended and characterized by a larger aperture angle (i.e., the angle spanned at small radii by the isodensity surface that represents the boundary of the central toroidal structure). For high values of the central rotation strength parameter χ, a smaller central toroidal structure appears also in the equipotential surfaces (see the escape energy profile of the fastest rotating model in Fig. 4.12). These two structures can be characterized in terms of θ_p and θ_d, defined as the complements of the semi-aperture angle of the inner cusp of toroidal structures in the equipotential and isodensity surface, respectively. In fact, since the boundary of the central cusp of the toroidal structures, is defined by $\psi(\hat{r}, \theta) = \Psi$, and $\hat{\rho}(\hat{r}, \theta, \psi) = \hat{\rho}_0$, by using the relevant asymptotic expansion up to second order in $\hat{r}$ given in Eqs. (4.41) and (4.38), the following expressions for the angles are obtained:

$$\cos^2\theta_p = \frac{3 + (5/2)^{1/2} C_2/2}{(3/2)(5/2)^{1/2} C_2} \,, \tag{4.56}$$

$$\cos^2\theta_d = \frac{3 + (5/2)^{1/2} C_2/2 - 9\chi}{(3/2)(5/2)^{1/2} C_2 - 9\chi} \,. \tag{4.57}$$

The two angles are related, because

$$\cos^2\theta_d = \frac{(3/2)(5/2)^{1/2} C_2 \cos^2\theta_p - 9\chi}{(3/2)(5/2)^{1/2} C_2 - 9\chi} \,. \tag{4.58}$$

Note that θ_p and θ_d decrease as the values of $|C_2|$ and χ increase (we recall that C_2 is negative-definite), that is the corresponding semi-aperture angles become larger.

For high values of the central rotation strength χ, which imply a high degree of quadrupolar deformation, as measured by the quantity $|C_2|$, it is easy to see that $\cos^2\theta_p \to 1/3$; interestingly, we also found (numerically) that a limiting value exists also for θ_d, given by $\cos^2\theta_d \to 2/3$. By inserting the limiting value of θ_p in Eq. (4.58), the condition for the maximum value of the angle θ_d (i.e., $\cos^2\theta_d < 2/3$) can be translated in a simple condition for the central rotation strength parameter

$$\chi < \frac{1}{6}\left(\frac{5}{2}\right)^{1/2} |C_2| \,, \tag{4.59}$$

which basically provides a limit to the deformation induced by the central rotation itself. The previous condition has been checked numerically and we found that, for values of χ above the threshold, the iteration scheme used for the solution of the Poisson equation does not converge.

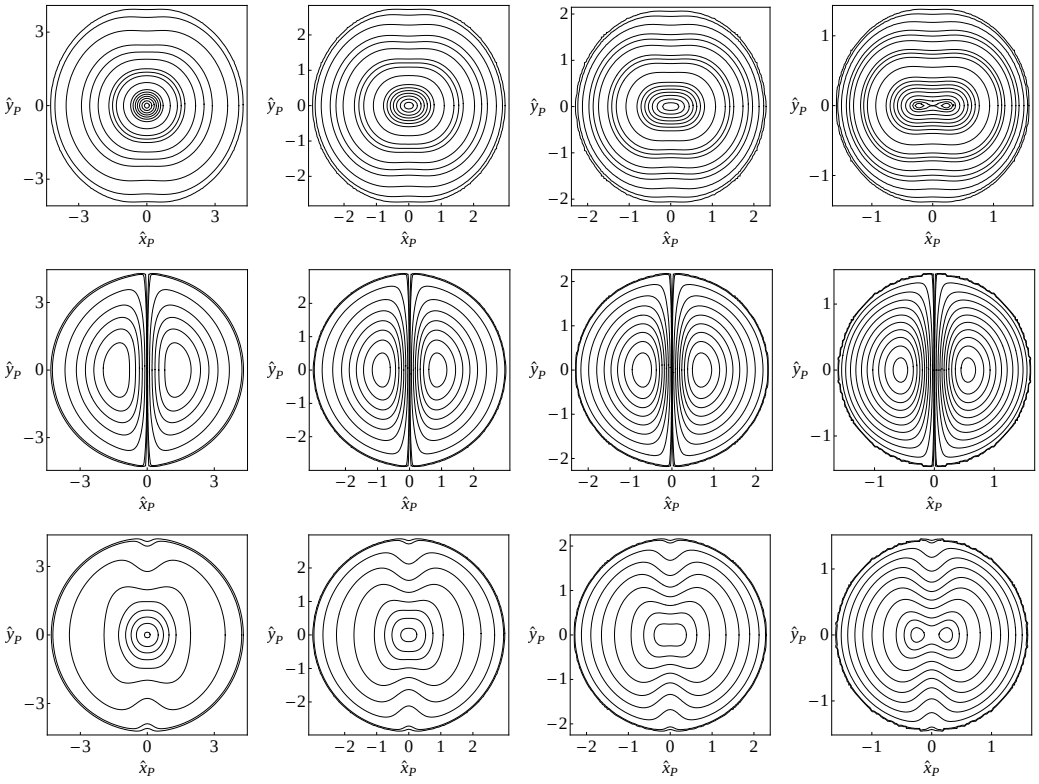

Figure 4.20: Contour maps of the surface density, mean line-of-sight velocity, and line-of-sight velocity dispersion (from top row to bottom row) of the differentially rotating models with $\Psi = 2$, $\bar{b} = c = 1$, and $\chi = 0.04, 0.16, 0.36, 1.00$ (from left to right, as in Fig. 4.13), projected along the $\hat{x}$-axis of the intrinsic coordinate system ("edge-on" view, so that $\hat{x}_P$ and $\hat{y}_P$ correspond to the $\hat{y}$ and $\hat{z}$ axes of the intrinsic system, respectively). In the panels in the first row, solid lines represent the isophotes corresponding to selected values of Σ/Σ_0 in the range $[1.02, 10^{-7}]$; only the last (fastest rotating) model shows values $\Sigma/\Sigma_0 > 1$, when the toroidal structure appears. Panels in the second row illustrate the contours of the dimensionless rotation velocity in the range $[0.5, 10^{-5}]$ at intervals of 0.05 (from left to right, the values of the innermost contours are $0.25, 0.35, 0.4, 0.45$, respectively.). Panels in the last row show the contours of the projected velocity dispersion in the range $[0.4, 10^{-5}]$ at intervals of 0.05 (the values of the innermost contours are 0.3 for the first three models and 0.4 for the last one).

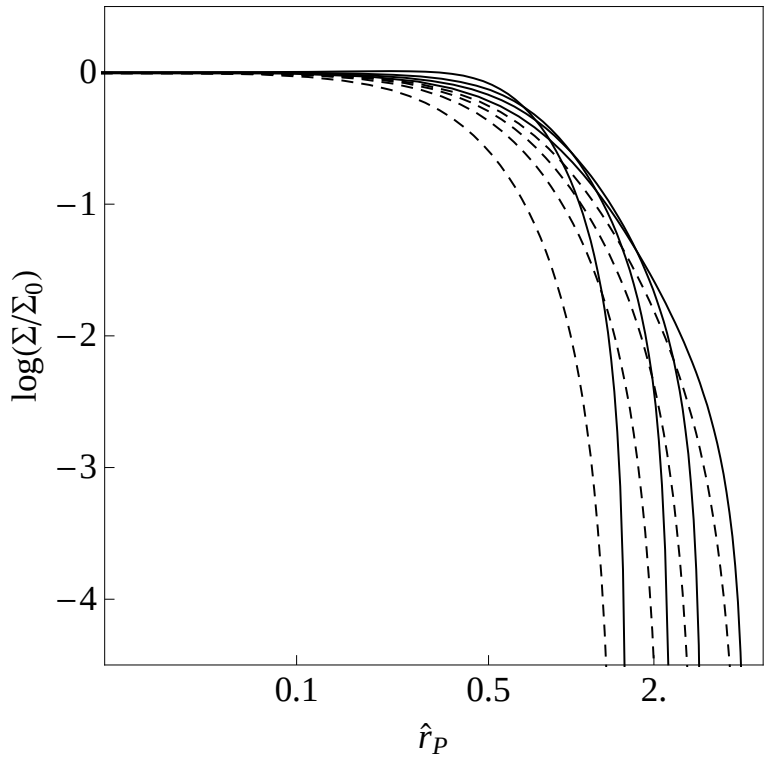

Figure 4.21: Surface density profiles (normalized to the central value) of the differentially rotating models with $\Psi = 2$, $\bar{b} = c = 1$, and $\chi = 0.04, 0.16, 0.36, 1.00$ (from right to left; same sequence illustrated in Fig. 4.20), evaluated along the $\hat{x}_P$-axis (solid lines) and $\hat{y}_P$-axis (dashed lines) of the projection plane ("edge-on" view).

4.5 Projected properties of the differentially rotating models

4.5.1 The surface density profile

The calculation of the projected properties has been performed by following the same projection rules described in Sect. 4.2.4, that is the line of sight corresponds to the $\hat{z}_P$-axis of a new frame of reference in which the projection plane is denoted by $(\hat{x}_P, \hat{y}_P)$. In particular, we studied in detail the "edge-on" view, that is the projection along the $\hat{x}$-axis of the intrinsic frame of reference ($\hat{z}_P = \hat{x}$, $\hat{x}_P = \hat{y}$, and $\hat{y}_P = \hat{z}$, i.e., the viewing angles of the rotation matrix are $\theta = \pi/2$, $\phi = 0$). The dimensionless surface density distribution $\hat{\Sigma}(\hat{x}_P, \hat{y}_P)$ has been calculated by numerical integration of Eq. (4.21) on an equally-spaced square cartesian grid on the projection plane.

The first row of Fig. 4.20 shows the contour maps of the surface density of selected differentially rotating models in the moderate and rapid rotation regime. As result of projection, the dimples on the rotation axis, which are prominent in the corresponding intrinsic isodensity surfaces (see Fig. 4.13 for the meridional sections of the same sequence of models), are less pronounced. In addition, the central toroidal structure in the projected density distribution is visible only if it has a reasonable size in the intrinsic density distribution (see third and last model of the sequence illustrated in Fig. 4.20).

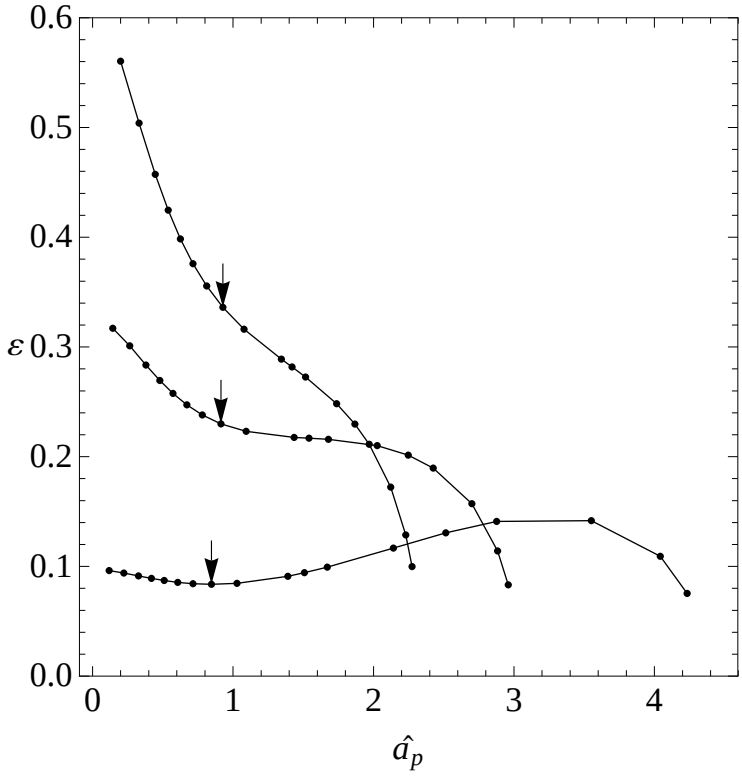

Figure 4.22: Ellipticity profiles, as functions of the semi-major axis of the projected image $\hat{a}_P$, of the first three differentially rotating models illustrated in Fig. 4.21 (from bottom to top; "edge-on" view). Dots correspond to the isophotes shown in the first row of Fig. 4.20 and arrows mark the position of the half-light isophote.

The surface density profiles of the same sequence of differentially rotating models, evaluated along the principal axes of the projection plane, are presented in Fig. 4.21. For the configurations in which the central toroidal structure in projection is absent, we calculated the relevant ellipticity profiles, as functions of the semi-major axis of the projected image $\hat{a}_P$, and they are reported in Fig. 4.22. As expected, the configurations in the moderate rotation regime are characterized by nonmonotonic ellipticity profiles, while models in the rapid rotation regime have monotonically *decreasing* profiles; to some extent, this morphological feature is complementary to that of the uniformly rotating models, in which the configurations are always characterized by monotonically *increasing* ellipticity profiles. Interestingly, the behavior of the ellipticity profiles does not necessarily correlate with the mean line-of-sight velocity profiles (see next subsection), that is configurations with a nonmonotonic velocity profile may have a monotonic ellipticity profile.

In addition, the isophotes of models show clear departures from a pure ellipse, which, at variance with the family of rigidly rotating models, can be characterized as a "boxy" overall trend, particularly evident in the intermediate parts of the configurations (see third and fourth panels of the first row of Fig. 4.20).

4.5.2 The line-of-sight velocity distribution

The projected velocity moments are calculated by integrating along the line of sight (weighted by the intrinsic density) the corresponding intrinsic quantities. As for the surface density distribution, we studied in detail the kinematics projected along the $\hat{x}$-axis of the intrinsic coordinate system. Therefore, the dimensionless mean line-of-sight velocity and the line-of-sight velocity dispersion can be written as

$$\langle \hat{v}_P \rangle (\hat{x}_P, \hat{y}_P) = -\frac{1}{\hat{\Sigma}(\hat{x}_P, \hat{y}_P)} \int_{\hat{z}_{sp}}^{\hat{z}_{sp}} d\hat{z}_P \, \hat{\rho}(\hat{\mathbf{r}}_P) \, \frac{\langle \hat{v}_\phi \rangle \, \hat{x}_P}{(\hat{z}_P^2 + \hat{x}_P^2)^{1/2}} \, , \tag{4.60}$$

$$\hat{\sigma}_P^2 (\hat{x}_P, \hat{y}_P) = \frac{1}{\hat{\Sigma}(\hat{x}_P, \hat{y}_P)} \int_{\hat{z}_{sp}}^{\hat{z}_{sp}} d\hat{z}_P \, \hat{\rho}(\hat{\mathbf{r}}_P) \, \left[\frac{1}{\hat{z}_P^2 + \hat{x}_P^2} (\hat{z}_P^2 \hat{\sigma}_{rr}^2 + \right.$$
$$\left. \hat{x}_P^2 \hat{\sigma}_{\phi\phi}^2 + \langle \hat{v}_\phi \rangle^2 \hat{x}_P^2) + \langle \hat{v}_P \rangle^2 + 2 \langle \hat{v}_P \rangle \langle \hat{v}_\phi \rangle \frac{\hat{x}_P}{(\hat{z}_P^2 + \hat{x}_P^2)^{1/2}} \right] \, . \tag{4.61}$$

Selected mean line-of-sight velocity profiles (for the sequence of models presented in Fig. 4.21), evaluated along the $\hat{x}_P$-axis of the projection plane, are illustrated in Fig. 4.23, where the sign of the mean velocity in the two half-planes is consistent with Eq. (4.60). As the value of the central rotation strength parameter increases, the slope of the inner part of the profile becomes steeper, since the asymptotic behavior of the intrinsic velocity in the central regions is approximately that of a rigid rotation, with the angular velocity proportional to $\chi^{1/2}$ (see Eq. (4.44)); in addition, because the entire configuration becomes more compact, the radial position of the peak of the velocity profile shrinks progressively.

The line-of-sight velocity dispersion profiles of the same sequence of models, evaluated along the principal axes of the projection plane, are presented in Fig. 4.24. For configurations in the moderate rotation regime, the variations in the slope at intermediate and outer radii, which characterize the azimuthal component of the intrinsic velocity dispersion tensor, are still visible in projection, while the inner part of the profile has a flat core. For models in the rapid and extreme rotation regime, the maximum value of the profile is displaced from the geometric center; in this case, the inner part of the profile has a nontrivial gradient.

We also calculated the ratio of the mean line-of-sight (rotation) velocity to the central line-of-sight velocity dispersion, as a measure of the amount of ordered motions compared to random motions (see Fig. 4.25 for relevant profiles evaluated along the $\hat{x}_P$-axis, for the sequence of models discussed above). The models in the moderate rotation regime show values that are consistent with those observed in Galactic globular clusters (see Introduction). The configurations in the rapid and extreme rotation regime are characterized by higher values of the ratio, that can be even greater than one; such high values are measured only in the class of elliptical galaxies known as fast rotators (see Davies et al. 1983). Of course, the values of this ratio strongly depend on the line of sight on which the projection is performed (we recall that here we illustrate the results obtained only from the "edge-on" view, which is the most favorable for the detection of ordered motions).

4.6 Effect of truncation in phase space

To explore the nontrivial effects of the two options for the truncation prescription of the family of differentially rotating models (see Sect. 4.3.1; see also Hunter 1977), we selected

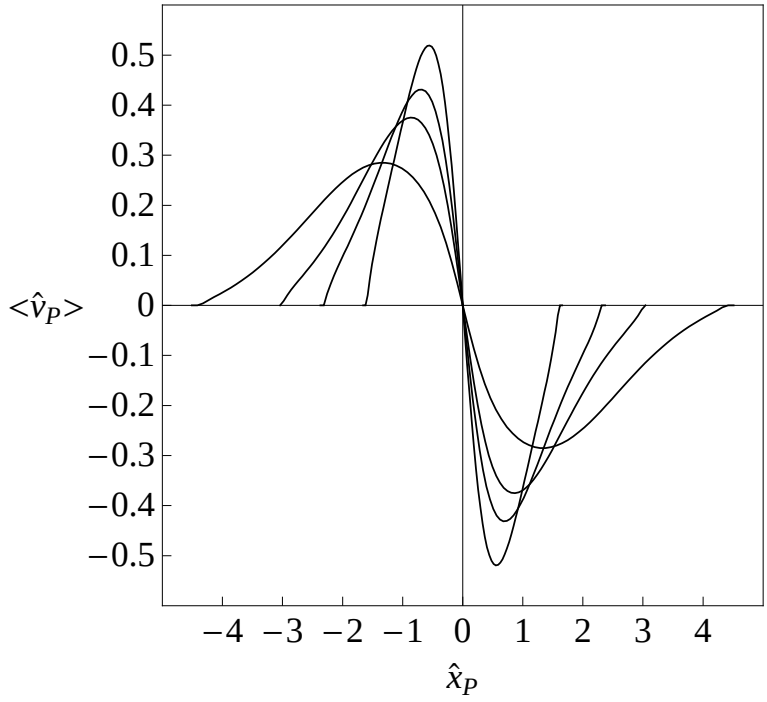

Figure 4.23: Mean line-of-sight rotation velocity profiles of the differentially rotating models with $\Psi = 2$, $\bar{b} = c = 1$, and $\chi = 0.04, 0.16, 0.36, 1.00$ (slower rotating models are more extended; same sequence illustrated in Fig. 4.21), evaluated along the $\hat{x}_P$-axis of the projection plane ("edge-on" view).

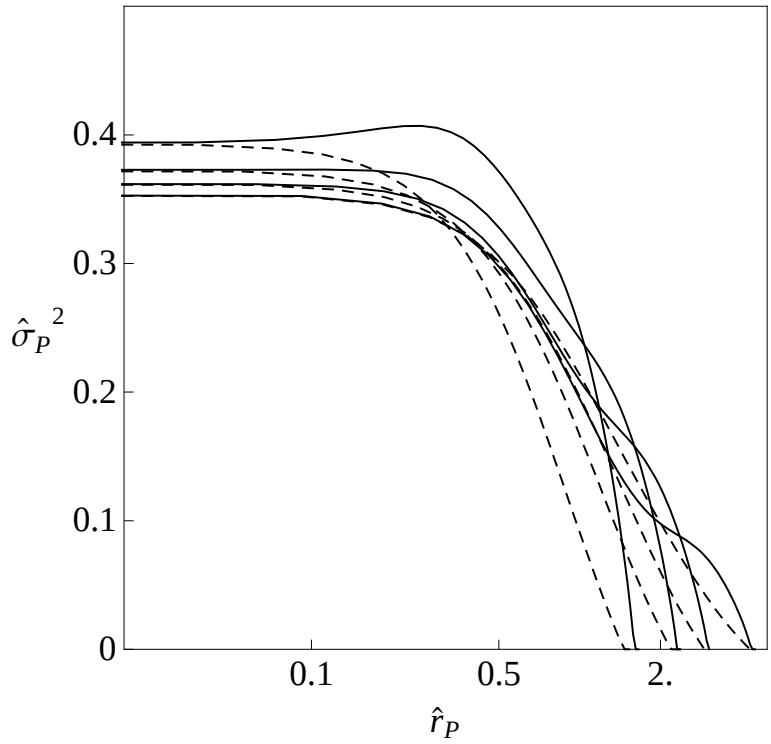

Figure 4.24: Squared line-of-sight velocity dispersion profiles of the differentially rotating models illustrated in Fig. 4.23, evaluated along the $\hat{x}_P$-axis (solid lines) and $\hat{y}_P$-axis (dashed lines) of the projection plane ("edge-on" view).

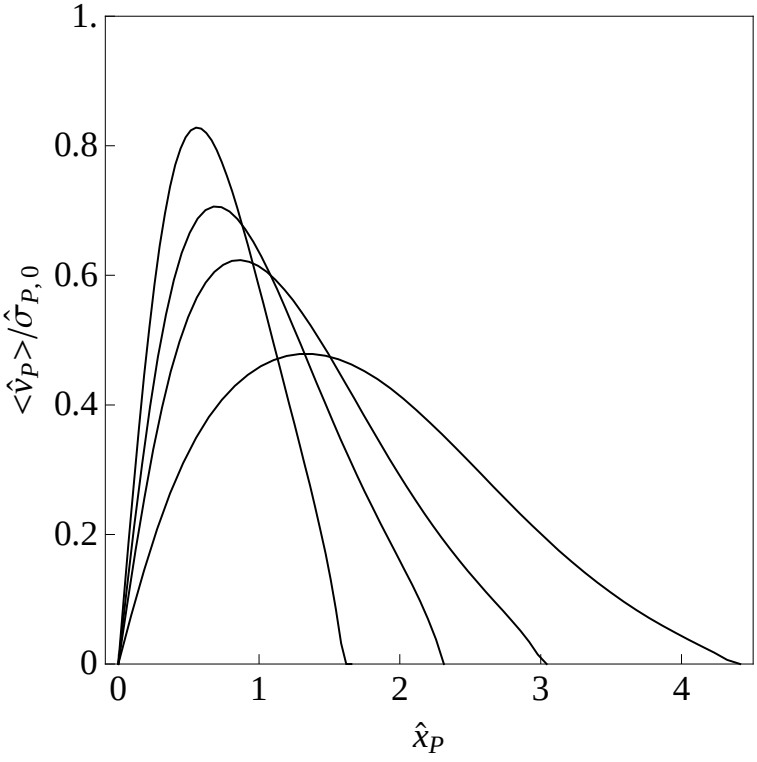

Figure 4.25: Ratio of mean line-of-sight (rotation) velocity to the central line-of-sight velocity dispersion of the differentially rotating models illustrated in Figs. 4.23 and 4.24, evaluated along the $\hat{x}_P$-axis of the projection plane ("edge-one" view). The first and second models are in the moderate rotation regime, the third has rapid rotation, and the last represents the beginning of the extreme rotation regime.

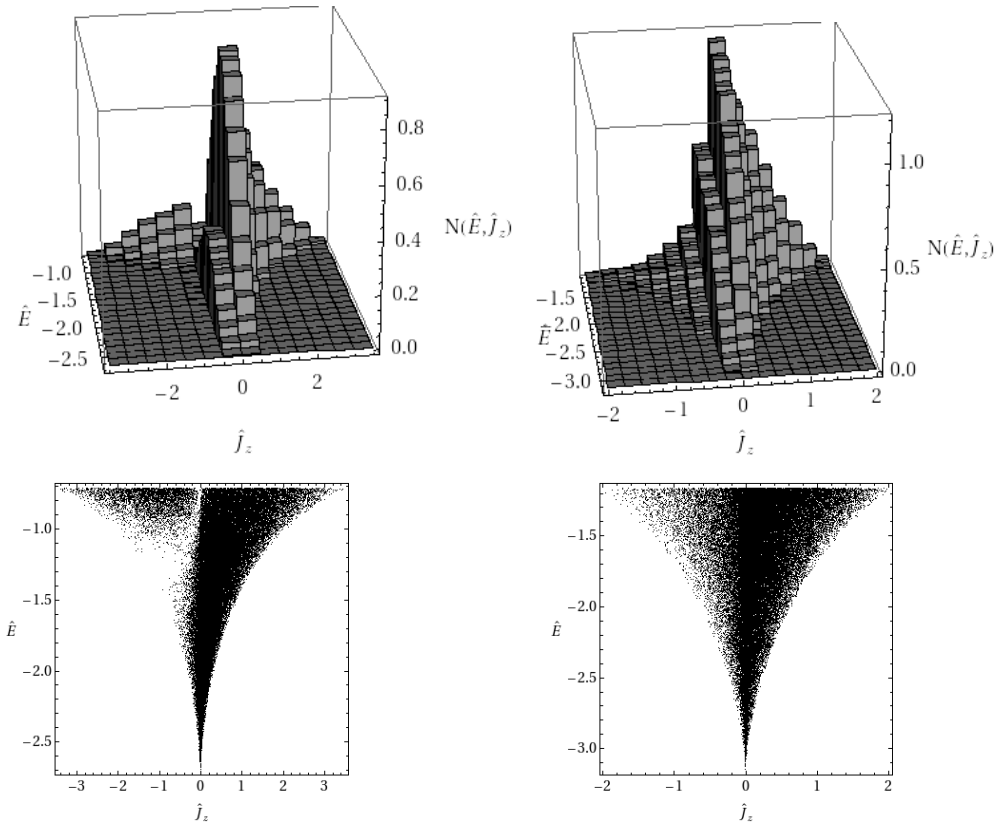

Figure 4.26: Top panels: histogram (scaled to unity) of the phase space density $N(\hat{E}, \hat{J}_z)$ for a differentially rotating model characterized by Wilson truncation (left) with $\Psi = 2, \chi = 0.16, \bar{b} = c = 1$, and for one characterized by plain truncation (right) with $\Psi = 2, \chi = 0.36, \bar{b} = c = 1$. Both models are characterized by $\hat{\omega}/\hat{\omega}_{max} \approx 0.2$. Bottom panels: Lindblad diagrams for the same models presented in the top panels. The graphs have been obtained by a Monte Carlo sampling of the relevant distribution functions with $65\,536$ particles.

two representative models and studied the relevant phase space density $N(\hat{E}, \hat{J}_z)$, defined in such a way that the total dimensionless mass is given by $\hat{M} = \int N(\hat{E}, \hat{J}_z) d\hat{E}\, d\hat{J}_z$, with the specific energy $\hat{E} = a\, E$ and z-component of the specific angular momentum $\hat{J}_z = (\hat{\mathbf{r}} \times \hat{\mathbf{v}})_z = \hat{v}_\phi \hat{r} \sin\theta$. The histograms of the phase space density, constructed by means of a Monte Carlo sampling of the distribution functions, are presented in the top panels of Fig. 4.26.

We also constructed the corresponding Lindblad diagrams (Lindblad 1933), that is the representation in the plane $(\hat{E}, \hat{J}_z)$ of orbits in phase space in a given model (see bottom panels of Fig. 4.26). For any given $\hat{J}_z$, the orbit with the lowest energy corresponds to a circular orbit in the equatorial plane; therefore, in both families of models, the circular orbits form the lower cuspy boundary of the model in the diagram. The upper boundary corresponds to the energy truncation, introduced by the cut-off constant $\hat{E}_0$. Of course, since both families of models are characterized by internal rotation, the distribution of the orbits is asymmetric with respect to the z-component of the angular momentum, but different truncation prescriptions determine a different distribution of the orbits in phase space. In particular, the Wilson truncation introduces a sharp depopulation of retrograde orbits with intermediate energy, while the plain truncation is associated with a smooth decrease of the number of retrograde orbits with high energy. Alternative options for the truncation prescription in rotating models correspond to a distribution of orbits in different regions of the diagram (see Fig. 1 in Rowley 1988). Note that a truncation with respect to the Jacobi integral $H = E - \omega J_z$ only, as in our family of rigidly rotating models $f_K^r(H)$ (see Eq. (4.3)), corresponds to a region in the diagram bounded by a straight line (with ω as slope) and the curves corresponding to the energy of circular orbits.

In addition, as the concentration of the models increases, the cusp of the lower boundary, given by the energy of circular orbits, becomes sharper; as noted also by Rowley (1988), this is the reason why centrally concentrated configurations with rigid rotation cannot be very flat, except for the outer parts, as described in Sect. 4.2.4.

4.7 Spherical limit of rotating models

The spherical nonrotating limit of the families of rotating models considered in the present Chapter are defined by the following distribution functions

$$f_{PT}(E) = A \mathrm{e}^{-aE_0} \mathrm{e}^{-a(E-E_0)}\,, \tag{4.62}$$

$$f_K(E) = A \mathrm{e}^{-aE_0} \left[\mathrm{e}^{-a(E-E_0)} - 1\right]\,, \tag{4.63}$$

$$f_{WT}(E) = A \mathrm{e}^{-aE_0} \left[\mathrm{e}^{-a(E-E_0)} - 1 + a(E-E_0)\right]\,, \tag{4.64}$$

if $E \leq E_0$ and $f_i(E) = 0$ otherwise (in the following, the index $i = 1, 2, 3$ denotes the models defined by Eqs. (4.62)-(4.64), in the same order). In particular, $f_K(E)$ defines the King (1966) models and represents the spherical nonrotating limit of the family of rigidly rotating models defined by $f_K^r(H)$ (see Eq. (4.3)); $f_{WT}(E)$ and $f_{PT}(E)$ are the spherical isotropic limit of the Wilson (1975) and Prendergast & Tomer (1970) models, and represent the spherical nonrotating limit of our differentially rotating models defined by $f_{WT}^d(I)$ (see Eq. (4.23)) and $f_{PT}^d(I)$ (see Eq. (4.24)), respectively. In the previous expressions, A, a, are positive constants, defining two dimensional scales, while E_0 is

the cut-off energy, which implies the existence of a truncation radius r_{tr} for the spherical system. For all the families of models considered here one important parameter is the central concentration, as measured by the depth of the dimensionless central potential well $\Psi = \psi(0) = a[E_0 - \Phi(0)]$ or by the parameter $c = \log(\hat{r}_{tr})$. Note that, if we compare three models (one for each family) having the same value of Ψ, the corresponding values of c are not the same, that is the relevant dimensionless truncation radii are different ($\hat{r}_{tr}$ increases from $f_{PT}(E)$, to $f_K(E)$, to $f_{WT}(E)$). In other words, the structure of the outer parts of a spherical isotropic truncated model strictly depends on the truncation prescription; this property is particularly relevant for the interpretation of the photometric profiles of globular clusters (see the systematic comparison between spherical King and Wilson models performed by McLaughlin & van der Marel (2005).

From the integration of the distribution functions in velocity space, the corresponding intrinsic density distributions are recovered. Using the same dimensionless units introduced in the main text, we denote the dimensionless density profiles by $\hat{\rho}_{i,S} = \rho_{i,S}/\hat{A}$ (for the definition of $\hat{A}$, see Eq. (4.11)), with

$$\hat{\rho}_{i,S}(\psi) = D_i \, \mathrm{e}^{\psi} \gamma \left(E_i, \psi\right) \ , \tag{4.65}$$

here ψ indicates the dimensionless escape energy, defined as in Eq. (4.26) .

Similarly, the trace of the pressure tensor in dimensionless form (divided by a factor 3) can be written as $\hat{p}_{i,S} = (a/\hat{A}) p_{i,S}$, where

$$\hat{p}_{i,S}(\psi) = P_i \, \mathrm{e}^{\psi} \gamma \left(E_i + 1, \psi\right) \ ; \tag{4.66}$$

D_i, P_i, and E_i are numerical coefficients resulting from the integration in velocity space and are summarized in Tab. 4.2. Note that the coefficient appearing as first argument of the incomplete gamma function in the pressure profile is related to the corresponding coefficient in the density profile, because they are, respectively, the second-order and zeroth-order moment of the distribution function in velocity space.

Table 4.2: Coefficients for the spherical nonrotating models

Model	D	P	E
Prendergast-Tomer	$3/2$	1	$3/2$
King	1	$2/5$	$5/2$
Wilson	$2/5$	$4/35$	$7/2$

4.8 Plain-truncated rotating models

We summarize here the intrinsic properties of the family of models defined by $f^d_{PT}(I)$ (see Eq. (4.24)), for a comparison with the corresponding quantities derived from the family of models defined by $f^d_{WT}(I)$ (see Eq. (4.23)). The density profile in dimensionless form can be written as

$$\hat{\rho}_{PT}(\hat{r}, \theta, \psi) = \hat{\rho}_{WT}(\hat{r}, \theta, \psi) + \psi^{3/2} + \frac{2}{5}\psi^{5/2} \ ; \tag{4.67}$$

the asymptotic behavior of the density profile in the outer parts ($\psi \to 0$), with respect to the dimensionless escape energy, is given by:

$$\hat{\rho}_{PT}(\hat{r},\theta,\psi) = \psi^{3/2} + \frac{2}{5}\psi^{5/2}\left(1 + \frac{9}{2}\chi\hat{r}^2\sin^2\theta\right) + \mathcal{O}(\psi^{7/2}) \,. \tag{4.68}$$

In the central region ($\hat{r} \to 0$), the expansion to second order in radius is

$$\hat{\rho}_{PT}(\hat{r},\theta,\Psi) = \hat{\rho}_{PT,0} + \frac{1}{2}\left[9\chi\hat{r}^2\sin^2\theta \mathrm{e}^{\Psi}\gamma\left(\frac{5}{2},\Psi\right) + \frac{3}{4}\mathrm{e}^{\Psi}\gamma\left(\frac{1}{2},\Psi\right)\left.\frac{\partial^2\psi}{\partial\hat{r}^2}\right|_0\right]\hat{r}^2 + \mathcal{O}(\hat{r}^4) \,, \tag{4.69}$$

where the central value is $\hat{\rho}_{PT,0} = 3/2\,\mathrm{e}^{\Psi}\gamma\,(3/2,\Psi) = \hat{\rho}_{PT,S}(\Psi)$, consistent with the value of the corresponding nonrotating model.

The mean velocity is in the azimuthal direction. In dimensionless units it is given by

$$\langle\hat{v}_\phi\rangle_{PT}(\hat{r},\theta,\psi) = \frac{3\,\mathrm{e}^{\psi}}{2^{3/2}\,\hat{\rho}_{PT}}\int_0^{\psi} ds\,\mathrm{e}^{-s}s\int_{-1}^{+1} dt\,t\,g(s,t,\hat{r},\theta) \,, \tag{4.70}$$

which, in the outer parts of the models reduces to

$$\langle\hat{v}_\phi\rangle_{PT}(\hat{r},\theta,\psi) = \psi\frac{6}{5}\chi^{1/2}\hat{r}\sin\theta + \mathcal{O}(\psi^{3/2}) \,. \tag{4.71}$$

The expansion for $\hat{r} \to 0$ to first order in radius can be written as

$$\langle\hat{v}_\phi\rangle_{PT}(\hat{r},\theta,\Psi) = 2\frac{\gamma(5/2,\Psi)}{\gamma(3/2,\Psi)}\chi^{1/2}\hat{r}\sin\theta + \mathcal{O}(\hat{r}^3) \,; \tag{4.72}$$

at variance with the family defined by $f^d_{WT}(I)$, the dimensionless angular velocity depends also on the concentration parameter.

As far as the pressure tensor is concerned, we recall that by construction $\hat{p}_{rr} = \hat{p}_{\theta\theta}$. The dimensionless radial component is given by

$$\hat{p}_{PT,rr}(\hat{r},\theta,\psi) = \hat{p}_{W,rr}(\hat{r},\theta,\psi) + \frac{2}{5}\psi^{5/2} + \frac{4}{35}\psi^{7/2} \,, \tag{4.73}$$

which, expanded in ψ (as is appropriate for the outer parts), reduces to

$$\hat{p}_{PT,rr}(\hat{r},\theta,\psi) = \frac{2}{5}\psi^{5/2} + \frac{4}{35}\psi^{7/2}\left(1 + \frac{9}{2}\chi\hat{r}^2\sin^2\theta\right) + \mathcal{O}(\psi^{9/2}) \,. \tag{4.74}$$

In the inner parts it can be approximated to second order in radius, by the following expression

$$\hat{p}_{PT,rr}(\hat{r},\theta,\Psi) = \hat{p}_{PT,0} + \frac{1}{2}\left[\frac{18}{5}\chi\hat{r}^2\sin^2\theta\mathrm{e}^{\Psi}\gamma\left(\frac{7}{2},\Psi\right) + \frac{3}{2}\mathrm{e}^{\Psi}\gamma\left(\frac{3}{2},\Psi\right)\left.\frac{\partial^2\psi}{\partial\hat{r}^2}\right|_0\right]\hat{r}^2 + \mathcal{O}(\hat{r}^4) \,, \tag{4.75}$$

where the central value is given by $\hat{p}_{PT,0} = \mathrm{e}^{\Psi}\gamma(5/2,\Psi) = \hat{p}_{PT,S}(\Psi)$, consistent with the value of the corresponding model in the limit of vanishing rotation.

The azimuthal component of the pressure tensor can be written as

$$\begin{aligned}\hat{p}_{PT,\phi\phi}(\hat{r},\theta,\psi) &= \hat{p}_{W,\phi\phi}(\hat{r},\theta,\psi) + \frac{2}{5}\psi^{5/2} + \frac{4}{35}\psi^{7/2} + \\ &\hat{\rho}_{WT}\langle\hat{v}_\phi\rangle^2_{WT} - \hat{\rho}_{PT}\langle\hat{v}_\phi\rangle^2_{PT}\,, \end{aligned} \tag{4.76}$$

which at the boundary is approximated by

$$\begin{aligned}&\hat{p}_{PT,\phi\phi}(\hat{r},\theta,\psi) = \frac{2}{5}\psi^{5/2} + \\ &\frac{4}{35}\psi^{7/2}\left(1 - \frac{9}{10}\chi\hat{r}^2\sin^2\theta\right) + \mathcal{O}(\psi^{9/2})\,. \end{aligned} \tag{4.77}$$

Close to the center we find

$$\begin{aligned}&\hat{p}_{PT,\phi\phi}(\hat{r},\theta,\Psi) = \hat{p}_{PT,0} + \frac{1}{2}\left\{6\chi\sin^2\theta\left[\frac{9}{5}\mathrm{e}^{\Psi}\gamma\left(\frac{7}{2},\Psi\right) - \right.\right. \\ &\left.\left. 2\mathrm{e}^{\Psi}\frac{\gamma(5/2,\Psi)^2}{\gamma(3/2,\Psi)}\right] + \frac{3}{2}\mathrm{e}^{\Psi}\gamma\left(\frac{3}{2},\Psi\right)\frac{\partial^2\psi}{\partial\hat{r}^2}\bigg|_0\right\}\hat{r}^2 + \mathcal{O}(\hat{r}^4)\,. \end{aligned} \tag{4.78}$$

Therefore, the models in this family are characterized by pressure isotropy in the central region, radially-biased pressure anisotropy in the intermediate part, and pressure isotropy at the boundary (since, for both $\hat{p}_{rr}$ and $\hat{p}_{\phi\phi}$, the term of lower order in ψ is given by $2/5\,\psi^{5/2}$), at variance with the family defined by $f^d_{WT}(I)$ in which tangentially-biased anisotropy is present.

Using the asymptotic expression of the density in the central regions recorded above, in this case, the condition for the existence of the central toroidal structure is given by

$$\chi > \frac{\gamma(1/2,\Psi)}{12\gamma(5/2,\Psi)}\left[3 + \frac{C_2}{2}\left(\frac{5}{2}\right)^{1/2}\right]\,, \tag{4.79}$$

where C_2 is defined as in Eq. (A.2). By evaluating the sign of the velocity and pressure term in the radial component of the Jeans equation (see Eq. (4.54)), we found that, in this case, the requirement of positivity of the velocity term is just a necessary but *not* sufficient condition for the existence of the central toroidal structure. In other words, in this family, configurations with angular velocity higher than the angular velocity associated with the circular orbit of a single star but *without* a central toroidal structure can exist. The condition for maximally rotating configurations, which, in this case, is given by

$$\chi < \frac{\gamma(1/2,\Psi)}{8\,\gamma(5/2,\Psi)}\left(\frac{5}{2}\right)^{1/2}|C_2|\,, \tag{4.80}$$

completes the summary of the intrinsic properties of the family of plain-truncated differentially rotating models.

4.9 Discussion and conclusions

In this Chapter we have constructed two new families of self-consistent axisymmetric models of quasi-relaxed stellar systems, characterized by the presence of internal rotation (see Table 1); a full description in terms of the intrinsic and projected properties has been provided. The main results can be summarized as follows:

- Driven by general statistical mechanics considerations, we started by constructing a family of rigidly rotating dynamical models; this family is defined as an extension of the King (1966) models to the case of axisymmetric equilibria flattened by solid-body rotation, with the relevant distribution function dependent only on the Jacobi integral. The configurations have been constructed self-consistently by solving the Poisson-Laplace equation for the mean-field potential by means of a perturbation method (described in Chapter 2), using a measure of the rotation strength as the expansion parameter. The two-dimensional parameter space which characterizes the family (concentration and rotation strength) can be described in terms of two regimes. Models in the low-deformation regime are almost indistinguishable from the corresponding spherical King models. Highly-deformed models are quasi-spherical in the central regions and show significant deviations from spherical symmetry in the outer parts; in particular, they are flattened toward the equatorial plane and exhibit a sort of "disky" appearance. The resulting eccentricity profile is a monotonically increasing function of radius; the (finite) central value can be expressed analytically in terms of the rotation strength parameter. From the kinematical point of view, the models are characterized by pressure isotropy and cylindrical rotation.

- In view of possible applications to globular clusters, we have constructed a second family of dynamical models, characterized by differential rotation, designed to be approximately rigid in the central regions and to vanish in the outer parts, where the imposed energy truncation is effective. In this case, the relevant Poisson equation is solved by means of a spectral iteration method based on the Legendre expansion of the density and the potential. The full parameter space is now four-dimensional, with two additional parameters, defining the shape of the rotation profile. Three rotation regimes can be introduced, namely of moderate, rapid, and extreme rotation. However, significant variations in the structure of the models are primarily associated with concentration and central rotation strength, as for the previous family. We explored the properties of the configurations resulting from two options for the truncation prescription, with emphasis on the family which, in the limit of vanishing internal rotation, reduces to the spherical limit of the models proposed by Wilson (1975). In particular, configurations in the rapid and extreme rotation regimes exhibit a central toroidal structure, the volume of which increases with the value of the central rotation strength parameter. By making use of asymptotic expansions of the density, mean velocity, and pressure tensor components for small radii, we found the condition for the existence of such central toroidal structure, as well as the condition for the maximum value of the central rotation strength parameter admitted by a configuration with a given concentration.

- The differentially rotating models show a variety of realistic velocity dispersion profiles, characterized by the presence of pressure isotropy and radially-biased anisotropy in the central and intermediate regions, respectively. The kinematical behavior in the outer parts depends on the adopted truncation prescription; in particular, the family which, in the nonrotating limit, reduces to the Wilson spheres is characterized by tangentially-biased anisotropy. This kinematical feature (rarely obtained in equilibrium models) is of great interest for two reasons: (i) Tangentially-biased pressure anisotropy is observed in the presence of internal rotation in globular clusters. For example, the full three-dimensional view of the velocity space of ω Cen, obtained from proper motions and radial velocities measurements, has revealed that this object is characterized by significant rotation and

tangential anisotropy in the outer parts (van de Ven et al. 2006). (ii) The dynamical evolution of a cluster in a tidal field is known to induce a rapid development of tangential anisotropy in the outer parts of the stellar system. In fact, if a cluster fills its Roche lobe and starts losing mass, there is a preferential loss of stars on radial orbits induced by the external tidal field at large radii, where tangential anisotropy in velocity space is thus established (Takahashi & Lee 2000; Baumgardt & Makino 2003).

- The presence of differential rotation may induce nontrivial gradients in the line-of-sight velocity dispersion profile of a stellar system, even if the amount of rotation is modest. Therefore, this important physical ingredient should be taken into account properly. In this respect, dynamical studies of globular clusters and other low-mass stellar systems by means of models based on the use of the Jeans equations are less satisfactory, because, at least in their most popular (nonrotating) application, they are used to reproduce variations in the slope of the kinematical profile of a system only by means of a (sometimes significant) amount of pressure anisotropy.

- As expected, differential rotation also induces nontrivial deviations from spherical symmetry; in fact, the models are characterized by a great variety of (projected) ellipticity profiles, dependent on the combined effect of concentration and central rotation strength. Configurations in the moderate rotation regime are characterized by realistic nonmonotonic ellipticity profiles (e.g., see Geyer et al. 1983), while models in the rapid rotation regime have monotonically decreasing profiles. To some extent, this morphological feature is complementary to that of the uniformly rotating models, in which the configurations are always characterized by monotonically increasing ellipticity profiles. Interestingly, the behavior of the ellipticity profiles is not necessarily correlated with the mean line-of-sight velocity profiles, that is configurations with a nonmonotonic mean velocity profile may have a monotonic ellipticity profile. In addition, the isophotes of the relevant surface density distribution tend to be characterized by a "boxy" structure.

- From a comparison of the equilibrium configurations resulting from two options for the truncation prescription of the family of differentially rotating models, we confirm that the interplay between internal rotation, anisotropy in velocity space, and truncation in phase space is highly nontrivial. In fact, as also noted by Hunter (1977), the structure of the outer parts of a model is particularly sensitive, both from the morphological and the kinematical point of view, to the adopted truncation. One way to select the most appropriate truncation from the physical point of view will be to address the issue in the context of formation and evolution of the class of stellar systems under consideration (see also last item below).

- Models in the moderate rotation regime seem to be particularly appropriate for describing rotating globular clusters, since the relevant configurations are characterized by a number of realistic properties, such as the presence of nonmonotonic ellipticity profile, the behavior of surface density profile in the outer parts similar to the one associated with spherical Wilson models, the existence of pressure isotropy in the central regions and tangentially-biased anisotropy at the boundary, as well as realistic values of the ratio $\langle v_P \rangle / \sigma_{P,0}$. In Chapter 7, we apply our family of differentially rotating models to selected Galactic globular clusters that show the presence of significant rotation, such as ω Cen, 47 Tuc, and M15.

- Configurations with strong differential rotation, characterized by the presence of a sizable central toroidal structure and by a off-centered peak of the surface brightness profiles, may be useful to shed light on the internal dynamics of the so-called "ring clusters". This class of object, originally observed in the Small Magellanic Cloud (Hill & Zaritsky 2006) and subsequently noted also in the Large Magellanic Cloud (Werchan & Zaritsky 2011), is characterized by a sizable dimple of the central surface brightness, resulting in an off-centered peaked density profile. A proper dynamical interpretation of these objects is currently missing.
- The families of models illustrated in the present Chapter may also help to clarify the role of angular momentum in the formation and dynamical evolution of globular clusters. The results of an extensive survey of N-body simulations, designed to study the dynamical stability and the long term evolution of the models described here, will be presented in the next chapters (see also Varri et al. in preparation).

CHAPTER 5

Dynamical stability of differentially rotating stellar systems

5.1 Introduction

The analysis of the stability properties of the equilibrium configurations of self-gravitating rotating systems is a classical problem in stellar and fluid dynamics, starting with the study of the ellipsoidal figures of equilibrium (for an elegant summary, see Chandrasekhar 1969). The sequence of Maclaurin spheroids, as parametrized by the ratio of the rotational kinetic energy to the magnitude of the gravitational energy $t = K/|W|$ (often denoted as β), shows the presence of a bifurcation point (at $t_s = 0.13572$), where an additional sequence of solutions, which break the axial symmetry, branches off (Jacobi ellipsoids). It has been proved that a Maclaurin spheroid with $t > t_s$ is *secularly* unstable with respect to bar modes ($m = 2$). Further along the Maclaurin sequence, when $t > t_d = 0.2738$, a dynamical instability with respect to bar modes sets in.

In the context of the theory of rotating stars, the investigation of the properties of self-gravitating rotating fluid bodies has been generalized to the case of configurations with nonuniform density, with particular attention to polytropic fluids with rigid (see James 1964; Stoeckly 1965; Lai et al. 1993) and differential rotation (see Tohline et al. 1985; Hachisu 1986; Houser et al. 1994; New et al. 2000, among others).

In the study of the stability properties of rotating stellar systems, general results are relatively few and they are derived primarily in the context of the global stability analysis of stellar disks. Ostriker & Peebles (1973) confirmed and extended the first results on rigidly rotating systems by Hohl (1971) to the case of differentially rotating disks. They studied a set of N-body simulations of a truncated Mestel disk characterized by different values of internal rotation and found that systems with $t > t_{OP} = 0.14 \pm 0.02$ are *dynamically* unstable with respect to bar modes (note that $t_{OP} \approx t_s$). Hence, they proposed the condition $t < t_{OP}$ as an *empirical* necessary (but not sufficient) criterion for the stability of *any* rotating stellar system with respect to barlike modes.

Over the years, attempts at providing a physical interpretation of the Ostriker & Peebles (1973) criterion have been made (in particular, see Vandervoort 1982). Yet, the stability properties of differentially rotating *spheroidal* stellar systems are largely unexplored and the connection with the corresponding fluid systems is only partially understood (Christodoulou et al. 1995a,b). Few exceptions are represented by the collisionless counterparts of the rigidly rotating polytropes (Vandervoort 1980), Riemann ellipsoids (Vandervoort & Welty 1982), and Maclaurin spheroids (Vandervoort 1991), for which analytical studies of the normal modes of oscillations have demonstrated that the dynamical instability with respect to $m = 2$ mode sets in at lower values of rotation with respect to the case of the Maclaurin fluid sequance (at $t = 0.17114$, see Christodoulou et al. 1995a).

Recently, there has been a revival of interest in the study of the stability of differentially rotating fluids, kindled by the surprising discovery by Centrella et al. (2001) of an unstable $m = 1$ azimuthal mode in highly differentially rotating polytropes with $n = 3.33$ and $t \approx 0.14$. Since then, several numerical studies have confirmed that $m = 1, 2$ modes can become unstable in a variety of differentially rotating fluid models having $t \ll t_d$, that is, well below the range of values in which dynamical instability is expected to occur, according to the Maclaurin fluid pattern (Shibata et al. 2002, 2003; Saijo et al. 2003; Karino & Eriguchi 2003).

The study of the stability of differentially rotating spherical shells (Watts et al. 2003, 2004) suggest that the low t instabilities are triggered by the presence of corotation points associated with the unstable modes within the differentially rotating configurations. In particular, Watts et al. (2005) argued that this class of instabilities occurs when the degree of differential rotation, defined as the difference between the maximum and the minimum angular velocities within a rotating configuration, exceeds a critical value and when the relevant modes can cross into the corotation band. Numerical investigations performed by Saijo & Yoshida (2006) and Ou & Tohline (2006) strengthened this interpretation.

In this Chapter we report the results of the stability analysis performed on the family of self-consistent equilibria introduced in Chapter 4, designed to describe differentially rotating spheroidal stellar systems. In particular, we focus on the strong differential rotation regime, where several models of the family present dynamical instabilities with respect to $m = 1, 2$ modes. Such instabilities show striking similarities with the low t dynamical instabilities observed in differentially rotating fluid polytropes; therefore, this result help to clarify the interpretation of the analogies between stellar and fluid rotating spheroidal systems in a regime currently unexplored. In particular, the selection of models presented in this Chapter should be interpreted as possible stellar counterparts of the fluid systems examined by Centrella et al. (2001) and Saijo et al. (2003). In addition, since a detailed investigation of the corotations points within our stellar rotating models confirms that corotation plays a significant role in the excitation of the unstable modes, we performed the same analysis on the "standard" disk model presented by Ostriker & Peebles (1973), to evaluate if their stability criterion may be included in this framework of interpretation.

The structure of this Chapter is as follows. Section 5.2 describes the initial conditions sampled from the family of models presented in Chapter 4, summarizes the setup of the N-body simulations performed to investigate the dynamical evolution of the models, and introduces the diagnostics tools used to characterize the instabilities. The results obtained from the stability analysis are described in Sect. 5.3 and our conclusions are presented in Sect. 5.4.

5.2 Method and Initial conditions

5.2.1 N-body simulations

We consider the class of axisymmetric rotating equilibria defined by the distribution function $f^d_{WT}(I) = A\mathrm{e}^{-aE_0}\left[\mathrm{e}^{-a(I-E_0)} - 1 + a(I - E_0)\right]$ if $E \leq E_0$ and $f^d_{WT}(I) = 0$ otherwise; the relevant integral of motion $I = I(E, J_z)$ is such that $I \sim E$ for stars with relatively high z-component of the angular momentum, while $I \sim H = E - \omega J_z$ (i.e., the Jacobi integral) for relatively low values of J_z. Such configurations are defined to have differential rotation, designed to be rigid in the center and to vanish at the boundary. The family of models is characterized by two dimensionless parameters (Ψ, χ), measuring

Table 5.1: Summary of the N-body simulations for the dynamical stability analysis

Id	N	Ψ	χ	$\hat{\omega}/\hat{\omega}_{max}$	t	ρ_{max}/ρ_0	σ_1	σ_2
(1)	(2)	(3)	(4)	(5)	(6)	(7)	(8)	(9)
C200R40	65536	2	0.75	0.4	0.11	1.43	-	1.71
C200R50	65536	2	1.21	0.5	0.12	1.92	-	1.81
C200R70	65536	2	2.37	0.7	0.14	3.35	3.66	1.16
C200R90	65536	2	3.92	0.9	0.16	5.37	2.90	1.49
SOP73	16384	-	-	-	0.38	1	-	1.45

Note. — Summary of the initial conditions of the N-body simulations presented in this Chapter. Col. (1): label; Col. (2): number of particles N; Col. (3): initial concentration of the model (in the literature, the parameter Ψ is often denoted by W_0); Col. (4): rotation strength dimensionless parameter; Col. (5): ratio of the central dimensionless angular velocity of the model to the maximum value associated with a given concentration Ψ; Col. (6): ratio of the rotational kinetic energy to the absolute value of the gravitational energy; Col. (7): ratio of the maximum intrinsic density to the central intrinsic density; Col. (8): eigenfrequency of the $m = 1$ unstable mode, if present (expressed in units of $1/T_D$); Col. (9): eigenfrequency of the $m = 2$ unstable mode, if present (expressed in units of $1/T_D$).

concentration and central rotation strength, respectively. Two additional dimensionless parameters (namely c and $\bar{b}$) determine the shape of the rotation profile. Details on the construction of the models, along with a full description in terms of the intrinsic and projected properties are provided in Chapter 4. In this Chapter we consider configurations in the regime of strong differential rotation, that is, such that $0.4 \leq \hat{\omega}/\hat{\omega}_{max} \leq 1.0$, where $\hat{\omega} = 3\chi^{1/2}$ is the central dimensionless angular velocity of the models and $\hat{\omega}_{max}$ denotes the maximum value of the central angular velocity admitted by a model with a given concentration Ψ (for details about the condition for maximally rotating models, see Chapter 4, Subsections 4.4.3 and 4.4.4). The properties of the initial conditions considered here are summarized in Table 5.1, together with the label used below to refer to them. In this regime, our configurations are always characterized by the presence of a central toroidal structure, that is, the density maximum is located in a torus the size of which increases with the rotation parameter χ. [1]

The dynamical evolution of the models is studied by means of direct N-body simulations performed with the STARLAB[2] software environment (Portegies Zwart et al. 2001), accelerated by GRAPE-6 special-purpose hardware (Makino et al. 2003). For all the simulations presented here, the models are treated as isolated and composed by a single population of stars. Since our analysis is focused solely on the dynamical effects associated with the presence of internal rotation, primordial binaries and the effects of stellar evolution are not included in the simulations. The systems are followed until $T/T_D = 35$ and the mass loss associated to the dynamical evolution of the system is

[1] For rotating polytropic fluids, equilibria in the regime of strong differential rotation has been successfully explored, in particular thanks to the self-consistent field method of Hachisu (1986). In stellar dynamics, this regime has been rarely explored: only Lynden-Bell (1962) and Prendergast & Tomer (1970) noted that some of their models with strong differential rotation showed the density peak in a ring on their plane of symmetry, but a detailed description of the configurations is not provided.

[2] See http://www.manybody.org.

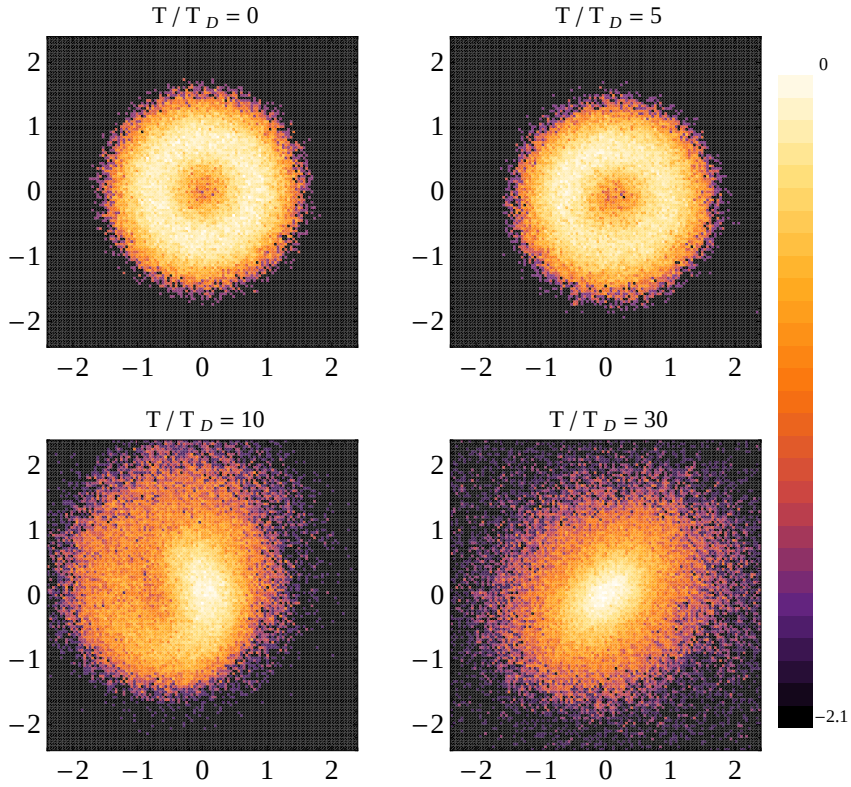

Figure 5.1: Time evolution of the surface density of the model C200R90, projected on the equatorial plane. In each snapshot, the density is normalized to the maximum value as $\log(\Sigma/\Sigma_{max})$. Time is expressed in units of the dynamical time and spatial coordinates are expressed in N-body units (e.g., see Heggie & Hut 2003).

negligible ($M_{final}/M(T=0) \geq 0.975$ in all cases). The time is measured in units of $T_D = [3\pi/(16G\rho_{90})]^{1/2}$, which is the dynamical time associated to the sphere enclosing 90% of the mass of the system, with mean density $\rho_{90} = 3M_{90}(T=0)/(4\pi R_{90}^3)$; in the following, the spatial coordinates are expressed in standard N-body units (e.g., see Heggie & Hut 2003).

5.2.2 Diagnostics tools

The instabilities are characterized by means of a Fourier decomposition of the intrinsic density distribution of the models. Following Tohline et al. (1985) and Centrella et al. (2001), at any given time we consider the density distribution in N_A coaxial and linearly spaced cylindrical annuli of radii R and $R + \Delta R$ and height $\Delta z = \Delta R$, where $\Delta R = 2R_{max}/N_A$ (R_{max} denotes the maximum radius of the initial distribution of particles); for a given annulus labelled by (R, z), we define the complex coefficient associated to the mode of azimuthal number m as

$$C_m(R,z) = \frac{1}{2\pi}\int_0^{2\pi} \rho(R,z,\phi)\, e^{-im\phi} d\phi \,, \tag{5.1}$$

with the corresponding normalized coefficient $A_m(R,z,t) = C_m(R,z,t)/C_0(R,z,t)$, where C_0 denotes the mean density in a given annulus. The tangent of the phase angle of the m-th modes is then defined as the ratio between the imaginary and real part of the relevant normalized coefficient

$$\phi_m = \tan^{-1}\left[\frac{\Im(A_m)}{\Re(A_m)}\right] , \tag{5.2}$$

and the associated eigenfrequency is given by $\sigma_m = \partial\phi_m/\partial t$ or equivalently by $\sigma_m = 2\pi/T_m$ where T_m is the period of the cosine of the phase angle. The relevant corotation point is defined as the radial position in the configuration at which the pattern speed of a given mode is equal to the angular velocity of the system $\omega(R_{cor}) = \sigma_m/m$. As noted also by Ou & Tohline (2006), in our N-body simulations the measurement of an eigenfrequency is accurate only when the corresponding mode dominates the Fourier decomposition.

5.3 Low $T/|W|$ dynamical instability

The model C200R90, with initial $t = 0.16$, is characterized by a high degree of differential rotation (90% of the maximum value admitted for configurations of concentration $\Psi = 2$) and a well-developed central toroidal structure (see the first panel in Fig. 5.1), with a density peak of $\rho_{max}/\rho_0 \approx 5$. During the early dynamical evolution, at $T/T_D \approx 8$, the torus experiences a rapid deformation into a single high-density region, which eventually progresses toward the geometric center of the configuration (see second and third panels in Fig. 5.1). In the subsequent phase, the central density distribution becomes progressively more elongated and evolves into a bar-like structure (see fourth panel in Fig. 5.1).

This morphological evolution is described quantitatively by the Fourier decomposition of the intrinsic density distribution of the model. The time evolution of the amplitudes $|A_m|$ of the first four modes calculated in the annulus with $0.36 < R < 0.72$ (corresponding roughly to the inner half of the central torus) is presented in the top panel of Fig. 5.2. The first evolution phase is clearly dominated by an $m = 1$ mode, then an $m = 2$ unstable mode develops and eventually dominates the Fourier decomposition. The eigenfrequencies of the two unstable modes are easily determined from the period of the cosine of the relevant phase angle. Due to the major structural evolution of the initial configuration determined by the $m = 1$ instability, the eigenfrequency associated with the $m = 2$ mode, which is subdominant yet characterized by a rapidly increasing amplitude in the first phase, can be measured accurately in both phases and shows a significant variation at $T/T_D \approx 16$.

To assess the importance of corotation in association with the existence of unstable modes, we analyzed the time evolution of the radial profile of the angular velocity of the model, measured on the equatorial plane, as illustrated in Fig. 5.3. Interestingly, from the calculation of the pattern speed of the $m = 1, 2$ modes at different time of the evolution, it appears that, mainly as a result of the progressive lowering of the central angular velocity, the corotation point associated to the $m = 1$ mode disappears almost exactly at the moment in which the $m = 1$ becomes subdominant with respect to the $m = 2$ mode ($T/T_D \approx 8$). On the other hand, the corotation point associated with the $m = 2$ mode is always present, but, as a result of the variation of the relevant eigenfrequency, at different radial positions in the two phases.

The same analysis has been performed on the other models listed in Table 5.1. In particular, model C200R70 shows a dynamical evolution similar to that of model C200R90,

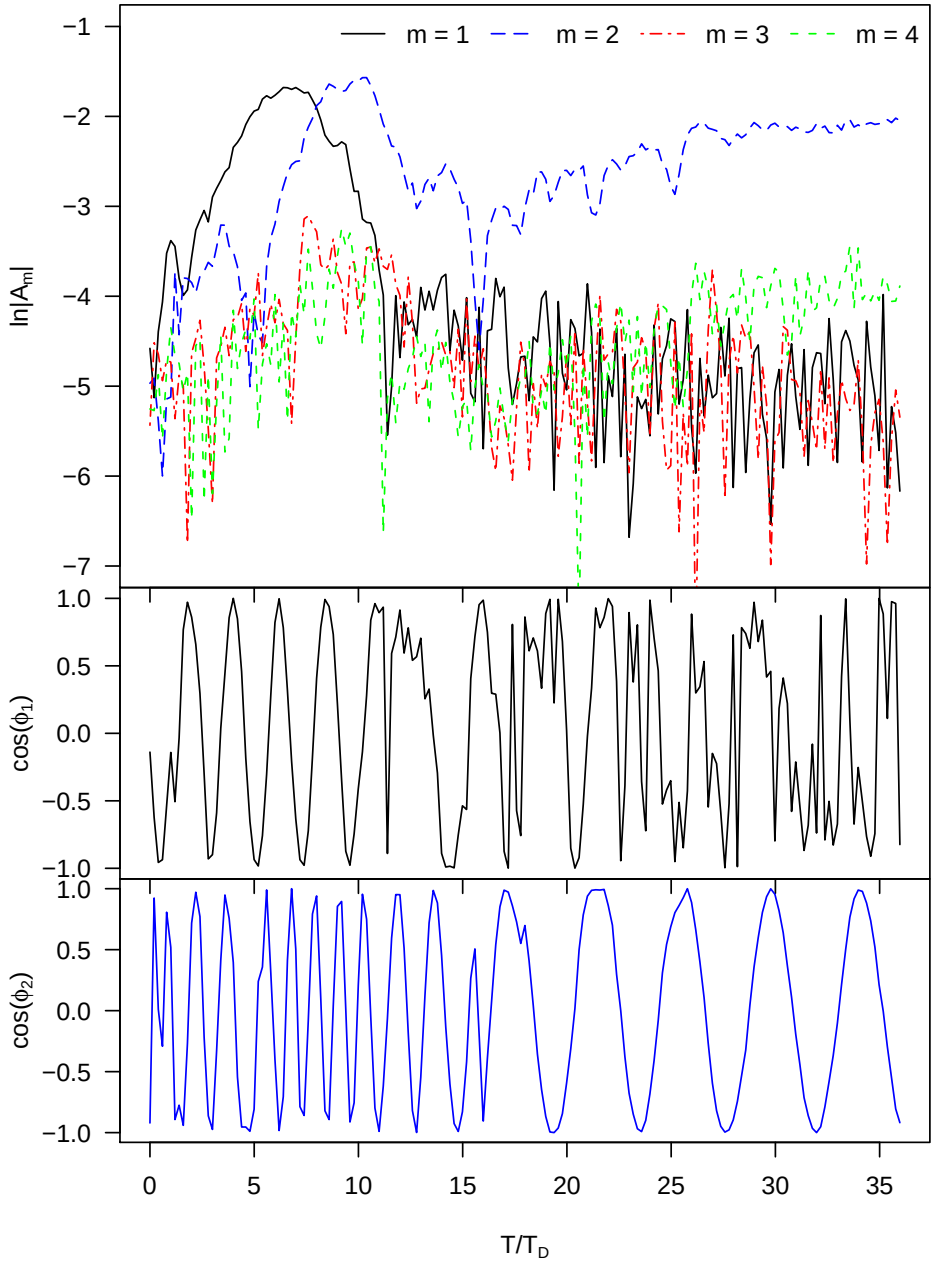

Figure 5.2: Fourier analysis of the intrinsic density of the model C200R90. Top panel (a): Growth of the amplitude of the normalized complex coefficient $|A_m|$, for $m = 1, 2, 3, 4$. Bottom panels (b), (c): Cosine of the phase angle ϕ_m for the dominant modes with $m = 1, 2$.

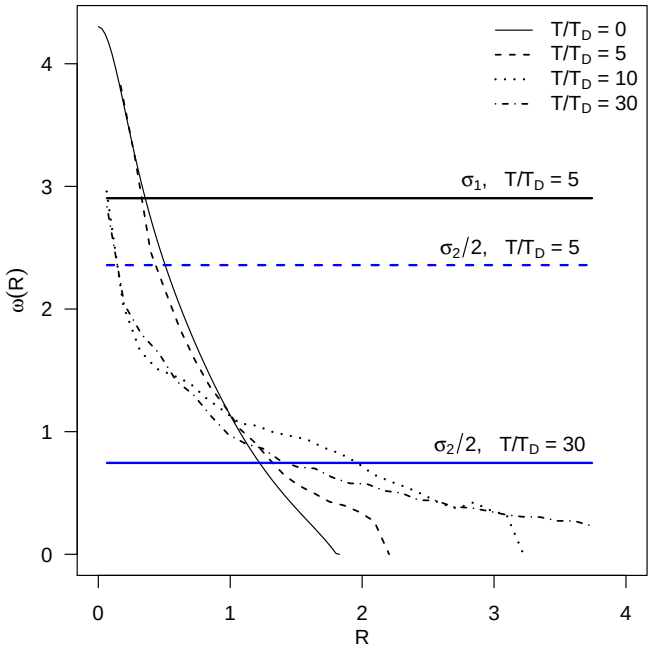

Figure 5.3: Radial profile of the angular velocity of the model C200R90 illustrated at different times of the evolution. Thick horizontal lines depict the eigenfrequencies of the two dominant modes $m = 1, 2$ in the two phases of the evolution.

where an initial $m = 1$ instability triggers the existence of an $m = 2$ unstable mode that appears to survive in the subsequent evolution (the relevant eigenfrequencies are reported in the last two columns of Table 5.1). In models characterized by a lower (yet significant, that is, $\geq 40\%$ of the maximum value admitted for configurations with $\Psi = 2$) degree of differential rotation, such as C200R50 and C200R40, the $m = 1$ instability is absent or limited to a very short time at the beginning of the evolution; therefore, the Fourier decomposition of the density distribution is dominated by the $m = 2$ unstable mode.

To evaluate the possibility of some dependence of the properties of the dynamical instabilities on the number of particles, we performed an additional set of simulations starting from the same self-consistent equilibrium models, but sampled with $N = 32768$ particles. The scaling test suggests that the observed instabilities indeed develops on the dynamical time scale and do not depend on the number of particles.

Finally, we performed a separate set of simulations designed to study the dynamical evolution of the "standard" disk model presented by Ostriker & Peebles (1973), in order to evaluate the role played by corotation in this case. The initial conditions have been generated by using the *mkop73* routine (available within the software package NEMO, see Teuben 1995), which samples a Mestel disk by following the Ostriker & Peebles (1973) original prescriptions. Initially, we considered configurations with $N = 150, 300$, to verify the consistency of our simulations with the original results. Having found a good agreement in this preliminary test, we then performed a full scaling test by considering initial conditions sampled with up to $N = 16384$ particles. For brevity, only the $N = 16k$

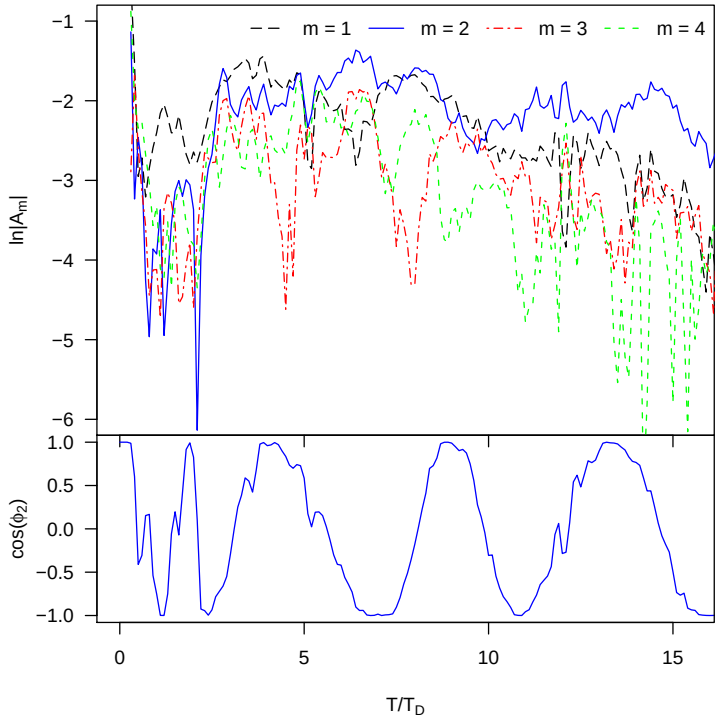

Figure 5.4: Fourier analysis of the intrinsic density of the "standard" model presented by Ostriker & Peebles (1973). Top panel (a): Growth of the amplitude of the complex coefficient $|A_m|$ for $m = 1, 2, 3, 4$. Bottom panel (b): Cosine of the phase angle ϕ_m for the $m = 2$ dominant mode.

run is reported in the present Chapter. As expected, the Fourier analysis of the density distribution allows us to identify the $m = 2$ unstable bar mode, which becomes visible already at $T/T_D \approx 5$ and dominates the decomposition starting from $T/T_D \approx 9$ (see Fig. 5.4). The evolution experienced by the disk in the very first units of dynamical time significantly alters the angular velocity radial profile, with the subsequent formation (at $T/T_D \approx 5$) of the corotation point associated with the $m = 2$ mode (see Fig. 5.5).

5.4 Discussion and conclusions

The dynamical evolution of the rotating stellar systems presented in this Chapter presents striking similarities to the one experienced by some differentially rotating fluid polytropes. The evolution of our models C200R90 ($t = 0.16$) and C200R70 ($t = 0.14$), characterized by an initial $m = 1$ instability which triggers a subsequent $m = 2$ unstable mode, is very similar to the fluid polytropic model with $t = 0.14$, polytropic index $n = 3.33$ and $\rho_{max}/\rho_0 = 1.88$ examined by Centrella et al. (2001) (see their Fig. 2) and to the models denoted as II(c) and III(d) in Saijo et al. (2003) (with $t = 0.147$, $n = 3$, and $\rho_{max}/\rho_0 = 3.07,\ 1.44$, respectively; see their Figs. 11, 16).

To conform with the cases analyzed by Centrella et al. (2001), the values of the parameter t of the models presented here fall exclusively in the range $[0.11, 0.16]$. We also

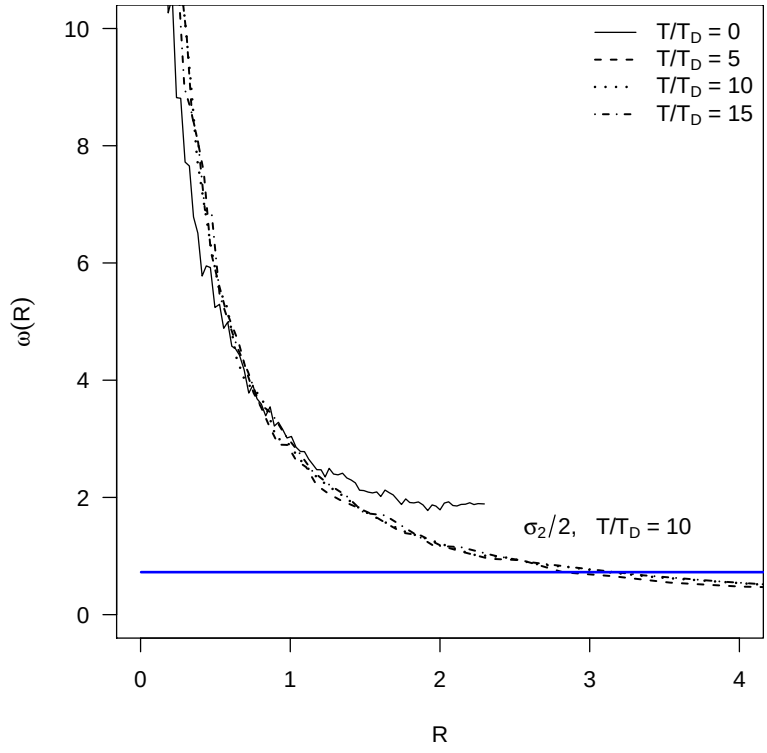

Figure 5.5: Radial profile of the angular velocity of the the "standard" model presented by Ostriker & Peebles (1973) at different times of the evolution. Thick horizontal line depicts the eigenfrequency of the dominant modes $m = 2$ at $T/T_D = 10$.

explored the dynamical evolution of models in the regime of moderate differential rotation ($0.2 \leq \hat{\omega}/\hat{\omega}_{max} \leq 0.4$) and we found that, in such regime, configurations characterized by the presence of a central toroidal structure can be dynamically stable. Therefore, as for differentially rotating fluid polytropes (see Saijo et al. 2003), the presence of a central torus is *not* a sufficient condition for the existence of unstable modes on dynamical timescale. For the complete sequence of differentially rotating models of which the strong rotation regime is addressed here, the transition from stable to unstable configurations takes place in the moderate differential rotation regime, at $t \approx 0.10$ (for the models presented by Centrella et al. 2001, such transition takes place at $t \sim 0.09$).

We also extended our analysis to other sequences of models of the family defined by f^d_{WT}, characterized by higher values of central concentration (e.g., $\Psi = 6$). Within such family, configurations with high central concentration may reach values of as high as $t \sim 0.22$ in the strong rotation regime. Similar dynamical instabilities are observed also in those sequences.

The detailed analysis of the model C200R90 shows that the formation of the corotation points within a rotating configuration is strictly connected to the excitation of the corresponding modes, as suggested by Watts et al. (2005) for differentially rotating fluid polytropes. Furthermore, the analysis performed on the "standard" Ostriker & Peebles (1973) model offers an additional evidence that corotation and dynamical instabilities are deeply connected. This result suggests that the degree of differential rotation,

which eventually determines the existence of corotation points, is the fundamental physical ingredient which motivates the existence such dynamical instabilities. Therefore, as already argued by Christodoulou et al. (1995a) and by other investigators who found counterexamples to the Ostriker & Peebles (1973) criterion (e.g., see Zang & Hohl 1978; Berman & Mark 1979), instabilities do not depend exclusively on the value of the parameter t. In fact, the global amount of rotation, as measured by the parameter t, and the degree of differential rotation are in principle decoupled factors. A strong initial degree of differential rotation may indeed determine the appearance of such dynamical instabilities in stellar dynamical configurations with relatively low values of t. On the other hand, at variance with rotating fluid polytropes in which the rotation law can be easily controlled by assuming a priori a distribution of the angular momentum, for stellar dynamical models it may be nontrivial to study the total amount of rotation and the degree of differentiality as truly independent parameters (in the f^d_{WT} family of models, the ratio $\hat{\omega}/\hat{\omega}_{max}$ offers a measure of the degree of differential rotation).

This interpretative scenario not only provides a meaningful guide to the investigation of the analogies between fluid and stellar rotating systems, but enriches the physical interpretation of the traditional Ostriker & Peebles (1973) criterion; it also allows to form a more general picture, by allowing to study modes of general order m. In this context, it should be recalled that dynamical instabilities associated with the presence of corotation points are also well known in accretion disk theory (e.g., Papaloizou & Pringle 1985).

The physical mechanism responsible for the *growth* of the amplitude of the unstable modes is still only partially understood, even in the context of fluid systems. In particular, it has been proposed that a resonant cavity resulting from a local minimum in the radial vortensity profile of the rotating configuration may play a important role in amplifying the unstable mode (Ou & Tohline 2006). This analysis will be the subject of future investigations.

CHAPTER 6

Long-term evolution of isolated rotating stellar systems

6.1 Introduction

Many investigations have studied the role of rotation in the general context of the dynamical evolution of globular clusters, but a solid interpretation is still missing. Early investigations (Agekian 1958; Shapiro & Marchant 1976) suggested that initially rotating systems should experience a loss of angular momentum induced by evaporation, that is, angular momentum would be removed by stars escaping from the cluster. Because of the small number of particles, N-body simulations were initially (Aarseth 1969; Wielen 1974) unable to clearly describe the complex interplay between relaxation and rotation.

In particular, from the study of adiabatically confined rotating cylindrical shells, Hachisu (1979) found that, if angular momentum is removed from a shell, gravitational contraction results in an increase in angular velocity, which leads to a runaway angular momentum transport and central contraction. In analogy with the "gravothermal catastrophe", this effect has been called "gravo-gyro catastrophe", and the physical origin in the latter case is a negative specific moment of inertia, analogously to the negative specific heat in the former case. The first application of this interpretative framework to the case of rotating spheroidal stellar systems has been performed by Akiyama & Sugimoto (1989), by means of specifically designed N-body simulations, but with only $N = 1000$ particles. Although the relatively low number of particles affects significantly the statistical quality of the results, Akiyama & Sugimoto (1989) interpreted the long-term evolution of rotating stellar systems as consisting of different phases, namely (1) violent relaxation, (2) gravo-gyro instability, (3) static evolution, (4) gravothermal collapse.

Later investigations, primarily conducted by following the evolution of a rotating stellar system by solving the relevant orbit-averaged Fokker-Planck equation in (E, J_z) space (as pioneered by Goodman (1983)), have strengthened this picture, not only by testing the proposed mechanism of angular momentum removal by escaping stars, but also by showing that rotation accelerates the entire dynamical evolution of the system (Einsel & Spurzem 1999; Kim et al. 2002; Fiestas et al. 2006). In particular, More recent N-body simulations (Boily 2000; Ernst et al. 2007; Kim et al. 2008) confirm these conclusions and show that, when a three-dimensional tidal field is included, such acceleration is enhanced even further. The mechanism of angular momentum removal is generally considered to be the reason why Galactic globular clusters are much rounder than the (younger) clusters in the Magellanic Clouds, for which an age-ellipticity relation has been noted (Frenk & Fall 1982), but other mechanisms might operate to produce the observed correlations (Meylan & Heggie 1997; van den Bergh 2008).

In the present Chapter we wish to study, by means of specifically designed N-body simulations, the long-term dynamical evolution of selected configurations from the family of differentially rotating models presented in Chapter 4. In particular, we will focus

Table 6.1: Summary of the N-body simulations for the long-term evolution analysis

Id	N	Ψ	χ	$\hat{\omega}/\hat{\omega}_{max}$	$t_{struct}/t_{rh}(0)$	$t_{cc}/t_{rh}(0)$
(1)	(2)	(3)	(4)	(5)	(6)	(7)
C600R10	16384	6.00	0.011	0.1	0.0	11.0
C600R00	16384	6.00	0.000	0.0	0.0	13.0
C735R00	16384	7.35	0.000	0.0	5.7	10.7
C600R20	16384	6.00	0.045	0.2	0.0	13.3
C550R00	16384	5.50	0.000	0.0	0.0	15.5
C600R30	16384	6.00	0.102	0.3	0.0	14.0
C425R00	16384	4.25	0.000	0.0	0.0	17.5
C690R00	16384	6.90	0.000	0.0	5.5	13.9

Note. — Summary of the initial conditions of the N-body simulations presented in this Chapter. Col. (1): label; Col. (2): number of particles N; Col. (3): initial concentration of the model (in the literature, the parameter Ψ is often denoted by W_0); Col. (4): rotation strength dimensionless parameter; Col. (5): ratio of the central dimensionless angular velocity of the model to the maximum value associated with a given concentration Ψ; Col. (6): time (expressed in units of the initial half-mass relaxation time) at which a given differentially rotating model (first entry in each table section) is structurally equivalent to a selected nonrotating configuration (second and third entries in each table section) ; Col. (7): core-collapse time, expressed in units of the initial half-mass relaxation time.

on the investigation of the properties of isolated rotating configurations, in direct comparison with appropriately selected nonrotating models. In fact, we will compare the evolution of several pairs of models, having the same initial structural properties (up to the half-mass radius), but characterized by different kinematic properties (i.e, in the presence or absence of internal rotation). Method and initial conditions are described in detail in Sect. 6.2, the general results are discussed in Sect. 6.3, and the conclusions are summarized in Sect. 6.4.

6.2 Method and initial conditions

We consider the class of axisymmetric rotating equilibria defined by the distribution function $f^d_{WT}(I) = A\mathrm{e}^{-aE_0}\left[\mathrm{e}^{-a(I-E_0)} - 1 + a(I-E_0)\right]$ if $E \leq E_0$ and $f^d_{WT}(I) = 0$ otherwise, with $I = I(E, J_z)$ (see Chapter 4, Eq. (4.23)). In this Chapter we focus on configurations in the regime of moderate differential rotation, that is, such that $\hat{\omega}/\hat{\omega}_{max} \leq 0.2$, where $\hat{\omega} = 3\chi^{1/2}$ is the central dimensionless angular velocity of the models and $\hat{\omega}_{max}$ denotes the maximum value of the central angular velocity admitted by a model with a given concentration Ψ (for details about the condition for maximally rotating models, see Chapter 4, Subsections 4.4.3 and 4.4.4). The properties of the initial conditions considered here are summarized in Table 6.1, together with the label used below to refer to them. The rotating models under consideration (listed as the first entry in each section of Table 6.1) are characterized by the same value of the central concentration parameter $\Psi = 6$ and increasing values of the rotation strength parameter $\chi = 0.011, 0.045, 0.102$, which can be expressed in terms of the central dimensionless angular velocity as $\hat{\omega}/\hat{\omega}_{max} = 0.1, 0.2, 0.3$, respectively. In all cases, the additional pa-

rameters $\bar{b}$ and c, which determine the shape of the rotation curve, are fixed to the values $\bar{b} = c = 1$.

In this regime, our configurations are always characterized by the absence of a central toroidal structure, that is, the density maximum is located in the geometrical center of the configuration (at variance with the models characterized by strong differential rotation considered in Chapter 5, which show a central toroidal structure, with the density peak in a ring on their plane of symmetry). In addition, by performing a dynamical stability analysis equivalent to the investigation described in Chapter 5, we found that the configurations considered in the present Chapter are dynamically stable with respect to modes with azimuthal number $m = 2$ or higher.

The long-term dynamical evolution of the models is studied here by means of direct N-body simulations performed with the STARLAB[1] software environment (Portegies Zwart et al. 2001), accelerated by GRAPE-6 special-purpose hardware (Makino et al. 2003). For all the simulations presented here, the models are treated as isolated and composed by a single population of stars. Since our analysis is focused primarily on the dynamical effects associated with the presence of internal rotation, primordial binaries and the effects of stellar evolution are not included in the simulations. The case of stellar systems characterized by the presence of a tidal boundary will be the subject of future investigations. Here the systems are followed until $T/t_{rh}(0) \approx 25$. The time is measured in units of the initial half-mass relaxation time, as defined in Eq. (1.4); in the following, the spatial coordinates are expressed in standard N-body units (e.g., see Heggie & Hut 2003).

As discussed in detail in Chapter 4, the presence of differential rotation may affect significantly the structure and morphology of a truncated stellar system, not only because it breaks the spherical symmetry, but also because the nontrivial interplay between the energy truncation and the detailed internal angular momentum distribution may introduce significant variations in the density distribution of the rotating configurations, with respect to the corresponding nonrotating model, especially in the outer and intermediate parts. In particular, we recall that, in a sequence of models characterized by the same value of the central concentration parameter Ψ and increasing values of the rotation strength parameter χ, configurations with a higher internal rotation become progressively more compact. In order to perform a meaningful comparison between the dynamical evolution of rotating and nonrotating configurations, this effect should be taken into account; as a result, in the presence of nonvanishing total angular momentum, the traditional concentration parameter associated with the depth of the central potential well of a stellar system may not be sufficient to fully characterize the structure of a configuration.

In view of these remarks, instead of simply comparing the sequence of rotating models under consideration (denoted as C600R10, C600R20, C600R30, respectively) with the "corresponding" spherical nonrotating model, that is, with by the same value of the concentration parameter $\Psi = 6$, in the limit of vanishing internal rotation $\chi \to 0$, we decided to compare each rotating model with a nonrotating configuration characterized by the same initial structure, that is, selected in order to have approximately the same initial values of the relevant (spherical) lagrangian radii, at least up to the radius enclosing 50% of the total mass [2]. Note that, in principle, the nonrotating configurations may have a different value of the central concentration parameter with respect to the rotating

[1] See http://www.manybody.org.

[2] In the present investigation, we considered as reference the set of spherical lagrangian radii that enclose 1%, 5%, 10%, 25%, 50%, 75%, 90% of the total mass of a configuration, denoted as $(r01, r05, r10, r25, r50, r75, r90)$, respectively (e.g., see Figs. 6.1, 6.2, and 6.3).

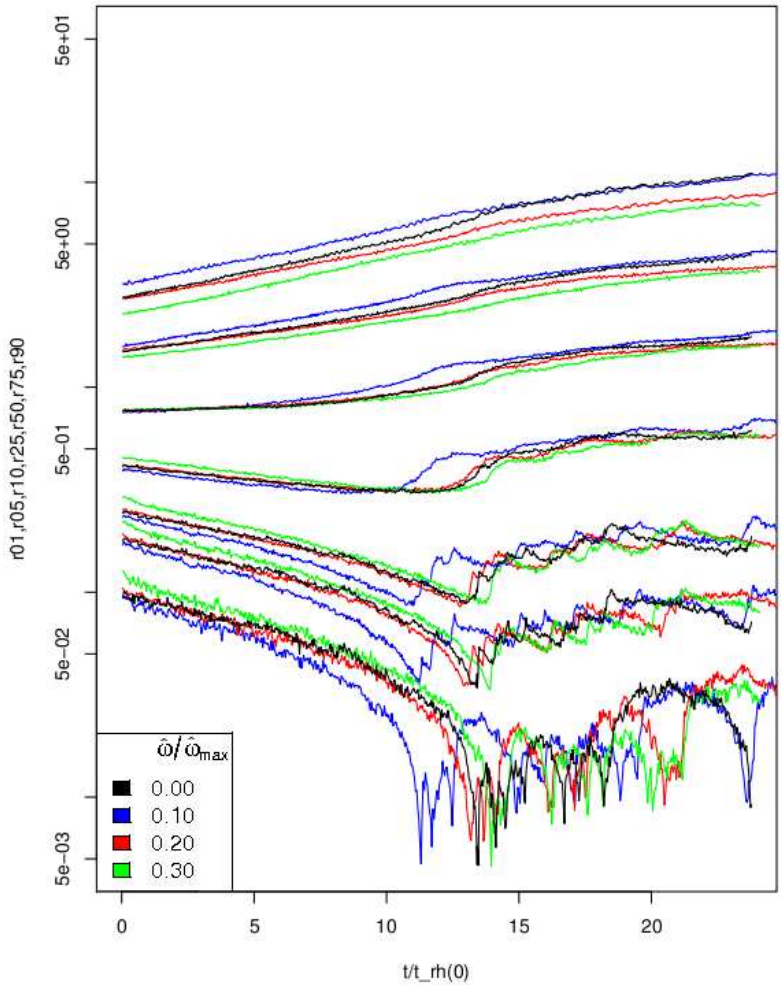

Figure 6.1: Evolution of selected lagrangian radii of four differentially models, characterized by the same value of the concentration parameter ($\Psi = 6$) and increasing values of internal rotation $\hat{\omega}/\hat{\omega}_{max} = 0.00, 0.10, 0.20, 0.30$ denoted by black, blue, red, and green lines, respectively.

models; in fact, the difference in concentration Ψ becomes more significant as the value of the rotation strength parameter increases (see Table 6.1).

Previous studies of the long-term dynamical evolution of rotating stellar systems, either based on a Fokker-Planck approach or by means of N-body simulations (Goodman 1983; Lagoute & Longaretti 1996; Longaretti & Lagoute 1996; Einsel & Spurzem 1999; Kim et al. 2002; Fiestas et al. 2006; Ernst et al. 2007; Kim et al. 2008), have considered as initial conditions configurations selected almost exclusively from the family of the truncated rotating Maxwellian distribution function, defined as:

$$f(E, J_z) = A(e^{-aE} - e^{-aE_0})e^{-\beta J_z} \tag{6.1}$$

for $E < E_0$ and $f = 0$ otherwise; this family of models reduces, in the limit of van-

ishing internal rotation, to spherical isotropic nonrotating King (1966) models. Those studies often investigated the properties of a given sequence of rotating configurations, characterized by the same value of central concentration and increasing values of the dimensionless rotation parameter (associated with the parameter β), in direct comparison with the spherical King model which represents the nonrotating limit of the sequence under consideration (i.e., for $\beta \to 0$).

6.3 General results and discussion

As discussed in the previous Section, the comparison between rotating and nonrotating configurations performed exclusively with reference to the nominal value of the central concentration parameter gives only a partial indication of the effect of internal rotation on the long-term dynamical evolution of a model. Nonetheless, in Figure 6.1 we report the evolution of selected spherical lagrangian radii of the three rotating models under consideration, compared with the nonrotating model characterized by the same value of central concentration Ψ. Surprisingly, we found that only the model characterized by the lowest value of internal rotation ($\hat{\omega}/\hat{\omega}_{max} = 0.10$, C600R10) reaches core collapse more rapidly compared to the nonrotating model (C600R00), whereas the evolution of the other two rotating configurations ($\hat{\omega}/\hat{\omega}_{max} = 0.20, 0.30$, i.e., C600R20, C600R30) is comparable to the nonrotating one. This result should be interpreted as an evidence of the fact that the study of rotating configurations should not be performed by taking into account exclusively the kinematical properties, as the structural one may play a significant role in driving the dynamical evolution of dense stellar systems.

The previous picture, from which, apparently, the presence of internal rotation can actually slow down the dynamical evolution of a stellar system, is somehow reversed if the rotating models are compared with the nonrotating configurations characterized by the same initial values of the first lagrangian radii (in Fig. 6.1, it is particularly evident that model C600R30 is structurally different from the nonrotating model C600R00). Figures 6.2 and 6.3 illustrate such analysis for models C600R10 and C600R30. In the first case, the relevant nonrotating model is still represented by model C600R00, while in the second case, the nonrotating model is characterized by a much lower value of the central concentration parameter. In both cases, the rotating models reach core collapse more rapidly compared to the nonrotating configurations (see also Table 6.1).

The long-term dynamical evolution of the rotating models under consideration can be therefore interpreted, as already discussed in particular by Akiyama & Sugimoto (1989) and Einsel & Spurzem (1999), as composed of two phases. During the first phase the gravo-gyro instability takes place, and subsequently levels off, and, as a result, the dynamical evolution of rotating configurations progresses more rapidly compared to nonrotating configurations with *the same initial structural properties*. At variance, during the second phase second phase, rotating models experience gravothermal catastrophe and reach core collapse; in this phase, the overall dynamical evolution of the rotating configurations is consitent with the one experienced by nonrotating models. To substantiate this interpretation, we performed two additional simulations of nonrotating models which show approximately the same values of the lagrangian radii of the rotating ones at $t/t_{rh}(0) \approx 5.5$. The relevant nonrotating configurations are characterized by higher values of the central concentration parameter with respect to the nonrotating models selected to be structurally equivalent to the rotating ones at $t/t_{rh}(0) = 0$ (see the last entry in the first and third section of Table 6.1; the evolution of the lagrangian radii of the additional nonrotating models is marked as red lines in Figs. 6.2 and 6.3). This fact is consistent with a traditional result regarding nonrotating configurations, for which

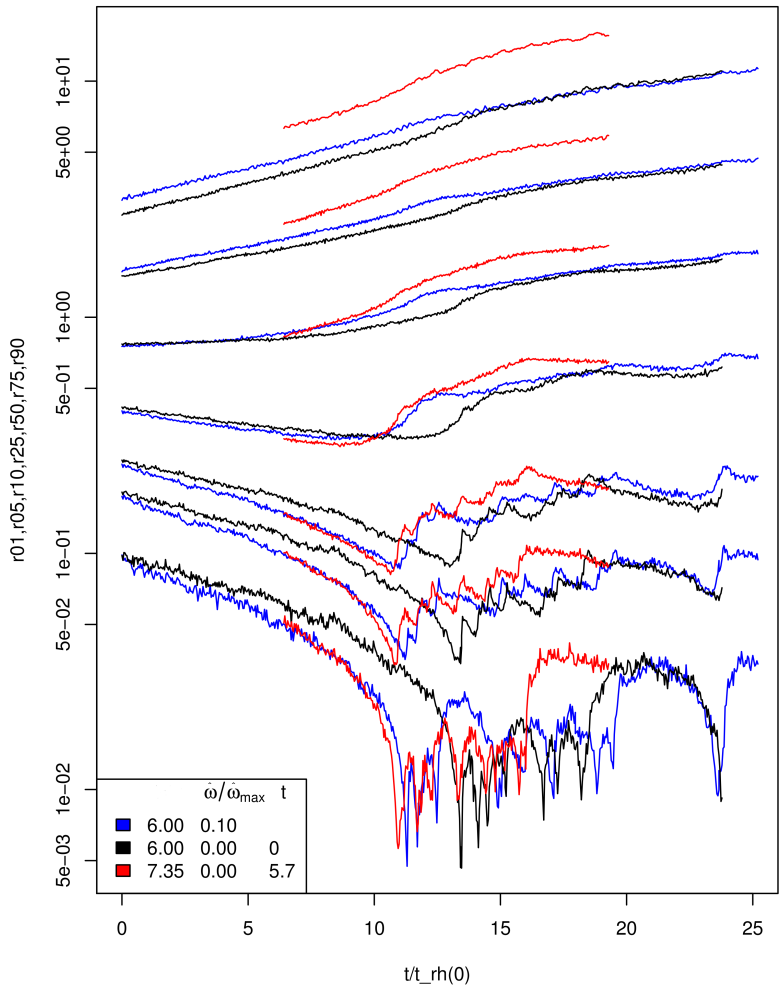

Figure 6.2: Evolution of selected lagrangian radii of the differentially model with $\Psi = 6$ and $\hat{\omega}/\hat{\omega}_{max} = 0.10$ (C600R10, blue lines). The rotating model is compared with two nonrotating models (with $\Psi = 6$ and $\Psi = 7.35$, marked with black anf red lines, respectively), which are structurally equivalent to the rotating configuration at $t/t_{rh}(0) = 0$ and $t/t_{rh}(0) = 5.7$, respectively.

the dynamical evolution of a dense stellar system can be interpreted, in a first-order description, as a sequence of equilibrum configurations characterized by increasing values of central concentration. Note that the additional nonrotating models experience core collapse at approximately the same moment of the rotating models. This result confirms that, in the second phase, the presence of internal rotation no longer significantly affect the dynamical evolution of the configurations. In addition, this analysis sets a superior limit ($t/t_{rh}(0) \approx 5.5$) to time at which the rotating configurations experience the transition from the first to the second phase.

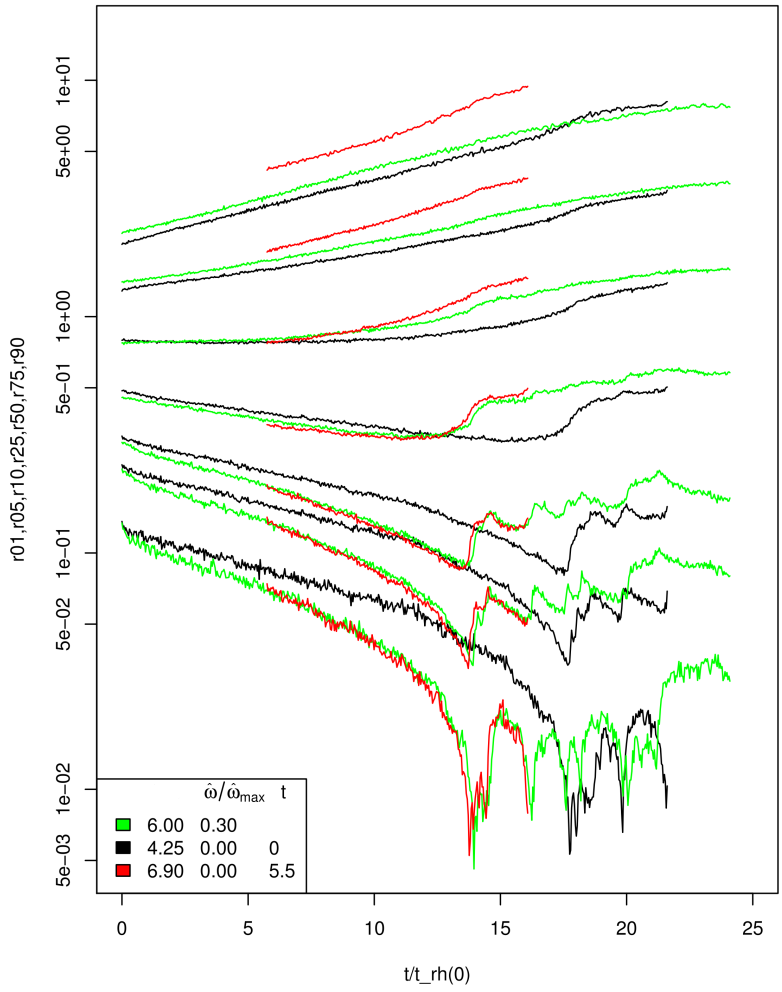

Figure 6.3: Evolution of selected lagrangian radii of the differentially model with $\Psi = 6$ and $\hat{\omega}/\hat{\omega}_{max} = 0.30$ (C600R30, green lines). The rotating model is compared with two nonrotating models (with $\Psi = 4.25$ and $\Psi = 6.90$, marked with black anf red lines, respectively), which are structurally equivalent to the rotating configuration at $t/t_{rh}(0) = 0$ and $t/t_{rh}(0) = 5.5$, respectively.

To further characterize the two phases of the evolution, we studied the distribution of z-component of the angular momentum j_z within the spherical lagrangian radii used as reference in the previous analysis. The evolution of j_z for the C600R10 and C600R30 rotating models is represented in Figs. 6.4 and 6.5, respectively. From the inspection of the previous figures, it appears that, whitin a rotation configuration, the angular momentum is transported outward, as the angular momentum in the inner lagrangian shells experiences a significant decrease, while in the outer ones a mild increase.

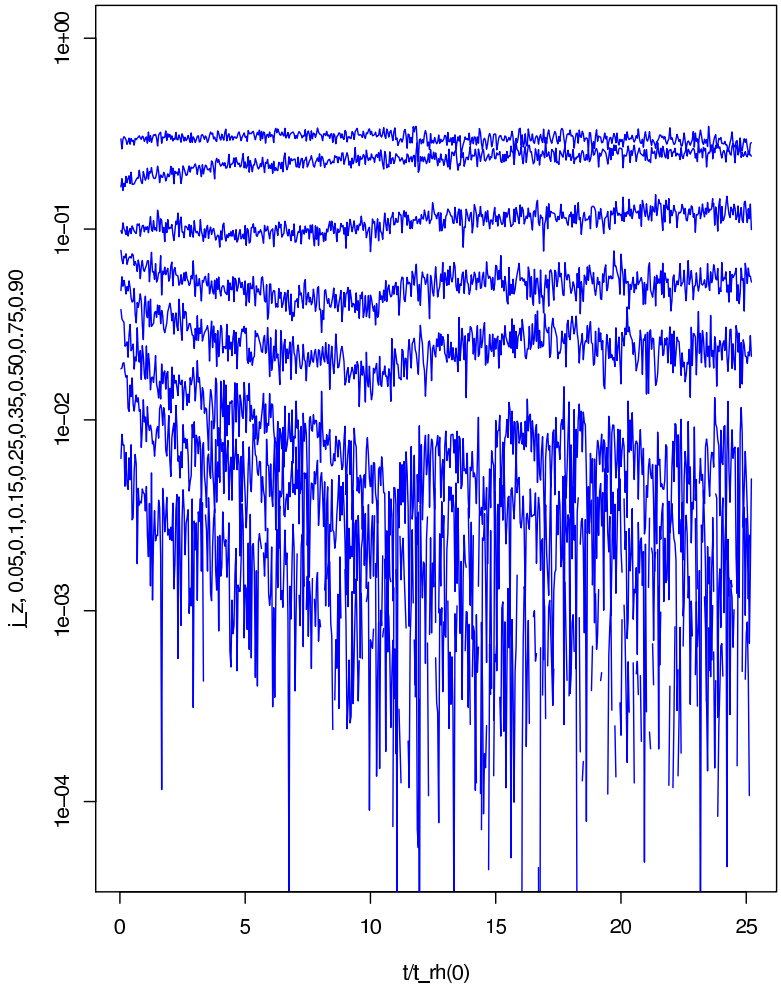

Figure 6.4: Evolution of the distribution of the z-component of the angular momentum j_z, in selected lagrangian shells, for the differentially rotating model with $\Psi = 6$ and $\hat{\omega}/\hat{\omega}_{max} = 0.10$ (C600R10).

In addition, we also studied the evolution of selected local structural and kinematical properties, namely the density, the velocity dispersion, and the ratio between ordered and random motions V/σ, evaluated in the very central region of the rotating models under consideration (i.e., calculated with reference to a thin disk on the equatorial plane enclosing 3% of the total mass of the system; see Figs. 6.6 and6.7, for model C600R10 and C600R30, respectively). In particular, from the inspection of the evolution of the central values of V/σ (see Figs. 6.6.c and6.7.c), it results that such quantity drops significantly during the first phase of evolution, meaning that the presence of ordered motions in the central regions becomes less significant.

The previous result should be interpreted with reference to the evolution of the global kinematical quantity $t = T/|W|$, that is, the ratio between the kinetic energy and the magnitude of the gravitational energy of the system (see Fig. 6.8). From the inspec-

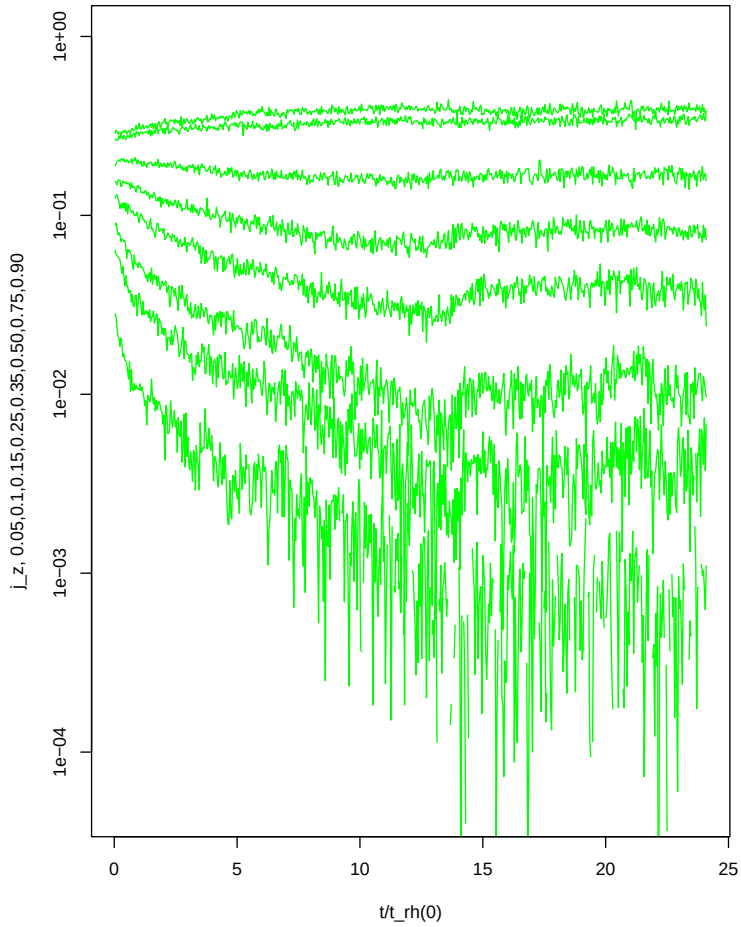

Figure 6.5: Evolution of the distribution of the z-component of the angular momentum j_z, in selected lagrangian shells, for the differentially rotating model with $\Psi = 6$ and $\hat{\omega}/\hat{\omega}_{max} = 0.30$ (C600R30).

tion of the evolution of such global quantity, the existence of the two phases is clearly visible, the first phase being again characterized by a rapid decrease, which should be interpreted as evidence of the fact that the energy contribution of the ordered motions is becoming less significant. Therefore, from the evolution of the central value of V/σ and of $T/|W|$, it seems that the presence of internal rotation affects the dynamical evoltuion of the systems only if the amount in the central regions is nonnegligible, although the the configuration may still be characterized by nonvanishing global angular momentum.

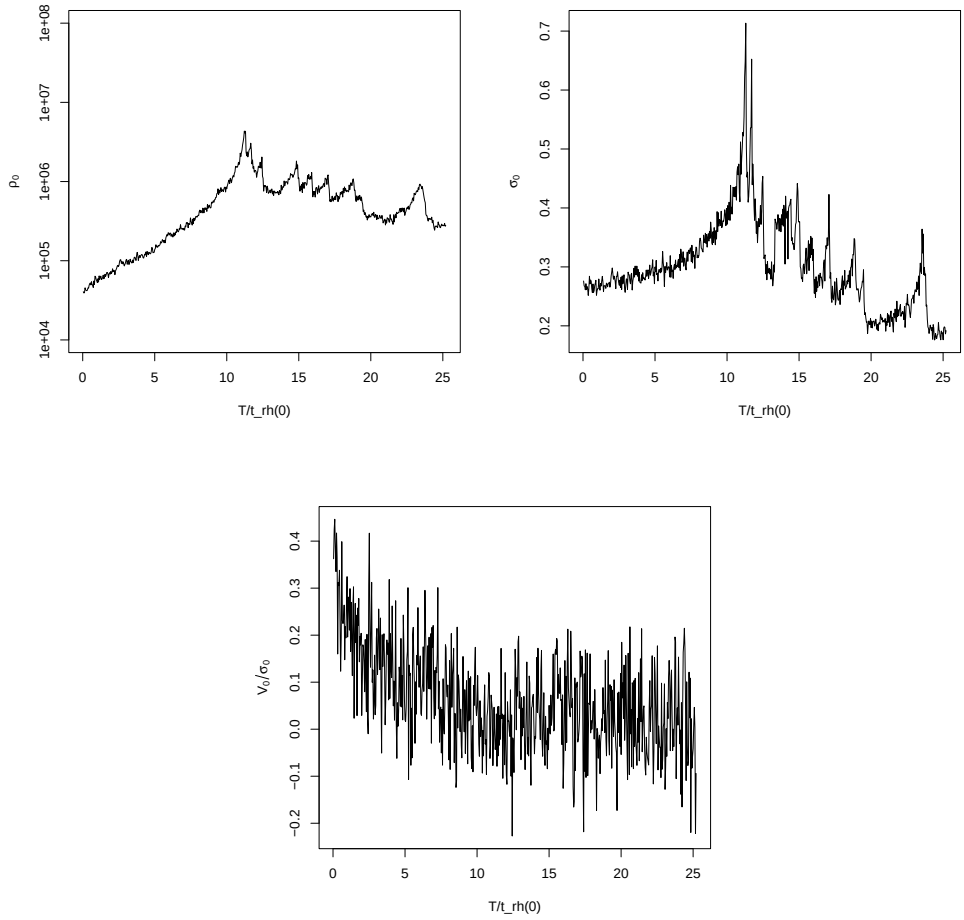

Figure 6.6: Evolution of the central properties of the differentially rotating model with $\Psi = 6$ and $\hat{\omega}/\hat{\omega}_{max} = 0.10$. From top left to bottom, clockwise: (a) central density, (b) central velocity dispersion, (d) central value of the ratio V/σ.

6.4 Conclusions

The analysis discussed in the present Chapter is the result of a preliminary investigation, as the description of the dynamical evolution of the relevant rotating models in terms of additional local and global diagnostics tools is currently in progress, with particular attention to the morphological evolution of the configurations. The first results of this study can be therefore summarized as follows:

- Following the early investigations by Akiyama & Sugimoto (1989) and Einsel & Spurzem (1999), we have interpreted the long-term dynamical evolution of a rotating stellar system by distinguishing between a first phase, in which the gravo-gyro instability takes place and subsequently levels off, and a second phase in which the system experiences the gravothermal catastrophe and reaches the core collapse, as

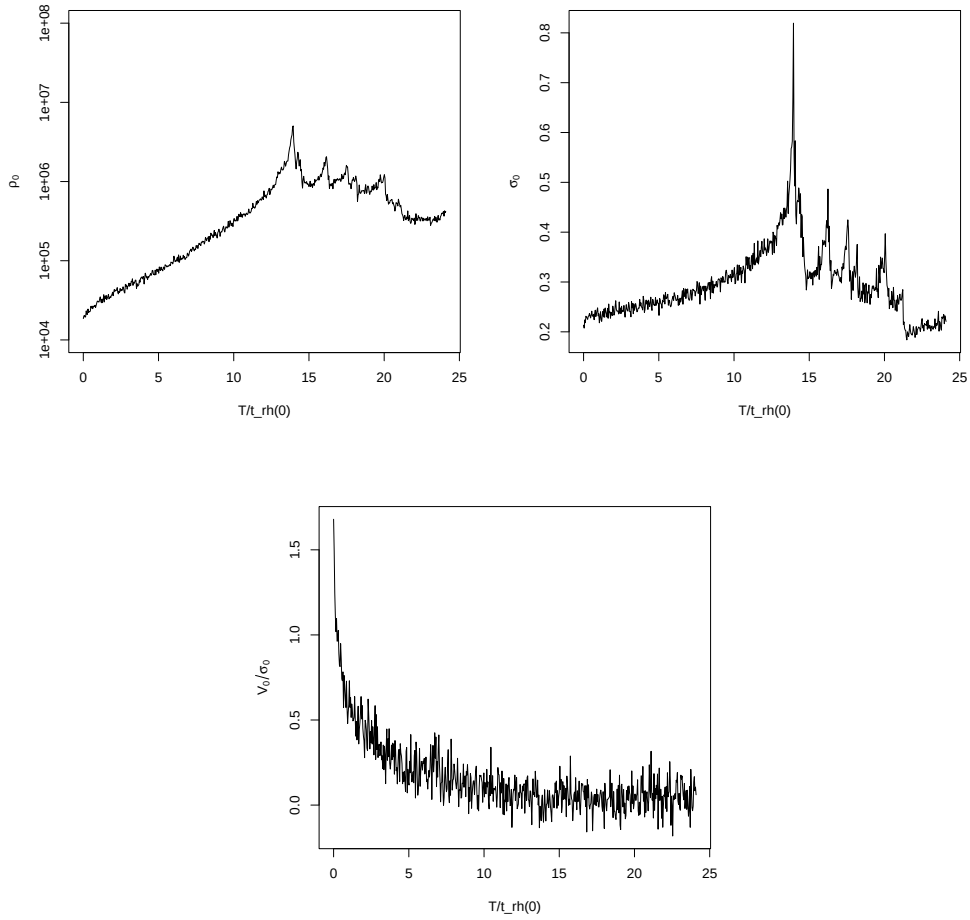

Figure 6.7: Evolution of the central properties of the differentially rotating model with $\Psi = 6$ and $\hat{\omega}/\hat{\omega}_{max} = 0.30$. From top left to bottom, clockwise: (a) central density, (b) central velocity dispersion, (d) central value of the ratio V/σ.

it happens for nonrotating configurations.

- A proper comparison between rotating and nonrotating configurations requires great attention to the initial structural properties of the models. The evaluation of simple sequences of models characterized by the same value of the concentration parameter and an increasing value of the rotation parameter can be misleading.

- A rotating model with the same initial structural properties of a nonrotating one reaches core- collapse more rapidly, as an effect of the internal rotation in the early phase of the dynamical evolution.

- Gravo-gyro instability takes place in the first phase of the long-term evolution and induces a nonnegligible variation of the structure of a rotating configuration, es-

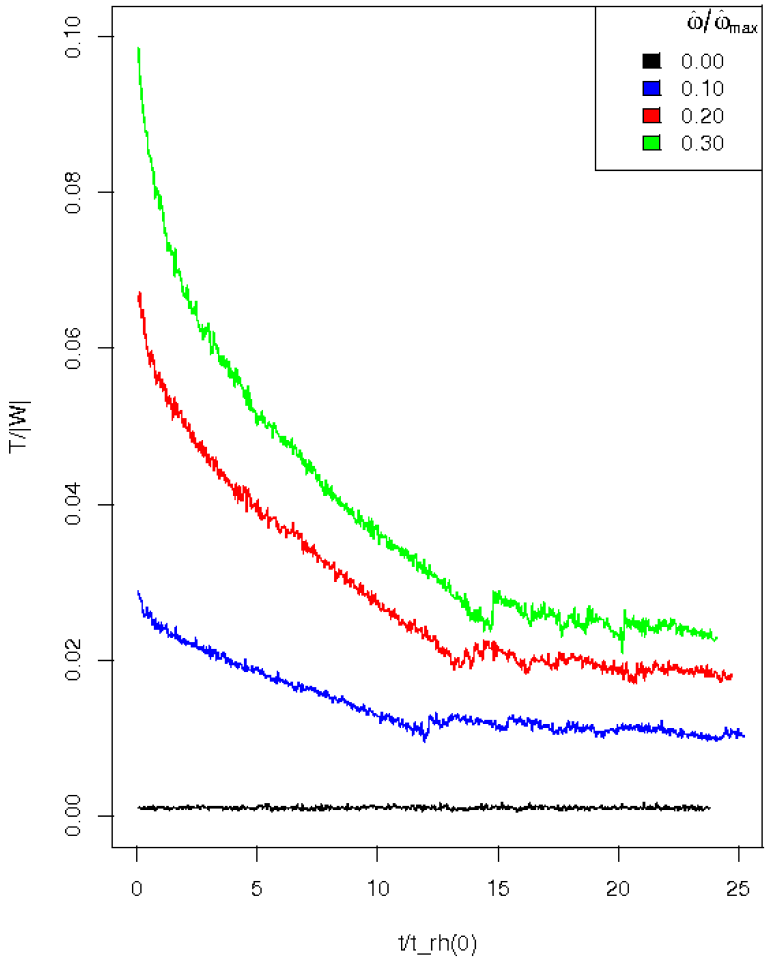

Figure 6.8: Evolution of the parameter $T/|W|$ for differentially rotating models DRM with $\Psi = 6$ and $\hat{\omega}/\hat{\omega}_{max} = 0.00, 0.10, 0.20, 0.30$ (black, blue, red, and green lines, respectively).

pecially in the central regions, which seems to be responsible for the subsequent alteration of the core-collapse time scale.

- Two-body relaxation processes induce angular momentum transport toward the outer parts of a rotating configuration, significantly reducing the amount of rotation in the center. After a few half-mass relaxation times, the presence of internal rotation (mainly located beyond the half-mass radius) no longer affects the evolution of the configuration.
- We decided to focus our attention first on the study of models in the moderate rotation regime because they seem to be particularly appropriate for describing

rotating globular clusters, since the relevant configurations are characterized by a number of realistic properties, such as the presence of nonmonotonic ellipticity profile, the behavior of surface density profile in the outer parts similar to the one associated with spherical Wilson models, the existence of pressure isotropy in the central regions and tangentially-biased anisotropy at the boundary, as well as realistic values of the ratio V/σ (see Chapter 7 for the application to selected Galactic globular clusters). We should mention that the study of the long-term evolution of configurations in the regime of strong differential rotation may be relevant for stellar systems characterized by higher values of internal rotation, such as low-luminosity ellipticals and bulges; this analysis will be the subject of future investigations.

CHAPTER 7

Observational signatures of internal rotation in Galactic globular clusters

7.1 Introduction

As discussed in Chapter 1, spherical isotropic models (in particular, the King 1966 models and the spherical Wilson 1975 models) have indeed been shown to provide a satisfactory zero-order description of the main observed dynamical properties of globular clusters (for a recent dynamical study of large samples of globular clusters, see McLaughlin & van der Marel 2005).

However, the acquisition of high-quality data is rapidly bringing us well beyond such simple picture. In particular, deviations from sphericity have been observed and measured (see Geyer et al. 1983, WS87, and CC10; see also Sect. 1.1.1 for a general comment on ellipticity measurements). In addition, significant internal rotation has been detected in a growing number of Galactic globular clusters from line-of-sight velocity measurements (see Sects. 1.1.1 and 1.4.3 for an extended introductory discussion) and, in a few cases, from kinematical measurements in the plane of the sky (e.g., for M22 see Peterson & Cudworth 1994, for ω Cen see Le Poole & van Leeuwen 2002, and for 47 Tuc see Anderson & King 2003). Detailed three-dimensional kinematics are thus available for selected Galactic clusters. As to the measurement of proper motions, the Hubble Space Telescope (HST) is best used to probe the central regions of the systems (McLaughlin et al. 2006; Anderson & van der Marel 2010), whereas ground-based observations are considered for wide-field coverage (van Leeuwen et al. 2000; Bellini et al. 2009; Sariya et al. 2012). The future mission GAIA is planned to provide three-dimensional kinematical data for a large number of stars in globular clusters (except for the center of very dense objects affected by crowding). All this progress calls for the development of a more complex and realistic dynamical modeling framework, in which internal rotation and deviations form sphericity are fully taken into consideration.

Internal rotation, external tides, and pressure anisotropy are the main physical factors that could be responsible for the observed flattening of globular clusters, but we still do not know which is the dominant cause of the observed deviations from spherical symmetry (van den Bergh 2008). The suggestion that internal rotation plays a role in determining the structure and morphology of globular clusters is not new (King 1961; Fall & Frenk 1985). However, in only few cases has internal rotation been studied by a quantitative application of nonspherical rotating dynamical models. In this respect, the most significant examples are the orbit-based axisymmetric modeling of ω Cen and M15 (van de Ven et al. 2006; van den Bosch et al. 2006, respectively), the study of ω Cen by means of axisymmetric Wilson 1975 models (Sollima et al. 2009), and the analysis of the internal dynamics of a small sample of Galactic globular clusters by means of dedicated 2D Fokker-Planck models (Fiestas et al. 2006).

Internal rotation may also play an indirect role in the controversial issue of the presence of Intermediate Mass Black Holes (IMBH) in globular clusters. In fact, sizable central gradients in the velocity dispersion profiles are often ascribed to the presence of an IMBH, because a massive IMBH can influence stellar kinematics out to the half-mass radius of the cluster (Baumgardt et al. 2005b). A critical discussion of the observed gradients is often reduced to the application of the Jeans equations in which variations of the slope of the velocity dispersion profile are obtained by varying only the amount of pressure anisotropy (without considering rotation; e.g., see Lützgendorf et al. 2011 and Anderson & van der Marel 2010). However, differential rotation and pressure anisotropy can cooperate to produce nontrivial gradients in the velocity dispersion profiles (see Chapter 4) and might thus be an important element to be considered in the interpretation of the data.

In the present Chapter we apply the family of differentially rotating global models introduced in Chapter 4 to three Galactic globular clusters, namely ω Cen, 47 Tuc, and M15, that have been observed in great detail and are known to exhibit evidence for rotation. The differential behavior of the rotation profile has been clearly noted in ω Cen and 47 Tuc (Meylan & Mayor 1986) , for which the ellipticity profiles are also available, even though they are not radially extended as desired. The dynamical models will be compared with the relevant photometric and kinematic observables, with particular attention to the global characteristics of the three-dimensional kinematics. The selection of the appropriate dynamical models will allow us to obtain also an estimate of the distance of the clusters. Furthermore, by taking into consideration the inclination angle of the rotation axis of the stellar systems with respect to the line-of-sight, we will perform a detailed analysis of the morphology of the three clusters, thus testing whether, for these cases, the observed deviations from spherical symmetry can be explained by rotation. The three clusters are known to be in different relaxation states (according to the categorization that will be introduced in Chapter 8, 47 Tuc and M15, with $\log T_c < 8$, fall in the class of fully relaxed clusters, whereas ω Cen, with $\log T_c < 9$, should be considered as only partially relaxed; T_c indicates the core relaxation time expressed in years). Given the physical arguments used to introduce the distribution function $f^d_{WT}(I)$, the degree of relaxation will be an element to be considered in the final assessment of the quality of the fits obtained in this study.

The Chapter is organized as follows. In Sect. 7.2 we present the available data sets for ω Cen, 47 Tuc, and M15 and describe the procedure followed to construct the profiles of the relevant photometric and kinematic observables. In Sect. 7.3 we introduce the method used to identify the dynamical models that best reproduce the data available for the three clusters. In Sect. 7.4 we provide some general remarks on the analysis. The detailed results on ω Cen, 47 Tuc, and M15 are reported in Sects. 7.5, 7.6, and 7.7. Finally, in Sect. 7.9 we summarize the conclusions that can be drawn from our study.

7.2 Observational data and relevant profiles

In this section we describe the kinematic and photometric data sets that will be considered in the dynamical analysis and the methods used to construct the relevant profiles, with particular attention to the construction of the rotation profiles. Table 7.1 summarizes the basic properties of the globular clusters ω Cen, 47 Tuc and M15, based primarily on the Harris 2010 catalog, with additional information about the data sets considered in the present Chapter.

7.2.1 Kinematic data

To construct radially extended kinematic profiles, the kinematic data sets have been selected by considering two main requirements: the kinematic data points should (1) cover a wide radial extent of the cluster, with good coverage also of the central regions, (2) be uniformly distributed in the plane of the sky. To meet these requirements, we decided to combine different data sets, when necessary, as described below.

For ω Cen, two different data sets of line-of-sight velocities are considered: 1589 line-of-sight velocities from Reijns et al. (2006) and 649 line-of-sight velocities from Pancino et al. (2007) for the central part of the cluster. After removing the stars in common between the two samples, the final combined data set is composed of $N_{\rm los}$=1868 data, reaching a radial extent of approximately half truncation radius, with an average error of 1.98 km s^{-1}. The proper motions are taken from van Leeuwen et al. (2000), with a total of 9847 ground-based measured proper motions; each star is provided with a membership probability and is classified according to the disturbance of the image due to neighboring stars on a scale from 0 to 4 (i.e., from nondisturbed to highly disturbed stars). We decided to select a subsample composed of stars with a membership probability higher than 68%, belonging to class 0, and with error measurements lower than 0.25 mas yr^{-1} (for a similar selection, see van de Ven et al. 2006). The final sample is thus composed of $N_{\rm pm}$ = 2740 proper motions, with a radial extent of approximately half truncation radius and an average error of 0.16 mas yr^{-1} (corresponding to 3.89 km s^{-1} for an assumed distance of 5.2 kpc).

For 47 Tuc, the line-of-sight velocities data set results from two data sets combined by following the procedure described in Chapter 8: 499 line-of-sight velocities from Gebhardt et al. (1995) for the inner region ($R < 100$ arcsec) and 1977 line-of-sight velocities from Lane et al. (2011) for the outer parts ($R > 100$ arcsec). As noted in Lane et al. (2011), the latter data set shows a mean velocity of -16.85 km s^{-1}, which differs significantly from the value obtained from the former data set, -18.34 km s^{-1}; this is likely to be due to a systematic uncertainty between the zero-point of the two velocity systems. To correct for this offset we have subtracted from each data set the corresponding measured mean velocities. The final line-of-sight velocities sample is composed of $N_{\rm los}$ = 2476 velocities covering the entire radial extent of the cluster and with an average error of 2.29 km s^{-1}. The proper motions are taken from McLaughlin et al. (2006), which is a data set composed of N$_{pm}$ = 12 974 Hubble Space Telescope proper motions selected on the basis of the star magnitude (V<20) and quality (i.e., we consider data with probability $P(\chi^2) > 0.001$); unfortunately, the data cover only the central region out to ≈100 arcsec (approximately 4 core radii); the measurements have an average error of 0.27 mas yr^{-1} (corresponding to 5.76 km s^{-1} at a distance of 4.5 kpc).

For M15 we used a single data set composed of $N_{\rm los}$ = 1777 line-of-sight velocities from Gebhardt et al. (2000); this sample is centrally concentrated, with $\approx$ 80% of the stars being inside $10\,R_c$ and with an average error of 3.79 km s^{-1}. In addition, we used the sample of $N_{\rm pm}$ = 703 Hubble Space Telescope proper motions in the central region of the cluster (R< $2\,R_c$), as reported by McNamara et al. (2003), with an average error of 0.14 mas yr^{-1} (corresponding to 6.79 km s^{-1} at a distance of 10.2 kpc).

We recall that the procedure used to obtain the proper motions data sets described above will not reveal any solid body rotation in the plane of the sky, as well as any systematic motions of contraction or expansion (e.g., see Vasilevskis et al. 1979; McLaughlin et al. 2006; Anderson & van der Marel 2010), because the proper motions measurements are relative measurements (no absolute reference frame is available for measuring the star displacements at different epochs). van de Ven et al. (2006) show how to compen-

Table 7.1: Properties of ω Cen, 47 Tuc, and M15.

Globular Cluster	$d_\odot$	R_c	C	$\log T_\mathrm{c}$	ε		ϕ	PA	i	N_los	N_pm
	(1)	(2)	(3)	(4)	(5)	(6)	(7)	(8)	(9)	(10)	(11)
ω Cen	5.2	142.20	1.31	9.60	0.21	0.17	6	12	50	1868	2740
47 Tuc	4.5	21.60	2.07	7.84	0.16	0.09	123	136	45	2476	12 974
M15	10.4	8.40	2.29	7.84	0.19	0.05	215	106	60	1777	703

Notes. For each cluster we list: (1) the distance from the Sun $d_\odot$ in kpc; (2) the core radius R_c in $''$; (3) the concentration parameter C; (4) the logarithm of the core relaxation time $\log T_\mathrm{c}$ in years; the ellipticity $\varepsilon = 1 - b/a$, as reported by (5) CC10 and (6) WS87; (7) the position angle of the photometric minor axis ϕ measured in degrees (from North to East); (8) the position angle of the kinematic rotation axis PA on the plane of the sky measured in degrees (from North to East); (9) the inclination i of the rotation axis with respect to the line-of-sight measured in degrees; the number of data points for the samples of (10) line-of-sight velocities N_los and (11) proper motions N_pm.

References. From Col. (1) to Col. (4) Harris (2010); Col. (5) CC10; Cols. (6) and (7) WS87; Col. (9) van de Ven et al. (2006), Anderson & King (2003), van den Bosch et al. (2006) (from top to bottom, that is, for ω Cen, 47 Tuc, and M15, respectively); Cols. (8), (10), and (11) the present work.

sate for the missed solid body component under the assumption of axisymmetry, by combining line-of-sight velocities and proper motions. We apply the related correction to the ω Cen data. For 47 Tuc and M15, given the fact that the data sets are centrally concentrated, we argue that, in the very central regions of the clusters, the amount of solid body rotation associated with this effect is negligible and therefore we do not apply any correction (see van den Bosch et al. 2006, who first noted that the result of the correction for M15 is below the measurement errors and therefore can be ignored). Therefore, for the last two clusters no sign of rotation in the plane of the sky is expected from the proper motions data sets considered above; however, for 47 Tuc rotation in the plane of the sky has been clearly detected by Anderson & King (2003).

Finally, an additional correction is applied to the ω Cen and 47 Tuc data, to correct for the apparent rotation resulting from their large angular extent and their global orbital motion in the Galaxy; to this purpose, we followed closely the procedure described by van de Ven et al. (2006).

Coordinate systems

A common coordinate system for the line-of-sight velocities and proper motions data sets must be defined. This is identified by the Cartesian coordinate system (X,Y), the origin of which corresponds to the center of the cluster, with X in the West direction and Y in the North direction. Given the position of every star in equatorial coordinates (α,δ), the corresponding Cartesian coordinates can be expressed as (see van de Ven et al. 2006)

$$\begin{aligned} X &= -\gamma_0 \cos\delta \sin\Delta\alpha \\ Y &= \gamma_0(\sin\delta\cos\delta_0 - \cos\delta\sin\delta_0\cos\Delta\alpha), \end{aligned} \tag{7.1}$$

where $\Delta\alpha = \alpha - \alpha_0$ and (α_0, δ_0) is the position of the center of the cluster. The scaling factor $\gamma_0 = 10800/\pi$ gives the coordinates in arcminutes.

An additional change of coordinates is needed to align the vertical and the horizontal axes with the observed minor and major axes of the cluster. This is done by rotating (X,Y) over the position angle (PA) of the minor axis, which is defined as the angle between the minor axis and the North direction (measured from North to East); the procedure used to measure this position angle is described in Subsect. 7.2.2. The new coordinate system in the plane of the sky is defined by (x_p, y_p), with x_p and y_p aligned with the major and minor axes, respectively. The z_p axis identifies the line-of-sight direction.

Finally, in the following analysis we will refer to proper motions as decomposed in a polar coordinate system (R, Θ), with the projected radius $R = \sqrt{x_p^2 + y_p^2}$ and Θ defining the angle between $\vec{R}$ and x_p. The relation between proper motions in polar coordinates (μ_R, μ_t) and proper motions in Cartesian coordinates (μ_{x_p}, μ_{y_p}) is given by

$$\begin{aligned} \mu_R &= \mu_{x_p}\cos\Theta + \mu_{y_p}\sin\Theta \\ \mu_t &= -\mu_{x_p}\cos\Theta + \mu_{y_p}\sin\Theta. \end{aligned} \tag{7.2}$$

Stars as kinematic tracers

In the dynamical analysis we will assume that the stars are fair kinematic tracers of the true underlying stellar mass population of the system. Because our dynamical models are one-component models, they assume that the underlying stellar population is homogeneous. In reality, the presence of multiple stellar populations and mass segregation would induce different spatial distributions and kinematics for masses of different

types. Indeed, Anderson & van der Marel (2010) noted that in their sample of proper motions referred to the central region of ω Cen, stars with lower masses tend to have higher velocity dispersion, although not as high as complete equipartition would predict ($\sigma \propto m^{-1/2}$); therefore, this problem should be discussed in further detail. Even though a deeper analysis would bring us beyond the goals of the present study, we would like to mention at least that some caution will be required in the final interpretation of our results from the adopted kinematic data sets. In fact, in our study we will carry out a dynamical analysis using both line-of-sight velocities and proper motions: usually stars for which we have proper motions (measured with HST) are less massive than stars for which we have line-of-sight measurements; the latter are relatively bright stars from the giant or subgiant branch, whereas the former are main sequence stars.

7.2.2 Kinematic profiles

The present dynamical study is based on a combined analysis of the following kinematic profiles: (1) three rotation profiles, (2) three velocity dispersion profiles, and (3) the pressure anisotropy profile. The general procedure adopted to construct the kinematic profiles is the traditional binning approach, that is, the data are divided in bins containing an equal number of stars. In particular, radial bins are used to construct the velocity dispersions and anisotropy profiles, whereas the line-of-sight rotation profile is constructed by taking into consideration exclusively the data along the observed major axis. As in Chapter 8, we chose a binning criterion that represents the best compromise between having a rich radial sampling and accurate data points.

To calculate the mean velocity and the velocity dispersion, with the associated errors, a Maximum Likelihood technique is applied to the data, following the method described by Pryor & Meylan (1993). The details of the procedure used to obtain the different profiles are given below.

Rotation profiles

The first step in building a rotation profile consists in identifying the position angle (PA) of the projected rotation axis in the plane of the sky. To identify the PA the following standard procedure is used (e.g., see Cote et al. 1995; Bellazzini et al. 2012): the line-of-sight velocities data set is divided in two halves by a line passing through the center with a given PA and for each subsample the mean line-of-sight velocity is computed; the PA is varied in steps of 10° and the difference between the mean velocities ΔV is plotted against PA. The resulting pattern is fitted with a sine function (see Fig. 7.1): the PA at which the maximum difference in mean velocities is reached corresponds to the rotation axis and the amplitude of the sine function gives an estimate of the significance of the internal rotation. The values obtained for the PA are used to rotate the Cartesian coordinate system in the plane of the sky by aligning x_p and y_p with the major and minor axes, respectively (Subsect. 7.2.1). The results are listed in Tab. 7.1 and compared to the position angles of the photometric minor axes ϕ reported by WS87.

The position angles of the kinematic minor axes of ω Cen and 47 Tuc are in good agreement with the photometric ones, suggesting a direct connection between the presence of internal rotation and observed flattening. A discrepancy is found instead for M15: for this cluster the small observed flattening ($\varepsilon \approx 0.05$) makes the identification of the minor axis nontrivial. Various estimates of the photometric position angle are given in the literature, ranging from 215° to 135°, suggesting a possible twisting of the position angle of both the photometric and kinematic minor axes (Gebhardt et al. 2000; van den

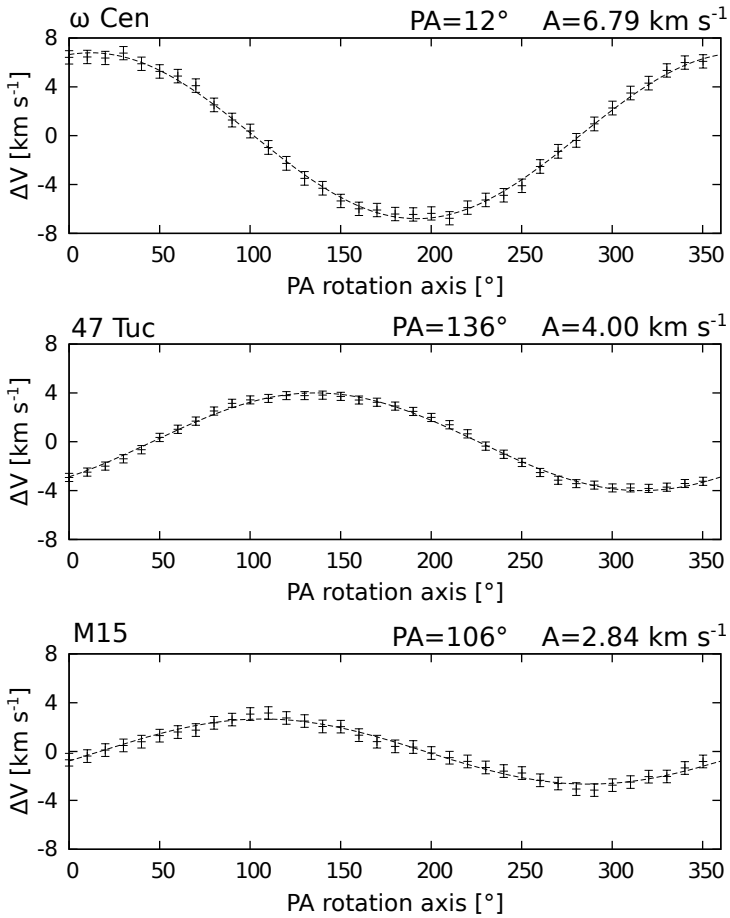

Figure 7.1: Difference of the mean velocities calculated on each side of the system divided by a line passing through the center with a given position angle PA. The PA at which the maximum difference is reached corresponds to the position of the rotation axis. The best-fit sine function in plotted (solid line) and the corresponding PA and amplitude A are indicated.

Bosch et al. 2006).

Table 7.2: Internal rotation: position angle of the rotation axis and rotation amplitude referred to disks of different radii.

ω Cen				47 Tuc			
$R_{\max}$	A	PA	N	$R_{\max}$	A	PA	N
(1)	(2)	(3)	(4)	(1)	(2)	(3)	(4)
all	6.79	12	1868	*all*	4.00	136	2476
$10\,R_c$	6.91	12	1827	$80\,R_c$	4.11	136	2414
$8\,R_c$	7.09	10	1737	$40\,R_c$	4.41	137	2058
$6\,R_c$	7.73	7	1481	$20\,R_c$	4.53	136	1358
$4\,R_c$	7.58	11	1026	$10\,R_c$	3.32	139	800
$2\,R_c$	6.95	22	398	$5\,R_c$	2.24	164	526
$1\,R_c$	3.97	57	91	$2\,R_c$	2.64	180	388
$0.9\,R_c$	1.25	-4	73	$1\,R_c$	4.07	199	114
$0.7\,R_c$	1.98	23	42	$0.8\,R_c$	4.05	171	78
$0.6\,R_c$	7.04	10	27	$0.7\,R_c$	5.99	167	61
$0.5\,R_c$	13.93	-8	19	$0.6\,R_c$	4.78	206	39

M15			
$R_{\max}$	A	PA	N
(1)	(2)	(3)	(4)
all	2.84	106	1777
$30\,R_c$	2.89	106	1671
$10\,R_c$	2.93	102	1467
$8\,R_c$	3.00	99	1293
$5\,R_c$	1.94	118	916
$4\,R_c$	1.43	140	724
$2\,R_c$	2.14	147	319
$1\,R_c$	1.19	253	128
$0.6\,R_c$	4.68	272	65
$0.5\,R_c$	6.95	253	52
$0.4\,R_c$	13.00	261	31

Notes. For each cluster we report the value of the position angle of the rotation axis PA measured in degrees from North to East [Col. (3)] and the rotation amplitude A in km s^{-1} [Col. (2)] obtained from a fit of a sine function of N data [Col. (4)] inside $R_{\max}$ [Col. (1)]. For each cluster, the first row corresponds to the results illustrated in Fig. 1.

We also checked whether a radial variation of the position angle and of the rotation amplitude is present in our line-of-sight data sets. To do so, we repeated the procedure outlined above on subsamples of data with $R < R_{\max}$, for decreasing values of $R_{\max}$. Table 7.2 lists the position angles and rotation amplitudes for given values of $R_{\max}$. To assess whether the number of data available for the different cases is sufficiently large to reach a significant measure of the position angles and of the rotation amplitudes, we tested the method used on simulated data drawn from a rotating model of the family introduced in Sect. 7.1. We find that the estimates of the position angles obtained from samples of data with $N \lesssim 100$ have a typical uncertainty (associated with a 68% confidence level) greater than $\pm 25°$. We conclude that no significant PA variation is present

in 47 Tuc and ω Cen, whereas for M15 a twisting is detected from 260° in the innermost region (on the scale of the core radius) to 106° in the outer parts (thus confirming the result found by Gebhardt et al. 2000).

Moreover, we found that the rotation amplitude A changes across the clusters. In general, it reaches a maximum at intermediate values of $R_{\max}$. This can be taken as an indication of differential rotation (as illustrated by the shape of the rotation profiles, see Figs. 7.2, 7.7, and 7.11). Interestingly, all three clusters show a sharp increase of the rotation amplitude in the very central regions. This feature may be interpreted as a signature of a complex rotation pattern, characterized by spinning cores, as reported by van de Ven et al. (2006) and van den Bosch et al. (2006), for a disk-like rotating component in ω Cen and a decoupled rotating core in M15. The last rows in Tab. 7.2 show that ω Cen reaches an amplitude of $A = 13.93$ km s^{-1} for $R < 0.5\,R_c$, 47 Tuc $A = 4.78$ km s^{-1} for $R < 0.6\,R_c$ and M15 $A = 13.00$ km s^{-1} for $R < 0.4\,R_c$. The probability of measuring so high rotation amplitudes by chance when no rotation is present is 7%, 32%, and $\lesssim 1\%$ for ω Cen, 47 Tuc, and M15, respectively. We conclude that the central increase measured in 47 Tuc is not statistically significant, whereas it can be taken as a sign of genuine high rotation in the central regions of M15; this interpretation marginally applies also to the case of ω Cen.

After identifying the rotation axis, we can now proceed to build the rotation profiles. First we subtract from each data set the measured mean systemic velocity; then we divide the line-of-sight velocities data set in bins along the major axis x_p; each bin is assigned an x_i position calculated as the mean of the x positions of the stars in the bin. Finally, the mean velocity in every bin is computed. In the case of the proper motion data set, the rotation profile is constructed by dividing the data set in radial bins and by computing for each of them the mean radial distance and the mean velocity, separately for the tangential and projected radial components. We then end up with three rotation profiles, one for the line-of-sight, $V_{\rm los}(x_p)$, and two for the proper motions, $V_{\rm t}(R)$ and $V_{\rm R}(R)$.

Velocity dispersion and anisotropy profiles

The velocity dispersion profiles are computed by dividing the data sets in radial bins; by considering the mean velocity of the entire data set as a constant value throughout the cluster, we calculate the velocity dispersion for each bin with the associated uncertainty. The profiles obtained are $\sigma_{\rm los}(R)$, $\sigma_{\rm t}(R)$, and $\sigma_{\rm R}(R)$, respectively for the line-of-sight velocities, tangential component and projected radial component of proper motions.

From the dispersion profiles of the proper motions we also calculate the anisotropy profile: this is defined here as the ratio of the velocity dispersion in the tangential component to the velocity dispersion in the radial component, $\sigma_{\rm t}(R)/\sigma_{\rm R}(R)$. Values of $\sigma_{\rm t}/\sigma_{\rm R} \approx 1$ indicate isotropy in velocity space, $\sigma_{\rm t}/\sigma_{\rm R} > 1$ indicate the presence of tangential anisotropy, and $\sigma_{\rm t}/\sigma_{\rm R} < 1$ radial anisotropy.

7.2.3 Photometric profiles

The photometric quantities that we will use in the dynamical analysis are the surface brightness profile and the ellipticity profile. Below we briefly describe the data sets available for the construction of these profiles.

Surface brightness profiles

The surface brightness profiles are taken from Trager et al. (1995) and they are treated as in Chapter 8; they are V-band surface-brightness profiles, built by dividing the data in circular annuli, so that the surface brightness $m_{\rm V}(R)$, measured in mag arcsec^{-2}, is reported as a function of projected radius.

Since the central regions correspond to the least reliable parts of the profiles of Trager et al. (1995), a combination of different data sets is needed. The more accurate data available from Noyola & Gebhardt (2006) are used for 47 Tuc and M15. For 47 Tuc the data from the two sources are simply co-added; for M15 the two data sets are combined by removing the points from Trager et al. (1995) that do not agree with the profile by Noyola & Gebhardt (2006). In the case of ω Cen the inner points from Noyola et al. (2008) are added to the Trager et al. (1995) surface-brightness profile.

Ellipticity

From the morphological point of view, globular clusters present only small deviations from spherical symmetry. Yet, there is observational evidence of flattening, as measured by the ellipticity parameter, defined as $\epsilon = 1 - b_p/a_p$, where b_p/a_p is the ratio of the minor to major axis of the projected image of a cluster in the plane of the sky. For a long time, the WS87 database represented the only comprehensive collection of ellipticity measurements for the Galactic globular clusters; recently, an alternative homogeneous database of ellipticities has been published by CC10. The two distributions of values show significant differences: in fact, from the WS87 database (93 objects), Galactic clusters appear to be predominantly round, with the peak of the distribution at $\epsilon \approx 0.05$, maximum value of the entire sample given by $\epsilon \approx 0.3$, and axial ratios randomly oriented in space. In contrast, the distribution of the CC10 ellipticities (116 objects, 82 in common with the other database) is peaked at $\epsilon \approx 0.15$, with the majority of values falling in the range $[0.05, 0.25]$, and maximum value $\epsilon \approx 0.45$. In addition, especially for the clusters in the region of the Galactic bulge, their major axes preferentially point toward the Galactic center.

In the present study we will use the ellipticity profile of ω Cen taken from Geyer et al. (1983). It is the most extended ellipticity profile available for a Galactic globular cluster, as it reaches $\approx 0.5\, r_{\rm tr}$. In addition, Anderson & van der Marel (2010) report the ellipticity profile of the central region ($R \lesssim 250$ arcsec); in the following analysis both data sets will be taken into consideration. For 47 Tuc and M15 we will use the profiles constructed by eye-inspection of Fig. 5 in WS87. They reach $\approx 0.2\, r_{\rm tr}$ and $\approx 0.4\, r_{\rm tr}$, respectively. We note that a genuine radial variation is present in the three ellipticity profiles. This is particularly evident for ω Cen, which exhibits a nonmonotonic behavior.

7.3 Model identification and predictions

In principle, the comparison between the differentially rotating models introduced in Chapter 4 and the observations could be carried out by means of a standard fitting procedure, leading to the best-fit models for the clusters. In addition to the four dimensionless parameters (actually three, because we decided to set $c = 1$; see Sect. 1) that characterize the internal structure of our family of axisymmetric models, the final model to be used for a given cluster requires the specification of five additional quantities: two physical scales (e.g., the radial scale r_0 and the velocity scale v_0); the mass-to-light ratio (to convert density profiles into surface-brightness profiles); the inclination angle i between

the rotation axis and the line-of-sight direction; the distance to the cluster (required to convert the proper motions in km s^{-1}). A parameter space with such a high number of dimensions might lead to a high degree of degeneracy. Therefore, we decided to take a different approach that points directly to the main physical ingredient that we are interested in: the presence of internal rotation. We thus separate the procedure to identify a reasonable model for a cluster in three parts. First, we determine the dimensionless parameters by following few natural selection criteria based on the observed kinematics, then we proceed to set the physical scales by means of a few standard statistical fits, and finally we check some properties of the models as predictions in relation to other observational data not used in the first two steps.

7.3.1 Dimensionless parameters

From Subsection 7.2.2 it is clear that the globular clusters under consideration are characterized by significant global internal rotation. Therefore, we start from the observed rotation properties to identify the natural ranges of the three dimensionless parameters that characterize our family of differentially rotating models. In particular, the parameters should lead to configurations that successfully reproduce the following observations: (1) the observed value of $V_{\rm max}^{\rm rot}/\sigma_0$, that is, the ratio of the peak of the rotation velocity profile to the central velocity dispersion for the line-of-sight kinematic data; (2) the observed shape of the rotation profile along the line-of-sight, in particular the position $R_{\rm max}^{\rm rot}$ of the rotation peak (relative to the cluster half-light radius); (3) the qualitative behavior of the anisotropy profile (when available), defined as the ratio between the tangential and the radial component of the velocity dispersion tensor projected in the plane of the sky, in particular the radial position $R_{\rm a}$ (relative to the half-light radius) of the transition from radial anisotropy to tangential anisotropy. The relevant observational quantities to be matched by application of the above selection criteria are listed in Tab. 7.3.

Table 7.3: Kinematic observables used to identify the dimensionless parameters of a model.

GC	σ_0	$V_{\rm max}^{\rm rot}$	$V_{\rm max}^{\rm rot}/\sigma_0$	$R_{\rm max}^{\rm rot}$	$R_{\rm a}$
	(1)	(2)	(3)	(4)	(5)
ω Cen	17.31	5.80	0.34	1.7	3.45
47 Tuc	13.06	3.26	0.25	1.8	...
M15	12.93	≈ 3.00	0.23	≈ 1.3	...

Notes. For each cluster we report in Col. (1) the observed central line-of-sight velocity dispersion σ_0 in km s^{-1}, in Col. (2) the maximum of the line-of-sight rotation profile $V_{\rm max}^{\rm rot}$ in km s^{-1}, in Col. (3) the ratio $V_{\rm max}^{\rm rot}/\sigma_0$, in Col. (4) the position of the maximum of the rotation profile $R_{\rm max}^{\rm rot}$ expressed in units of the half-light radius $R_{\rm h}$, in Col. (5) the position $R_{\rm a}$ of the transition between the regime of radial anisotropy and tangential anisotropy in units of the half-light radius $R_{\rm h}$. The last three columns guide our choice of the three dimensionless parameters that characterize the internal structure of the models.

Given a set of parameters $(\Psi, \chi, \bar{b})$, the models are projected on the plane of the sky by assuming a known inclination angle i, as reported in Tab. 7.1. The projection is performed by sampling from the relevant distribution function a discrete set of $N = 2\,048\,000$ particles and then by performing a rotation of such discrete system to match the relevant inclination angle. The theoretical kinematic and photometric profiles[1] are

[1]The profiles thus constructed are discrete profiles, which are then interpolated to obtain continuous pro-

then constructed by following the procedures described in Subsections 7.2.2 and 7.2.3. The central dispersion σ_0, the maximum of the rotation profile $V_{\rm max}^{\rm rot}$, and its position $R_{\rm max}^{\rm rot}$ are calculated in view of the above-mentioned selection criteria. As to the morphological aspects, the projected isodensity contours are calculated based on the projected number density distribution, calculated on an equally spaced Cartesian grid defined on the plane of the sky, and then normalized to the central value (calculated as the average of the four central Cartesian cells). The relevant ellipticity profiles are then constructed by considering the ratio of the principal axes of approximately one hundred isodensity contours, corresponding to selected values of the normalized projected number density in the range $[0.9, 10^{-3}]$; smooth profiles are then obtained by performing an average on subsets made of ten to twenty individual ellipticity values (depending on the concentration of the configuration).

The dimensionless parameters are varied until the kinematic selection criteria are reasonably met. The exploration of the complete 3D dimensionless parameter space is guided by the following general properties of the models: (1) large values of the concentration parameter Ψ determine spatially extended configurations, in terms of the relevant units of length (see Chapter 4 for details); (2) configurations characterized by a given value of concentration and increasing values of the rotation strength parameter χ are progressively more compact because of the adopted truncation prescription in phase space, which sets the spatial extent of the models; (3) the parameters $\bar{b}$ determines the shape of the line-of-sight rotation profile (in particular, it regulates the radial position of the velocity peak).

7.3.2 Physical scales

Once a set of dimensionless parameters is identified, we proceed to determine the relevant physical scales. This is done by fitting the models to the observed profiles, that is, by minimizing a chi-squared. Two fits are performed. With the photometric fit to the surface brightness profile we determine two scales: the central surface brightness μ_0 and the radial scale r_0 [the scale r_0 is the standard length scale of King models]. The velocity scale v_0 is determined by means of the kinematic fit, which is performed by minimizing a combined chi-squared defined as the sum of the contributions from the line-of-sight rotation profile and velocity dispersion profile. Finally, the mass-to-light ratio is directly connected to the central surface brightness by the following relation $M/L = \hat{\Sigma}(0) 10^{\mu_0/2.5}$, where $\hat{\Sigma}(0)$ denotes the central surface density expressed in the relevant units. The details of the fitting procedure are given in Appendix B of Zocchi et al. (2012).

7.3.3 Distance measurement

Part of the kinematic information associated with the proper motions is used to make a dynamical measurement of the distance to the cluster. The relation between proper motions μ measured in mas yr^{-1} and proper motions v expressed in km s^{-1} is

$$\left[\frac{v}{\rm km/s}\right] = 4.74 \left[\frac{d}{\rm kpc}\right] \left[\frac{\mu}{\rm mas/yr}\right], \tag{7.3}$$

where d is the distance from the observer to the globular cluster. Therefore, with all the dimensionless parameters and physical scales fixed from the previous analysis, a best-fit

files. The statistical scatter associated with the use of discrete model-points is well under control, given the high number of sampling particles considered.

distance d (hereafter referred to as dynamical distance) is obtained by a combined fit to the observed tangential σ_t and radial σ_R velocity dispersion profiles (i.e., by minimizing a combined chi-squared defined as the sum of the contributions of the two velocity dispersion profiles in the plane of the sky).

7.3.4 Predicted profiles

At this stage for a given cluster the model and the relevant scales have all been determined. A number of other observable quantities are then predicted and the predictions can be checked on the available observations. In particular, we wish to include in this category the following quantities: the anisotropy profile σ_t/σ_R, the proper motion rotation profiles V_t and V_R, the ellipticity profile ϵ, and the 2D structure of the isodensity contours.

7.4 General results

Before providing In the following sections a detailed description of the results for each individual cluster, we summarize here the main properties of the models that have been identified. The values of the dimensionless parameters, the physical scales, and the best-fit dynamical distance for the selected models are listed in Tab. 7.5. In Tab. 7.6 we report the derived structural properties of the clusters.

The procedure outlined in the previous section allows us to identify the self-consistent models that we propose to interpret the observed structure and kinematics of ω Cen, 47 Tuc, and M15. We recall that the procedure starts from a preliminary inspection of the general properties of part of the kinematical data (in particular, the shape of the line-of-sight rotation and velocity dispersion profiles; to identify the three dimensionless parameters that determine the internal structure of the model) that is then followed by a standard statistical analysis to find the relevant physical scales. This approach, which emphasizes the importance of the kinematical data, in particular of those that give evidence for internal rotation, leads quickly and naturally to the identification of a global self-consistent dynamical model. In contrast, the more traditional approach is generally based on a best-fit procedure, frequently carried out, in practice, only in relation to the available photometric profiles (see Trager et al. 1995 and McLaughlin & van der Marel 2005), without the corresponding tests on the associated kinematical profiles that are implied by the use of self-consistent models.

The profiles that contribute to the determination of the physical scales of the models are the line-of-sight rotation profile, the line-of-sight velocity dispersion profile, and the surface brightness profile. The quality of the results is summarized in Figs. 7.2, 7.7, and 7.11 for ω Cen, 47 Tuc, and M15, respectively. The solid lines are the model profiles, the open circles are the observation data points. For the kinematic profiles the data points are associated with a horizontal bar, representing the size of the radial bin, and a vertical bar, indicating the errors associated with the measurements. Quantitative information about the quality of the fits for the determination of the physical scales is given in Tab. 7.4, where the reduced chi-squared, the corresponding two-sided 90% confidence interval (CI), and the number of degrees of freedom are listed. In each case, the value of the photometric chi-squared $\widetilde{\chi}^2_{\rm p}$ is larger than the value of the kinematic chi-squared $\widetilde{\chi}^2_{\rm k}$. This is due to the fact that the kinematic profiles are characterized by a large number of points with larger error bars. Note that the value of the reduced chi-squared of the kinematic fits of M15 is inside the corresponding 90% CI.

Table 7.4: Quality of the fits.

Globular Cluster	Photometric fit				Kinematic fit				Distance fit			
	$n_{\rm p}$	$\widetilde{\chi}^2_{\rm p}$	$\widetilde{\chi}^2_{\rm inf}$	$\widetilde{\chi}^2_{\rm sup}$	$n_{\rm k}$	$\widetilde{\chi}^2_{\rm k}$	$\widetilde{\chi}^2_{\rm inf}$	$\widetilde{\chi}^2_{\rm sup}$	$n_{\rm d}$	$\widetilde{\chi}^2_{\rm d}$	$\widetilde{\chi}^2_{\rm inf}$	$\widetilde{\chi}^2_{\rm sup}$
	(1)	(2)	(3)	(4)	(5)	(6)	(7)	(8)	(9)	(10)	(11)	(12)
ω Cen	70	4.73	0.74	1.29	39	1.75	0.66	1.40	53	1.43	0.70	1.34
47 Tuc	229	5.55	0.85	1.16	39	4.00	0.66	1.40	39	1.35	0.66	1.40
M15	308	5.11	0.87	1.14	31	1.08	0.62	1.45	7	0.41	0.31	2.01

Notes. For each cluster, separately for the photometric, kinematic, and distance fits, we provide the number of degrees of freedom [Cols. (1), (5), and (9)], the reduced best-fit chi-squared [Cols. (2), (6), and (10)], and the lower [Cols. (3), (7), and (11)] and upper [Cols. (4), (8), and (12)] boundaries of the two-sided 90% confidence level interval for the reduced χ^2-distribution with n degrees of freedom.

Table 7.5: Dimensionless parameters and physical scales of the best-fit models.

Globular cluster	Dimensionless parameters				Physical scales			Dynamical distance
	Ψ	χ	b	c	μ_0	r_0	v_0	d
	(1)	(2)	(3)	(4)	(5)	(6)	(7)	(8)
ω Cen	5.8	14.4×10^{-3}	0.040	1	16.43 ± 0.05	134.54 ± 1.13	15.87 ± 0.27	4.25 ± 0.08
47 Tuc	7.6	1.6×10^{-3}	0.008	1	14.30 ± 0.08	24.41 ± 0.14	13.35 ± 0.21	4.15 ± 0.07
M15	6.8	1.6×10^{-3}	0.035	1	14.65 ± 0.01	13.33 ± 0.20	12.52 ± 0.24	10.52 ± 0.38

Notes. For each cluster we list: the concentration parameter Ψ in Col. (1), the rotation strength parameter χ in Col. (2), the $\bar{b}$ parameter of the rotating models in Col. (3), the V-band central surface brightness μ_0 in mag arcsec^{-2} in Col. (4), the radial scale r_0 in arcsec in Col. (5), the velocity scale v_0 in km s^{-1} in Col. (6), and the best-fit dynamical distance d in kpc in Col. (8). Note that r_0 is an intrinsic quantity; it is recorded here in arcseconds, for easier comparison with the observations,

Table 7.6: Derived parameters.

GC	C	$R_{\rm c}$	$R_{\rm h}$	$r_{\rm tr}$	M	M/L	ρ_0
	(1)	(2)	(3)	(4)	(5)	(6)	(7)
ω Cen	1.27	127.76	282.53	2400.29	20.20	2.77	3.737
47 Tuc	1.87	24.55	162.81	1814.88	6.23	1.69	4.752
M15	1.94	12.85	43.72	1118.92	4.55	1.45	5.090

Notes. For each cluster we provide the structural parameters derived for the best-fit models: (1) the concentration parameter $C = \log(r_{\rm tr}/R_{\rm c})$, (2) the projected core radius $R_{\rm c}$ in arcsec, (3) the projected half-mass radius $R_{\rm h}$ in arcsec, (4) the truncation radius $r_{\rm tr}$ in arcsec, (5) the total mass of the cluster M in units of $10^5 M_\odot$, (6) the V-band mass-to-light ratio in solar units, (7) the logarithm of the central density mass ρ_0 in units of $M_\odot$ pc^{-3}.

7.5 ω Cen

The globular cluster ω Cen is the cluster for which the most complete photometric and kinematic data are available. In particular, the kinematic profiles along the line-of-sight and on the plane of the sky extend out to $\approx 0.5 r_{\rm tr}$; therefore, a thorough comparison between models and observations can be carried out.

7.5.1 Photometry and kinematics

In general, the selected model is in satisfactory agreement with the surface brightness profile and the line-of-sight kinematic profiles, as shown in Fig. 7.2. For the photometric profile, the model reproduces well the central regions and the intermediate parts, but it underestimates the last two data points. For the line-of-sight kinematic profiles, the model is able to reproduce simultaneously the shape of the rotation profile and the shape of the dispersion profile reasonably well, with one important failure: the central values (inside ≈ 200 arc sec) of the line-of-sight velocity dispersion are severely underestimated by our model. It is interesting to note that any quasi-Maxwellian dynamical model applied to ω Cen is unable to reproduce the cuspy behavior observed in the central regions (e.g., see the application of spherical King models and of spherical Wilson models presented by McLaughlin & van der Marel 2005 in their Fig. 11; see also the fit by means of the rotating Wilson 1975 model performed by Sollima et al. 2009). In this respect, radially-biased anisotropic models appear to perform better (in particular, see the application of the $f^{(\nu)}$ models discussed in Chapter 8, with reference to Fig. 8.3). On the one hand, this feature has sometimes been considered as evidence for the presence of a central IMBH. On the other hand, the same feature may indicate that ω Cen, because of its relatively high relaxation times (see Tab. 1), is only partially relaxed and characterized by a higher degree of radial anisotropy with respect to the case of more relaxed stellar systems, as also suggested by Fig. 7.3. Curiously, even though [see Subsection 7.2.2] the line-of-sight data indicate high rotation in the very central regions ($R < 0.5 R_{\rm c}$), which is naturally interpreted as the signature of a complex rotating central structure, this does not appear to affect the quality of our results on the rotation profile; in fact, the selected model reproduces the central part of the line-of-sight rotation curve surprisingly well (see Fig. 2).

In addition, the model thus identified by our procedure is associated with specific proper motions dispersion profiles, and these can be scaled to the data, as shown in Fig. 7.3, to determine the dynamical distance d. Therefore, the model is actually able

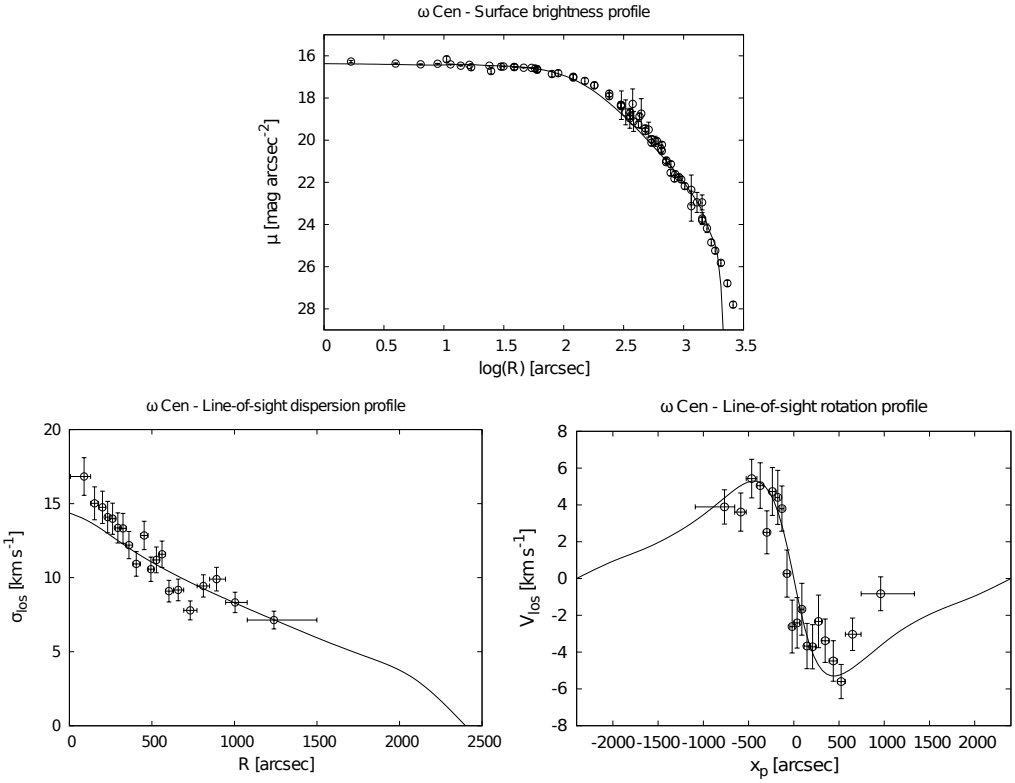

Figure 7.2: Surface brightness profile, line-of-sight velocity dispersion profile, and line-of-sight rotation profile (measured along the projected major axis; for the definition of the x_p coordinate and the way the data are binned, see Sect. 2) for ω Cen. Solid lines represent the model profiles and open circles the observational data points. Vertical bars represent the measured errors and horizontal bars indicate the size of the bins. These fits have determined the three physical scales of the model (μ_0, r_0, v_0) (see Table 7.5).

to reproduce reasonably well all three components of the projected velocity dispersion tensor. Interestingly, the shape of the anisotropy profile built from the proper motion dispersions is consistent with the general properties of the selected model, which is characterized by isotropy in the central region, weak radial anisotropy in the intermediate region and tangential anisotropy in the outer parts. The transition between the region characterized by radial anisotropy to the region characterized by tangential anisotropy takes place at $R \approx 1200$ arcsec. The data indeed show signs of radial anisotropy in the intermediate region and of tangential anisotropy outside $R \approx 1000$ arcsec. The existence of tangential anisotropy found in the present study is consistent with the results of previous investigations, namely van de Ven et al. (2006) and van der Marel & Anderson (2010) (see their Fig. 6). We wish to emphasize that such behavior of the anisotropy profile in the outer parts of the equilibrium configuration is a natural property of the family of models at the basis of the present work; in particular, the general shape of the anisotropy profile is determined by the values of the three relevant dimensionless parameters mentioned in Sect. 1.

Finally, we can also compare the rotation on the plane of the sky predicted by the

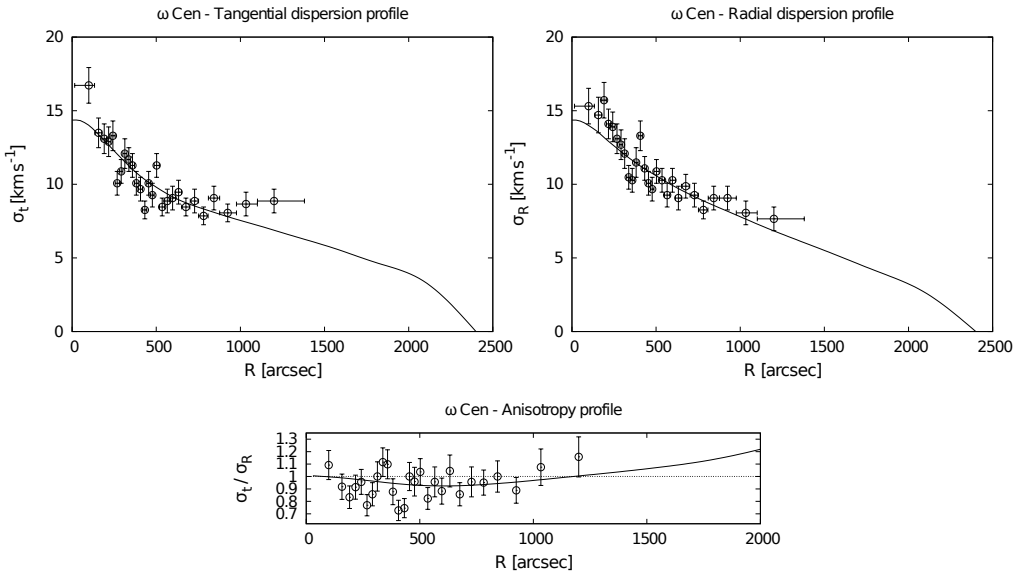

Figure 7.3: The top panels illustrate the fit to the proper motion dispersion profiles along the projected tangential and radial directions; this fit has determined the dynamical distance d. The bottom panel shows the predicted anisotropy profile against the available data. Solid lines represent the model profiles and open circles the observational data points. Vertical bars indicate the measured errors and horizontal bars indicate the size of the bins.

model with the observed mean-velocity profiles along the tangential and radial directions. Figure 7.4 shows that the rotation profile $V_t(R)$ is well reproduced by the model, confirming the presence of differential rotation. In the radial direction the model predicts an overall flat shape with vanishing velocity; in the external regions ($R > 1000$ arcsec), the observed proper motion mean-velocity in the radial direction reaches a value of $V_{\rm R} \approx 5$ km s^{-1}, indicating the presence of a systematic expansion. This feature was noticed also by van Leeuwen et al. (2000), who ascribed it to systematic errors in the measurement procedures. At this point, we should also mention that, as already discussed in Sect. 7.2.1, the procedure used to measure the proper motions removes any sign of solid-body rotation in the plane of the sky; therefore a correction to recover the solid-body mean velocity component has been applied to the data, following (van de Ven et al. 2006). This fact introduces some uncertainties in the final profiles and might account for some of the discrepancies between the model and the observed proper motion mean-velocity profiles.

In conclusion, aside from the inner cusp problem, the generally good agreement between model and proper motion mean-velocity and velocity dispersion profiles is quite remarkable, because the model was selected only to match the velocity-to-dispersion ratio along the line-of-sight $V^{\rm rot}_{\rm max}/\sigma_0$, the location of the peak in the rotation profile along the line-of-sight $R^{\rm rot}_{\rm max}$, and the location of the transition from radial to tangential anisotropy in the plane of the sky.

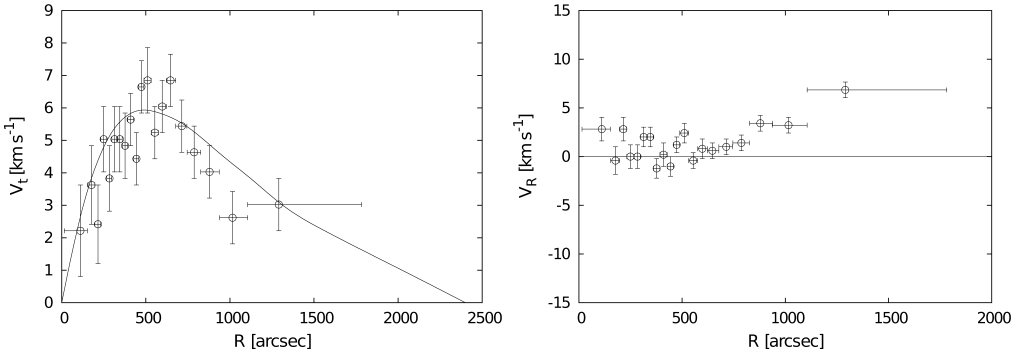

Figure 7.4: Predicted proper motion mean-velocity profiles along the tangential and radial directions for ω Cen. Solid lines represent the model profiles and open circles the observational data points. Vertical bars indicate the measured errors and horizontal bars the size of the bins. Note that the data give a hint of a possible overall expansion, which is obviously not present in the model.

7.5.2 Dynamical distance

The rescaling of the model profiles to match the observed proper motion dispersion profiles allows us to derive an estimate for the distance of the cluster (see Sect. 7.3.3). The dynamical distance thus obtained for ω Cen is $d = 4.25 \pm 0.08$ kpc. This value is significantly smaller than the distance estimated with photometric methods (e.g., $d = 5.2$ kpc from Harris 2010) and also smaller than other estimates obtained by means of the application of other dynamical models ($d = 4.70 \pm 0.06$ kpc from van der Marel & Anderson 2010; $d = 4.8 \pm 0.3$ kpc from van de Ven et al. 2006).

As also noted by van de Ven et al. (2006), a low value of the distance is expected when either the line-of-sight velocity dispersion is underestimated or the proper motion dispersion is overestimated. In our case, it is clear from the previous Section and from Fig. 7.2, that our dynamical model underestimates the central value of the line-of-sight velocity dispersion. Therefore, our distance estimate is affected by the corresponding systematic error. The dynamical distances obtained by van der Marel & Anderson (2010) and van de Ven et al. (2006) are based on a Jeans model and on an orbit-based model, respectively; previous studies based on the application of quasi-Maxwellian dynamical models, such as spherical King or spherical Wilson models, do not report distance estimates for this object.

7.5.3 Deviations from spherical symmetry

The selected axisymmetric model is associated with a well defined ellipticity profile, which is the morphological counterpart to the presence of rotation. The comparison with the corresponding observed profile is illustrated in Fig. 7.5; the open circles represent the profile from Anderson & van der Marel (2010), the black dots represent the profile from Geyer et al. (1983), and the solid line the profile derived from our model. The two profiles are discrepant in the central regions: in Geyer et al. (1983) the ellipticity profile starts from a value of $\varepsilon \approx 0.05$ at $R \approx 80$ arcsec and rapidly increases to $\varepsilon \approx 0.16$ at $R \approx 500$, whereas the ellipticity profile from Anderson & van der Marel (2010) shows an almost constant ellipticity $\varepsilon \approx 0.12$ inside $R \lesssim 250$ arcsec region, with significant scatter at $R \lesssim 100$ arcsec. For completeness, in Fig. 7.6 we present the projected isodensity contours

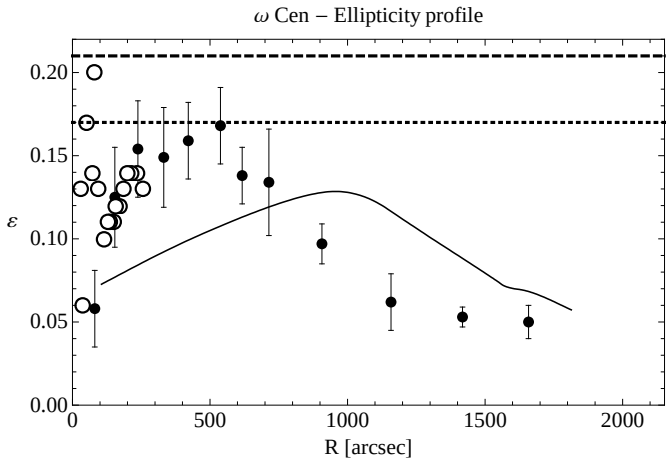

Figure 7.5: Ellipticity profile for ω Cen. The solid line represents the predicted profile derived from our rotating axisymmetric model, the open circles mark the observed ellipticities from Anderson & van der Marel (2010), and the black dots are the observed ellipticities from Geyer et al. (1983). Dotted and dashed lines mark the average values reported by WS87 and CC10, respectively.

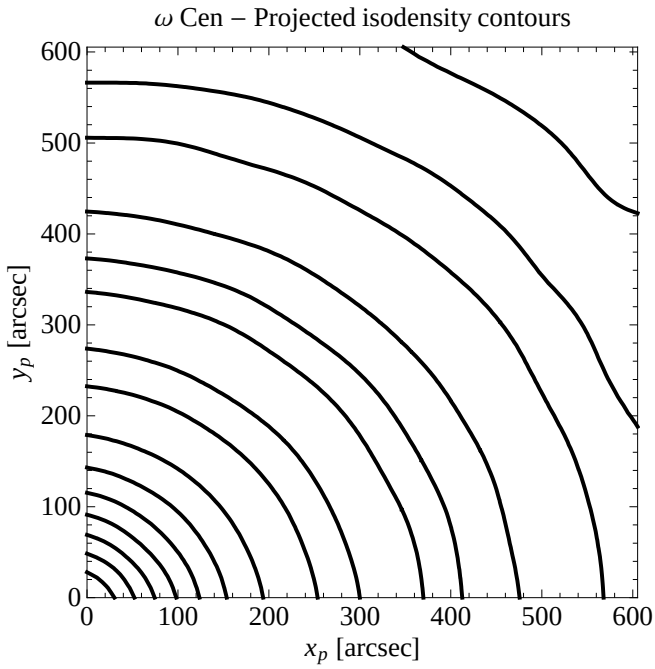

Figure 7.6: Predicted projected isodensity contours of the model for ω Cen. The contours are calculated in the first quadrant of the plane of the sky and correspond to selected values of the projected number density (normalized to the central value) in the range $[0.9, 10^{-2}]$. The area represented in the figure covers a square of side length approximately equal to $2R_h$.

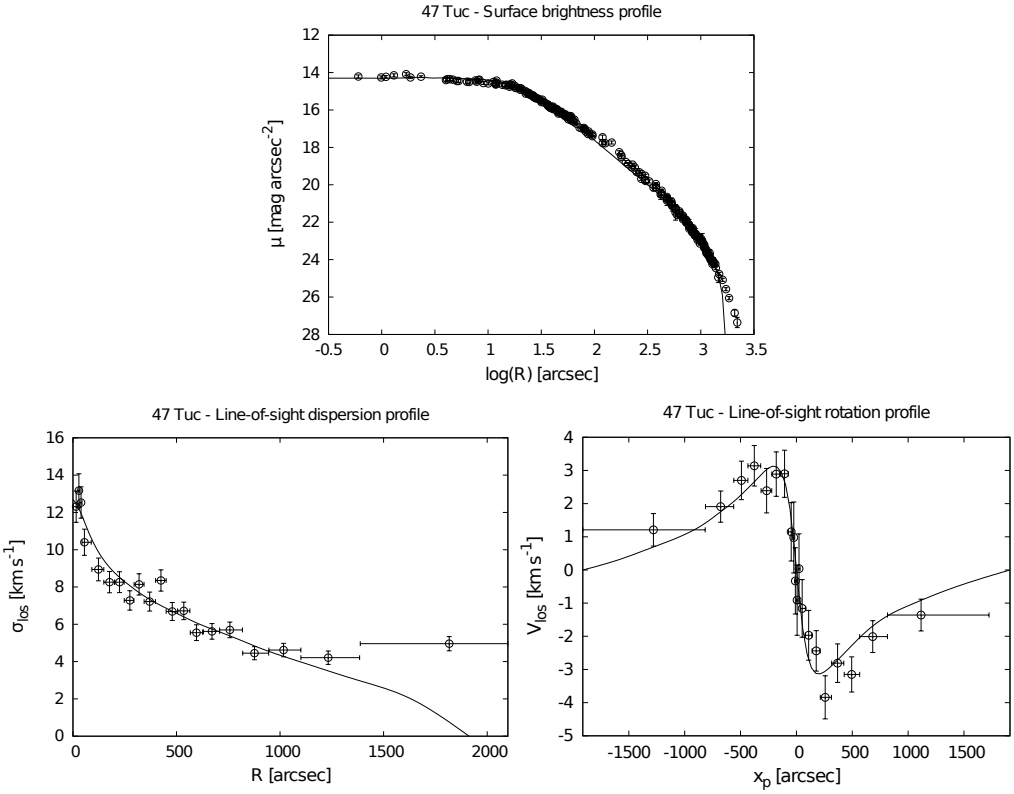

Figure 7.7: Surface brightness profile, line-of-sight velocity dispersion profile, and line-of-sight rotation profile for 47 Tuc. Solid lines represents the model profiles, open circles the observational data. Vertical bars indicate the measured errors, horizontal bars indicate the size of the bins.

predicted by our model, which clearly shows deviations from spherical symmetry.

Therefore, the model ellipticity profile is characterized by a general trend similar to that of the Geyer et al. (1983) measurements, but it predicts the peak of maximum flattening too far out, at about $R \approx 1000$ arcsec. In turn, our model would not be able to reproduce the finite central flattening observed by Anderson & van der Marel (2010), if confirmed. If we calculate the average ellipticity in the radial range covered by the data, we find an average flattening in reasonable agreement with the observed average flattening. In other words, we are led to conclude that the observed deviations from sphericity are likely to be originated by the presence of internal rotation. In our opinion, the discrepancy between predicted and observed morphology only confirms the complex nature of ω Cen, and, in particular, the conditions of partial relaxation of the cluster. In this respect, we expect that our models of quasi-relaxed stellar systems should perform better for globular clusters (such as 47 Tuc and M15) characterized by shorter relaxation times.

7.6 47 Tuc

For the globular cluster 47 Tuc the line-of-sight kinematical data cover the full radial extent of the cluster, out to approximately the truncation radius. In turn, the proper motion data are limited to a disk of radius $4R_{\rm c}$.

7.6.1 Photometry and kinematics

As illustrated in Fig. 7.7, the surface brightness profile and the line-of-sight rotation and velocity dispersion profiles are well reproduced by the selected model. In particular, the rotation profile is well matched throughout the extension of the cluster, showing clearly the position of the maximum rotation velocity, the characteristic rigid rotation behavior in the central region, and the relatively sharp decrease in the outer parts. The observed line-of-sight velocity dispersion profile is characterized by one data-point at $R \gtrsim 30$ arcmin deviating from the model profile. This outer rise in the velocity dispersion has been also been noted by Lane et al. (2010a). A corresponding discrepancy is found also for the surface-brightness profile, at approximately the same radial position (the last four photometric data-points). These two features may be interpreted in terms of the population of "potential escapers" resulting from the tidal interaction between the cluster and the host Galaxy (see Küpper et al. 2010a; Lane et al. 2012).

As to the proper motions data, the relevant profiles, although limited to the central region, show a satisfactory general agreement with the model predictions (see Fig. 7.8). In the intermediate regions ($50 \lesssim R \lesssim 1000$ arcsec) the model predicts weak radial anisotropy and tangential anisotropy in the outer parts. It would be interesting to acquire more spatially extended proper motion measurements to confirm this prediction [in line with the results obtained for the anisotropy profile of ω Cen (see Fig. 7.3)].

Rotation in the plane of the sky is not available from the proper motions data set McLaughlin et al. (2006). However, as noted in Sect. 2, proper motion rotation has been measured by Anderson & King (2003), by using the Hubble Space Telescope and by considering background stars of the Small Magellanic Cloud as an absolute reference frame. The observed rotation corresponds to a velocity of 4.97 ± 1.17 km s^{-1} (based on the assumed distance of 4.5 kpc) at a projected radius of 5.7 arcmin (corresponding approximately to the position of the rotation peak). Within the uncertainties, this is well consistent with our model, which predicts a value of 4.13 km s^{-1} at 5.7 arcmin.

7.6.2 Dynamical distance

The comparison of the observed proper motion dispersion profiles with the model predictions allows us to derive an estimate of the distance to the cluster (see Subsection 7.3.3). For 47 Tuc the best-fit distance is $d = 4.15 \pm 0.07$ kpc, with associated reduced chi-squared $\widetilde{\chi}^2_{\rm d} = 1.35$, inside the corresponding 90% CI. This value is consistent with the dynamical distance reported by McLaughlin et al. (2006) $d = 4.02 \pm 0.35$ kpc, measured under the simple assumptions of spherical symmetry, velocity dispersion isotropy, and absence of internal rotation from the same proper motion data set used in the present work. Our value is lower than the standard value of $d = 4.5$ kpc reported in the Harris Catalogue (Harris 2010) and lower than other distance estimates obtained by means of photometric methods, such as main sequence fitting, RR Lyrae, and white-dwarf cooling sequence fitting (for a recent summary of results, see Table 1 of Woodley et al. 2012 or Bono et al. 2008).

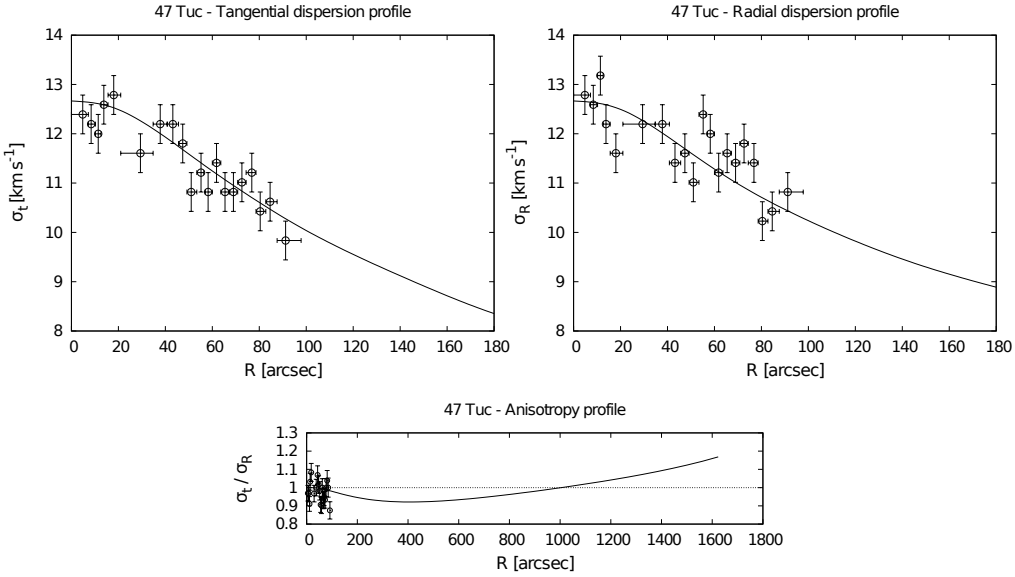

Figure 7.8: Proper motions dispersion profiles along the tangential and radial directions (top panels) and anisotropy profile (bottom panel) for 47 Tuc. Solid lines are the model profiles, open circles represent the observational data. Vertical bars indicate the measured errors, horizontal bars the size of the bins.

7.6.3 Deviations from spherical symmetry

Figure 7.9 shows the ellipticity profile predicted by our model plotted together with the ellipticity data available for 47 Tuc. Figure 7.10 illustrates the projected isodensity contours derived from our model. In this cluster, the deviations from spherical symmetry are naturally explained by the selected model with a surprising degree of accuracy. In fact, the ellipticity profile derived by our model reproduces the radial variation of the observed ellipticity over the entire spatial range covered by the data (the flattening of 47 Tuc increases from a value of $\varepsilon \approx 0$ to a maximum value of $\varepsilon \approx 0.12$ at $R \approx 450$ arcsec). We recall that the ellipticity profile associated with the selected self-consistent model is a structural property completely determined by the dimensionless parameters and physical scales identified during the model selection procedure. In this case we can thus state with confidence that internal rotation is the physical ingredient responsible for the observed global deviations from spherical symmetry. In this respect, we emphasize that the relation between the shapes of the rotation profile and the ellipticity profile is highly nontrivial; in particular, the peak of the rotation profile does not correspond to a peak in the ellipticity profile (at variance with what is often believed, e.g. Meylan & Mayor 1986).

7.7 M15

The studies of the globular cluster M15 are largely focused on its the central region. In fact, the cluster is believed to be in a post-core-collapse phase, it is a candidate host of an intermediate mass black hole, and mass segregation is thought to play a role in its dynamics. In particular, the sharp gradient of the central luminosity is thought to be

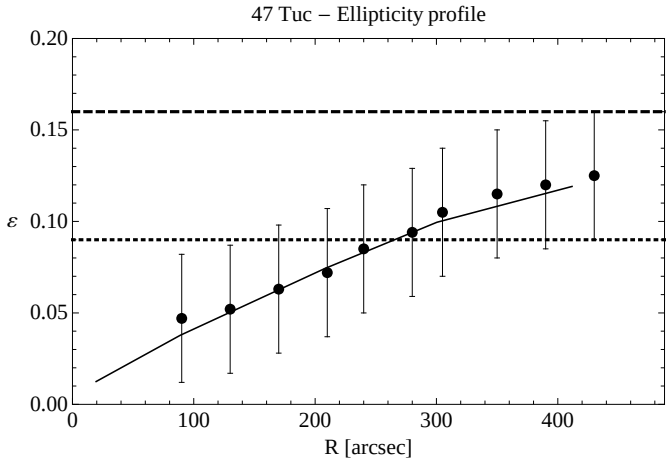

Figure 7.9: Ellipticity profile for 47 Tuc. The solid line represents the profile predicted by our axisymmetric rotating model, the black dots mark the observed ellipticities presented by WS87. Dotted and dashed lines mark the average values reported by WS87 and CC10, respectively.

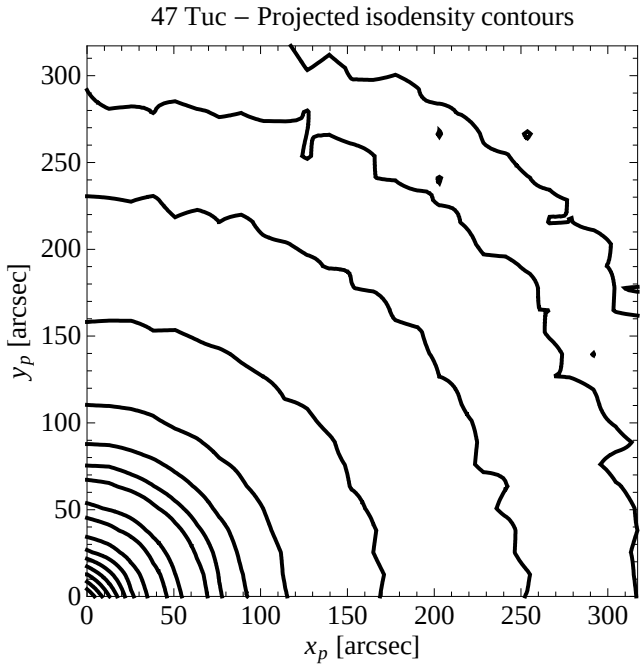

Figure 7.10: Projected isodensity contours predicted by our global self-consistent model of 47 Tuc, in the same format as in Fig. 7.6.

the result of the dynamical evolution of the cluster (e.g, see Baumgardt et al. 2003 and Murphy et al. 2011) or of the presence of a central intermediate mass black hole (e.g., see Gerssen et al. 2002). The available kinematic data are limited to the central regions. The proper motion data set is not as rich, both in terms of quality and quantity, as for the other two clusters studied in this paper.

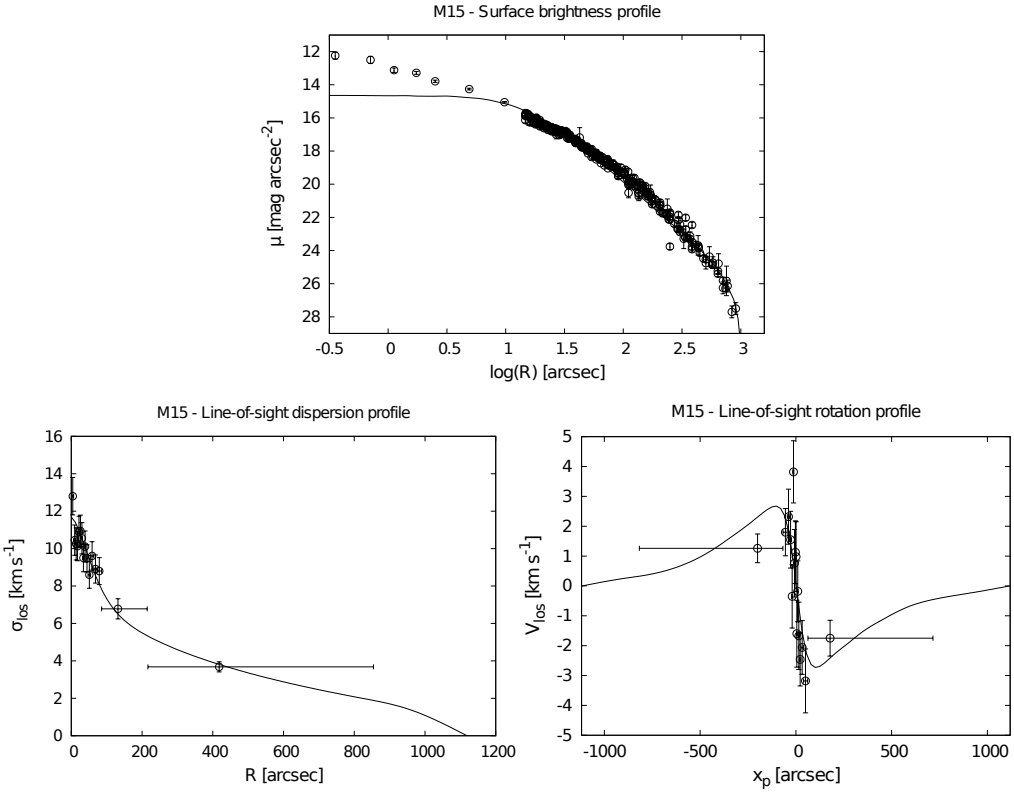

Figure 7.11: Surface brightness profile, line-of-sight velocity dispersion profile, and line-of-sight rotation profile for M15. Solid lines represent model profiles, open circles are the observational data. Vertical bars indicate the measured errors, horizontal bars indicate the size of the bins.

7.7.1 Photometry and kinematics

Remarkably, except for the most central region, the selected model offers a good description of both the line-of-sight kinematic profiles and the surface brightness profile (see Fig. 7.11). The line-of-sight velocity dispersion profile is well reproduced by the model out to the last available bin, located at approximately $0.5r_{\rm tr}$.

As to the line-of-sight rotation profile, a large scatter is present in the central regions, where the number of data is higher compared to the outer parts. Indeed, the measurement errors on the velocities are high, with an average error of 3.79 km s^{-1} (significantly higher than the error for ω Cen and 47 Tuc, given by 1.98 km s^{-1} and 2.29 km s^{-1}, respectively). Unfortunately, the kinematic data set does not reach the region where the peak of the rotation curve is expected. More accurate and better distributed line-of-sight velocity measurements would be required to build a more reliable and complete rotation

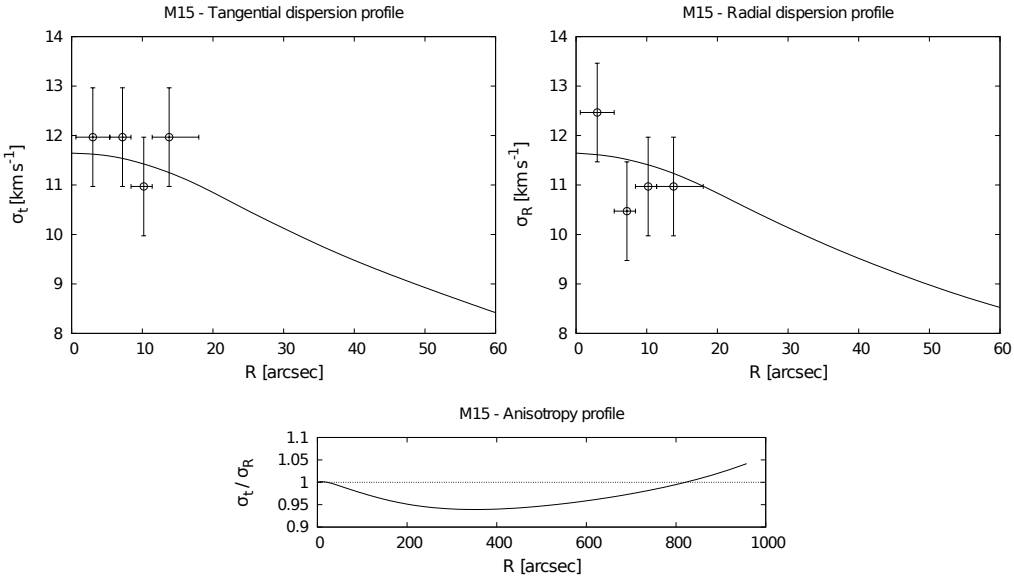

Figure 7.12: Proper motion dispersion profiles along the tangential and radial directions (top panels) and anisotropy profile (bottom panel) for M15. Solid lines represent the model profiles, open circles are the observational data. Vertical bars indicate the measured errors, horizontal bars indicate the size of the bins. No data points are shown for the anisotropy profile because they are too concentrated in the central region.

profile. However, it is interesting to note that the rotation profile in the central regions, characterized by a solid-body behavior, is well accounted for by the model, although the high rotation detected in the center, sometimes interpreted as a signature of the possible presence of a decoupled rotating core (see Subsect. 7.2.2), is basically missed by the model.

For the proper motions, given the small number of data and the low accuracy of the measurements, we decided to divided the sample in only 4 bins to avoid excessive statistical noise; the relevant profiles are illustrated in Fig. 7.12. Such profiles may be used to constrain the kinematic behavior of the cluster only in relation to the very central regions. In turn, the selected model leads to specific predictions about the anisotropy profile in the intermediate and outer parts of the object, which are expected to first show weak radial anisotropy and then tangential anisotropy. Unfortunately, for this object no information about the rotation on the plane of the sky is available in the literature.

7.7.2 Dynamical distance

The dynamical distance obtained from the procedure described in Subsection 7.3.3 yields a distance of $d = 10.52 \pm 0.38$ kpc, with a reduced $\widetilde{\chi}^2_{\rm d} = 0.41$ inside the corresponding 90% CI. This is consistent with the kinematic distance obtained by McNamara et al. (2004) of $d = 9.98 \pm 0.47$ kpc and the value obtained by van den Bosch et al. (2006) of $d = 10.3 \pm 0.4$ kpc; these two estimates are based on the same proper motion data set considered in the present work. In particular, the value obtained by McNamara et al. (2004), which is based

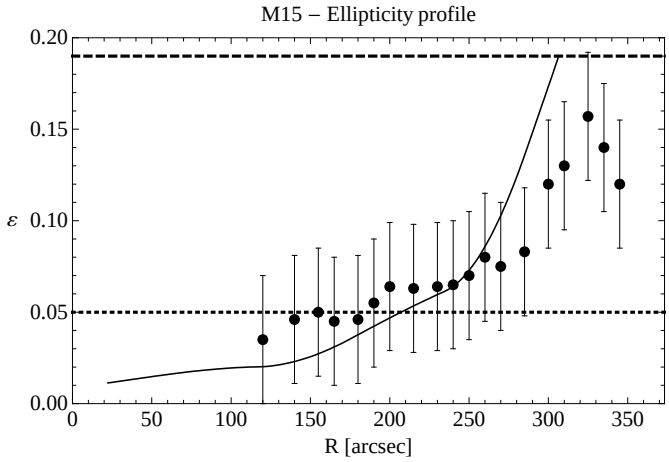

Figure 7.13: Ellipticity profile for M15. The solid line represents the profile predicted by our model, the black dots mark the observed ellipticities presented by WS87. Dotted and dashed lines mark the average values reported by WS87 and CC10, respectively

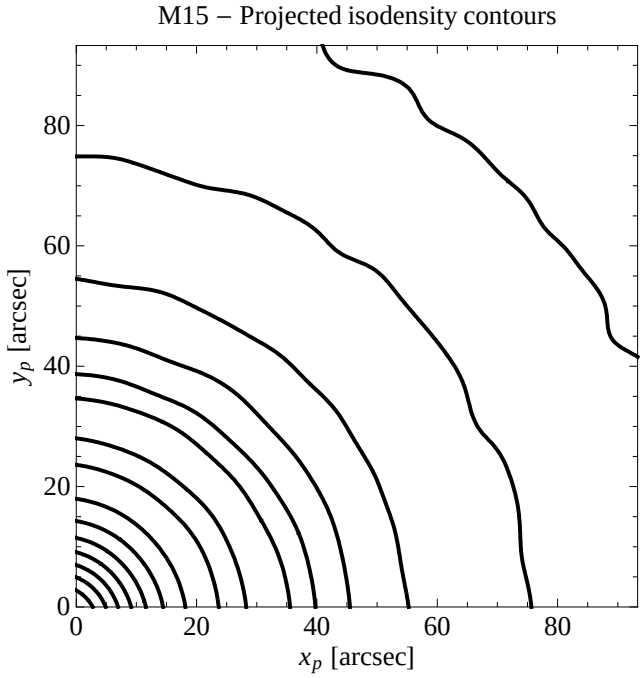

Figure 7.14: Projected isodensity contours from our selected model for M15. The same remarks presented in Figure 7.6 apply here.

on the simplifying assumptions of spherical symmetry, isotropy in velocity space, and no rotation, is lower than the value obtained in the present paper and the one obtained by van den Bosch et al. (2006) (in which anisotropy, rotation, and flattening are taken into account). Moreover, our distance is in agreement with other distance estimates based on photometric methods, such as the one reported in the Harris Catalogue (Harris 2010) $d = 10.3$ kpc. In this case, the conclusion drawn by Bono et al. (2008), according to which distances obtained from kinematic data are systematically lower than distances obtained from other methods, does not hold.

7.7.3 Deviations from spherical symmetry

The comparison between the observed ellipticity profile and the one derived from the selected model is illustrated in Fig. 7.13. The relevant projected isodensity contours are presented in Fig. 7.14. Our model predicts a value of ellipticity close to zero in the very central regions and an increase of the flattening thereafter. The trend of the predicted profile is consistent with the one observed. In particular, we note that our predicted profile seems to overlap smoothly with the observed profile in the region sampled by the data. Moreover, the observed average flattening is consistent with the value predicted by our model. We thus conclude that our dynamical model, and consequently the presence of internal rotation, can naturally explain the observed deviations from spherical symmetry of M15.

7.8 Comparison with previous studies

The results of the dynamical analysis performed in the present investigation are now briefly compared with the results obtained from previous studies based on spherical nonrotating models. Table 7.7 summarizes and compares the following derived structural properties: concentration parameter C, core radius $R_{\rm c}$, total mass M, and global mass-to-light ratio M/L.

Table 7.7: Comparison of the structural parameters from the best-fit models of the present investigation with those obtained from spherical models in previous studies. Notation and units are the same as in Tab. 7.6.

GC	Ref.	C	$R_{\rm c}$	M	M/L
ω Cen	(0)	1.27	127.76	20.20	2.77
	(1)	1.35	127.68	26.45	1.93
	(2)	1.32	171.20	25.11	2.05
	(3)	1.31	142.20	...	...
47 Tuc	(0)	1.87	24.55	6.23	1.69
	(1)	2.01	22.60	7.18	1.34
	(2)	2.57	32.08	10.71	1.17
	(3)	2.07	21.60	...	...
M15	(0)	1.94	12.85	4.55	1.45
	(1)	1.87	7.51	3.98	1.12
	(2)	...	...	...	...
	(3)	2.29	8.40	...	...

References. (0) This Chapter; (1) Spherical King models from Chapter 8; (2) Spherical Wilson models from McLaughlin & van der Marel (2005); (3) Harris (2010).

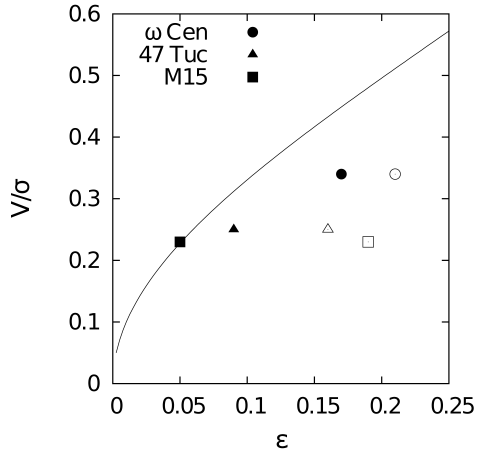

Figure 7.15: V/σ vs. ellipticity ε for ω Cen, 47 Tuc, and M15. Filled and empty symbols denote the pairs (V/σ,ε), in which the ellipticity values are determined by WS87 and CC10, respectively. The solid line indicates the relation expected for isotropic oblate rotators projected with an inclination angle of $i = 90^\circ$ ("edge-on" view).

In general, the values of the derived structural parameters agree, within the uncertainties, with the values derived in the other studies. Spherical nonrotating Wilson models tend to lead to larger truncation radii, which is expected. We can also compare the values of these global quantities to the results of the application of dynamical models in which internal rotation and deviations from sphericity are taken into account, in particular the orbit-based axisymmetric dynamical models available for ω Cen and M15 (van de Ven et al. 2006; van den Bosch et al. 2006). Remarkably, the best-fit model for M15 is characterized by a total mass and a mass-to-light ratio fully consistent with our results, that is, $4.4 \times 10^5 M_\odot$ and 1.6 $M_\odot/L_\odot$, respectively.

In the case of ω Cen, in the present study we derive a lower value for the total mass and a higher value for the mass-to-light ratio. Here the discrepancy with respect to the other studies reflects our estimate of the distance to the object, which we find to be smaller than the distance reported in the literature (by adopting a distance of $d = 4.8$ kpc, the resulting total mass associated with our rotating model would be $M = 2.28 \times 10^6 M_\odot$, whereas for $d = 5.2$ kpc, the total mass would be $M = 2.47 \times 10^6 M_\odot$).

The three globular clusters under consideration are known to be in different evolutionary states. In fact, the core relaxation time of ω Cen is significantly higher than the relaxation times of 47 Tuc and M15 (see Tab. 7.1). This suggests that ω Cen should be in only a partially relaxed state. The cuspy behavior of the velocity dispersion profile in the central regions of ω Cen may thus reflect a condition of partial relaxation; this interpretation is supported by the fact that models with sizable radially-biased pressure anisotropy, such as the family of $f^{(\nu)}$ models, are able to reproduce this controversial kinematic feature (see Chapter 8). Indeed, the rotating models presented in Chapter 4 and applied in this study are characterized by the presence of only weak radial anisotropy in the intermediate radial range, because they have been constructed under the assumption that the stellar system is quasi-relaxed.

For the two more relaxed clusters, 47 Tuc and M15, probably the most significant discrepancy is that of the core radius of M15. This is not surprising, given the known

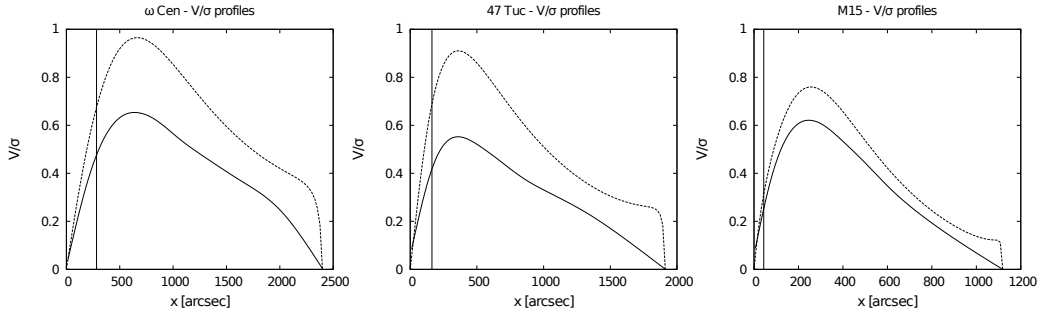

Figure 7.16: V/σ profiles for ω Cen, 47 Tuc, and M15, respectively. The solid line represents the projected profile observed along the major axis; the dashed line represents the intrinsic profile along the equatorial plane. The vertical line indicates the position of the half light radius $R_{\rm h}$. All the profiles shown are constructed starting from the selected models of the three clusters.

difficulties of the models considered in the table in fitting the central region of the surface brightness profile of this cluster. We recall that M15 is generally considered to be a post-core collapse cluster (Murphy et al. 2011), a physical property not considered by our models. The cuspy behavior of the surface-brightness profile in the central region is a signature of such a dynamical state. For this cluster, the outer regions are well fitted by our rotating model (Fig. 7.11), at variance with the spherical King models, which severely underestimate the surface-brightness (see Fig. 8.1 in Chapter 8).]

In our opinion, the points of discrepancy noted here and in the previous sections do not diminish the important result of the present study, that is, the possibility to provide a conceptually simple global description of the internal structure and dynamics of three rotating globular clusters by means of one physically justified family of fully self-consistent axisymmetric models. In particular, we have demonstrated in various ways that that the global flattening observed in the clusters is likely to be produced by internal rotation.

Finally, we wish to comment on a tool commonly used to assess the importance of rotation in determining the global shape of a stellar system, that is the plot V/σ vs. ε (in the context of elliptical galaxies, see Davies et al. 1983 and Emsellem et al. 2011). The V/σ parameter is frequently defined as the ratio between the maximum of rotational velocity and the central velocity dispersion $V^{\rm rot}_{\rm max}/\sigma_0$; both quantities are measured along the line of sight. We note that the definition of the maximum of velocity $V^{\rm rot}_{\rm max}$ strictly depend on the method adopted for the construction of the relevant rotation profile.

In Fig. 7.15, the quantity V/σ is the ratio of the observed maximum of the line-of-sight rotation profile to the central line-of-sight velocity dispersion, as reported in Col. (1) of Tab. 7.3. The values of the ellipticity ε are those reported by WS87 and by CC10. In the figure, the solid line indicates the relation expected for isotropic oblate rotators (Binney 1978), with a projection angle of $i = 90^\circ$ ("edge-on" view). According to this diagram, the flattening observed in the three globular clusters could be considered consistent with being originated by the presence of internal rotation. The deviations from the line of isotropic rotators may be interpreted as due to the combined effects of inclination, differential rotation, and pressure anisotropy. The cluster for which the deviation is most significant is ω Cen, confirming the anomalous trends of the cluster (which we have argued to be the result of its only partial relaxation state).

We recall that the V/σ parameter is a local quantity, since both the rotation and dis-

Table 7.8: The V/σ parameter.

GC	$V^{\rm rot}_{\rm max}/\sigma_0$ (1)	$(V/\sigma)_{R_h}$ (2)	ε (3)
ω Cen	0.34	0.48	0.17
47 Tuc	0.25	0.42	0.09
M15	0.23	0.26	0.05

Notes. For each cluster we list the: (1) the ratio between the maximum of line-of-sight rotation profile and central line-of-sight velocity dispersion, (2) the value of the V/σ profile on the projected major axis evaluated at $R_{\rm h}$ derived from the model, (3) the observed ellipticity from WS87.

persion profiles depend on the radial position. Therefore, it is appropriate to construct a V/σ radial profile and to introduce the quantity $(V/\sigma)_{R_{\rm h}}$, that is the value that the profile reaches at the half light radius $R_{\rm h}$. In Fig. 7.16 we report the V/σ profiles derived from the rotating models that reproduce the clusters under consideration; the profiles are calculated by making use of the line-of-sight rotation curves and velocity dispersion profiles calculated along the major axis, and the values of $(V/\sigma)_{R_{\rm h}}$ are reported in Tab. 7.8. For completeness, in the same Figure we also show the intrinsic V/σ radial profiles, constructed by considering the relevant intrinsic kinematic profiles evaluated on the equatorial plane; in particular, for the scalar velocity dispersion we considered the trace of the full three dimensional velocity dispersion tensor, defined as $\sigma^2 = (\sigma_r^2 + \sigma_\theta^2 + \sigma_\phi^2)/3$. Indeed, projection effects play a fundamental role in determining the shape (and in particular in reducing the maximum value) of the V/σ profiles.

7.9 Conclusions

The main results of the analysis illustrated in the present Chapter can be summarized as follows:

- The models selected to reproduce 47 Tuc and M15 are in excellent agreement with the relevant kinematic and photometric profiles. In addition, the predicted morphology of the models describe surprisingly well the ellipticity profiles, where available.

- The model selected for ω Cen is not able to reproduce the central behavior of the line-of-sight velocity dispersion profile, as expected, given the condition of partial relaxation of this stellar system. In addition, this discrepancy affects the distance estimate, which results to be smaller compared to the the values reported in the literature. On the other hand, the model provide a very satisfactory global interpretation of the complex three dimensional kinematics available for this object. In particular, the behavior of the anisotropy profile is successfully described, including the presence of tangential anisotropy in the outer parts of the system.

- We calculated new estimates of the distances of the stellar systems under consideration, by performing a comparison between the proper motions measured in the central regions of the clusters and the corresponding predictions derived by our dynamical models. This approach is only rarely followed (see D'Souza & Rix 2005, van de Ven et al. 2006, Anderson & van der Marel 2010), and it appears that the distance estimates based on dynamical models are systematically lower compared

to the distance moduli determined with photometric methods (e.g., see Bono et al. 2008).

- Inclination angle may play a fundamental role. This quantity is difficult to constraint and, in general, renovated effort should be invested in the comparison of nonspherical models with basic morphological observables. Driven by this motivations, a new method to simultaneously determine the distance and the inclination angle of an axisymmetric stellar system, based on the combined use of proper motions and line-of-sight velocities will be presented in a subsequent paper.

- The analysis presented in the present Chapter and in Chapter 8 demonstrate that an approach which gives priority to the kinematics is very satisfactory. A number of fundamental dynamical issues can be tested exclusively by making use of appropriate kinematical data (e.g., the presence of dark matter, dark remnants, dynamical signatures of mass segregation, binary fraction, role of internal rotation, central IMBHs, distance determination), which are truly crucial for a meaningful interpretation of the internal dynamics of stellar systems (see also Sollima et al. 2012). Three-dimensional kinematics will be available for an increasing number of Galactic globular clusters, such a tremendous amount of information deserve a more advanced interpretation by means of realistic dynamical models.

- Rotation plays a fundamental role in shaping the structure of the three clusters under consideration. To be noted that the physical origin of the small observed deviations from spherical symmetry among external tidal field, internal rotation, and pressure anisotropy is still to be determined.

- More advanced global and local morphological observables should be considered (e.g., isophotes shapes and quadrupole moment tensors). At a more basic level, new ellipticity profiles of Galactic globular clusters are much needed, as they provide a very valuable constraint in the selection of the most appropriate nonspherical models. Ultimately, detailed morphological information will allow us to gain insight about the formation and evolution of low mass stellar systems (e.g., in the context of dwarf galaxies, see the recent investigation by Łokas et al. 2012 about the morphological signatures of the tidal stirring scenario).

Part III
Pressure Anisotropy

CHAPTER 8

Galactic globular clusters in different relaxation conditions

8.1 Introduction

In the present Chapter, we wish to check whether indeed King models perform better in more relaxed systems, by studying the combined photometric and kinematical profiles for a sample of globular clusters. We will refer to the surface brightness profiles collected by Trager et al. (1995) (supplemented by more recent data, when available), in order to deal with a homogeneous sample, and limit our discussion to one-component dynamical models (leaving aside the issues of core collapse and mass segregation; we will thus exclude from our sample clusters with evidence of core collapse). Our sample will then be basically defined by the requirement that a sufficient number of kinematical data-points is available from the literature, so as to define a reasonably accurate and radially extended kinematic profile for a test of a dynamical model at the global level.

Many large globular clusters have very long relaxation times. Therefore, we have decided to model the same data also by means of models (the $f^{(\nu)}$ models; see Bertin & Trenti 2003) explicitly constructed for the context of violently relaxed elliptical galaxies. In other words, we wish to check whether less relaxed clusters tend to conform to the picture of formation via incomplete violent relaxation, which has the characteristic signature of radially-biased pressure anisotropy for less bound stars. The use of the $f^{(\nu)}$ models is preferred to other options (for example to the use of King-Michie models, Michie 1963), because these models are based on a detailed physical justification and have been shown to perform well both in relation to the observations of bright ellipticals and to the properties of the products of incomplete violent relaxation found in numerical simulations of collisionless collapse (over a range of nine orders of magnitude in the computed density profiles, with an excellent fit to the properties of the generated pressure anisotropy profiles; see Trenti et al. 2005). For a fair comparison with the King models we should have referred to truncated $f^{(\nu)}$ models; for the present simple exploratory investigation, and in order to keep the comparison between models characterized by the same number of parameters, we have decided to use the non-truncated $f^{(\nu)}$ models.

The Chapter is organized as follows. In Sect. 8.2 we introduce the sample of globular clusters selected for this study. In Sect. 8.3 we describe the available data sets and the procedure we followed to obtain the radial profiles used in our analysis. In Sect. 8.4 we show the results of our work and in Sect. 8.5 we draw our conclusions.

8.2 The selected sample

In this Chapter we wish to analyze globular clusters characterized by different relaxation conditions, measured by the central (core) relaxation time T_c as listed in the Harris

Table 8.1: The selected globular clusters.

Globular Cluster	$d_\odot$	C	$\log T_\mathrm{c}$	$\log T_\mathrm{M}$	e	v_rot	N_v	N_e	$\frac{R_\mathrm{K}}{R_\mathrm{e}}$	$\frac{R_\mathrm{K}}{r_\mathrm{t}}$	Ref.
NGC 362	8.6	1.76	7.76	8.93	0.01	0.0	208	92	4.22	0.33	(1)
NGC 7078 (M15)	10.4	2.29	7.84	9.32	0.05	1.7	1777	1298	16.94	0.62	(2)
NGC 104 (47 Tuc)	4.5	2.07	7.84	9.55	0.09	2.2	2638	709	19.27	1.44	(3), (4)
NGC 6121 (M4)	2.2	1.65	7.90	8.93	0.00	0.9	200	55	10.36	0.87	(4)
NGC 6341 (M92)	8.3	1.68	7.96	9.02	0.10	2.5	295	42	13.96	1.14	(5)
NGC 6218 (M12)	4.8	1.34	8.19	8.87	0.04	0.15	242	58	10.38	1.06	(4)
NGC 6254 (M10)	4.4	1.38	8.21	8.90	0.00	...	147	47	5.22	0.55	(6)
NGC 6656 (M22)	3.2	1.38	8.53	9.23	0.14	1.5	345	116	8.40	0.88	(4)
NGC 3201	4.9	1.29	8.61	9.27	0.12	1.2	399	201	10.35	1.27	(7)
NGC 6809 (M55)	5.4	0.93	8.90	9.29	0.02	0.25	728	311	7.79	1.44	(4)
NGC 288	8.9	0.99	8.99	9.32	...	0.25	171	68	5.53	0.93	(4), (6)
NGC 5139 (ω Cen)	5.2	1.31	9.60	10.09	0.17	7.9	2060	554	5.97	0.62	(8), (9)
NGC 2419	82.6	1.37	9.87	10.63	0.03	0.6	166	38	14.63	1.74	(10)

Notes. From left to right, the following quantities are displayed: distance from the Sun (kpc), concentration parameter, logarithm of the core relaxation time (years), logarithm of the half-mass relaxation time (years), ellipticity, rotational velocity (km s^{-1}), total number of velocity data-points available, number of velocity data-points inside the projected half-light radius, ratio of the radius of the outermost velocity point to the projected half-light radius, and ratio of the radius of the outermost velocity point to the truncation radius. The sources of the kinematical data are listed in the last column (see main text for references of the other quantities).

References. (1) Fischer et al. 1993; (2) Gebhardt et al. 2000; (3) Gebhardt et al. 1995; (4) Lane et al. 2011; (5) Drukier et al. 2007; (6) Carretta et al. 2009; (7) Cote et al. 1995; (8) Mayor et al. 1997; (9) Reijns et al. 2006; (10) Ibata et al. 2011.

catalog (Harris 2010). We decided to order globular clusters according to the core relaxation time, rather than to the half-mass relaxation time, because in general $T_{\rm c}$ is less model-dependent (as pointed out in Sect. 8.4.2). We checked that, by ordering the sample with respect to the half-mass relaxation time, some changes in the composition of the three classes identified below would occur (this fact can be easily seen by inspecting the values of these time scales for the globular clusters listed in Table 8.1), but with minor effects in relation to the general conclusions of the study.

Looking at the values of the relevant relaxation times recorded in the available catalog for the globular cluster system of our Galaxy, we see that the distinction between relaxed and partially relaxed globular clusters is not sharp. Therefore, we introduce a simple criterion to classify globular clusters according to their relaxation state. We consider three relaxation classes: relaxed globular clusters, for which $\log T_{\rm c} < 8$ (first class); globular clusters in an intermediate relaxation condition, for which $8 < \log T_{\rm c} < 9$ (second class); partially relaxed globular clusters, for which $\log T_{\rm c} > 9$ (third class; $T_{\rm c}$ is expressed in years).

The sample of globular clusters has been selected on the basis of the following criteria: (i) We exclude post-core-collapse globular clusters, that is, we reject the clusters labeled as post-core-collapse by Harris (2010). The reason is that we wish to test King models on the global scale, avoiding the subtle modeling issues that characterize the central regions of these systems, especially if phenomena a priori known to go beyond the King modeling are involved. (ii) We choose globular clusters for which an accurate and extended surface brightness profile is available. (iii) We select clusters for which at least 140 stellar radial (line-of-sight) velocities have already been measured. We impose a lower limit to the number of measured velocities, because we wish to extract from such data a reasonably well-defined velocity dispersion profile; the value of this limit is fixed in a way that allows us to include in the analysis globular clusters that belong to the different relaxation classes defined previously. (iv) We exclude from our list all the clusters that have less than 35 stellar radial velocities inside the projected half-light radius $R_{\rm e}$ (also called effective radius; the values of this quantity are reported in the Harris catalog, where the notation is $r_{\rm h}$). We introduce this further requirement, because we wish to analyze velocity dispersion profiles that characterize the stellar systems on the largest radial extent. For bright elliptical galaxies the kinematical data-points inside $R_{\rm e}$ are usually the easiest to get, and often turn out to discriminate among very different models. To test how well the King models perform, the central regions are a natural ground for comparison with other models.

The most restrictive elements in identifying a significant sample of globular clusters are the requirements on the radial velocity data, because for only few globular clusters the desired data are available. Indeed, of the 28 Galactic globular clusters with a reasonable number of radial velocities (i.e., at least 40 line-of-sight velocity measures on the entire spatial extent of the cluster), 3 are flagged as post-core-collapse, 9 have less than 140 velocity data, and 3 have less than 35 data inside their projected half-light radius. In the Harris catalog, NGC 362 and NGC 7078 are indicated as possible post-core-collapse clusters, but we decided to keep them because, according to their concentration parameter in the Harris catalog, it is still possible to obtain an acceptable fit with King models. In this way, we are left with 13 globular clusters that match our selection criteria. In relation to the relaxation classes defined above, our set of globular clusters contains 5 well-relaxed clusters, 6 clusters in an intermediate relaxation condition, and 2 partially relaxed clusters.

To better characterize our sample in terms of the radial extent of their radial velocity data, we consider the ratio of the radius of the last kinematical point to the projected

half-light radius[1], $R_{\rm K}/R_{\rm e}$, and the ratio of the radius of the last kinematical point to the truncation radius[2], $R_{\rm K}/r_{\rm tr}$. We judge the following values of the two ratios, $R_{\rm K}/R_{\rm e} \geq 3$ and $R_{\rm K}/r_{\rm tr} \geq 0.8$, to be satisfactory. All the selected globular clusters satisfy the first relation, and all but four globular clusters satisfy the second condition.

Table 8.1 gives the sample of selected globular clusters, listed in order of increasing core relaxation time $\log T_{\rm c}$. The first part of the table contains relaxed globular clusters, the second part those in an intermediate relaxation condition, and partially relaxed clusters are shown in the last part. For each object, the values of the adopted cluster distance from the Sun $d_\odot$ (expressed in kpc), the concentration parameter C, the logarithm of the core relaxation time $\log T_{\rm c}$, the logarithm of the half-mass relaxation time $\log T_{\rm M}$ (where $T_{\rm c}$ and $T_{\rm M}$, in other papers often indicated with the symbols $t_{\rm rc}$ and $t_{\rm rh}$, are expressed in years) and the ellipticity e are recorded (as listed in the Harris 2010 catalog). In addition, the maximum rotational velocity $v_{\rm rot}$ (in km s^{-1}; the references for these values are Lane et al. 2011 for the globular clusters for which we use the kinematic data published in this paper, and Meylan & Heggie 1997 for the others), the number of velocity data-points available $N_{\rm v}$, the number of velocity data-points inside the projected half-light radius $N_{\rm e}$, the ratios of the radius of the outermost velocity point $R_{\rm K}$ to the projected half-light radius $R_{\rm e}$ (in the Harris catalog and in other papers often indicated as $r_{\rm h}$) and to the truncation radius $r_{\rm tr}$, and the sources of the kinematic data are given in the last columns.

8.3 The data sets

8.3.1 The surface brightness profiles

To deal with a homogeneous sample, we decided to use the surface brightness profiles provided by Trager et al. (1995) (this is the same starting point of McLaughlin & van der Marel 2005). This choice guarantees that the profiles have been constructed with the same method, even though the actual data come from different sources.

For each globular cluster, the profile is composed of $N_{\rm p}$ photometric data-points, given by $\log R_i$, the logarithm of the radius R_i, measured in arcsec, and by $m_{\rm V}(R_i)$, the V band surface brightness measured in mag arcsec^{-2} at the radial position R_i. The data also include $m_{\rm V,C}(R_i)$, the surface brightness calculated with the Chebyshev polynomials, which provides an accurate approximation to the overall profile; $m_{\rm V}(R_i) - m_{\rm V,C}(R_i)$, the Chebyshev residual; w_i, a weight that the authors assign to each measurement. All the surface brightness profiles considered in this Chapter are relative to the V band.

These data have to be properly corrected and treated before a comparison can be made with the theoretical models. First, we introduced an extinction correction, under the assumption that such extinction can be considered to be constant over the entire extent of each globular cluster. We calculated the extinction $A_{\rm V}$ from the reddening listed in the Harris catalog and obtained $m(R_i) = m_{\rm V}(R_i) - A_{\rm V}$, for $i = 1, \ldots, N_{\rm p}$. This is the only correction applied to the data: we assume that Trager et al. (1995) already removed any foreground and background contamination that could affect the measurements. Then, we followed the procedure described by McLaughlin & van der Marel (2005) to estimate the uncertainties δm_i on the data: starting from the weights, we calculated[3] $\delta m_i = \sigma_\mu / w_i$

[1] We always indicate with R the projected (two-dimensional) radial scales, and with r the intrinsic (three-dimensional) radial scales.

[2] In the latest version of the Harris catalog (Harris 2010), the values of the truncation radii are not listed; we calculated them from the available values of $R_{\rm c}$ and C, as: $r_{\rm tr} = R_{\rm c}\, 10^C$ (see notes in the Harris catalog bibliography).

[3] σ_μ is a constant that varies from cluster to cluster, the value of which can be found in Table 6 in McLaughlin

(note that in the fits we use only the points with weights $w_i \geq 0.15$ in the original profile, as suggested by McLaughlin & van der Marel 2005).

Usually, the less reliable parts in the profiles published by Trager et al. (1995) are the central regions. Therefore, we decided to combine these profile with the more recent and accurate surface brightness profiles by Noyola & Gebhardt (2006), when available. For the globular clusters NGC 104 and NGC 6341, we simply combined the profiles from the two sources; for NGC 6254 and NGC 7078, we decided to combine the two data sets by removing the points from Trager et al. (1995), when they do not match the profile by Noyola & Gebhardt (2006) (the removed points are inside $3.5''$ and $14.5''$, respectively). In the case of NGC 7078, it should be emphasized that, with this treatment, the profile changes significantly in the central regions, and the central slope becomes steeper.

In the case of NGC 5139 (ω Cen) we decided to add to the surface brightness profile the inner points that Eva Noyola kindly provided us (Noyola et al. 2008); still the number of data-points in our final composite surface brightness profile of this cluster is significantly smaller than that of the other clusters.

8.3.2 The velocity dispersion profiles

We divided the data (see Table 8.1 for detailed references) in several radial bins containing an equal number of stars; we chose the binning that represents the best compromise between having a rich profile and having accurate points (by increasing the number of bins, that is by decreasing the number of points per bin, the errors on the velocity dispersion increase). In principle, we might consider using unbinned data, to avoid loss of information (for the study of dwarf spheroidals, see Wilkinson et al. 2002). Here we preferred to follow the more traditional approach of constructing the associated one-dimensional profiles, a method that can be applied in a similar way to both kinematical and photometric data and that allows us to follow well-established fitting procedures used in the past (especially in studies of elliptical galaxies). For the clusters with less numerous kinematical data-points, we did experiment with changing the radial binning and checked the related consequences.

The method used to calculate the mean velocity and the velocity dispersion from stellar radial velocities is basically the one described by Pryor & Meylan (1993). We started by calculating the mean $v_{\rm r}$ and the dispersion $\sigma_{\rm c}$ for the entire set of velocities. The mean velocity represents the overall velocity of the entire cluster. Then, taking this value as a constant for the entire cluster, we calculated the line-of-sight velocity dispersion $\sigma(R_i)$ and the related accuracy $\delta\sigma_i$ inside the bins in which the data have been divided. For each bin, we indicate the distance from the center R_i as the mean of the radial positions of the stars that it contains. In this study we ignore the possible presence of rotation and therefore consider the various kinematical data-points in each bin, after subtraction of the systemic velocity, to contribute only to velocity dispersion (random motions).

For the majority of the clusters in our sample, only one data-set of stellar radial velocities is available; in the following we discuss in detail the cases in which a composition of different data-sets has been performed or which require some additional comments. For NGC 104, two data-sets of radial velocities are available; we noticed that the data from Gebhardt et al. (1995) are more centrally concentrated than those from Lane et al. (2011).[4] In order to have a complete sampling on the entire radial extent of the cluster,

& van der Marel (2005).

[4]Giersz & Heggie (2011) make some cautionary remarks about the velocity dispersion profile reported by these authors. In particular, the selection criteria adopted by Lane et al. (2011) could lead to the exclusion of some high-velocity stars, with consequent lowering of the central velocity dispersion, and to the inclusion of

Table 8.2: Dimensionless parameters and physical scales of the best-fit models.

	King Models				$f^{(\nu)}$ Models			
NGC	Ψ	r_0	μ_0	V	Ψ	$r_{\rm scale}$	μ_0	V
(1)	(2)	(3)	(4)	(5)	(6)	(7)	(8)	(9)
104	8.58 ± 0.01	23.09 ± 0.23	14.33 ± 0.01	12.27 ± 0.19	8.21 ± 0.02	250.44 ± 1.46	14.29 ± 0.01	14.07 ± 0.22
288	4.82 ± 0.10	91.03 ± 2.86	20.02 ± 0.03	2.85 ± 0.19	3.91 ± 0.24	79.54 ± 5.37	19.88 ± 0.03	3.70 ± 0.25
362	7.80 ± 0.03	10.21 ± 0.11	14.66 ± 0.01	8.31 ± 0.44	6.86 ± 0.05	52.73 ± 1.09	14.70 ± 0.01	9.26 ± 0.50
2419	6.62 ± 0.04	19.70 ± 0.31	19.43 ± 0.03	5.04 ± 0.43	4.24 ± 0.09	29.86 ± 0.83	19.44 ± 0.04	7.28 ± 0.61
3201	6.17 ± 0.11	76.99 ± 3.05	18.35 ± 0.08	4.28 ± 0.19	4.09 ± 0.40	103.48 ± 11.71	18.33 ± 0.08	5.01 ± 0.23
5139	6.27 ± 0.05	136.94 ± 2.33	16.42 ± 0.04	14.83 ± 0.25	4.31 ± 0.07	150.63 ± 3.07	16.35 ± 0.04	23.41 ± 0.40
6121	7.32 ± 0.07	74.56 ± 1.76	17.00 ± 0.11	4.01 ± 0.30	7.39 ± 0.09	464.49 ± 20.40	17.01 ± 0.11	4.21 ± 0.31
6218	6.11 ± 0.07	51.56 ± 1.51	17.65 ± 0.07	3.93 ± 0.30	4.00 ± 0.14	60.69 ± 2.52	17.57 ± 0.07	5.58 ± 0.42
6254	6.26 ± 0.04	53.63 ± 0.60	16.88 ± 0.09	6.21 ± 0.37	2.67 ± 0.13	51.48 ± 1.45	16.84 ± 0.09	9.69 ± 0.59
6341	7.54 ± 0.02	14.72 ± 0.13	15.31 ± 0.01	9.28 ± 0.41	5.99 ± 0.04	50.00 ± 0.80	15.44 ± 0.01	12.77 ± 0.56
6656	6.47 ± 0.11	86.18 ± 2.34	16.41 ± 0.11	6.47 ± 0.38	5.99 ± 0.26	241.58 ± 26.46	16.41 ± 0.11	7.19 ± 0.42
6809	4.44 ± 0.11	129.11 ± 4.06	19.12 ± 0.04	2.92 ± 0.13	3.92 ± 0.19	101.53 ± 5.39	18.99 ± 0.04	3.61 ± 0.17
7078	8.09 ± 0.02	7.72 ± 0.13	14.07 ± 0.03	11.83 ± 0.24	8.17 ± 0.05	65.88 ± 0.94	13.59 ± 0.06	12.79 ± 0.26

Notes. For each cluster, named in column (1), for King and $f^{(\nu)}$ models, we list: the concentration parameter Ψ, in other papers often indicated as W_0 (Col. (2) and (6)), the scale radius, expressed in arcsec (r_0 in Col. (3) and $r_{\rm scale}$ in Col. (7), as defined in Eq. (4.6); note that they are intrinsic quantities; they are recorded here in arcseconds, for easier comparison with the observations, as shown in Figs. 8.1-8.3), the V band central surface brightness μ_0 in mag arcsec^{-2} (Col. (4) and (8)), and the central line-of-sight velocity dispersion V in km s^{-1} (Col. (5) and (9)). Formal errors on the various parameters are also recorded.

we decided to define a mixed data-set, composed of 499 data from Gebhardt et al. (1995), located inside $100''$, and 2139 data from Lane et al. (2011), located outside that radius. The second case is cluster NGC 288, studied by Carretta et al. (2009) and by Lane et al. (2011). Since these papers publish the coordinates of each star, we were able to single out the stars in common between the two data-sets: for the stars in the overlap, velocity measures by Carretta et al. (2009), being more accurate, have been preferred. Finally, we excluded three stars for which the value of the velocity deviates by more than $4\sigma_{\rm c}$ from the mean radial velocity $v_{\rm r}$, obtaining a final sample of 171 data.

For the globular clusters NGC 6121, NGC 6656 and NGC 6809, in addition to recent data from Lane et al. (2011), older radial velocity measures are available in the literature, but we decided to consider only the data-sets from Lane et al. (2011), because they are more complete and more radially extended.

In the case of NGC 5139, we merged the largest sample of velocity data available (Reijns et al. 2006) with the sample provided by Mayor et al. (1997), which provides measurements for stars located in the central region of the cluster. A delicate issue regarding this cluster is the controversial position of its center, which plays an important role also in our analysis, because we wish to build a radial-dependent velocity dispersion profile, starting from stellar positions expressed in right ascension and declination (for Reijns et al. 2006). To carry out a proper merging of the two data-sets, we have used the position of the center proposed by Mayor et al. (1997); to calculate radial distances, we have followed the procedure described by van de Ven et al. (2006).

8.4 Description in terms of partially and quasi-relaxed models

8.4.1 Relaxation classes

The values of the dimensionless parameters and the physical scales of the two families of models determined by the photometric and kinematic fits are presented in Table 8.2. Note that, in general, for the $f^{(\nu)}$ models relatively low values of the concentration parameter Ψ are identified. Quantitative information about the best-fit models and the observational profiles, such as the number of the photometric and kinematic points, the values of the relevant reduced chi-squared, and the corresponding residuals, are listed in Table 8.3.

The surface brightness and the line-of-sight velocity dispersion profiles determined by the fit procedure for the models, together with the observed profiles for selected clusters in the first, second, and third relaxation class, are shown in Figs. 8.1, 8.2, and 8.3, respectively (see Zocchi et al. 2012 for the illustration of the relevant profiles and a detailed discussion of all the clusters under consideration in the present study). In the panels, solid lines correspond to the best-fit King models and dotted lines to the best-fit $f^{(\nu)}$ models. The vertical solid line marks the position of the King model projected half-light radius, the dotted one the position of the $f^{(\nu)}$ model projected half-light radius. For the surface brightness profiles, the data from Trager et al. (1995) are indicated with circles, the data from other sources with squares. For the velocity dispersion data, the horizontal bars indicate the length of the radial bin in which the data-points have been calculated; they do not have a role in determining the fit. For each data-point the errors are shown as vertical error bars. Note that, even if we insisted on selecting clusters

nonmember stars affecting the outer part of the profile. By using the composite data-set described above, we should be able to obtain reliable values of the velocity dispersion in the central regions, while the outermost points may still be affected by the inclusion of nonmember stars.

with a reasonable number of data inside R_e, for about half of the clusters, the kinematic profiles are undersampled in their central region.

In the following part of this subsection we will try to give a general assessment of the quality of the fits in the various cases. As a general rule, for a given cluster the family of models yielding the lowest values of the best-fit photometric and kinematic chi-squared is preferred. Table 8.3 shows that generally, for a given cluster, $\widetilde{\chi}^2_p > \widetilde{\chi}^2_k$, because the photometric profiles are characterized by a larger number of data-points with reported smaller error-bars.

Within the class of relaxed globular clusters, for NGC 7078 King models can not reproduce the observed surface brightness profiles, and $f^{(\nu)}$ models perform better, *especially for describing the outer parts of the cluster*. As to the observed velocity dispersion profiles, we see that for NGC 7078 the $f^{(\nu)}$ profile is formally more adequate (at the 99.9% confidence level, which, in the following, we denote by CL), while for NGC 362 the King profile is the closer to the observations (at the 90% CL). We should recall that these two globular clusters are flagged in the Harris catalogue as post-core-collapse clusters, although the value of the concentration parameter C is smaller than 2.5. Indeed, the observations indicate that there are some processes that cannot be captured by King models (with particular reference to the shallow cusp in the photometric profile of NGC 7078). By looking at the plots in Fig. 8.1, NGC 104 appears to have both observed surface brightness and velocity dispersion profiles well represented by King models. Curiously, NGC 6121 is equally well described by the two models; the values of the reduced chi-squared are slightly lower for the King model, but in practice the quality of the two fits is similar. We notice that for NGC 104 and NGC 6121 it is particularly evident that the last point in the velocity dispersion profile is significantly higher than expected by both models. A partial explanation of this fact could be the very large extent of the radial interval in which it is calculated. Therefore, it is important to obtain more velocity data-points in the outer regions to clarify this issue.

Best-fit profiles for selected globular clusters in the intermediate relaxation class are shown in Fig. 8.2. For NGC 288, NGC 6218, and NGC 6809 King models provide a better fit to both the surface brightness and the velocity dispersion profile (at the 90% CL in all cases). For the other globular clusters in this relaxation class the results are less sharp. In fact, for NGC 3201 and NGC 6254 the surface brightness profiles are formally better reproduced by $f^{(\nu)}$ models (for the first, at 95% CL), while the corresponding velocity dispersion profiles are formally better described by King models (at the 95% and 90% CL, respectively). For NGC 6656 both the surface brightness and the velocity dispersion profile are approximately equally well reproduced by the two families of models (at the 90% CL in all cases). For NGC 3201, NGC 6656, and NGC 6809 the velocity dispersion profiles have an irregular shape in the central regions: even if King models formally perform better than $f^{(\nu)}$ models, they are unable to reproduce the observations. We tried to choose a different binning for the data and we found that this irregularity does not depend on the way in which the observed velocity dispersion profile is constructed from the available data-set. Clearly, more data are necessary in order to obtain a more convincing description of these systems.

In Fig. 8.3, we show the best-fit profiles for partially relaxed globular clusters. For these two clusters we see discordant results: for NGC 2419 $f^{(\nu)}$ models are more adequate for describing the data (at the 99.99% CL and 90% CL for the photometric and kinematic fit, respectively), while for NGC 5139 King models provide a better fit to the observed profiles. Even if formally King models perform better in describing the kinematic profiles of NGC 5139, they do not provide a satisfactory description of the kine-

Table 8.3: Quality of the fits.

			King Models						$f^{(\nu)}$ Models					
NGC	$N_{\rm p}$	$N_{\rm k}$	$\widetilde{\chi}^2_{\rm p}$	$\langle\Delta\mu\rangle$	$(\Delta\mu)_{\rm max}$	$\widetilde{\chi}^2_{\rm k}$	$\langle\Delta\sigma\rangle$	$(\Delta\sigma)_{\rm max}$	$\widetilde{\chi}^2_{\rm p}$	$\langle\Delta\mu\rangle$	$(\Delta\mu)_{\rm max}$	$\widetilde{\chi}^2_{\rm k}$	$\langle\Delta\sigma\rangle$	$(\Delta\sigma)_{\rm max}$
(1)	(2)	(3)	(4)	(5)	(6)	(7)	(8)	(9)	(10)	(11)	(12)	(13)	(14)	(15)
104	231	16	3.487	0.41	4.68	7.411	1.03	3.39	6.433	0.24	1.53	10.367	1.34	2.98
288	85	6	1.251	0.30	0.98	0.442	0.21	0.33	3.891	0.46	1.10	2.040	0.46	0.78
362	239	8	3.113	0.58	7.09	1.307	0.99	1.74	1.563	0.15	0.92	3.345	1.55	2.45
2419	137	6	1.983	0.21	1.10	1.344	0.98	2.21	1.492	0.16	0.83	0.471	0.50	0.83
3201	80	16	1.308	0.38	1.49	1.783	0.83	1.73	1.289	0.36	1.48	4.005	1.21	2.29
5139	72	37	3.750	0.36	2.08	1.974	1.73	4.90	21.742	0.80	1.62	3.406	2.07	4.38
6121	228	10	1.460	0.27	1.33	0.450	0.47	0.94	1.710	0.29	1.33	0.581	0.52	0.93
6218	143	11	1.185	0.32	1.12	0.584	0.54	0.91	2.663	0.40	1.12	0.765	0.59	1.10
6254	162	6	5.046	0.37	2.75	0.606	0.48	0.65	4.372	0.22	1.12	1.844	0.89	1.15
6341	118	8	8.439	0.41	2.51	1.418	0.51	1.02	20.589	0.33	1.06	2.354	1.01	2.37
6656	143	7	1.019	0.23	0.66	0.942	0.67	1.36	1.056	0.23	0.66	1.699	0.89	1.83
6809	114	13	1.165	0.32	1.04	1.103	0.40	0.96	4.404	0.59	1.34	2.967	0.64	1.35
7078	310	35	6.136	0.75	5.00	3.229	1.33	3.06	3.813	0.36	1.41	1.981	1.37	3.25

Notes. For each cluster, named in column (1), we provide the number of points in the surface brightness (2) and in the velocity dispersion (3) profile. For King and $f^{(\nu)}$ models, we list: the reduced best-fit photometric chi-squared $\widetilde{\chi}^2_{\rm p}$ (Col. (4) and (10)), the mean (Col. (5) and (11)) and maximum (Col. (6) and (12)) photometric residuals, the reduced best-fit kinematic chi-squared $\widetilde{\chi}^2_{\rm k}$ (Col. (7) and (13)), the mean (Col. (8) and (14)) and maximum (Col. (9) and (15)) kinematic residuals.

Table 8.4: Derived structural properties.

	King Models							$f^{(\nu)}$ Models						
NGC	c	$R_{\rm c}$	$r_{\rm M}$	$r_{\rm tr}$	M	M/L	ρ_0	$R_{\rm c}$	$r_\alpha/r_{\rm M}$	$r_{\rm M}$	r_α	M	M/L	ρ_0
(1)	(2)	(3)	(4)	(5)	(6)	(7)	(8)	(9)	(10)	(11)	(12)	(13)	(14)	(15)
104	2.00	22.60	2.57	2335.74	7.181	1.34	5.011	23.25	1.783	4.82	8.59	8.047	1.50	5.094
288	0.99	79.49	7.51	896.85	0.740	1.88	2.043	58.24	0.866	7.53	6.53	0.850	2.18	2.427
362	1.77	9.88	2.65	605.79	1.867	1.05	4.826	11.34	1.786	2.13	3.80	1.828	1.03	4.761
2419	1.42	18.58	19.56	516.97	7.843	1.72	1.874	20.01	0.958	23.97	22.95	10.912	2.40	2.081
3201	1.30	71.58	3.85	1532.62	1.131	1.91	3.012	72.31	0.915	5.14	4.70	1.088	1.86	3.026
5139	1.32	127.68	7.51	2861.08	26.446	1.93	3.537	98.89	0.978	7.46	7.30	35.427	2.58	4.049
6121	1.62	71.31	2.62	3144.17	0.654	1.10	3.656	72.45	1.868	4.40	8.23	0.750	1.26	3.661
6218	1.28	47.81	2.47	982.45	0.614	1.96	3.306	43.45	0.890	3.03	2.69	0.786	2.52	3.577
6254	1.32	50.02	2.48	1125.66	1.532	1.61	3.741	47.97	0.564	3.35	1.89	2.161	2.67	4.003
6341	1.69	14.18	2.12	724.28	2.866	1.83	4.638	17.12	1.523	2.43	3.70	3.956	2.53	4.691
6656	1.38	80.92	3.13	2057.81	2.081	1.11	3.636	82.71	1.523	4.53	6.89	2.337	1.24	3.652
6809	0.92	110.09	5.90	1072.17	0.604	1.12	2.214	74.28	0.867	5.83	5.06	0.627	1.16	2.628
7078	1.86	7.51	1.70	560.55	3.976	1.12	5.207	6.27	1.793	2.92	5.24	4.056	1.14	5.420

Notes. For each cluster, listed in column (1), for the King models, we provide (2) the concentration index $c = \log(r_{\rm tr}/r_0)$ (see Eq. (4.6)) and (5) the truncation radius $r_{\rm tr}$, in arcsec; for the $f^{(\nu)}$ models, in Col. (10) the ratio between the anisotropy and the half-mass radius and in Col. (12) the anisotropy radius r_α, defined as $\alpha(r_\alpha) = 1$ (see Eq. (4.51) for the definition of α), in pc. For both King and $f^{(\nu)}$ models, we list: the core radius $R_{\rm c}$ (defined in the standard way) in arcsec (Col. (3) and (9)), the intrinsic half-mass radius $r_{\rm M}$, in pc (Col. (4) and (11), respectively), the total mass M of the cluster (Col. (6) and (13)) expressed in units of 10^5 $M_\odot$, the V band mass-to-light ratio in solar units (Col. (7) and (14)) and the logarithm of the central mass density ρ_0 in $M_\odot$ pc^{-3} (Col. (8) and (15)).

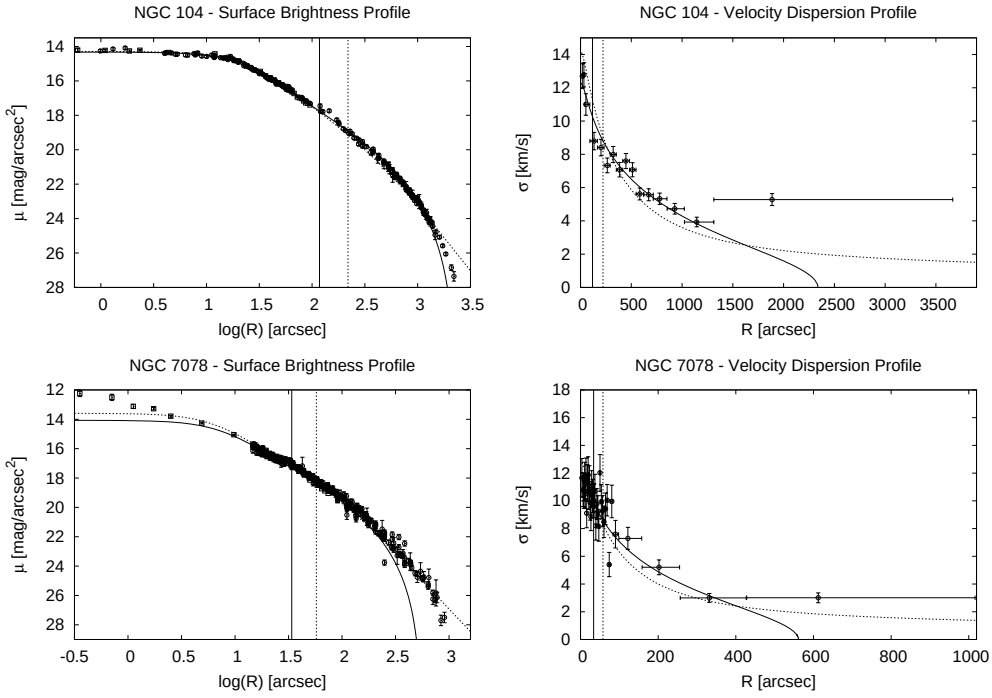

Figure 8.1: Fits by King models and $f^{(\nu)}$ models to the surface brightness profiles and to the line-of-sight velocity dispersion profiles of selected relaxed globular clusters (NGC 104 and NGC 7078). In all panels, solid lines correspond to the King-model fits, dotted lines to $f^{(\nu)}$-model fits; the vertical solid line marks the position of the King model projected half-light radius, $R_{\rm e}$, the dotted one the position of the $f^{(\nu)}$ model projected half-light radius, $R_{\rm e}$. For the surface brightness profiles, the data from Trager et al. (1995) are indicated with circles, the data from other sources (see Sect. 8.3.1) with squares. For each data-point, errors are shown as vertical error bars; in the case of the velocity dispersion profile, the horizontal bars indicate the length of the radial bin in which the data-points have been calculated and have no role in the fitting procedure.

matics of the central parts of the cluster (see Fig. 8.3); in this respect, the $f^{(\nu)}$ models give a better representation of the inner kinematics.

To summarize, we found that, as expected, $f^{(\nu)}$ models tend to perform globally better than King models for the least relaxed globular cluster of our sample, NGC 2419. For NGC 2419, the good performance of $f^{(\nu)}$ models might correspond to the partial relaxation condition of the cluster, consistent with the physical picture that motivates the definition of the $f^{(\nu)}$ models, as outlined in the Introduction. In addition, for three clusters in the second relaxation class (NGC 3201, NGC 6254,and NGC 6656), $f^{(\nu)}$ models are competitive with King models. Furthermore, $f^{(\nu)}$ models can describe well a relatively steep central slope of the velocity dispersion profile, even when the corresponding photometric profile is cored, while King models and other isotropic truncated models (such as Wilson models) are unable to reproduce this kinematical behavior. This fact is evident from the kinematic fits for NGC 2419, NGC 5139 and for possibly one cluster in the intermediate relaxation condition (NGC 6218).

As far as the behavior of the photometric profiles at large radii is concerned, we see that, especially for NGC 104, NGC 362, NGC 6254, NGC 6341, and NGC 7078 King

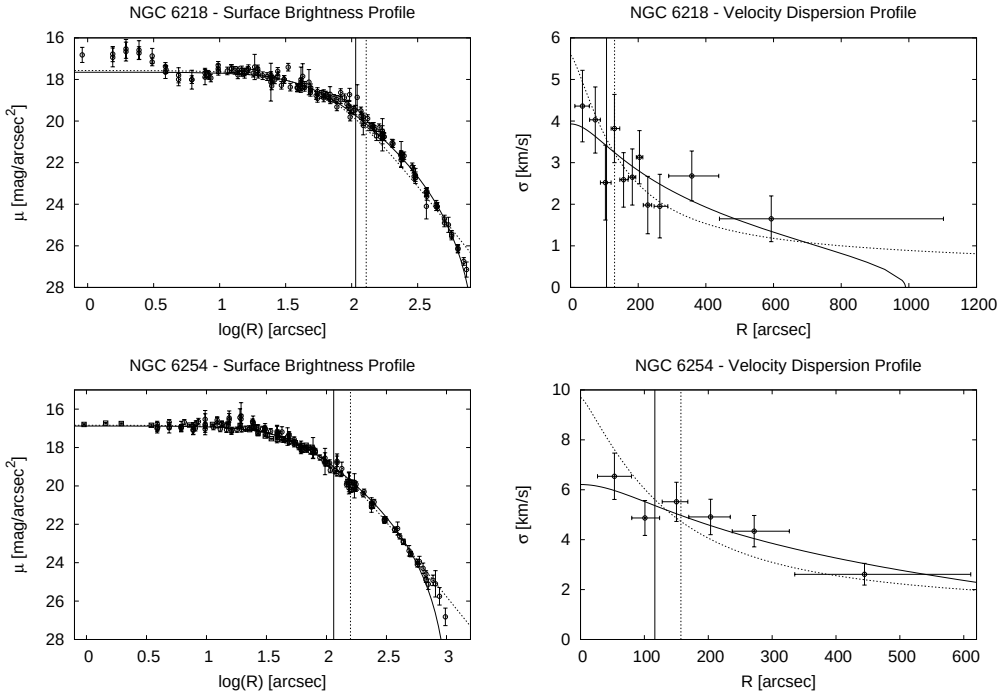

Figure 8.2: Fits by King models and anisotropic $f^{(\nu)}$ models to the surface brightness profiles and to the line-of-sight velocity dispersion profiles of selected globular clusters in the intermediate relaxation condition (NGC 6218 and NGC 6254), in the same format as in Fig. 8.1.

models do not provide a good description of the truncation, as noted in a number of previous studies (in particular, see McLaughlin & van der Marel 2005; Jordi & Grebel 2010; Küpper et al. 2010a, in which the outermost parts of the surface brightness profiles are appropriately modeled by using N-body simulations). In some cases, the observed profile falls between the King and the $f^{(\nu)}$ profiles. This suggests that truncated $f^{(\nu)}$ models might behave systematically better than King models for describing these stellar systems. To a large extent, the modification by truncation in phase space of the anisotropic (nontruncated) $f^{(\nu)}$ models is complementary to the generalization of the isotropic (truncated) King models to models characterized by anisotropic pressure, that is, the so-called Michie-King models (in which the truncated Maxwellian is associated with the anisotropic factor of the Eddington models; see Michie 1963, Gunn & Griffin 1979). At this stage, it would be interesting to compare the behavior of the outer photometric and kinematic profiles of the two families of anisotropic truncated models, to evaluate the interplay between truncation and pressure anisotropy in the two different cases. Of course, the simple physical picture offered by King, $f^{(\nu)}$, and Michie-King models still suffers from a number of limitations, as discussed in the Introduction. Such a simple picture is bound to fail in the modeling of clusters in which core collapse has taken place. Therefore, it is not surprising that clusters such as NGC 362 and NGC 7078, even if they belong to the first relaxation class, are not described by isotropic King models as well as expected.

In closing, we wish to reiterate that, in general, the kinematic fits are crucial to as-

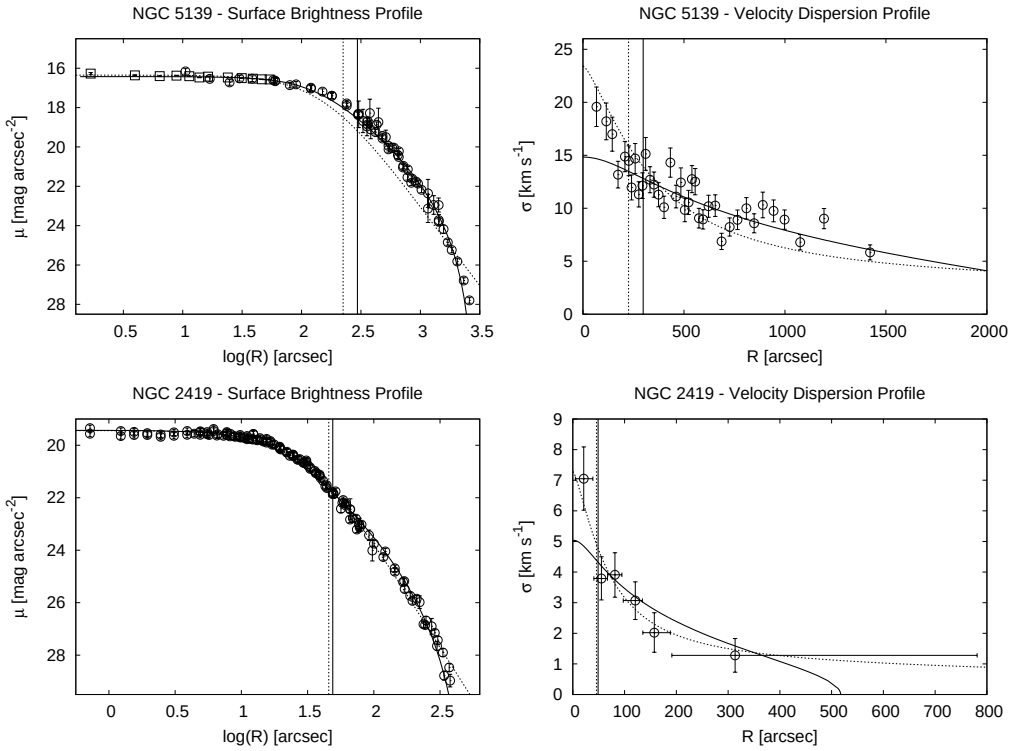

Figure 8.3: Fits by King models and anisotropic $f^{(\nu)}$ models to the surface brightness profiles and to the line-of-sight velocity dispersion profiles of partially relaxed globular clusters, in the same format as in Fig. 8.1.

sess if a model is actually able to describe a given globular cluster. Unfortunately, the observed velocity dispersion profiles are generally less accurate and less reliable, with respect to the surface brightness profiles; not only the outer parts (radii close to the truncation radius), but also the inner parts (inside the half-light radius) are often not well sampled as would be desired. The present study confirms that in the future it would be desirable to acquire new and better kinematic data.

8.4.2 King models vs. $f^{(\nu)}$ models

The values of the relevant structural parameters derived from the best-fit models are presented in Table 8.4. For the majority of the globular clusters considered in our sample, the values of the half-mass radius from $f^{(\nu)}$ models are larger than those obtained from King models; only for NGC 362 the opposite is true. For NGC 288, NGC 5139 and NGC 6809 the values calculated from the two models basically coincide. By comparing the values of the total mass and of the central mass density calculated with the two families of models, we see that for the whole sample (with few exceptions) the values calculated with $f^{(\nu)}$ models are larger than those calculated with King models; this fact is not at all surprising, since the $f^{(\nu)}$ models are not truncated. As to the mass-to-light ratios, we see that there is not a tight correlation between the values calculated with King and $f^{(\nu)}$ models, the latter being almost always larger. Similar trends are noted also in the

Table 8.5: Core and half-mass relaxation times for the best-fit King and $f^{(\nu)}$ models.

	King Models		$f^{(\nu)}$ Models	
NGC	$\log T_{\rm c}$	$\log T_{\rm M}$	$\log T_{\rm c}$	$\log T_{\rm M}$
(1)	(2)	(3)	(4)	(5)
362	7.565	8.971	7.713	8.825
7078	7.620	8.820	7.491	9.176
6121	7.818	8.774	7.836	9.137
104	7.846	9.198	7.922	9.629
6341	7.881	8.904	8.142	9.052
6218	8.140	8.725	8.142	8.902
6254	8.269	8.892	8.334	9.150
6656	8.418	9.099	8.451	9.361
3201	8.523	9.123	8.545	9.305
6809	8.835	9.289	8.529	9.288
288	8.969	9.482	8.750	9.509
5139	9.515	10.140	9.429	10.191
2419	9.812	10.537	9.970	10.731

structural properties derived from (isotropic) models characterized by a more spatially extended truncation, such as the Wilson models (see McLaughlin & van der Marel 2005).

In Table 8.5, we list the values of the core and half-mass relaxation times calculated by using the two best-fit dynamical models for each globular cluster; the clusters are listed in order of increasing King core relaxation times, and the separation in three classes of relaxation here adopted is marked with horizontal lines.

When considering the core relaxation times (calculated according to Eq. (10) of Djorgovski (1993), as in the Harris 2010 catalog), we see that the original division in the relaxation classes proposed in this study on the basis of the values listed in the Harris catalog is confirmed. The only exception is NGC 6341: according to the value of the core relaxation time calculated with its best-fit $f^{(\nu)}$ model, this cluster should belong to the second class, rather than to the first. When we list globular clusters according to increasing core relaxation times estimated with the models identified in this study, we see that the order of relaxed globular clusters changes with respect to that of Table 8.1. However, there is a general agreement between values of these quantities calculated with the two families of models.

To calculate the half-mass relaxation times we followed the definition of Eq. (5) in Spitzer (1987), which is based on the half-mass radius. We see that the values from $f^{(\nu)}$ models are larger than those from King models, except for NGC 362 and NGC 6809 (for the latter cluster, the estimated values are approximately equal). In contrast with the case of the core relaxation times, the values of the half-mass relaxation time turn out to be more model-dependent. Such dependence is likely to be due to the differences between the density profiles of the two families of models, which, in general, are less significant in the central regions and become more evident at radii larger than the half-mass radius. The introduction of a truncation for $f^{(\nu)}$ models would also lead to different values of these parameters. We notice that usually the half-mass relaxation time is calculated by inserting in the relevant definition directly the (projected) half-light radius (see, for example, Harris 2010 and McLaughlin & van der Marel 2005). By following the same procedure, we found that the values of the half-mass relaxation times are less

model dependent, and closer to the values listed in the Harris catalog.

8.4.3 Central slope of the photometric and kinematic profiles

When considering the surface brightness profiles of our selected globular clusters, we note that there are cases in which the observed photometric profiles deviate from the calculated ones at small radii. In particular, by focusing on the innermost regions of the profiles, we see that this is the case for NGC 6121, NGC 6218, and NGC 7078, for which the models are underluminous, and NGC 288, NGC 6656, and NGC 6809, in which the models are overluminous, and NGC 3201, for which the observed central surface brightness appears to oscillate; in spite of these local discrepancies, the global values of the statistical indicators may be satisfactory.

As far as the velocity dispersion profiles are concerned, in four cases (NGC 288, NGC 3201, NGC 6121, and NGC 6656), both models overpredict the central data-points, while, as mentioned in Sect. 8.4.1, four clusters (NGC 2419, NGC 5139, and, possibly, NGC 6218 and NGC 6254) show a relatively large gradient of the profile in the central regions. At variance with the study of elliptical galaxies, the kinematic profiles of globular clusters are often undersampled inside the half-light radius.

Recently, the central cusps in the observed photometric and kinematic profiles of some globular clusters have been interpreted as clues of the presence of an intermediate-mass black hole (IMBH) in the center of the system (see the analytical model by Bahcall & Wolf 1976 and the N-body simulations by Baumgardt et al. 2005b and Noyola & Baumgardt 2011), and a variety of dynamical models (either defined from distribution functions or as solutions of the Jeans equations), have been used in order to constrain the mass of such central object (the best known example is the controversial case of ω Cen, studied by Noyola et al. 2008 and van der Marel & Anderson 2010, with different conclusions). However, Vesperini & Trenti (2010) showed that these shallow photometric cusps are not decisive signatures of the presence of an IMBH, and that they might be related to other dynamical processes; moreover, the authors emphasize the fact that the typical accuracy in the data may be insufficient to characterize the slope of the profile as desired.

As shown in the previous sections, the presence of radially-biased pressure anisotropy (which occurs in the context of the family of $f^{(\nu)}$ models or of the Michie-King models, see Michie 1963) can also produce a relatively rapid decline in the central part of the velocity dispersion profile. Therefore, here we are reiterating a point already noted in the literature, that the presence of a central IMBH should not be considered as the only physical explanation of the existence of a central kinematical peak[5]. Unfortunately, our independent conclusion only confirms that the interpretation of this interesting kinematical feature is more model dependent than desired. We recall that $f^{(\nu)}$ models are characterized by a "realistic" anisotropy profile (see Fig. 6 in Trenti & Bertin 2005): the central regions are more isotropic than the outer ones in velocity space, because the models represent a scenario in which violent relaxation has acted more efficiently in the center. This differential kinematical feature is not always present in dynamical models based on the Jeans approach, which, to obtain a fast decline in the velocity dispersion profile in the absence of a central IMBH, usually requires very high values of the anisotropy parameter, even in the central regions of the cluster (see, for example, Sect 4.2 in Noyola et al. 2008 or Sect 5.3 in Lützgendorf et al. 2011).

[5]Of course, $f^{(\nu)}$ models are able to reproduce a slope in both the photometric and kinematic profile, only when high values of the concentration parameter are considered.

8.5 Discussion and conclusions

In this Chapter we have performed a detailed combined photometric and kinematic study of a sample of Galactic globular clusters, representing systems under different relaxation conditions. For these objects, surface brightness and velocity dispersion profiles have been fitted by means of two different families of dynamical models, the truncated isotropic King models and the non-truncated, anisotropic $f^{(\nu)}$ models. The analysis has been carried out by following the same procedure used in the past to study the dynamics of elliptical galaxies. Each globular cluster is then associated with two best-fit models. The main conclusions can be summarized as follows:

- The expected trend, that King models should perform better for more relaxed globular clusters, has been checked to exist but it is not as sharp as anticipated. The two clusters (NGC 104 and NGC 6341) for which the global fit by King models is most convincing indeed belong to the class of relaxed objects. King models tend to offer a good representation of the observed photometric profiles (as is commonly reported), regardless of the relaxation condition of the system. However, the quality of the fits by King models to the kinematic profiles remains to be proved, even for relaxed clusters, because of the few data-points and the large error bars in the observed profiles. Three clusters for which the King models appear to be inadequate do not actually come as a surprise: NGC 2419 is the least relaxed cluster of the sample and NGC 362 and NGC 7078 are suspected to be post-core-collapse clusters.

- The second expected trend, that less relaxed clusters might exhibit the characteristic signature of incomplete violent relaxation, is also partly present but is not as sharp as might have been hoped for. Some cases indeed point to a significant role of radially-biased pressure anisotropy. The least relaxed cluster, NGC 2419, is well described by the $f^{(\nu)}$ models. For the second least relaxed cluster, NGC 5139, the central shallow cusp in the velocity dispersion profile appears to be well captured by the $f^{(\nu)}$ models. A marginal indication in favor of the $f^{(\nu)}$ models also comes from inspection of the inner kinematic profiles of NGC 6218 and NGC 6254, although these two clusters are not among the least relaxed objects. In contrast, King models and other isotropic models (such as the spherical Wilson models) have difficulty in matching significant velocity gradients inside the half-light radius. Therefore, the partial success of the $f^{(\nu)}$ models suggests that for some globular clusters radially-biased pressure anisotropy may be important. This property could be examined further by means of better spatially-resolved kinematic data in the inner regions (i.e., at radii out to approximately the half-light radius). This result is in line with the conclusions of recent papers: in particular, see Ibata et al. 2011 and references therein, based on the application of King-Michie models.

- In some clusters, regardless of the relaxation condition, some qualitative characteristics of the observed profiles are missed by both families of models considered in this Chapter. It may be that part of these cases would be resolved by a study in terms of *truncated* $f^{(\nu)}$ models. But it may also be that other ingredients ignored in the present study, such as rotation (solid-body or differential), play a role.

- The study demonstrates that the values of some structural parameters, such as the total mass and the half-mass radius, can be significantly model-dependent. In view of the results listed in the previous items, this is a clear warning against an

indiscriminate use of structural parameters for globular clusters based on only one family of models (the spherical King models).

- In general, the kinematic fits are crucial to assess if a model is actually suited to describe a given globular cluster. The main issue in testing dynamical models on globular clusters is therefore the general lack of good kinematic data: the data are available for a small fraction of the population of Galactic globular clusters and generally made of a small number of data-points, not well distributed in radius. Surprisingly, the kinematic profile is often not well sampled as desired inside the half-mass radius. As discussed in the Chapter this is a key region for confronting the performance of different dynamical models. In addition, accurate data in the outermost parts, close to the truncation radius,would touch on other important issues, such as the role of tides. Only after the acquisition of good kinematical profiles will it be possible to address properly the issue of dark matter in globular clusters.

Future directions

Within the analytical framework offered by the families of dynamical models developed in the present Thesis, a number of projects can be devised, as a natural extension of the line of research. In particular, the following separate yet related issues will be addressed in the near future:

The role of angular momentum in the formation of star clusters: The majority of present-day star clusters are only slowly rotating, but the role of angular momentum during the initial stages of cluster formation indeed requires clarification. N-body simulations of the merging process of two star clusters have shown that the resulting system may be characterized by a significant amount of global angular momentum (Makino et al. 1991); therefore, in some cases, the presence of relatively strong internal rotation has been interpreted as a signature of a past merger event (for a recent example, see Lane et al. 2010a). In turn, in the context formation scenarios by dissipationless collapse, relatively few investigations have considered the role of angular momentum in numerical experiments of "violent relaxation" (Gott 1973). Interestingly, the final equilibrium configurations resulting from such scenario show a central region with solid body rotation, whereas the external parts are characterized by differential rotation. Since this kinematic behavior characterizes the family of differentially rotating models studied in Chapter 4, it would be interesting to perform a dedicated survey of N-body simulations and to compare the systems resulting from the early violent dynamical evolution with the rotating equilibrium configurations introduced in the present Thesis.

A link between internal rotation and multiple stellar populations in globular clusters: The investigation described above is particularly interesting also in view of the need to find a dynamical characterization of multiple stellar populations, the observational evidence of which is shown by a very high fraction of the globular clusters studied to date (D'Ercole et al. 2010). In fact, on the observational side, a number of correlations between internal rotation and chemical properties (such as the metallicity or the Horizontal Branch Morphology parameter) have been recently found (Bellazzini et al. 2012); on the theoretical side, hydrodynamical simulations suggest that some globular clusters composed of two generations of stars had a significant amount of rotation when they were formed (Bekki 2010). Therefore, the differentially rotating models presented in Chapter 4 may provide the appropriate initial conditions for numerical simulations designed to investigate the puzzling existence of multiple stellar populations in globular clusters, which are normally studied under the simplifying assumption of the absence of internal rotation. In addition, we plan to carry out an

extensive survey of N-body simulations, in which the effects of stellar evolution are taken into account, to explore the early and long-term dynamical evolution of the differences between the amount of rotation of the first and the second generation stars. The results obtained from this study are expected to provide a useful guide in the interpretation of the relevant kinematical and chemical observables that suggest the existence of a link between internal rotation and multiple stellar populations in globular clusters.

Central kinematic gradients: IMBH, rotation, or pressure anisotropy? The family of differentially rotating models might help clarify the controversial issue about the use of gradients in the velocity dispersion profiles as unequivocal signature of the presence of an Intermediate Mass Black Hole (IMBH) in globular clusters. High-precision astrometric techniques with the HST has already made possible to use proper motions to measure the plane-of-the-sky rotation in globular clusters (Anderson & King 2003). The future mission GAIA will provide three-dimensional kinematical data of stars in globular clusters, except for the center of very dense objects, where crowding might be a problem. Yet, even in such cases, the physical origin of a gradient in the velocity dispersion profiles can be clarified with the help of new kinematic data. In fact, on the one hand, the influence of a massive IMBH is expected to extend nearly out to the half-mass radius of the globular cluster (Baumgardt et al. 2005b), and, on the other hand, a number of differentially rotating configurations studied in the present Thesis show nontrivial gradients in the intermediate and outer parts of the cluster, where the crowding should not be a problem. Models based on the use of the Jeans equations seem to be less satisfactory in this respect, because, at least in their most popular (nonrotating) application, they are used to reproduce variations in the slope of the velocity dispersion profile of a system only by tuning the amount of pressure anisotropy (e.g., see Lützgendorf et al. 2011). The purpose of a study in this direction is thus twofold: (i) on the observational side, we plan to apply the rotating models to the interpretation of the kinematics of the central regions of clusters that are claimed to host an IMBH, such as ω Cen (Jalali et al. 2012) or NGC 6388 (Lützgendorf et al. 2011), in particular, we plan to estimate if a realistic amount of internal rotation can mimic such signatures in the velocity space; (ii) on the theoretical side, we will carry out a survey of N-body simulations of realistic star clusters, characterized by either the presence of an IMBH or an appropriate amount of central rotation, and we will perform synthetic observations of simulation snapshots, consistent with the requirements of current HST and future GAIA observations (for a similar approach, see Trenti et al. 2010).

What is the appropriate dynamical interpretation of the "extra-tidal" lights? The existence of structures in the surface brightness profile of Galactic and extragalactic globular clusters extending beyond what is prescribed by spherical King models is frequently reported (e.g., for recent studies of the structure and morphology of globular clusters in the Milky Way, M31, NGC 5128 and M87, see Jordi & Grebel 2010, Barmby et al. 2007, Harris et al. 2006, Madrid et al. 2009, respectively). In this context, spherical Wilson (1975) models, which are characterized by a different truncation prescription in phase space, seem to be more successful than King models in describing the photometric profiles of a significant fraction of globular clusters, especially in their outer parts (for a comparison of the two families of models on a sample of globular clusters in the Local Group and in NGC 5128, see McLaughlin & van der Marel 2005 and McLaughlin et al. 2008, respectively). Since the triaxial models described in the present Thesis fully take into account the external tidal field, they are

intrinsically more elongated than spherical King models, which simply heuristically mimic the effect of tides, but neglect the relevant geometrical distortions. Therefore, the triaxial models might be useful for interpreting this photometric feature and for providing a proper dynamical interpretation of the tidal effects on the structure of star clusters (e.g., see the recent application of the models to the globular clusters in M87 by Webb et al. 2012). For this purpose, when possible, the use of high resolution imaging from the HST combined with ground-based wide-field imaging and detailed spectroscopic information is highly desirable in order (i) to accurately select stars, leading to a proper separation of members and interlopers; this selection is critical to determine the true extension of the outskirts of a globular cluster; (ii) to characterize the deformations induced by the external tidal fields over the entire radial extent of the stellar system; (iii) to detect the possible presence of tidal tails, to be distinguished from nonspherical tidal structures made of stars energetically bound to the cluster.

Escape from star clusters as self-consistent tidal models: As a star exchanges energy with other single and binary stars in a cluster due to close and distant encounters, it can reach an energy in excess of the escape energy and escape from the cluster. In order to investigate the dynamical evolution of a cluster, it is necessary to understand the rate at which this process takes place and the spatial distribution of the escapers inside the cluster itself. Both quantities have been successfully modelled in the case of clusters treated as isolated systems (for an summary, see Chap. 16 in Heggie & Hut 2003). Besides, when a cluster is considered as limited by the tidal field of a galaxy, the definition of escape becomes nontrivial. If the presence of the external tidal field is properly modelled (as opposed to being treated in a simplified way by introducing, for example, a spatial or an energy cutoff), stars can escape the cluster only through the Lagrangian points of the galaxy-cluster system. It has been demonstrated that the time needed for a star with an energy greater than the escape energy to flow through one of the Lagrangian points and actually escape from the cluster is not negligible Fukushige & Heggie (2000); Baumgardt (2001). In addition, stars on stable orbits with energies above the escape energy exist and actually dominate the outer parts of a cluster, with significant effects on the global observable velocity dispersion profile Küpper et al. (2010a). Driven by these motivations, it may be interesting to extend the analysis of the escape process to the case in which the perturbation induced by the external tidal field is treated self-consistently, as in the models studied in Part I of the present Thesis, with particular attention to the estimate of the relevant time scale (as in Fukushige & Heggie 2000) and spatial distribution of the escapers (as in Johnstone 1993). Any result of this investigation will then require a comparison with appropriate N-body simulations.

Self-consistent rigidly rotating tidally perturbed models: The families of nonspherical models discussed in the present Thesis analyze the effects of internal rotation and external tidal field on the structure of stellar systems only as separate physical ingredients. A more realistic family of models should take into account the presence of perturbations resulting from combined rotational and tidal effects. The general case of a cluster in an external tidal field and characterized by internal rotation about an axis with arbitrary orientation with respect to the direction of the orbital angular momentum can be greatly simplified by assuming a circular orbit for the cluster in host galaxy and rigid internal rotation about an axis parallel to the axis of the orbital motion; to fully appreciate the perturbation induced by internal rotation, the latter should be characterized by a different angular velocity with respect

to that of the orbital motion. In this case, a generalization of the family of spherical King models can be defined by using the relevant approximate energy integral in an appropriate frame of reference. The perturbation method developed for the construction of tidally perturbed models can be applied for the solution of the relevant Poisson equation, provided that the deviations from synchronous conditions are modest; the configurations should be characterized by a nontrivial geometry, with reflection symmetry with respect to the equatorial plane. An similar physical and mathematical problem arises in the determination of the structure of the equilibrium configurations of a nonsynchronous circular binary star system, for which a generalization of the traditional Roche model has been presented (see Kruszewski 1963 and Limber 1963).

Appendices

APPENDIX A

Details of the perturbation method

A.1 The general equation

From the Taylor expansion about $\epsilon = 0$ of the right-hand side of Eq. (2.17), the structure of the equations for $\psi_k^{(int)}$ (with $k \geq 2$) can be expressed as:

$$\left[\hat{\nabla}^2 + R_1(\hat{r};\Psi)\right] \psi_k^{(int)} = -\left(\sum_{j=2}^{k} R_j(\hat{r};\Psi)\, X_{k,j}\right) , \tag{A.1}$$

where $X_{k,j}$ denotes the terms that arise from the derivatives of $\psi^{(int)}(\hat{r};\epsilon)$ with respect to ϵ, thus expressed as products of $\psi_i^{(int)}$ (with $i = 1,..,k-1$). For fixed k and j, the quantity $X_{k,j}$ is thus a sum of products of $\psi_i^{(int)}$ with subscripts that are j-part partitions of the integer k. Each product of $\psi_i^{(int)}$ is multiplied by a numerical factor defined as the ratio between $k!$ and the factorials of the integers that are parts of the associated partition (if an integer appears m times in the partition, the factor must also be divided by $m!$). In particular, for $k = 3$ we have:

$$X_{3,2} = 3\psi_2^{(int)}\psi_1^{(int)} \text{ and } \quad X_{3,3} = (\psi_1^{(int)})^3 , \tag{A.2}$$

because the 2-part partition of 3 is $2+1$ and the 3-part partition is trivially $1+1+1$, thus the relevant equation is:

$$\left[\hat{\nabla}^2 + R_1(\hat{r};\Psi)\right] \psi_3^{(int)} = -R_2(\hat{r};\Psi)\, 3\psi_2^{(int)}\psi_1^{(int)} - R_3(\hat{r};\Psi)\,(\psi_1^{(int)})^3 . \tag{A.3}$$

Therefore, this formulation of the right-hand side of the general equation (together with the term $R_1(\hat{r};\Psi)\psi_k^{(int)}$ on the left-hand side) brings in the *Faá di Bruno formula* (Faá di Bruno 1855) for the k-th order derivative of a composite function in which the inner one is expressed as a series in the variable with respect to which the derivation is performed.

A.2 The equation for the second order radial problem

The expansion in spherical harmonics of $(\psi_1^{(in)})^2$, which involves the product of two spherical harmonics with $l = 0$ or $l = 2$ (with m positive and even), can be performed by means of the so-called 3-j Wigner symbols [1]. Equation (2.33) thus corresponds to the

[1] For the definition of 3-j Wigner symbols and the expression of the harmonic expansion of the product of two spherical harmonics, see, e.g., Edmonds (1960), Eqs. (3.7.3) and (4.6.5), respectively.

following set of six equations:

$$\mathcal{D}_0\psi^{(int)}_{2,00} = -R_2(\hat{r};\Psi)\frac{1}{2\sqrt{\pi}}\left[(\psi^{(int)}_{1,00})^2 + (\psi^{(int)}_{1,20})^2 + (\psi^{(int)}_{1,22})^2\right], \tag{A.1}$$

$$\mathcal{D}_2\psi^{(int)}_{2,20} = -R_2(\hat{r};\Psi)\frac{1}{7}\sqrt{\frac{5}{\pi}}\left[\frac{7}{\sqrt{5}}\psi^{(int)}_{1,00}\,\psi^{(int)}_{1,20} + (\psi^{(int)}_{1,20})^2 - (\psi^{(int)}_{1,22})^2\right], \tag{A.2}$$

$$\mathcal{D}_2\psi^{(int)}_{2,22} = -R_2(\hat{r};\Psi)\frac{1}{\sqrt{\pi}}\left[\psi^{(int)}_{1,00}\,\psi^{(int)}_{1,22} - \frac{2\sqrt{5}}{7}\psi^{(int)}_{1,20}\,\psi^{(int)}_{1,22}\right], \tag{A.3}$$

$$\mathcal{D}_4\psi^{(int)}_{2,40} = -R_2(\hat{r};\Psi)\frac{1}{7\sqrt{\pi}}\left[3(\psi^{(int)}_{1,20})^2 + \frac{1}{2}(\psi^{(int)}_{1,22})^2\right], \tag{A.4}$$

$$\mathcal{D}_4\psi^{(int)}_{2,42} = -R_2(\hat{r};\Psi)\frac{1}{7}\sqrt{\frac{15}{\pi}}\,\psi^{(int)}_{1,20}\,\psi^{(int)}_{1,22}, \tag{A.5}$$

$$\mathcal{D}_4\psi^{(int)}_{2,44} = -R_2(\hat{r};\Psi)\frac{1}{2}\sqrt{\frac{5}{7\,\pi}}\,(\psi^{(int)}_{1,22})^2. \tag{A.6}$$

A.3 The asymptotic matching for the first order solution

To derive the first order solution, the matching between the pairs $(\psi^{(int)},\psi^{(lay)})$ and $(\psi^{(ext)},\psi^{(lay)})$ requires that the internal (external) solution is expanded in a Taylor series around $\hat{r} = \hat{r}_{tr}$ up to terms of order $\mathcal{O}((\hat{r}-\hat{r}_{tr})^2)$, expressed with scaled variables, expanded up to $\mathcal{O}(\epsilon^2)$, and re-expressed with non-scaled variables:

$$\begin{aligned}[\psi^{(\,)}]^{(2)}(\hat{r},\theta,\phi) &= \psi_0^{(\,)}(\hat{r}_{tr}) - {\psi_0^{(\,)}}'(\hat{r}_{tr})(\hat{r}_{tr}-\hat{r}) + \frac{1}{2}{\psi_0^{(\,)}}''(\hat{r}_{tr})(\hat{r}_{tr}-\hat{r})^2 \\ &+ \left[\psi_1^{(\,)}(\hat{r}_{tr},\theta,\phi) - \frac{\partial\psi_1^{(\,)}}{\partial\hat{r}}(\hat{r}_{tr},\theta,\phi)(\hat{r}_{tr}-\hat{r})\right]\epsilon + \frac{1}{2}\psi_2^{(\,)}(\hat{r}_{tr},\theta,\phi)\epsilon^2 .\end{aligned} \tag{A.1}$$

Here the closed parentheses include either "int" or"ext", to denote internal or external solution, while the notation $[\ ]^{(2)}$ on the left-hand side indicates that a second order expansion in ϵ has been performed.

The boundary layer solution in the vicinity of $\eta = 0$ up to $\mathcal{O}(\eta^2)$, expressed with non-scaled variables and expanded (formally) up to third order in ϵ is given by:

$$\begin{aligned}[\psi^{(lay)}]^{(3)}(\hat{r},\theta,\phi) &= F_0(\theta,\phi)(\hat{r}_{tr}-\hat{r}) + \frac{F_0(\theta,\phi)}{\hat{r}_{tr}}(\hat{r}_{tr}-\hat{r})^2 \\ &+[G_0(\theta,\phi) + F_1(\theta,\phi)(\hat{r}_{tr}-\hat{r})]\epsilon + G_1(\theta,\phi)\epsilon^2 .\end{aligned} \tag{A.2}$$

By equating equal powers of ϵ and $(\hat{r}_{tr} - \hat{r})$ in (A.1) and (A.2), we find:

$$\psi_0^{(int)}(\hat{r}_{tr}) = 0 = \alpha_0 - \frac{\lambda_0}{\hat{r}_{tr}} , \tag{A.3}$$

$$-\psi_0^{(int)'}(\hat{r}_{tr}) = F_0(\theta,\phi) = -\frac{\lambda_0}{\hat{r}_{tr}^2} , \tag{A.4}$$

$$\frac{1}{2}\psi_0^{(int)''}(\hat{r}_{tr}) = \frac{F_0(\theta,\phi)}{\hat{r}_{tr}} = -\frac{\lambda_0}{\hat{r}_{tr}^3} , \tag{A.5}$$

$$\psi_1^{(int)}(\hat{r}_{tr},\theta,\phi) = G_0(\theta,\phi) = \alpha_1 - \frac{\lambda_1}{\hat{r}_{tr}} - \frac{T_{00}(\hat{r}_{tr})}{2\sqrt{\pi}} - \sum_{l=1}^{\infty}\sum_{m=-l}^{l}\left[\frac{a_{lm}}{\hat{r}_{tr}^{l+1}} + T_{lm}(\hat{r}_{tr})\right] Y_{lm}(\theta,\phi) , \tag{A.6}$$

$$-\frac{\partial\psi_1^{(int)}}{\partial\hat{r}}(\hat{r}_{tr},\theta,\phi) = F_1(\theta,\phi) = -\frac{\lambda_1}{\hat{r}_{tr}^2} + \frac{T_{00}(\hat{r}_{tr})}{\sqrt{\pi}\hat{r}_{tr}} - \sum_{l=1}^{\infty}\sum_{m=-l}^{l}\left[\frac{(l+1)a_{lm}}{\hat{r}_{tr}^{l+2}} - \frac{2T_{lm}(\hat{r}_{tr})}{\hat{r}_{tr}}\right] Y_{lm}(\theta,\phi) , \tag{A.7}$$

$$\frac{1}{2}\psi_2^{(int)}(\hat{r}_{tr},\theta,\phi) = G_1(\theta,\phi) = \frac{1}{2}\left[\alpha_2 - \frac{\lambda_2}{\hat{r}_{tr}} - \sum_{l=1}^{\infty}\sum_{m=-l}^{l}\frac{b_{lm}}{\hat{r}_{tr}^{l+1}}Y_{lm}(\theta,\phi)\right] , \tag{A.8}$$

where the equalities on the left-hand side arise from the matching of the pair $(\psi^{(int)}, \psi^{(lay)})$ and identify the free angular functions (2.54)-(2.57), while those on the right-hand side arise from the matching of the pair $(\psi^{(ext)}, \psi^{(lay)})$. We also note that (A.3) is consistent with the definition of the truncation radius and that (A.5) is equivalent to (A.4), because from Eq. (2.24) we have: $\psi_0^{(int)''}(\hat{r}_{tr}) = -(2/\hat{r}_{tr})\psi_0^{(int)'}(\hat{r}_{tr})$.

The free constants (2.58)-(2.61) are thus easily determined. For a given harmonic (l,m) of Eqs. (A.6) and (A.7), with $l \geq 1$, the constants A_{lm} and a_{lm} are governed by the linear system with $i,j = 1,2$:

$$M_{ij}u_j = v_i , \tag{A.9}$$

where the matrix M is given by

$$M = \begin{pmatrix} \gamma_l(\hat{r}_{tr}) & \hat{r}_{tr}^{-(l+1)} \\ -\gamma_l'(\hat{r}_{tr})\hat{r}_{tr} & (l+1)\hat{r}_{tr}^{-(l+1)} \end{pmatrix} , \tag{A.10}$$

and the vectors are defined as $(u_1,u_2) = (A_{lm}, a_{lm})$ and $(v_1,v_2) = -T_{lm}(\hat{r}_{tr})(1,-2)$. Such linear system (A.9) is well posed, i.e. $detM \neq 0$.

To show this, we may integrate Eq (2.31) for the regular solution, under the conditions $\gamma_l(0) = \gamma_l'(0) = 0$:

$$\gamma_l'(\hat{r})\hat{r}^2 = \int_0^{\hat{r}} [l(l+1) - R_1(\hat{r};\Psi)\hat{r}^2]\gamma_l(\hat{r})d\hat{r} . \tag{A.11}$$

In the vicinity of $\hat{r} = 0$ the quantity $R_1(\hat{r};\Psi)\hat{r}^2$ is vanishingly small, so that, if the quantity $R_1(\hat{r};\Psi)\hat{r}^2$ remains smaller than $l(l+1)$, then the regular solution, starting positive and monotonic, remains a positive and monotonically increasing function of $\hat{r}$. Indeed,

we have checked that this condition occurs for $l \geq 2$, because for $\Psi \in [0.5, 10]$ the quantity $R_1(\hat{r}; \Psi)\hat{r}^2$ has a maximum value in the range [4.229, 3.326]. Under this condition the function $\mu_l(\hat{r}) \equiv \gamma_l'(\hat{r})\hat{r} + (l+1)\gamma_l(\hat{r})$ cannot change sign, so that $detM = \hat{r}_{tr}^{-(l+1)}\mu_l(\hat{r}_{tr})$ cannot vanish. This argument does not work for the case $l = 1$, in which the function $\mu_l(\hat{r})$ does change sign at a point $0 < \hat{r}_0 < \hat{r}_{tr}$, but we have checked directly that the property $detM \neq 0$ is satisfied also in this case.

Then expressions (2.62) and (2.63) are easily recovered and we conclude that for the harmonics that are not "driven"by the tidal potential $T(\hat{\mathbf{r}})$ the related a_{lm} and A_{lm} must vanish.

Similarly, for a given harmonic (l, m) with $l \geq 1$, Eq. (2.64), which is obtained from the second order matching, and Eq. (A.8) can be cast in the form of Eq. (A.9), with $(u_1, u_2) = (B_{lm}, b_{lm})$ and $(v_1, v_2) = (-g_{lm}(\hat{r}_{tr}), \hat{r}_{tr}g_{lm}'(\hat{r}_{tr}))$. Therefore, the argument provided above applies and we can conclude that for those harmonics for which the particular solutions $g_{lm}(\hat{r})$ are absent (or, equivalently, Eq. [2.33] is homogeneous), the constants B_{lm} and b_{lm} must vanish. A linear system equivalent to (A.9) can be written for a fixed harmonic (l, m) with $l \geq 1$ of the solution of general order k and the same argument applies. Therefore, we conclude that the k-th order term of the solution contributes only to those harmonics for which the particular solutions are present.

A.4 The structure of k-th order term

Because we have noted (see argument introduced about the system [A.9]) that the k-th order term of the solution has non-vanishing contribution only in correspondence of those harmonics for which the component of Eq. (A.1) is non-trivial, the discussion about the structure of the term reduces to the analysis of the structure of the expansion in spherical harmonics of the right-hand side of that equation. Recalling that the harmonic expansion of the product of two spherical harmonics (l_1, m_1) and (l_2, m_2) can be expressed by means of 3-j Wigner symbols (see Edmonds 1960, Eq. [4.6.5]), we note that the composed harmonic (l, m) must satisfy the following *selection rules*: (i) $|l_1 - l_2| \leq l \leq l_1 + l_2$ ("triangular inequality"), (ii) $m_1 + m_2 = m$, and (iii) $l_1 + l_2 + l$ must be even. The last condition holds because in the cited expression the composed harmonic appears multiplied by the special case of the Wigner symbol with (l_1, l_2, l) as first row and $(0, 0, 0)$ as second row. Bearing in mind that the first order term is characterized by harmonics with $l = 0, 2$ and corresponding positive and even values of m and that the structure of the right-hand side of Eq. (A.1) can be interpreted by means of the partitions of the integer k, it can be proved *by induction* that the k-th order term is characterized by harmonics with $l = 0, 2, ..., 2k$ and corresponding positive and even values of m.

A.5 Application to the case rigidly rotating models

The solution up to second order in terms of matched asymptotic expansions presented in Sect. 2.4 can be adapted to the coase of the construction of rigidly rotating models without great effort. In fact, with respect to the calculation presented in Sect. 2.4 only two differences occur: (i) wherever the constant term $-\hat{\nabla}^2 T = -9(1-\nu)$ appears, it must be replaced here by $-\hat{\nabla}^2 C = 18$ (the sign is the same in the two cases, because $1 - \nu < 0$), and (ii) thanks to axisymmetry, in the angular part of the Laplacian the derivative with respect to the toroidal angle ϕ can be dropped and thus the terms of

the asymptotic series (2.22)- (2.23) can be expanded by means of Legendre polynomials[2] instead of spherical harmonics. The latter property implies that the radial part of each term of the asymptotic series is characterized by only one index, l, i.e. we can write $\psi^{(\,)}_{k,l}$. We note that the differential operator that appears on the left-hand side of the relevant equations for the solution defined in the internal region is still $\mathcal{D}_l$, and thus also the functions $\gamma_l(\hat{r})$ can be introduced in the same way as before. As to the equations corresponding to (2.51)-(2.53), the formal solutions of the equations in the boundary layer, the angular functions F_i and G_i (with $i = 0, 1, 2$) now depend only on the poloidal angle θ. About the external solution, an expression analogous to (2.36) can be used, with the particular solution given by χC instead of ϵT. The centrifugal potential contributes, as in the case of the tidal potential, only with monopole and quadrupole terms, explicitly:

$$C_0(\hat{r}) = -3\sqrt{2}\hat{r}^2 \,, \tag{A.1}$$

$$C_2(\hat{r}) = 3\sqrt{\frac{2}{5}}\hat{r}^2 \,. \tag{A.2}$$

Finally, as a result of the matching of the pair $(\psi^{(int)}, \psi^{(lay)})$ up to second order, the expressions for the angular functions (2.54)-(2.57) and (2.64)-(2.65) are still applicable. In addition, from the matching of the pair $(\psi^{(lay)}, \psi^{ext})$ up to second order, we find that the explicit expressions for the free constants follow Eqs. (2.58)-(2.63) and (2.66)-(2.71), provided that we drop everywhere the index m and we replace $3T_{00}(\hat{r}_{tr})/(2\sqrt{\pi})$ with $3C_0(\hat{r}_{tr})/\sqrt{2}$ in (2.60) and $T_{00}(\hat{r}_{tr})/(\sqrt{\pi}\hat{r}_{tr})$ with $2C_0(\hat{r}_{tr})/(\sqrt{2}\hat{r}_{tr})$ in (2.61). Obviously, the particular solutions f_0 and g_l (with $l = 0, 2, 4$) are different from the ones obtained in the tidal case, because the right-hand side of the relevant equations is different. Also in this case, it can be proved *by induction* that the k-th order term has non-vanishing contributions only for $l = 0, 2, ..., 2k$.

For completeness, we record the explicit expression of the second order equations in the internal region:

$$\mathcal{D}_0\psi^{(int)}_{2,0} = -R_2(\hat{r};\Psi)\frac{1}{\sqrt{2}}\left[(\psi^{(int)}_{1,0})^2 + (\psi^{(int)}_{1,2})^2\right] , \tag{A.3}$$

$$\mathcal{D}_2\psi^{(int)}_{2,2} = -R_2(\hat{r};\Psi)\frac{\sqrt{10}}{7}\left[\frac{7}{\sqrt{5}}\psi^{(int)}_{1,0}\,\psi^{(int)}_{1,2} + (\psi^{(int)}_{1,2})^2\right] , \tag{A.4}$$

$$\mathcal{D}_4\psi^{(int)}_{2,4} = -R_2(\hat{r};\Psi)\frac{3\sqrt{2}}{7}\,(\psi^{(int)}_{1,2})^2 \,. \tag{A.5}$$

We remark that the Legendre expansion of the product of two Legendre polynomials is straightforward, because the 3-j Wigner symbols of interest all belong to the special case with $(0, 0, 0)$ as second row.

[2]Following Abramowitz & Stegun (1965), we use Legendre polynomials as defined in (22.3.8), i.e. with Condon-Shortley phase, and normalized with respect to the relation (22.2.10). We remark that, although they are structurally equivalent to zonal spherical harmonics, the normalization is different.

APPENDIX B

Details of the iteration method

B.1 General solution for the radial part of the Laplacian

The ordinary differential equation of second order expressed in Eq. (2.82) can be easily solved by using the method of variation of the arbitrary constants, as the homogeneous solutions of the radial part of the three-dimensional Laplace differential operator in spherical coordinates are well-known

$$y_1(\hat{r}) = \hat{r}^l \tag{B.1}$$

$$y_2(\hat{r}) = \hat{r}^{-(l+1)}. \tag{B.2}$$

The method allows to find a particular solution characterized by the following structure

$$y_p = \varphi_1(\hat{r}) y_1(\hat{r}) + \varphi_2(\hat{r}) y_2(\hat{r}) \tag{B.3}$$

by imposing on the arbitrary functions φ_1 e φ_2 the condition that the function $y_p = y_p(\hat{r})$ could be derived with respect to the radial variable as if the two arbitrary functions were constants, i.e. by requiring that

$$\varphi_1'(\hat{r}) y_1(\hat{r}) + \varphi_2'(\hat{r}) y_2(\hat{r}) = 0. \tag{B.4}$$

By substituing y_p in (2.82) and by making use of the condition expressed in Eq. (B.4), a second equation for φ_1' e φ_2' is recovered, therefore the following system must be solved

$$\begin{cases} \varphi_1'(\hat{r}) y_1(\hat{r}) + \varphi_2'(\hat{r}) y_2(\hat{r}) = 0 \\ \varphi_1'(\hat{r}) y_1'(\hat{r}) + \varphi_2'(\hat{r}) y_2'(\hat{r}) = -\frac{9}{\hat{\rho}(\Psi)} \hat{\rho}_{lm}^{(n)}(\hat{r}) \end{cases}, \tag{B.5}$$

Actually, it can be readily verified that a unique solution for such system exists, as the determinant of the matrix of the coefficients of the system is the Wronskian $W(\hat{r})$ of the the two homogeneous solutions y_1 and y_2. By using the Cramer's rule, it is easily found that

$$\varphi_1'(\hat{r}) = \frac{9}{\hat{\rho}(\Psi)} \hat{\rho}_{lm}^{(n)}(\hat{r}) \frac{y_2(\hat{r})}{W(\hat{r})} \tag{B.6}$$

$$\varphi_2'(\hat{r}) = -\frac{9}{\hat{\rho}(\Psi)} \hat{\rho}_{lm}^{(n)}(\hat{r}) \frac{y_1(\hat{r})}{W(\hat{r})} \tag{B.7}$$

where $W(\hat{r}) = -(2l+1)/\hat{r}^2$. Therefore, the particular solution y_p can be written as:

$$y_p = -\frac{9}{(2l+1)\hat{\rho}(\Psi)} \left[\hat{r}^l \int_{\hat{r}_0}^{\hat{r}} \frac{\hat{\rho}_{lm}^{(n)}(\hat{r}')}{\hat{r}'^{l-1}} d\hat{r}' - \frac{1}{\hat{r}^{l+1}} \int_{\hat{r}_0}^{\hat{r}} \hat{r}'^{l+2} \hat{\rho}_{lm}^{(n)}(\hat{r}') d\hat{r}' \right] \tag{B.8}$$

and the general solution of Eq. (2.82) is given by

$$u_{lm}^{(n)}(\hat{r}) = y_p(\hat{r}; l, m) + \alpha_{lm}\hat{r}^l + \beta_{lm}\hat{r}^{-(l+1)}. \tag{B.9}$$

As for the function with $l = m = 0$, by using the two conditions at the origin the constants α_{00} and β_{00} are determined

$$\alpha_{00} = \Psi + \frac{9}{\hat{\rho}(\Psi)} \int_{\hat{r}_0}^{0} \hat{r}' \hat{\rho}_{00}^{(n)}(\hat{r}') d\hat{r}' \tag{B.10}$$

$$\beta_{00} = -\int_{\hat{r}_0}^{0} \hat{r}'^2 \hat{\rho}_{00}^{(n)}(\hat{r}') d\hat{r}' \tag{B.11}$$

therefore the function $u_{00}^{(n)}$ as expressed in Eq. (2.83) is now fully recovered. As for the other functions charaterized by $l > 0$ and any value of m, by using the second condition at the origin (i.e., concerning the behavior of the radial derivative) and the condition at large radii, the two constants assume the following expressions

$$\alpha_{lm} = \frac{9}{(2l+1)\hat{\rho}(\Psi)} \int_{\hat{r}_0}^{\infty} \hat{r}'^{1-l} \hat{\rho}_{lm}^{(n)}(\hat{r}') d\hat{r}' \tag{B.12}$$

$$\beta_{lm} = -\frac{9}{(2l+1)\hat{\rho}(\Psi)} \int_{\hat{r}_0}^{0} \hat{r}'^{l+2} \hat{\rho}_{lm}^{(n)}(\hat{r}') d\hat{r}' \tag{B.13}$$

which allow to reconver the the function $u_{lm}^{(n)}$ as expressed in Eq. (2.84).

B.2 Numerical procedure for the construction of differentially rotating models

The construction of the equilibrium configurations for the families of differentially rotating models, defined by Eqs. (4.23) and (4.24), has been performed by numerically solving the relevant Poisson equation as a nonlinear equation for the unknown potential ψ. The code which implements the iteration procedure described in Sect. 4.3.2 starts with the calculation of the "seed solution", given by a selected spherical configuration from the family of models that represent the limit in the case of vanishing internal rotation of the family of interest (i.e., defined by Eqs. (4.64) and (4.62), respectively). Such spherical solution is used, in the first step of the iteration, to evaluate (by means of a Double Gaussian Quadrature) the density distribution, given by $\hat{\rho}_{WT}$ or $\hat{\rho}_{PT}$, on a spherical grid in the meridional plane, defined by (r_i, θ_j). The grid is linear in the radial coordinate and the angular positions are defined by

$$\theta_j = \frac{\pi(2j+1)}{4\, l_{max}}\,, \tag{B.1}$$

where $j = 1, ..., 2l_{max} + 1$. Typically, we used ≈ 300 radial steps and we set $l_{max} = 21$, in order to have sufficient accuracy to describe the complex morphologies of the configurations in the rapid and extreme rotation regimes. The discrete direct and inverse Legendre transforms, required at each step of the iteration for the calculation of the density and potential coefficients, defined by Eqs. (4.28)-(4.27), are performed (up to the order l_{max}) by means of a package based on S2kit 1.0 by Kostelec & Rockmore (2004), which makes use of FFTW 3.2.1 by Frigo & Johnston (2005). The Cauchy problems for the potential

radial functions expressed in Eqs. (4.33)-(4.34) are evaluated by means of a numerical integration with Romberg's rule. The convergence condition for the solution at the n-th step of the iteration is formally defined as

$$\frac{\psi_{ij}^{(n)} - \psi_{ij}^{(n-1)}}{\psi_{ij}^{(n)}} < 10^{-3} \,, \tag{B.2}$$

for every i, j, where $\psi_{ij}^{(n)} = \psi^{(n)}(r_i, \theta_j)$; about 10 (25) iteration steps are needed for the construction of configurations characterized by low (high) values of χ. The accuracy of the solutions found with our code has been checked by the following tests: (i) the virial theorem is satisfied with accuracy of the order of 10^{-4} or better; (2) the radial component of the Jeans equation is satisfied with the accuracy of the order of 10^{-3} or better; (3) the asymptotic behaviors, both in the central and in the outer parts, of all the moments of the distribution function are confirmed.

Bibliography

Aarseth, S. J. 1969, *Mon. Not. R. Astron. Soc.*, 144, 537

Aarseth, S. J. 1999, *Publ. Astron. Soc. Pac.*, 111, 1333

Aarseth, S. J. & Heggie, D. C. 1998, *Mon. Not. R. Astron. Soc.*, 297, 794

Abramowitz, M. & Stegun, I. A. 1965, Handbook of mathematical functions with formulas, graphs, and mathematical tables (Dover Books on Advanced Mathematics, Mineola, NY)

Agekian, T. A. 1958, *Soviet. Astron.*, 2, 22

Aguilar, L. A. & Merritt, D. 1990, *Astrophys. J.*, 354, 33

Akiyama, K. & Sugimoto, D. 1989, *Publ. Astron. Soc. Jpn.*, 41, 991

Anderson, J. & King, I. R. 2003, *Astron. J.*, 126, 772

Anderson, J. & van der Marel, R. P. 2010, *Astrophys. J.*, 710, 1032

Arena, S. E. & Bertin, G. 2007, *Astron. Astrophys.*, 463, 921

Ashman, K. & Zepf, S. 2008, Globular Cluster Systems, Cambridge Astrophysics (Cambridge University Press)

Attico, N. & Pegoraro, F. 1999, Physics of Plasmas, 6, 767

Bahcall, J. N. & Wolf, R. A. 1976, *Astrophys. J.*, 209, 214

Barmby, P., McLaughlin, D. E., Harris, W. E., Harris, G. L. H., & Forbes, D. A. 2007, *Astron. J.*, 133, 2764

Barnes, J. & Hut, P. 1986, *Nature*, 324, 446

Baumgardt, H. 2001, *Mon. Not. R. Astron. Soc.*, 325, 1323

Baumgardt, H., Grebel, E. K., & Kroupa, P. 2005a, *Mon. Not. R. Astron. Soc.*, 359, L1

Baumgardt, H., Hut, P., Makino, J., McMillan, S., & Portegies Zwart, S. 2003, *Astrophys. J. Lett.*, 582, L21

Baumgardt, H. & Makino, J. 2003, *Mon. Not. R. Astron. Soc.*, 340, 227

Baumgardt, H., Makino, J., & Hut, P. 2005b, *Astrophys. J.*, 620, 238

Bekki, K. 2010, *Astrophys. J. Lett.*, 724, L99

Bellazzini, M., Bragaglia, A., Carretta, E., et al. 2012, *Astron. Astrophys.*, 538, A18

Bellazzini, M., Ibata, R. A., Chapman, S. C., et al. 2008, *Astron. J.*, 136, 1147

Bellini, A., Piotto, G., Bedin, L. R., et al. 2009, *Astron. Astrophys.*, 493, 959

Bender, Orszag, S. A. C. M. 1999, Advanced mathematical methods for scientists and engineers I: asymptotic methods and perturbation theory.

Berman, R. H. & Mark, J. W.-K. 1979, *Astron. Astrophys.*, 77, 31

Bertin, G. 2000, Dynamics of Galaxies (Cambridge University Press, Cambridge, UK)

Bertin, G., Ciotti, L., & Del Principe, M. 2002, *Astron. Astrophys.*, 386, 149
Bertin, G., Liseikina, T., & Pegoraro. 2003, *Astron. Astrophys.*, 405, 73
Bertin, G. & Stiavelli, M. 1993, Rep. Prog. Phys., 56, 493
Bertin, G. & Trenti, M. 2003, *Astrophys. J.*, 584, 729
Bertin, G. & Varri, A. L. 2008, *Astrophys. J.*, 689, 1005
Binney, J. 1978, *Mon. Not. R. Astron. Soc.*, 183, 501
Boily, C. M. 2000, in *Astron. Soc. Pac. Conf. Ser.*, Vol. 211, Massive Stellar Clusters, ed. A. Lançon & C. M. Boily, 190
Bono, G., Stetson, P. B., Sanna, N., et al. 2008, *Astrophys. J. Lett.*, 686, L87
Bontekoe, T. R. & van Albada, T. S. 1987, *Mon. Not. R. Astron. Soc.*, 224, 349
Brodie, J. P., Romanowsky, A. J., Strader, J., & Forbes, D. A. 2011, *Astron. J.*, 142, 199
Carretta, E., Bragaglia, A., Gratton, R. G., et al. 2009, *Astron. Astrophys.*, 505, 117
Centrella, J. M., New, K. C. B., Lowe, L. L., & Brown, J. D. 2001, *Astrophys. J. Lett.*, 550, L193
Chandrasekhar, S. 1933, *Mon. Not. R. Astron. Soc.*, 93, 390
Chandrasekhar, S. 1939, An introduction to the study of stellar structure (The University of Chicago Press, Chicago, IL)
Chandrasekhar, S. 1942, Principles of stellar dynamics (The University of Chicago Press, Chicago, IL)
Chandrasekhar, S. 1969, Ellipsoidal figures of equilibrium (Yale University Press, New Haven)
Chandrasekhar, S. & Lebovitz, N. R. 1962, *Astrophys. J.*, 136, 1082
Chen, C. W. & Chen, W. P. 2010, *Astrophys. J.*, 721, 1790
Chernoff, D. F. & Weinberg, M. D. 1990, *Astrophys. J.*, 351, 121
Christodoulou, D. M., Kazanas, D., Shlosman, I., & Tohline, J. E. 1995a, *Astrophys. J.*, 446, 472
Christodoulou, D. M., Kazanas, D., Shlosman, I., & Tohline, J. E. 1995b, *Astrophys. J.*, 446, 485
Ciotti, L. & Bertin, G. 2005, *Astron. Astrophys.*, 437, 419
Cohn, H. 1980, *Astrophys. J.*, 242, 765
Cote, P., Welch, D. L., Fischer, P., & Gebhardt, K. 1995, *Astrophys. J.*, 454, 788
Davies, R. L., Efstathiou, G., Fall, S. M., Illingworth, G., & Schechter, P. L. 1983, *Astrophys. J.*, 266, 41
Davoust, E. 1977, *Astron. Astrophys.*, 61, 391
Davoust, E. & Prugniel, P. 1990, *Astron. Astrophys.*, 230, 67
de Zeeuw, T. 1985, *Mon. Not. R. Astron. Soc.*, 216, 273
D'Ercole, A., D'Antona, F., Ventura, P., Vesperini, E., & McMillan, S. L. W. 2010, *Mon. Not. R. Astron. Soc.*, 407, 854
Di Cecco, A., Zocchi, A., Varri, A. L., et al. 2012, *Astrophys. J. Lett.*
Djorgovski, S. 1993, in Astronomical Society of the Pacific Conference Series, Vol. 50, Structure and Dynamics of Globular Clusters, ed. S. G. Djorgovski & G. Meylan, 373
Djorgovski, S. & Meylan, G. 1994, *Astron. J.*, 108, 1292
Drukier, G. A., Cohn, H. N., Lugger, P. M., et al. 2007, *Astron. J.*, 133, 1041
D'Souza, R. & Rix, H.-W. 2005, ArXiv Astrophysics e-prints
Edmonds, A. R. 1960, Angular Momentum in Quantum Mechanics (Princeton University Press, Princeton, NJ)
Einsel, C. & Spurzem, R. 1999, *Mon. Not. R. Astron. Soc.*, 302, 81

Elson, R. A. W., Fall, S. M., & Freeman, K. C. 1987, *Astrophys. J.*, 323, 54
Emsellem, E., Cappellari, M., Krajnović, D., et al. 2011, *Mon. Not. R. Astron. Soc.*, 414, 888
Ernst, A., Glaschke, P., Fiestas, J., Just, A., & Spurzem, R. 2007, *Mon. Not. R. Astron. Soc.*, 377, 465
Ernst, A., Just, A., Spurzem, R., & Porth, O. 2008, *Mon. Not. R. Astron. Soc.*, 383, 897
Evans, N. W. 1993, *Mon. Not. R. Astron. Soc.*, 260, 191
Faá di Bruno, C. F. 1855, in Annali di Scienze Matematiche e Fisiche, ed. B. Tortolini, Vol. 6, 476
Fall, S. M. & Frenk, C. S. 1985, in *IAU Symp.*, Vol. 113, Dynamics of Star Clusters, ed. J. Goodman & P. Hut, 285
Fiestas, J., Spurzem, R., & Kim, E. 2006, *Mon. Not. R. Astron. Soc.*, 373, 677
Fischer, P., Welch, D. L., Mateo, M., & Cote, P. 1993, *Astron. J.*, 106, 1508
Franx, M. 1988, *Mon. Not. R. Astron. Soc.*, 231, 285
Frenk, C. S. & Fall, S. M. 1982, *Mon. Not. R. Astron. Soc.*, 199, 565
Frigo, M. & Johnson, S. G. 2005, *IEEE Proc.*, 93, 216
Fukushige, T. & Heggie, D. C. 2000, *Mon. Not. R. Astron. Soc.*, 318, 753
Gaburov, E., Harfst, S., & Portegies Zwart, S. 2009, *New Astron.*, 14, 630
Gebhardt, K., Pryor, C., O'Connell, R. D., Williams, T. B., & Hesser, J. E. 2000, *Astron. J.*, 119, 1268
Gebhardt, K., Pryor, C., Williams, T. B., & Hesser, J. E. 1995, *Astron. J.*, 110, 1699
Geroyannis, V. S. 1990, *Astrophys. J.*, 350, 355
Gerssen, J., van der Marel, R. P., Gebhardt, K., et al. 2002, *Astron. J.*, 124, 3270
Geyer, E. H., Nelles, B., & Hopp, U. 1983, *Astron. Astrophys.*, 125, 359
Gieles, M. & Baumgardt, H. 2008, *Mon. Not. R. Astron. Soc.*, 389, L28
Giersz, M. 1998, *Mon. Not. R. Astron. Soc.*, 298, 1239
Giersz, M. 2001, *Mon. Not. R. Astron. Soc.*, 324, 218
Giersz, M. & Heggie, D. C. 1997, *Mon. Not. R. Astron. Soc.*, 286, 709
Giersz, M. & Heggie, D. C. 2011, *Mon. Not. R. Astron. Soc.*, 410, 2698
Goodman, J. J. 1983, PhD thesis, Princeton Univ., NJ.
Goodwin, S. P. 1997, *Mon. Not. R. Astron. Soc.*, 286, L39
Gott, III, R. J. 1973, *Astrophys. J.*, 186, 481
Gunn, J. E. & Griffin, R. F. 1979, *Astron. J.*, 84, 752
Hachisu, I. 1979, *Publ. Astron. Soc. Jpn.*, 31, 523
Hachisu, I. 1986, *Astrophys. J. Suppl.*, 62, 461
Han, C. & Ryden, B. S. 1994, *Astrophys. J.*, 433, 80
Harris, W. E. 2010, ArXiv e-prints
Harris, W. E., Harris, G. L. H., Barmby, P., McLaughlin, D. E., & Forbes, D. A. 2006, *Astron. J.*, 132, 2187
Harris, W. E., Harris, G. L. H., Holland, S. T., & McLaughlin, D. E. 2002, *Astron. J.*, 124, 1435
Heggie, D. & Hut, P. 2003, The Gravitational Million-Body Problem: A Multidisciplinary Approach to Star Cluster Dynamics (Cambridge University Press, Cambridge UK)
Heggie, D. C. & Ramamani, N. 1995, *Mon. Not. R. Astron. Soc.*, 272, 317
Hénon, M. 1971, *Astrophys. Space Sci.*, 13, 284
Hénon, M. 1975, in IAU Symposium, Vol. 69, Dynamics of the Solar Systems, ed. A. Hayli, 133

Hill, A. & Zaritsky, D. 2006, *Astron. J.*, 131, 414
Hohl, F. 1971, *Astrophys. J.*, 168, 343
Houser, J. L., Centrella, J. M., & Smith, S. C. 1994, *Phys. Rev. Lett.*, 72, 1314
Hunter, C. 1977, *Astron. J.*, 82, 271
Hunter, C. 2001, *Mon. Not. R. Astron. Soc.*, 328, 839
Ibata, R., Bellazzini, M., Chapman, S. C., et al. 2009, *Astrophys. J. Lett.*, 699, L169
Ibata, R., Sollima, A., Nipoti, C., et al. 2011, *Astrophys. J.*, 738, 186
Jackson, J. 1999, Classical Electrodynamics (Wiley)
Jalali, B., Baumgardt, H., Kissler-Patig, M., et al. 2012, *Astron. Astrophys.*, 538, A19
James, R. A. 1964, *Astrophys. J.*, 140, 552
Jarvis, B. J. & Freeman, K. C. 1985, *Astrophys. J.*, 295, 314
Jeans, J. H. 1928, Astronomy and cosmogony (Cambridge University Press, Cambridge UK)
Jedrzejewski, R. I. 1987, *Mon. Not. R. Astron. Soc.*, 226, 747
Johnstone, D. 1993, *Astron. J.*, 105, 155
Jordi, K. & Grebel, E. K. 2010, *Astron. Astrophys.*, 522, A71
Joshi, K. J., Rasio, F. A., & Portegies Zwart, S. 2000, *Astrophys. J.*, 540, 969
Karino, S. & Eriguchi, Y. 2003, *Astrophys. J.*, 592, 1119
Kim, E., Einsel, C., Lee, H. M., Spurzem, R., & Lee, M. G. 2002, *Mon. Not. R. Astron. Soc.*, 334, 310
Kim, E., Yoon, I., Lee, H. M., & Spurzem, R. 2008, *Mon. Not. R. Astron. Soc.*, 383, 2
King, I. R. 1961, *Astron. J.*, 66, 68
King, I. R. 1966, *Astron. J.*, 71, 64
Kormendy, J. & Anand, S. P. S. 1971, *Astrophys. Space Sci.*, 12, 47
Kostelec, P. J. & Rockmore, D. N. 2004, S2kit: A Lite Version of the Spharmonic Kit
Krogdahl, W. 1942, *Astrophys. J.*, 96, 124
Kruszewski, A. 1963, *Acta Astron.*, 13, 106
Kundic, T. & Ostriker, J. P. 1995, *Astrophys. J.*, 438, 702
Küpper, A. H. W., Kroupa, P., Baumgardt, H., & Heggie, D. C. 2010a, *Mon. Not. R. Astron. Soc.*, 407, 2241
Küpper, A. H. W., Kroupa, P., Baumgardt, H., & Heggie, D. C. 2010b, *Mon. Not. R. Astron. Soc.*, 401, 105
Küpper, A. H. W., Lane, R. R., & Heggie, D. C. 2012, *Mon. Not. R. Astron. Soc.*, 420, 2700
Küpper, A. H. W., MacLeod, A., & Heggie, D. C. 2008, *Mon. Not. R. Astron. Soc.*, 387, 1248
Lagoute, C. & Longaretti, P.-Y. 1996, *Astron. Astrophys.*, 308, 441
Lai, D., Rasio, F. A., & Shapiro, S. L. 1993, *Astrophys. J. Suppl.*, 88, 205
Landau, L. D. & Lifshitz, E. M. 1969, Statistical physics. Pt.1 (Pergamon Press, Oxford, UK)
Lane, R. R., Brewer, B. J., Kiss, L. L., et al. 2010a, *Astrophys. J. Lett.*, 711, L122
Lane, R. R., Kiss, L. L., Lewis, G. F., et al. 2009, *Mon. Not. R. Astron. Soc.*, 400, 917
Lane, R. R., Kiss, L. L., Lewis, G. F., et al. 2010b, *Mon. Not. R. Astron. Soc.*, 401, 2521
Lane, R. R., Kiss, L. L., Lewis, G. F., et al. 2010c, *Mon. Not. R. Astron. Soc.*, 406, 2732
Lane, R. R., Kiss, L. L., Lewis, G. F., et al. 2011, *Astron. Astrophys.*, 530, A31
Lane, R. R., Küpper, A. H. W., & Heggie, D. C. 2012, *Mon. Not. R. Astron. Soc.*, 423, 2845
Lanzoni, B., Dalessandro, E., Perina, S., et al. 2007, *Astrophys. J.*, 670, 1065
Le Poole, R. S. & van Leeuwen, F. 2002, in Astronomical Society of the Pacific Conference

Series, Vol. 265, Omega Centauri, A Unique Window into Astrophysics, ed. F. van Leeuwen, J. D. Hughes, & G. Piotto, 31
Lee, K. H., Lee, H. M., & Sung, H. 2006a, *Mon. Not. R. Astron. Soc.*, 367, 646
Lee, K. H., Lee, H. M., & Sung, H. 2006b, *Mon. Not. R. Astron. Soc.*, 367, 646
Limber, D. N. 1963, *Astrophys. J.*, 138, 1112
Łokas, E. L., Majewski, S. R., Kazantzidis, S., et al. 2012, *Astrophys. J.*, 751, 61
Longaretti, P.-Y. & Lagoute, C. 1996, *Astron. Astrophys.*, 308, 453
Louis, P. D. & Spurzem, R. 1991, *Mon. Not. R. Astron. Soc.*, 251, 408
Lupton, R. H. & Gunn, J. E. 1987, *Astron. J.*, 93, 1106
Lupton, R. H., Gunn, J. E., & Griffin, R. F. 1987, *Astron. J.*, 93, 1114
Lützgendorf, N., Kissler-Patig, M., Noyola, E., et al. 2011, *Astron. Astrophys.*, 533, A36
Lynden-Bell, D. 1962, *Mon. Not. R. Astron. Soc.*, 123, 447
Lynden-Bell, D. 1967, *Mon. Not. R. Astron. Soc.*, 136, 101
Lynden-Bell, D. & Eggleton, P. P. 1980, *Mon. Not. R. Astron. Soc.*, 191, 483
Mackey, A. D. & Gilmore, G. F. 2003a, *Mon. Not. R. Astron. Soc.*, 338, 120
Mackey, A. D. & Gilmore, G. F. 2003b, *Mon. Not. R. Astron. Soc.*, 338, 85
Mackey, A. D. & Gilmore, G. F. 2003c, *Mon. Not. R. Astron. Soc.*, 340, 175
Madrid, J. P., Harris, W. E., Blakeslee, J. P., & Gómez, M. 2009, *Astrophys. J.*, 705, 237
Makino, J., Akiyama, K., & Sugimoto, D. 1991, *Astrophys. Space Sci.*, 185, 63
Makino, J., Fukushige, T., Koga, M., & Namura, K. 2003, *Publ. Astron. Soc. Jpn.*, 55, 1163
Mayor, M., Meylan, G., Udry, S., et al. 1997, *Astron. J.*, 114, 1087
McLaughlin, D. E., Anderson, J., Meylan, G., et al. 2006, *Astrophys. J. Suppl.*, 166, 249
McLaughlin, D. E., Barmby, P., Harris, W. E., Forbes, D. A., & Harris, G. L. H. 2008, *Mon. Not. R. Astron. Soc.*, 384, 563
McLaughlin, D. E. & van der Marel, R. P. 2005, *Astrophys. J. Suppl.*, 161, 304
McNamara, B. J., Harrison, T. E., & Anderson, J. 2003, *Astrophys. J.*, 595, 187
McNamara, B. J., Harrison, T. E., & Baumgardt, H. 2004, *Astrophys. J.*, 602, 264
Merritt, D., Meylan, G., & Mayor, M. 1997, *Astron. J.*, 114, 1074
Meylan, G. & Heggie, D. C. 1997, *Astron. Astrophys. Rev.*, 8, 1
Meylan, G. & Mayor, M. 1986, *Astron. Astrophys.*, 166, 122
Meylan, G. & Mayor, M. 1991, *Astron. Astrophys.*, 250, 113
Meylan, G., Mayor, M., Duquennoy, A., & Dubath, P. 1995, *Astron. Astrophys.*, 303, 761
Michie, R. W. 1963, *Mon. Not. R. Astron. Soc.*, 125, 127
Milne, E. A. 1923, *Mon. Not. R. Astron. Soc.*, 83, 118
Misgeld, I. & Hilker, M. 2011, *Mon. Not. R. Astron. Soc.*, 414, 3699
Moffat, J. W. & Toth, V. T. 2008, *Astrophys. J.*, 680, 1158
Monaghan, F. F. & Roxburgh, I. W. 1965, *Mon. Not. R. Astron. Soc.*, 131, 13
Murphy, B. W., Cohn, H. N., & Durisen, R. H. 1991, *Astrophys. J.*, 370, 60
Murphy, B. W., Cohn, H. N., & Lugger, P. M. 2011, *Astrophys. J.*, 732, 67
New, K. C. B., Centrella, J. M., & Tohline, J. E. 2000, *Phys. Rev. D*, 62, 064019
Noyola, E. & Baumgardt, H. 2011, *Astrophys. J.*, 743, 52
Noyola, E. & Gebhardt, K. 2006, *Astron. J.*, 132, 447
Noyola, E., Gebhardt, K., & Bergmann, M. 2008, *Astrophys. J.*, 676, 1008
Oh, K. S. & Lin, D. N. C. 1992, *Astrophys. J.*, 386, 519
Ostriker, J. P. & Peebles, P. J. E. 1973, *Astrophys. J.*, 186, 467
Ou, S. & Tohline, J. E. 2006, *Astrophys. J.*, 651, 1068

Pancino, E., Galfo, A., Ferraro, F. R., & Bellazzini, M. 2007, *Astrophys. J. Lett.*, 661, L155
Papaloizou, J. C. B. & Pringle, J. E. 1985, *Mon. Not. R. Astron. Soc.*, 213, 799
Peterson, R. C. & Cudworth, K. M. 1994, *Astrophys. J.*, 420, 612
Portegies Zwart, S. F., McMillan, S. L. W., Hut, P., & Makino, J. 2001, *Mon. Not. R. Astron. Soc.*, 321, 199
Prendergast, K. H. & Tomer, E. 1970, *Astron. J.*, 75, 674
Press, W. H., Teukolsky, S. A., Vetterling, W. T., & Flannery, B. P. 1992, Numerical recipes in FORTRAN. The art of scientific computing (Cambridge University Press, Cambridge, UK)
Pryor, C. & Meylan, G. 1993, in Astronomical Society of the Pacific Conference Series, Vol. 50, Structure and Dynamics of Globular Clusters, ed. S. G. Djorgovski & G. Meylan, 357
Reijns, R. A., Seitzer, P., Arnold, R., et al. 2006, *Astron. Astrophys.*, 445, 503
Rowley, G. 1988, *Astrophys. J.*, 331, 124
Ryden, B. S. 1991, *Mon. Not. R. Astron. Soc.*, 253, 743
Ryden, B. S. 1996, *Astrophys. J.*, 461, 146
Saijo, M., Baumgarte, T. W., & Shapiro, S. L. 2003, *Astrophys. J.*, 595, 352
Saijo, M. & Yoshida, S. 2006, *Mon. Not. R. Astron. Soc.*, 368, 1429
Sanders, R. H. 2012, *Mon. Not. R. Astron. Soc.*, 419, L6
Sariya, D. P., Yadav, R. K. S., & Bellini, A. 2012, ArXiv e-prints
Schwarzschild, M. 1979, *Astrophys. J.*, 232, 236
Schwarzschild, M. 1982, *Astrophys. J.*, 263, 599
Shapiro, S. L. & Marchant, A. B. 1976, *Astrophys. J.*, 210, 757
Shibata, M., Karino, S., & Eriguchi, Y. 2002, *Mon. Not. R. Astron. Soc.*, 334, L27
Shibata, M., Karino, S., & Eriguchi, Y. 2003, *Mon. Not. R. Astron. Soc.*, 343, 619
Smith, B. L. 1975, *Astrophys. Space Sci.*, 35, 223
Smith, B. L. 1976, *Astrophys. Space Sci.*, 43, 411
Sollima, A., Bellazzini, M., & Lee, J.-W. 2012, ArXiv e-prints
Sollima, A., Bellazzini, M., Smart, R. L., et al. 2009, *Mon. Not. R. Astron. Soc.*, 396, 2183
Spitzer, L. 1987, Dynamical evolution of globular clusters (Princeton University Press, Princeton, NJ)
Spitzer, Jr., L. & Hart, M. H. 1971, *Astrophys. J.*, 166, 483
Springel, V., Yoshida, N., & White, S. D. M. 2001, *New Astron.*, 6, 79
Spurzem, R. 1999, Journal of Computational and Applied Mathematics, 109, 407
Stark, A. A. 1977, *Astrophys. J.*, 213, 368
Stoeckly, R. 1965, *Astrophys. J.*, 142, 208
Takahashi, K. & Lee, H. M. 2000, *Mon. Not. R. Astron. Soc.*, 316, 671
Takahashi, K., Lee, H. M., & Inagaki, S. 1997a, *Mon. Not. R. Astron. Soc.*, 292, 331
Takahashi, K., Lee, H. M., & Inagaki, S. 1997b, *Mon. Not. R. Astron. Soc.*, 292, 331
Tassoul, J.-L. 1978, Theory of rotating stars (Princeton University Press, Princeton, NJ)
Teuben, P. 1995, in Astronomical Society of the Pacific Conference Series, Vol. 77, Astronomical Data Analysis Software and Systems IV, ed. R. A. Shaw, H. E. Payne, & J. J. E. Hayes, 398
Tohline, J. E., Durisen, R. H., & McCollough, M. 1985, *Astrophys. J.*, 298, 220
Toomre, A. 1982, *Astrophys. J.*, 259, 535
Trager, S. C., King, I. R., & Djorgovski, S. 1995, *Astron. J.*, 109, 218

Trenti, M. & Bertin, G. 2005, *Astron. Astrophys.*, 429, 161
Trenti, M., Bertin, G., & van Albada, T. S. 2005, *Astron. Astrophys.*, 433, 57
Trenti, M., Vesperini, E., & Pasquato, M. 2010, *Astrophys. J.*, 708, 1598
van Albada, T. S. 1982, *Mon. Not. R. Astron. Soc.*, 201, 939
van de Ven, G., van den Bosch, R. C. E., Verolme, E. K., & de Zeeuw, P. T. 2006, *Astron. Astrophys.*, 445, 513
van den Bergh, S. 2008, *Astron. J.*, 135, 1731
van den Bosch, R., de Zeeuw, T., Gebhardt, K., Noyola, E., & van de Ven, G. 2006, *Astrophys. J.*, 641, 852
van der Marel, R. P. & Anderson, J. 2010, *Astrophys. J.*, 710, 1063
Van Dyke, M. 1975, Perturbation Methods in Fluid Mechanics (Parabolic Press, Stanford, CA)
van Leeuwen, F., Le Poole, R. S., Reijns, R. A., Freeman, K. C., & de Zeeuw, P. T. 2000, *Astron. Astrophys.*, 360, 472
Vandervoort, P. O. 1980, *Astrophys. J.*, 240, 478
Vandervoort, P. O. 1982, *Astrophys. J. Lett.*, 256, L41
Vandervoort, P. O. 1991, *Astrophys. J.*, 377, 49
Vandervoort, P. O. & Welty, D. E. 1982, *Astrophys. J.*, 263, 654
Varri, A. L. & Bertin, G. 2009, *Astrophys. J.*, 703, 1911
Varri, A. L. & Bertin, G. 2012, *Astron. Astrophys.*, 540, A94
Vasilevskis, S., van Leeuwen, F., Nicholson, W., & Murray, C. A. 1979, *Astron. Astrophys. Supp. Ser.*, 37, 333
Vesperini, E., McMillan, S. L. W., & Portegies Zwart, S. 2009, *Astrophys. J.*, 698, 615
Vesperini, E. & Trenti, M. 2010, *Astrophys. J. Lett.*, 720, L179
Watts, A. L., Andersson, N., Beyer, H., & Schutz, B. F. 2003, *Mon. Not. R. Astron. Soc.*, 342, 1156
Watts, A. L., Andersson, N., & Jones, D. I. 2005, *Astrophys. J. Lett.*, 618, L37
Watts, A. L., Andersson, N., & Williams, R. L. 2004, *Mon. Not. R. Astron. Soc.*, 350, 927
Webb, J. J., Sills, A., & Harris, W. E. 2012, *Astrophys. J.*, 746, 93
Weinberg, M. D. 1993, in *Astron. Soc. Pac. Conf. Ser.*, Vol. 48, The Globular Cluster-Galaxy Connection, ed. G. H. Smith & J. P. Brodie, 689
Werchan, F. & Zaritsky, D. 2011, *Astron. J.*, 142, 48
White, R. E. & Shawl, S. J. 1987, *Astrophys. J.*, 317, 246
Wielen, R. 1974, in Stars and the Milky Way System, ed. L. N. Mavridis, 326
Wilkinson, M. I., Kleyna, J., Evans, N. W., & Gilmore, G. 2002, *Mon. Not. R. Astron. Soc.*, 330, 778
Wilson, C. P. 1975, *Astron. J.*, 80, 175
Woodley, K. A., Goldsbury, R., Kalirai, J. S., et al. 2012, *Astron. J.*, 143, 50
Woolley, R. v. d. R. & Dickens, R. J. 1962, *Roy. Obs. Bull.*, 54
Zang, T. A. & Hohl, F. 1978, *Astrophys. J.*, 226, 521
Zocchi, A., Bertin, G., & Varri, A. L. 2012, *Astron. Astrophys.*, 539, A65
Zonoozi, A. H., Küpper, A. H. W., Baumgardt, H., et al. 2011, *Mon. Not. R. Astron. Soc.*, 411, 1989

List of Publications

As of June 2012

Refereed publications

- "Self-consistent models of quasi-relaxed rotating stellar systems"
  Varri, A. L., & Bertin, G., *Astron. Astrophys.*, 540, A94 (2012)
  (Chapter 4)

- "A dynamical study of Galactic globular clusters in different relaxation conditions"
  Zocchi, A., Bertin, G., **Varri, A. L.**, *Astron. Astrophys.*, 539, A65 (2012)
  (Chapter 8)

- "Properties of quasi-relaxed stellar systems in an external tidal field"
  Varri, A. L., & Bertin, G., *Astrophys. J.*, 703, 1911-1922 (2009).
  (Chapter 3)

- "The construction of nonspherical models for quasi-relaxed stellar systems"
  Bertin, G., & **Varri, A. L.**, *Astrophys. J.*, 689, 1005-1019 (2008).
  (Chapter 2)

Publications under review

- "On the density profiles of the globular cluster M92"
  Di Cecco, A., Zocchi, A., **Varri, A. L.**, Monelli, M., Bertin, G., Bono, G., Stetson, P. B., Buonanno, R., Ferraro, I., Iannicola, G., Kunder, A., Walker, A. R., submitted to *Astrophys. J. Lett.*

Publications in preparation

- "Low $T/|W|$ dynamical instability in differentially rotating stellar systems"
  Varri, A. L., Vesperini, E., McMillan, S. L. W., Bertin, G., to be submitted to *Astrophys. J. Lett.*
  (Chapter 5)

- "Rotating globular clusters"
  Bianchini, P., **Varri, A. L.**, Bertin, G., Zocchi, A., to be submitted to *Astron. Astrophys.*
  (Chapter 7)

- "Long-term evolution of rotating stellar systems - I. Isolated models"
  Varri, A. L., Vesperini, E., McMillan, S. L. W., Bertin, G.
  (Chapter 6)

Publications in conference proceedings

- "Models of partially relaxed and quasi-relaxed stellar systems"
  Bertin, G., **Varri, A. L.**, & Amorisco, N. C. "Recent Developments in Theoretical and Experimental General Relativity, Astrophysics, and Relativistic Field Theories", eds. T. Damour, and R. T. Jantzen, World Scientific Publishing, 2098-2100 (2012).

- "Dynamical stability and long term evolution of rotating stellar systems"
  Varri, A. L., Vesperini, E., McMillan, S. L. W., Bertin, G., *Bull. Ast. Soc.*, 43, 133.13 (2011).

- "Tides, rotation, and anisotropy: new self-consistent nonspherical models for globular clusters"
  Varri, A. L., & Bertin, G., *Bull. Ast. Soc.*, 43, 152.10 (2011).

- "Self-consistent models of quasi-relaxed rotating stellar systems"
  Varri, A. L., & Bertin, G., "Plasmas in the Laboratory and in the Universe: interactions, patterns, and turbulence", eds. G. Bertin, F. De Luca, G. Lodato, and M. Romé, *AIP Conf. Proc.*, 1242, 148-155 (2010).